Neutron star clues in tin nuclei pp. 232 & 260

Environment shapes behavior in human and nonhuman animals pp. 235 & 292

Combating "inactivism" in the climate fight p. 242

Science

$15
15 JANUARY 2021
sciencemag.org

AAAS



WIDE EYE SHUT

The death—and possible rebirth—of the Arecibo telescope p. 225

TRILLIONS OF MICROBES ONE ESSAY

The NOSTER *Science* Microbiome Prize is an international prize that rewards innovative research by investigators, under the age of 35, who are working on the functional attributes of the microbiota. The research can include any organism that has potential to contribute to our understanding of human or veterinary health and disease, or to guide therapeutic interventions. The winner and finalists will be chosen by a committee of independent scientists, chaired by a senior editor at *Science*. The top prize includes a complimentary membership to AAAS, an online subscription to *Science*, and $25,000 (USD). Submit your research essay today.



Oliver Harrison
2020 Grand Prize Winner

NOSTER | Science
MICROBIOME
PRIZE

Apply by 1/24/21 at www.sciencemag.org/noster

Sponsored by Noster Inc.

CONTENTS



15 JANUARY 2021 • VOLUME 371 • ISSUE 6526

225
On 1 December 2020, four cables snapped, and an icon was gone.

PHOTO: COURTESY OF THE ARECIBO OBSERVATORY, A U.S. NATIONAL SCIENCE FOUNDATION FACILITY

NEWS

IN BRIEF

216 News at a glance

IN DEPTH

218 Science could benefit as Democrats take power
Major shifts on climate and science policy expected, but political obstacles abound
By D. Malakoff and J. Mervis

219 Are monarchs in trouble?
U.S. mulls protection for iconic butterfly, but some experts say fears overblown
By E. Pennisi

221 Anemone shows mechanism of rapid evolution
Single genetic switch converts stinging cells into sticky ones that cling to surfaces
By E. Pennisi

222 Pandemic could mark 'turning point' for Chinese science
Despite missteps and government control, early findings guided other countries' fight against the coronavirus *By D. Normile*

223 Q&A: How to market vaccination
A business expert offers tips for "selling" COVID-19 vaccines *By W. Cornwall*

224 COVID-19 measures also suppress flu—for now
In downside, trend could weaken immunity and complicate vaccine formulation *By K. Servick*

FEATURES

225 Fallen giant
Engineering failures and a harsh climate conspired in the sudden collapse of the Arecibo telescope. Now, researchers are planning a rebirth *By D. Clery*
PODCAST

INSIGHTS

PERSPECTIVES

230 Herd immunity by infection is not an option
Difficult lessons are learned from a largely uncontrolled COVID-19 epidemic in Manaus, Brazil *By D. Sridhar and D. Gurdasani*
REPORT P. 288

232 From nuclear clusters to neutron stars
Measurements of α cluster formation in nuclear "skins" can improve neutron star models *By O. Hen*
REPORT P. 260

233 The language of a virus
Viral fitness and its immune escape can be modeled by using concepts of natural language *By Y.-A. Kim and T. M. Przytycka*
REPORT P. 284

234 Targeting metabolism to influence aging
Inhibition of glutamine metabolism promotes death of senescent cells and improves healthy life span in mice *By C. Pan and J. W. Locasale*
REPORT P. 265

235 Behavioral convergence in humans and animals
Local ecology combines with culture to produce behavioral variation in hunter-gatherers *By K. Hill and R. Boyd*
REPORT P. 292

237 Bioactive lipids in antiviral immunity
Lipids may influence entry, replication, and clearance and modulate immune responses
By K. N. Theken and G. A. FitzGerald

POLICY FORUM

239 Tracking, targeting, and conserving soil biodiversity
A monitoring and indicator system can inform policy *By C. A. Guerra* et al.

BOOKS *ET AL.*

242 Fighting the good fight
Fossil fuel advocates may have added strategic inaction to their arsenal, but there is reason for climate optimism
By A. Hollis

243 Deflating the opaque online ad bubble
A lightweight book aims a heavyweight punch at the digital advertising ecosystem
By S. Tadelis

LETTERS

244 Anomalous COVID-19 tests hinder researchers
By L. R. Robinson-McCarthy et al.

245 Data-driven solutions to U.S. polarization
By P. T. Coleman



245 China is pivotal to ocean's future
By A. F. Johnson and S. Lidström

246 Errata

RESEARCH

IN BRIEF

248 From *Science* and other journals

REVIEW

251 Phylodynamics
Phylodynamics for cell biologists
T. Stadler et al.

RESEARCH ARTICLES

252 Antifungal immunity
Aberrant type 1 immunity drives susceptibility to mucosal fungal infections *T. J. Break* et al.

253 Signal transduction
Noncanonical transnitrosylation network contributes to synapse loss in Alzheimer's disease *T. Nakamura* et al.

254 Coronavirus
Transmission heterogeneities, kinetics, and controllability of SARS-CoV-2 *K. Sun* et al.

255 Plant science
Controlled hydroxylations of diterpenoids allow for plant chemical defense without autotoxicity *J. Li* et al.

REPORTS

260 Nuclear physics
Formation of α clusters in dilute neutron-rich matter *J. Tanaka* et al.
PERSPECTIVE P. 232

265 Aging
Senolysis by glutaminolysis inhibition ameliorates various age-associated disorders *Y. Johmura* et al.
PERSPECTIVE P. 234

271 Immunology
GPER1 is required to protect fetal health from maternal inflammation *A. T. Harding* et al.

276 Plant science
Plant roots sense soil compaction through restricted ethylene diffusion *B. K. Pandey* et al.

280 Plasmonic chemistry
Driving energetically unfavorable dehydrogenation dynamics with plasmonics *K. Sytwu* et al.

284 Virology
Learning the language of viral evolution and escape *B. Hie* et al.
PERSPECTIVE P. 233

288 Coronavirus
Three-quarters attack rate of SARS-CoV-2 in the Brazilian Amazon during a largely unmitigated epidemic *L. F. Buss* et al.
PERSPECTIVE P. 230

292 Behavior
Local convergence of behavior across species *T. Barsbai* et al.
PERSPECTIVE P. 235; PODCAST

296 Quantum gases
Topological pumping of a 1D dipolar gas into strongly correlated prethermal states
W. Kao et al.

300 Structural biology
Cryo-EM structure of the B cell co-receptor CD19 bound to the tetraspanin CD81
K. J. Susa et al.

305 RNA splicing
Structure of a transcribing RNA polymerase II–U1 snRNP complex
S. Zhang et al.

DEPARTMENTS

213 Editorial
Public debate is good for science
By H. Holden Thorp

215 Editorial
Stem cells on the ballot
By Lawrence S. B. Goldstein and Robert N. Klein II

314 Working Life
No use in shouting
By Gabriela Goldberg

ON THE COVER

The 305-meter-wide radio dish of Puerto Rico's Arecibo Observatory, as seen from above in the late 1980s. For nearly 60 years, the telescope stood at the vanguard of astronomy, planetary science, and atmospheric science. On 1 December 2020, its heavy instrument platform collapsed after the failure of its suspension cables. Researchers are examining the causes of the disaster even as they advocate for rebuilding. See page 225. *Photo: Bruce Dale/National Geographic Image Sales*



PHOTO: YVAN COHEN/LIGHTROCKET/GETTY IMAGES

Science Staff 214
New Products 310
Science Careers 311

SCIENCE (ISSN 0036-8075) is published weekly on Friday, except last week in December, by the American Association for the Advancement of Science, 1200 New York Avenue, NW, Washington, DC 20005. Periodicals mail postage (publication No. 484460) paid at Washington, DC, and additional mailing offices. Copyright © 2021 by the American Association for the Advancement of Science. The title SCIENCE is a registered trademark of the AAAS. Domestic individual membership, including subscription (12 months): $165 ($74 allocated to subscription). Domestic institutional subscription (51 issues): $2148; Foreign postage extra: Air assist delivery: $98. First class, airmail, student, and emeritus rates on request. Canadian rates with GST available upon request, GST #125488122. Publications Mail Agreement Number 1069624. **Printed in the U.S.A.**
Change of address: Allow 4 weeks, giving old and new addresses and 8-digit account number. **Postmaster:** Send change of address to AAAS, P.O. Box 96178, Washington, DC 20090–6178. **Single-copy sales:** $15 each plus shipping and handling available from backissues.sciencemag.org; bulk rate on request. **Authorization to reproduce** material for internal or personal use under circumstances not falling within the fair use provisions of the Copyright Act can be obtained through the Copyright Clearance Center (CCC), www.copyright.com. The identification code for *Science* is 0036-8075. *Science* is indexed in the *Reader's Guide to Periodical Literature* and in several specialized indexes.

EDITORIAL

Public debate is good for science

In the age of the internet, there's no such thing as a private debate. But is that bad for science? Some scientists have had misgivings. When debates in any sector move beyond the halls of universities and government agencies, there is potential for misuse of information and public confusion. But open debate can also foster communication among scientists and between the scientific community and the public. During the pandemic, open debate on research, health, and policy—whether on television, in newspapers, or on social media—widened public attention and encouraged more diverse voices. If this trend spurs scientists to agree more quickly about the best solutions to our problems—and at the same time helps the public "see" the process of scientific discourse more clearly—then this is good for everyone, including scientists.

I pay attention to scientists' public conversations about COVID-19—including the fast-paced exchanges on Twitter—because my role in communicating science includes amplifying consensus while steering clear of becoming an armchair epidemiologist or immunologist. For most of the pandemic, the trusted experts have generally agreed on issues like social distancing and a rigorous analysis of clinical trial data by the U.S. Food and Drug Administration (FDA) and other agencies. But there have been areas where a consensus has not emerged, such as whether and when to close schools or the usefulness of masks.

More recently, a heated debate has taken place over how to distribute the COVID-19 vaccines. For those that require two shots, should the period between them be stretched so that more people can be vaccinated sooner? Should the second shot be dropped altogether? Should a half-dose of each shot be given to younger folks at less risk for infection? Outstanding scholars have taken different positions on this, and the United Kingdom decided to stretch the interval between doses substantially. The debate led to what seems like a good outcome in the United States: The FDA decided not to deviate from the protocols followed in the phase 3 clinical trials. That makes sense. Right now, the main constraint for mass vaccination lies in the logistics for administering the shots themselves, not in having a sufficient supply of vaccine. The Biden transition team just announced a plan to get more people vaccinated while working to ensure that enough vaccine will be in place for the second shots.

Although this seems like a sound decision, some have questioned the manner in which the debate was conducted. When epidemiologist Michael Mina and sociologist Zeynep Tufekci considered the issue in an op-ed in *The New York Times*, some scientific experts worried that such public speculation might create confusion or lead people to believe that disagreement over the details meant a lack of adequate scientific consensus over the safety and efficacy of the vaccines. Should such discussions take place only in scientific journals? Or only informally on Twitter?

> "...let the debates be transparent and vigorous, wherever they are held."

The anxiety seems misplaced. The days of going to a Gordon Conference or Asilomar and having a confidential debate about scientific issues are gone, and that's for the best because those gatherings were not diverse enough and excluded a lot of important voices. These days, the public can access debates about science regardless of where they take place, so the medium isn't so important anymore. What matters is getting to the right place in terms of the science—deciding what the question should be, the appropriate way of answering it, and the correct interpretation of the data. For many scientists, public debate is a new frontier and it may feel like the Wild West (it may well be). But rather than avoiding such conversations, let the debates be transparent and vigorous, wherever they are held. If we want the public to understand that science is an honorably self-correcting process, let's do away once and for all with the idea that science is a fixed set of facts in a textbook. Instead, let everyone see the noisy, messy deliberations that advance science and lead to decisions that benefit us all.

–H. Holden Thorp



H. Holden Thorp
Editor-in-Chief,
Science journals.
hthorp@aaas.org;
@hholdenthorp

PHOTO: CAMERON DAVIDSON

10.1126/science.abg4685

Science AAAS

Editor-in-Chief Holden Thorp, hthorp@aaas.org

Executive Editor Monica M. Bradford

Editors, Research Valda Vinson, Jake S. Yeston **Editor, Insights** Lisa D. Chong

DEPUTY EDITORS Julia Fahrenkamp-Uppenbrink (UK), Stella M. Hurtley (UK), Phillip D. Szuromi, Sacha Vignieri **SR. EDITORIAL FELLOW** Andrew M. Sugden (UK) **SR. EDITORS** Gemma Alderton (UK), Caroline Ash (UK), Brent Grocholski, Pamela J. Hines, Di Jiang, Marc S. Lavine (Canada), Yevgeniya Nusinovich, Ian S. Osborne (UK), Beverly A. Purnell, L. Bryan Ray, H. Jesse Smith, Keith T. Smith (UK), Jelena Stajic, Peter Stern (UK), Valerie B. Thompson, Brad Wible, Laura M. Zahn **ASSOCIATE EDITORS** Michael A. Funk, Priscilla N. Kelly, Tage S. Rai, Seth Thomas Scanlon (UK), Yury V. Suleymanov **LETTERS EDITOR** Jennifer Sills **LEAD CONTENT PRODUCTION EDITORS** Harry Jach, Lauren Kmec **CONTENT PRODUCTION EDITORS** Amelia Beyna, Jeffrey E. Cook, Chris Filiatreau, Julia Katris, Nida Masiulis, Suzanne M. White **SR. EDITORIAL COORDINATORS** Carolyn Kyle, Beverly Shields **EDITORIAL COORDINATORS** Aneera Dobbins, Joi S. Granger, Jeffrey Hearn, Lisa Johnson, Maryrose Madrid, Ope Martins, Shannon McMahon, Jerry Richardson, Hilary Stewart (UK), Alana Warnke, Alice Whaley (UK), Anita Wynn **PUBLICATIONS ASSISTANTS** Jeremy Dow, Alexander Kief, Ronmel Navas, Brian White **EXECUTIVE ASSISTANT** Jessica Slater **ASI DIRECTOR, OPERATIONS** Janet Clements (UK) **ASI SR. OFFICE ADMINISTRATOR** Jessica Waldock (UK)

News Editor Tim Appenzeller

NEWS MANAGING EDITOR John Travis **INTERNATIONAL EDITOR** Martin Enserink **DEPUTY NEWS EDITORS** Elizabeth Culotta, Lila Guterman, David Grimm, Eric Hand (Europe), David Malakoff **SR. CORRESPONDENTS** Daniel Clery (UK), Jon Cohen, Jeffrey Mervis, Elizabeth Pennisi **ASSOCIATE EDITORS** Jeffrey Brainard, Catherine Matacic **NEWS REPORTERS** Adrian Cho, Jennifer Couzin-Frankel, Jocelyn Kaiser, Kelly Servick, Robert F. Service, Erik Stokstad, Paul Voosen, Meredith Wadman **INTERNS** Lucy Hicks, Cathleen O'Grady **CONTRIBUTING CORRESPONDENTS** Warren Cornwall, Andrew Curry (Berlin), Ann Gibbons, Sam Kean, Eli Kintisch, Kai Kupferschmidt (Berlin), Andrew Lawler, Mitch Leslie, Eliot Marshall, Virginia Morell, Dennis Normile (Shanghai), Elisabeth Pain (Careers), Charles Piller, Michael Price, Tania Rabesandratana (Barcelona), Joshua Sokol, Emily Underwood, Gretchen Vogel (Berlin), Lizzie Wade (Mexico City) **CAREERS** Donisha Adams, Rachel Bernstein (Editor), Katie Langin (Associate Editor) **COPY EDITORS** Julia Cole (Senior Copy Editor), Cyra Master (Copy Chief) **ADMINISTRATIVE SUPPORT** Meagan Weiland

Creative Director Beth Rakouskas

DESIGN MANAGING EDITOR Marcy Atarod **GRAPHICS MANAGING EDITOR** Alberto Cuadra **PHOTOGRAPHY MANAGING EDITOR** William Douthitt **WEB CONTENT STRATEGY MANAGER** Kara Estelle-Powers **DESIGN EDITOR** Chrystal Smith **DESIGNER** Christina Aycock **GRAPHICS EDITOR** Nirja Desai **INTERACTIVE GRAPHICS EDITOR** Kelly Franklin **SENIOR SCIENTIFIC ILLUSTRATORS** Valerie Altounian, Chris Bickel **SCIENTIFIC ILLUSTRATOR** Alice Kitterman **SENIOR GRAPHICS SPECIALISTS** Holly Bishop, Nathalie Cary **SENIOR PHOTO EDITOR** Emily Petersen **PHOTO EDITOR** Kaitlyn Dolan **WEB DESIGNER** Jennie Pajerowski

Chief Executive Officer and Executive Publisher Sudip Parikh

Publisher, Science Family of Journals Bill Moran

DIRECTOR, BUSINESS SYSTEMS AND FINANCIAL ANALYSIS Randy Yi **DIRECTOR, BUSINESS OPERATIONS & ANALYSIS** Eric Knott **DIRECTOR OF ANALYTICS** Enrique Gonzales **MANAGER, BUSINESS OPERATIONS** Jessica Tierney **SENIOR BUSINESS ANALYST** Cory Lipman, Meron Kebede **FINANCIAL ANALYST** Alexander Lee **ADVERTISING SYSTEM ADMINISTRATOR** Tina Burks **SENIOR SALES COORDINATOR** Shirley Young **DIGITAL/PRINT STRATEGY MANAGER** Jason Hillman **QUALITY TECHNICAL MANAGER** Marcus Spiegler **ASSISTANT MANAGER DIGITAL/PRINT** Rebecca Doshi **SENIOR CONTENT SPECIALISTS** Steve Forrester, Jacob Hedrick, Antoinette Hodal, Lori Murphy **PRODUCTION SPECIALIST** Kristin Wowk **DIGITAL PRODUCTION MANAGER** Lisa Stanford **CONTENT SPECIALIST** Kimberley Oster **ADVERTISING PRODUCTION OPERATIONS MANAGER** Deborah Tompkins **DESIGNER, CUSTOM PUBLISHING** Jeremy Huntsinger **SR. TRAFFIC ASSOCIATE** Christine Hall **SPECIAL PROJECTS ASSOCIATE** Sarah Dhere

ASSOCIATE DIRECTOR, BUSINESS DEVELOPMENT Justin Sawyers **GLOBAL MARKETING MANAGER** Allison Pritchard **DIGITAL MARKETING MANAGER** Aimee Aponte **JOURNALS MARKETING MANAGER** Shawana Arnold **MARKETING ASSOCIATES** Tori Velasquez, Mike Romano, Ashley Hylton **DIGITAL MARKETING SPECIALIST** Asleigh Rojanavongse **SENIOR DESIGNER** Kim Huynh

DIRECTOR AND SENIOR EDITOR, CUSTOM PUBLISHING Sean Sanders **ASSISTANT EDITOR, CUSTOM PUBLISHING** Jackie Oberst

DIRECTOR, PRODUCT & PUBLISHING DEVELOPMENT Chris Reid **DIRECTOR, BUSINESS STRATEGY AND PORTFOLIO MANAGEMENT** Sarah Whalen **ASSOCIATE DIRECTOR, PRODUCT MANAGMENT** Kris Bishop **PRODUCT DEVELOPMENT MANAGER** Scott Chernoff **PUBLISHING TECHNOLOGY MANAGER** Michael Di Natale **SR. PRODUCT ASSOCIATE** Robert Koepke **SPJ ASSOCIATE** Samantha Bruno Fuller

DIRECTOR, INSTITUTIONAL LICENSING Iquo Edim **ASSOCIATE DIRECTOR, RESEARCH & DEVELOPMENT** Elisabeth Leonard **MARKETING MANAGER** Kess Knight **SENIOR INSTITUTIONAL LICENSING MANAGER** Ryan Rexroth **INSTITUTIONAL LICENSING MANAGER** Marco Castellan **MANAGER, AGENT RELATIONS & CUSTOMER SUCCESS** Judy Lillibridge **SENIOR OPERATIONS ANALYST** Lana Guz **FULFILLMENT COORDINATOR** Melody Stringer **SALES COORDINATOR** Josh Haverlock

DIRECTOR, GLOBAL SALES Tracy Holmes **US EAST COAST AND MID WEST SALES** Stephanie O'Connor **US WEST COAST SALES** Lynne Stickrod **US SALES MANAGER, SCIENCE CAREERS** Claudia Paulsen-Young **US SALES REP, SCIENCE CAREERS** Tracy Anderson **ASSOCIATE DIRECTOR, ROW** Roger Goncalves **SALES REP, ROW** Sarah Lelarge **SALES ADMIN ASSISTANT, ROW** Bryony Cousins **DIRECTOR OF GLOBAL COLLABORATION AND ACADEMIC PUBLISHING RELATIONS, ASIA** Xiaoying Chu **ASSOCIATE DIRECTOR, INTERNATIONAL COLLABORATION** Grace Yao **SALES MANAGER** Danny Zhao **MARKETING MANAGER** Kilo Lan **ASCA CORPORATION, JAPAN** Kaoru Sasaki (Tokyo), Miyuki Tani (Osaka) **COLLABORATION/ CUSTOM PUBLICATIONS/JAPAN** Adarsh Sandhu

DIRECTOR, COPYRIGHT, LICENSING AND SPECIAL PROJECTS Emilie David **RIGHTS AND LICENSING COORDINATOR** Jessica Adams **RIGHTS AND PERMISSIONS ASSOCIATE** Elizabeth Sandler **CONTRACTS AND LICENSING ASSOCIATE** Lili Catlett

---

MAIN HEADQUARTERS
Science/AAAS
1200 New York Ave. NW
Washington, DC 20005

SCIENCE INTERNATIONAL
Clarendon House
Clarendon Road
Cambridge, CB2 8FH, UK

SCIENCE CHINA
Room 1004, Culture Square
No. 59 Zhongguancun St.
Haidian District, Beijing, 100872

SCIENCE JAPAN
ASCA Corporation
Sibaura TY Bldg. 4F, 1-14-5
Shibaura Minato-ku
Tokyo, 108-0073 Japan

EDITORIAL
science_editors@aaas.org

NEWS
science_news@aaas.org

INFORMATION FOR AUTHORS
sciencemag.org/authors/science-information-authors

REPRINTS AND PERMISSIONS
sciencemag.org/help/reprints-and-permissions

MEDIA CONTACTS
scipak@aaas.org

MULTIMEDIA CONTACTS
SciencePodcast@aaas.org
ScienceVideo@aaas.org

INSTITUTIONAL SALES AND SITE LICENSES
sciencemag.org/librarian

PRODUCT ADVERTISING & CUSTOM PUBLISHING
advertising.sciencemag.org/products-services
science_advertising@aaas.org

CLASSIFIED ADVERTISING
advertising.sciencemag.org/science-careers
advertise@sciencecareers.org

JOB POSTING CUSTOMER SERVICE
employers.sciencecareers.org
support@sciencecareers.org

MEMBERSHIP AND INDIVIDUAL SUBSCRIPTIONS
sciencemag.org/subscriptions

MEMBER BENEFITS
aaas.org/membercentral

AAAS BOARD OF DIRECTORS
CHAIR Steven Chu
PRESIDENT Claire M. Fraser
PRESIDENT-ELECT Susan G. Amara
TREASURER Carolyn N. Ainslie
CHIEF EXECUTIVE OFFICER
Sudip Parikh
BOARD Cynthia M. Beall
Rosina M. Bierbaum
Ann Bostrom
Stephen P.A. Fodor
S. James Gates, Jr.
Laura H. Greene
Kaye Husbands Fealing
Maria M. Klawe
Robert B. Millard
Alondra Nelson
William D. Provine

BOARD OF REVIEWING EDITORS (Statistics board members indicated with **(S)**)

Takuzo Aida, *U. of Tokyo*
Leslie Aiello, *Wenner-Gren Foundation*
Deji Akinwande, *UT Austin*
Judith Allen, *U. of Manchester*
Marcella Alsan, *Harvard U.*
Sebastian Amigorena, *Institut Curie*
James Analytis, *UC Berkeley*
Trevor Archer, *NIEHS, NIH*
Paola Arlotta, *Harvard U.*
David Awschalom, *U. of Chicago*
Clare Baker, *U. of Cambridge*
Delia Baldassarri, *NYU*
Nenad Ban, *ETH Zürich*
Franz Bauer, *Pontificia U. Católica de Chile*
Ray H. Baughman, *UT Dallas*
Carlo Beenakker, *Leiden U.*
Yasmine Belkaid, *NIAID, NIH*
Philip Benfey, *Duke U.*
Kiros T. Berhane, *Columbia U.*
Bradley Bernstein, *Mass. General Hospital*
Joseph J. Berry, *NREL*
Alessandra Biffi, *Harvard Med.*
Chris Bowler, *École Normale Supérieure*
Ian Boyd, *U. of St. Andrews*
Emily Brodsky, *UC Santa Cruz*
Ron Brookmeyer, *UCLA* **(S)**
Christian Büchel, *UKE Hamburg*
Dennis Burton, *Scripps Res.*
Carter Tribley Butts, *UC Irvine*
György Buzsáki, *NYU School of Med.*
Mariana Byndloss, *Vanderbilt U. Med. Ctr*
Annmarie Carlton, *UC Irvine*
Nick Chater, *U. of Warwick*
Ling-Ling Chen, *SIBCB, CAS*
M. Keith Chen, *UCLA*
Zhijian Chen, *UT Southwestern Med. Ctr.*
Ib Chorkendorff, *Denmark TU*
James J. Collins, *MIT*
Robert Cook-Deegan, *Arizona State U.*
Virginia Cornish *Columbia U.*
Carolyn Coyne, *U. of Pitt.*
Roberta Croce, *VU Amsterdam*
Ismaila Dabo, *Penn State U.*
Jeff L. Dangl, *UNC*
Chiara Daraio, *Caltech*
Nicolas Dauphas, *U. of Chicago*
Christian Davenport, *U. of Michigan*
Frans de Waal, *Emory U.*
Claude Desplan, *NYU*
Sandra Díaz, *U. Nacional de Córdoba*
Ulrike Diebold *TU Wien*
Stefanie Dimmeler, *Goethe-U. Frankfurt*
Hong Ding, *Inst. of Physics, CAS*
Dennis Discher, *UPenn*
Jennifer A. Doudna, *UC Berkeley*
Raissa M. D'Souza, *UC Davis*
Bruce Dunn, *UCLA*
William Dunphy, *Caltech*
Scott Edwards, *Harvard U.*
Todd Ehlers, *U. of Tübingen*
Jennifer Elisseeff, *Johns Hopkins U.*
Andrea Encalada, *U. San Francisco de Quito*
Nader Engheta, *U. of Penn.*
Karen Ersche, *U. of Cambridge*
Beate Escher, *UFZ & U. of Tübingen*
Barry Everitt, *U. of Cambridge*
Vanessa Ezenwa, *U. of Georgia*
Michael Feuer, *GWU*
Toren Finkel, *U. of Pitt. Med. Ctr.*
Gwenn Flowers, *Simon Fraser U.*
Peter Fratzl, *Max Planck Inst. Potsdam*
Elaine Fuchs, *Rockefeller U.*
Jay Gallagher, *U. of Wisconsin*
Daniel Geschwind, *UCLA*
Sandra González-Bailón, *UPenn*
Elizabeth Grove, *U. of Chicago*
Nicolas Gruber, *ETH Zürich*
Hua Guo, *U. of New Mexico*
Taekjip Ha, *Johns Hopkins U.*
Sharon Hammes-Schiffer, *Yale U.*
Wolf-Dietrich Hardt, *ETH Zürich*
Louise Harra, *U. Coll. London*
Jian He, *Clemson U.*
Carl-Philipp Heisenberg, *IST Austria*
Ykä Helariutta, *U. of Cambridge*
Janet G. Hering, *Eawag*
Heather Hickman, *NIAID, NIH*
Hans Hilgenkamp, *U. of Twente*
Kai-Uwe Hinrichs, *U. of Bremen*
Deirdre Hollingsworth, *U. of Oxford*
Randall Hulet, *Rice U.*
Auke Ijspeert, *EPFL*
Akiko Iwasaki, *Yale U.*
Stephen Jackson, *USGS & U. of Arizona*
Erich Jarvis, *Rockefeller U.*
Peter Jonas, *IST Austria*
Matt Kaeberlein, *U. of Wash.*
William Kaelin Jr., *Dana-Farber Cancer Inst.*
Daniel Kammen, *UC Berkeley*
V. Narry Kim, *Seoul Nat. U.*
Robert Kingston, *Harvard Med.*
Nancy Knowlton, *Smithsonian Institution*
Etienne Koechlin, *École Normale Supérieure*
Alex L. Kolodkin, *Johns Hopkins U.*
Julija Krupic, *U. of Cambridge*
Gabriel Lander, *Scripps Res.* **(S)**
Mitchell A. Lazar, *UPenn*
Wendell Lim, *UCSF*
Luis Liz-Marzán, *CIC biomaGUNE*
Omar Lizardo, *UCLA*
Jonathan Losos, *Wash. U. in St. Louis*
Ke Lu, *Inst. of Metal Res., CAS*
Christian Lüscher, *U. of Geneva*
Jean Lynch-Stieglitz, *Georgia Inst. of Tech.*
David Lyons, *U. of Edinburgh*
Fabienne Mackay, *QIMR Berghofer*
Anne Magurran, *U. of St. Andrews*
Asifa Majid, *U. of York*
Oscar Marín, *King's Coll. London*
Charles Marshall, *UC Berkeley*
Christopher Marx, *U. of Idaho*
David Masopust, *U. of Minnesota*
Geraldine Masson, *CNRS*
Jason Matheny, *Georgetown U.*
Heidi McBride, *McGill U.*
C. Robertson McClung, *Dartmouth*
Rodrigo Medellín, *U. Nacional Autónoma de México*
Jane Memmott, *U. of Bristol*
C. Jessica Metcalf, *Princeton U.*
Baoxia Mi, *UC Berkeley*
Tom Misteli, *NCI, NIH*
Alison Motsinger-Reif, *NIEHS, NIH* **(S)**
Danielle Navarro, *U. of New South Wales*
Daniel Nettle, *Newcastle U.*
Daniel Neumark, *UC Berkeley*
Beatriz Noheda, *U. of Groningen*
Helga Nowotny, *Vienna Sci., Res. & Tech. Fund*
Rachel O'Reilly, *U. of Birmingham*
Pilar Ossorio, *U. of Wisconsin*
Andrew Oswald, *U. of Warwick*
Isabella Pagano, *Istituto Nazionale di Astrofisica*
Elizabeth Levy Paluck, *Princeton U.*
Jane Parker, *Max Planck Inst. Cologne*
Giovanni Parmigiani, *Dana-Farber Cancer Inst.* **(S)**
Daniel Pauly, *U. of British Columbia*
Samuel Pfaff, *Salk Inst.*
Julie Pfeiffer, *UT Southwestern Med. Ctr.*
Philip Phillips, *UIUC*
Matthieu Piel, *Institut Curie*
Kathrin Plath, *UCLA*
Martin Plenio, *Ulm U.*
Katherine Pollard, *UCSF*
Elvira Poloczanska, *Alfred-Wegener-Inst.*
Julia Pongratz, *Ludwig Maximilians U.*
Philippe Poulin, *CNRS*
Jonathan Pritchard, *Stanford U.*
Lei Stanley Qi, *Stanford U.*
Trevor Robbins, *U. of Cambridge*
Joeri Rogelj, *Imperial Coll. London*
Amy Rosenzweig, *Northwestern U.*
Mike Ryan, *UT Austin*
Miquel Salmeron, *Lawrence Berkeley Nat. Lab*
Nitin Samarth, *Penn State U.*
Erica Ollmann Saphire, *La Jolla Inst.*
Joachim Saur, *U. zu Köln*
Alexander Schier, *Harvard U.*
Wolfram Schlenker, *Columbia U.*
Susannah Scott, *UC Santa Barbara*
Anuj Shah, *U. of Chicago*
Vladimir Shalaev, *Purdue U.*
Jie Shan, *Cornell U.*
Beth Shapiro, *UC Santa Cruz*
Jay Shendure, *U. of Wash.*
Steve Sherwood, *U. of New South Wales*
Brian Shoichet, *UCSF*
Robert Siliciano, *JHU School of Med.*
Lucia Sivilotti, *U. Coll. London*
Alison Smith, *John Innes Centre*
Richard Smith, *UNC* **(S)**
Mark Smyth, *QIMR Berghofer*
John Speakman, *U. of Aberdeen*
Tara Spires-Jones, *U. of Edinburgh*
Allan C. Spradling, *Carnegie Institution for Sci.*
V. S. Subrahmanian, *Dartmouth*
Ira Tabas, *Columbia U.*
Eriko Takano, *U. of Manchester*
Patrick Tan, *Duke-NUS Med. School*
Sarah Teichmann, *Wellcome Sanger Inst.*
Rocio Titiunik, *Princeton U.*
Shubha Tole, *Tata Inst. of Fundamental Res.*
Kimani Toussaint, *Brown U.*
Wim van der Putten, *Netherlands Inst. of Ecology*
Reinhilde Veugelers, *KU Leuven*
Bert Vogelstein, *Johns Hopkins U.*
David Wallach, *Weizmann Inst.*
Jane-Ling Wang, *UC Davis* **(S)**
Jessica Ware, *Amer. Mus. of Natural Hist.*
David Waxman, *Fudan U.*
Chris Wikle, *U. of Missouri* **(S)**
Terrie Williams, *UC Santa Cruz*
Ian A. Wilson, *Scripps Res.* **(S)**
Yu Xie, *Princeton U.*
Jan Zaanen, *Leiden U.*
Kenneth Zaret, *UPenn School of Med.*
Bing Zhu, *Inst. of Biophysics, CAS*
Xiaowei Zhuang, *Harvard U.*
Maria Zuber, *MIT*

Science serves as a forum for discussion of important issues related to the advancement of science by publishing material on which a consensus has been reached as well as including the presentation of minority or conflicting points of view. Accordingly, all articles published in *Science*—including editorials, news and comment, and book reviews—are signed and reflect the individual views of the authors and not official points of view adopted by AAAS or the institutions with which the authors are affiliated.

EDITORIAL

Stem cells on the ballot

California's ballot measures often reveal much about the broader U.S. policy environment. This is particularly true of the approval by the state's voters in November of Proposition 14, The California Stem Cell Research, Treatments, and Cures Initiative of 2020. Proposition 14 extends the 2004 ballot Proposition 71, which established the California Institute for Regenerative Medicine (CIRM) and authorized $3 billion in state-issued bonds for CIRM to fund stem cell and regenerative research and medicine (restricted to California). Proposition 14, which authorizes $5.5 billion over the next 10 years to continue CIRM's work, succeeded in part by informing voters of CIRM's successes and that its conflict-of-interest provisions are extremely strong. This state-level action is critical because, contrary to opponents' opinions, the overall policy environment for human stem cell research in the United States is in some ways worse now than when Proposition 71 passed.

Since 2004, CIRM has funded groundbreaking work on immune disorders, cancer, spinal cord injury, diabetes, and more. The result has been more than 90 stem cell–related clinical trials (directly or indirectly supported by CIRM), almost 3000 scientific papers, and contributions to two cancer therapies approved by the U.S. Food and Drug Administration. The lives of many patients have improved because of CIRM. Notably, many CIRM-funded clinical trials rely on human embryonic or fetal stem cells, whereas the federal government currently does not fund any clinical trials using these types of cells.

Proposition 71 was motivated largely in response to restrictions on human embryonic stem cell research in the United States in 2004. However, although research was limited to a small number of human embryonic stem cell lines, there was no formal ban on federal funding of research on such stem cells. In addition, in 2004 there were no restrictions on federal funding of human fetal stem cell and tissue research; however, there is now near-complete blockage of federal funding for such research. And federal funding for human embryonic stem cell research is again at risk. On 4 September 2020, 22 Republican senators and 72 Republican House members wrote to President Trump requesting an end to all federal funding of human embryonic stem cell research. Could President Trump impose a ban that would be difficult to revoke? Or, could Republican senators manufacture a ban by legislative maneuvering on a budget reconciliation vote, which requires 60% support? Such maneuvering created the effectively permanent 1995 Dickey-Wicker amendment, which prohibits federal funding of any research in which human embryos are created or destroyed. Dickey-Wicker has limited research on in vitro fertilization methods and stalled progress on understanding early human development. It has not solved the problem of the many, perhaps 1 million frozen embryos in the United States that will not be used for in vitro fertilization and will be destroyed without benefit if not used for research. Vital long-term research is greatly harmed by the U.S. policy environment, with the likely outcome that many young scientists will avoid research using human embryonic stem cells and human fetal tissue.

> "Restrictions on valuable, ethical research appear particularly foolhardy during a deadly pandemic."

Restrictions on valuable, ethical research appear particularly foolhardy during a deadly pandemic. Research on viruses such as HIV and SARS-CoV-2 (severe acute respiratory syndrome coronavirus 2) can benefit greatly from work using mice that utilize human fetal stem cells and tissues to generate a human-like immune system. These mice allow evaluation of a human immune system in the contexts of infection mechanisms, generation of immunity, and drug response. These studies can be supported with Proposition 14 funds in California, but not with federal funds. It is crucial for the incoming Biden administration to evaluate the need for federal funding in these important areas with high-quality scientific input and evidence.

California's vote on Proposition 14 should also help the rest of the country appreciate the need to increase investments in biomedical research at the U.S. National Institutes of Health and other federal agencies. Current biomedical research expenditures amount to only a tiny fraction of the costs of disease, so an objective evaluation of appropriately increased research funding relative to disease costs is warranted. Once again, California is showing the way.

–Lawrence S. B. Goldstein* and Robert N. Klein II*

Lawrence S. B. Goldstein is a distinguished professor in the Department of Cellular and Molecular Medicine and in the Department of Neuroscience at the University of California, San Diego, CA, USA. lgoldstein@health.ucsd.edu

Robert N. Klein II is chairman of the Yes on Proposition 14 Campaign: Californians for Stem Cell Research, Treatments, and Cures Initiative. bobklein@klein-financial.com

*More author information is in the supplementary materials (science.sciencemag.org/content/371/6526/215/suppl/DC1).

10.1126/science.abf8704

NEWS



Rioting meant to stop Congress from officially finalizing the election of President-elect Joe Biden led to five deaths.

PHOTO: LEV RADIN/SIPA USA/AP IMAGES

IN BRIEF

Edited by **Jeffrey Brainard**

DEMOCRACY

Science groups call for Trump's removal over insurrection

Several science advocacy groups last week called for President Donald Trump to resign or be immediately removed from office for inciting the 6 January attack by a violent mob on the U.S. Capitol. The March for Science invited signatures on an online petition calling for Trump to be impeached or for Vice President Mike Pence and other officials to invoke the 25th Amendment to declare Trump unable to serve. The group, which organized pro-science demonstrations in Washington, D.C., in 2017 and 2018, also asked followers to contact their congressional representatives directly to urge the president's removal. The Union of Concerned Scientists (UCS), as well as the groups 500 Women Scientists and 314 Action—which was first formed to support science-oriented political candidates—released similar statements, arguing that a healthy democracy is critical for scientific progress. "There need to be consequences," says Andrew Rosenberg, director of UCS's Center for Science and Democracy. "This was a true threat to our democracy."

OK for fetal tissue research sought

BIOMEDICINE | Nearly 100 scientific, medical, and patient groups last week wrote to President-elect Joe Biden urging him "to swiftly rescind" restrictions on fetal tissue research imposed by President Donald Trump. The 7 January letter argues that human fetal tissue "is an essential resource for biomedical research," including studies of Parkinson's disease and the development of COVID-19 vaccines and therapeutics. The 2019 policy, supported by abortion opponents, bans National Institutes of Health (NIH) in-house scientists from performing research using tissue from elective abortions. Projects from outside scientists that have passed NIH peer review must go before a special ethics board, which last summer rejected 13 of 14 proposals. The policy, the letter argues, "must be revoked to restore the integrity of the peer review process" and remove barriers to research. Signatories include AAAS, which publishes *Science*.

U.K. may loosen biotech regs

POLICY | The United Kingdom's split with the European Union is tying up commerce in red tape, but it may ease regulations for U.K. biotechnologists. Last week, the United Kingdom's agriculture department said it would consider new policies governing the genetic modification of plants and animals that would depart from a 2018 ruling by the European Court of Justice. The court determined that all gene-edited plants, animals, and microbes should be regulated like transgenic organisms, in which genes have been inserted from other species. Many scientists prefer the position of the U.K. Department for Environment, Food and Rural Affairs (DEFRA), which has said transgenic regulations should not apply to modifications made by intraspecies gene editing that can also be done with traditional breeding. DEFRA said it will accept public comment on the issue

until 17 March, then decide whether to propose changing the regulations for England. (Other parts of the United Kingdom are responsible for their own such regulations.)

Nazi salute rocks conference

ARCHAEOLOGY | A participant at last week's virtual meeting of the Society for Historical Archaeology used a Nazi salute and phrase during an altercation. As Liz Quinlan, a doctoral student at the University of York, was speaking at the opening plenary session about her work as the conference's accessibility and inclusion coordinator, attendee Robert Schuyler, an archaeologist at the University of Pennsylvania and a past president of the society, interrupted her with unrelated questions. Quinlan tried to hold the floor, and Schuyler responded, "I have freedom of speech." Then he thrust his arm into the air and said "*Sieg heil* to you." Video clips of the incident, which was recorded on Zoom, went viral on social media. Quinlan filed a harassment complaint with the society, and Schuyler's department chair said he "will not be in the classroom this semester" as a result of his actions.

How a woodpecker gets unstuck

PHYSIOLOGY | Scientists say they have discovered why a woodpecker's beak doesn't get stuck when it drills into a tree. They took high-speed videos of two black woodpeckers (*Dryocopus martius*) pecking away at hardwood trunks and analyzed them frame by frame. The bird's secret: Once the bill hits the wood, its head rotates slightly to the side, and the top part of the beak moves independently from the skull. This action creates space between the beak tip and the wood inside the hole, allowing the bird to easily retract its beak, the team reported last week at the virtual annual meeting of the Society for Integrative and Comparative Biology. Until now, scientists thought woodpecker bills would need to be rigidly attached to the skull.



Scientists discovered a surprising adaptation in the woodpecker's beak.

PHOTO: SVEN ZACEK/MINDEN PICTURES

Cell Press invites diversity details

PUBLISHING | Cell Press, publisher of more than 50 journals, last week became one of the first to invite authors to add statements to their research papers describing diversity and inclusion aspects of their work. The declarations can highlight authors' personal characteristics or elements of a study's design, such as researchers' use of ethnically diverse cell lines and genomic data sets or efforts to ensure gender balance in samples and citations. Submitting such a declaration is not mandatory and will not affect whether manuscripts are accepted for publication, Cell Press said.

Ebola vaccine stockpile debuts

INFECTIOUS DISEASES | International health organizations announced on 12 January the first global stockpile of an Ebola vaccine, which they expect will help quash future outbreaks faster. These are relatively rare, so the vaccine has no natural market. The stockpile already has 6890 doses of a vaccine that was created and manufactured by Merck, used in recent years during outbreaks in Africa on an emergency basis, and later approved by U.S. and European regulators. Organizers say the total may reach the 500,000 doses recommended by experts within 2 to 3 years. Stored in Switzerland, the vaccine supply will be reserved for health care workers and other people at highest risk of contracting the often-fatal hemorrhagic disease during future outbreaks.

Twitter shuts Sci-Hub's account

PUBLISHING | Twitter last week shuttered the account of Sci-Hub, a website that has posted millions of freely accessible copies of scientific articles pirated from subscription journals. Twitter said Sci-Hub had violated its policy against promoting the sale of "counterfeit goods," according to Sci-Hub's founder, Alexandra Elbakyan. The notification came shortly after a court hearing in India about a lawsuit filed by three publishers—Elsevier, Wiley, and the American Chemical Society—seeking to block access to Sci-Hub in that country because of copyright infringement. Elbakyan says Sci-Hub's defense will rely in part on tweets from Indian scientists who supported continued access to Sci-Hub because, they said, they could not afford subscriptions to journal content.

COVID-19

Dispatches from the pandemic

U.S. to unleash vaccine stockpile

In a reversal, the Trump administration this week decided to release its entire stockpile of two authorized COVID-19 vaccines to speed a so far sluggish campaign to vaccinate the country. Until now, the government has kept half the vaccine in reserve to make sure that everyone would receive their second dose on time. But officials said they now have more confidence that the two companies providing the vaccines can meet future production targets. The officials also said the administration now urges states to move beyond the groups that have been prioritized to receive the vaccine first—health care workers and residents of long-term care facilities—to inoculate everyone 65 and older and people with conditions that make them more vulnerable to COVID-19. The government has offered states 38 million doses of vaccine, but only 9 million people have received their first shot.

Sweden adopts pandemic law

Facing full intensive care wards, Sweden's parliament last week passed a law that allows the government to impose nationwide restrictions to slow the spread of the coronavirus. The move is a striking change for a country that has conspicuously avoided such measures, which helps explain why it has one of the highest rates of COVID-19 cases in Europe. Sweden's leaders had relied on limiting large gatherings and recommending people voluntarily take precautions to control the pandemic. So far, the government has used the new law to reduce crowding in gyms, stores, and other spaces by limiting customers to one per 10 square meters.

London declares emergency

London's mayor declared a "major incident" in the city last week as rampant COVID-19 infections brought hospitals to the breaking point. Mayor Sadiq Khan said one out of every 30 Londoners was likely carrying the virus. Khan said emergency services including hospitals and ambulances "cannot guarantee their normal level of response." On 5 January, England's third national lockdown since the start of the pandemic closed schools and shuttered businesses, but it has yet to stem the spread of a new variant of the virus that experts estimate is approximately 50% more transmissible than its predecessors.



IN DEPTH

Democrats Jon Ossoff and Raphael Warnock (right) won Senate runoff elections in Georgia on 5 January. Their victories cemented Democratic control of the U.S. government.

U.S. GOVERNMENT

Science could benefit as Democrats take power

Major shifts on climate and science policy expected, but political obstacles abound

By **David Malakoff** *and* **Jeffrey Mervis**

Next week, Democrats will gain control of the White House and both chambers of Congress for the first time in a decade. That political shift could have momentous implications for science and climate policy. "Voters have delivered a pretty historic mandate to Congress and an administration to move forward in ways that are transformational and not incremental," says Rachel Cleetus, director of climate and energy programs at the Union of Concerned Scientists.

But, Cleetus adds, "We shouldn't be naïve … there are big obstacles." A narrowly divided and highly polarized Congress will likely constrain efforts to realize the most ambitious proposals put forward by policymakers and advocacy groups. And Democrats could have as little as 2 years to exercise their expanded powers.

The 20 January inauguration of President-elect Joe Biden means Democrats will gain broad powers to appoint federal officials, write regulations, and resume international commitments abandoned under President Donald Trump, including rejoining the Paris climate pact, the World Health Organization, and the Iran nuclear deal. And the arrival this month of two newly elected senators from Georgia, Raphael Warnock and Jon Ossoff, will give Democrats half of the Senate's 100 seats, with Kamala Harris providing the tie-breaking vote as vice president. Republicans have controlled the Senate since January 2015. (Democrats held onto their majority in the House of Representatives.)

The narrow edge in the Senate will make it easier for Biden to win confirmation of his appointees and for Congress to revoke controversial rules finalized in the final 5 months of the Trump administration. It could also help Democrats enact promised legislation aimed at ending the COVID-19 pandemic, rebuilding the economy, curbing climate change, and boosting federal investments in research, infrastructure, and public health.

The new majority leader, Senator Chuck Schumer (D–NY), will replace Senator Mitch McConnell (R–KY) as final arbiter of that body's legislative calendar. Schumer has shown keen interest in promoting clean energy and boosting federal research spending. Last year, he helped craft a bipartisan proposal, the Endless Frontiers Act, which calls for giving the National Science Foundation a sweeping makeover, including an additional $100 billion over 5 years. But Schumer will have to balance the many competing demands of his party, including a progressive agenda that includes a Green New Deal and providing free college to more students.

Each of the Senate's 20 permanent committees will get new leaders. The powerful Senate Appropriations Committee, which sets annual spending levels, will be chaired by Senator Patrick Leahy (D–VT), a longtime advocate of environmental protection. Senator Maria Cantwell (D–WA), a former technology executive who has a strong interest in research, will chair the Commerce, Science, and Transportation Committee. Senator Patty Murray (D–WA), a backer of biomedical science, will lead the health panel, which among other things oversees the National Institutes of Health and the Centers for Disease Control and Prevention. The homeland security panel, which oversees security and regulatory issues important to the science community, will be led by Senator Gary Peters (D–MI), who has extensive experience with research agencies.

Advocates for technological innovation to battle climate change will lead two key panels. Senator Tom Carper (D–DE), the author of numerous climate proposals that have not advanced in the Republican-led Senate, will lead the environment committee, while the energy panel will be chaired by Senator Joe Manchin (D–WV), who has backed the devel-

PHOTO: JIM WATSON/AFP/GETTY IMAGES

opment of technologies that would capture carbon dioxide produced by the burning of fossil fuels before it enters the atmosphere.

On paper, that Senate lineup—together with Democratic control of the House of Representatives—bodes well for more aggressive government action on climate change. Under Senate rules, however, most bills need 60 votes to advance, meaning Democrats backing climate action will need to find at least 10 Republican allies.

Cleetus sees opportunities for bipartisan cooperation on "common sense policies that both help reduce emissions [of warming gases] and help ameliorate the current economic crisis and create jobs." Investments in infrastructure, clean energy technology, and workforce training are all potential areas of bipartisan cooperation that do such "double duty," says climate policy specialist Kelly Sims Gallagher of the Fletcher School at Tufts University.

Such cooperation will be more likely if Democrats don't insist that their Republican colleagues publicly acknowledge that humans are a primary cause of planetary warming, says Bart Gordon, a former Democratic lawmaker who led the House science committee from 2007 to 2011. "I think it's possible to get a deal if you don't rub their nose in it," says Gordon, a lobbyist for K&L Gates. "I think there's been a change in [Republicans'] attitude toward climate change—most of them will now admit that it's real."

> **"I think there's been a change in [Republicans'] attitude toward climate change ..."**
>
> **Bart Gordon**, K&L Gates

Democrats would need few, if any, Republican votes, however, to advance bills under an obscure mechanism known as reconciliation. It allows each legislative body to use the annual budget-setting process to pass bills with a simple majority as long as they relate to government spending. In 2010, Democrats used reconciliation to advance then-President Barack Obama's health care law, and in 2017 Republicans used it to open Alaska's Arctic National Wildlife Refuge to oil drilling. But there is a downside to passing legislation with such a razor-thin margin: Any bill approved by reconciliation also can be repealed with just 51 votes in the Senate.

A simple majority vote of both the House and Senate is also all that is needed to revoke recent Trump administration regulations under the seldom-used Congressional Review Act (CRA), which gives Congress a brief window to reject new rules. In 2017, Republicans used the CRA, which also bars agencies from reissuing anything "substantially similar" to a revoked rule, to kill 14 rules. Now, some 1300 rules adopted since August 2020 are vulnerable before the CRA clock expires later this year, according to the George Washington University Regulatory Studies Center. But Susan Dudley, the center's director, says Senate leaders are likely to use the law selectively, because CRA votes could steal time from other priorities. Still, top targets for revocation could include rules that weakened environmental protections and limited the kinds of science the Environmental Protection Agency can use. (The Biden administration might also opt for the labor-intensive process of rewriting unwanted rules rather than killing them.)

Issues like climate and regulatory policy will remain contentious in the new Congress, but observers see possibilities for bipartisan agreement on other science-related topics. Gordon thinks the unprecedentedly fast development of vaccines to fight the COVID-19 pandemic has boosted public support for science and made it easier for advocates to push for greater federal investments in research.

Former Representative Daniel Lipinski (D–IL), who lost his seat to a primary challenger last spring, believes Biden and a Democratic Congress will also try to roll back Trump-era restrictions on immigration and international collaborations, while remaining vigilant against legitimate threats from China and other countries. Biden "won't want to look weak on national security," says Lipinski, who was a senior member of the science committee. "But Trump went after China in a way that was harmful to science without improving our national security. Biden is smart enough to protect the nation in a way that isn't detrimental to our traditional principles of openness."

Still, the deep political divisions in Congress and across the nation could pose a barrier to legislative deals. That polarization was recently on display within the House science panel, which enjoys a high degree of bipartisanship on many research issues. Ten of the 13 Republicans who served on the committee in the current Congress objected on 6 January to certifying Biden's electoral college wins in Arizona or Pennsylvania—an even higher level of support than Trump received in the House as a whole, where two-thirds of Republican members voted to overturn the presidential results.

Democrats in Congress, meanwhile, know their influence could be relatively fleeting. With the next elections set for November 2022, it's possible Republicans could regain control of one or both houses 2 years from now. ■

CONSERVATION BIOLOGY

Are monarchs in trouble?

U.S. mulls protection for iconic butterfly, but some experts say fears overblown

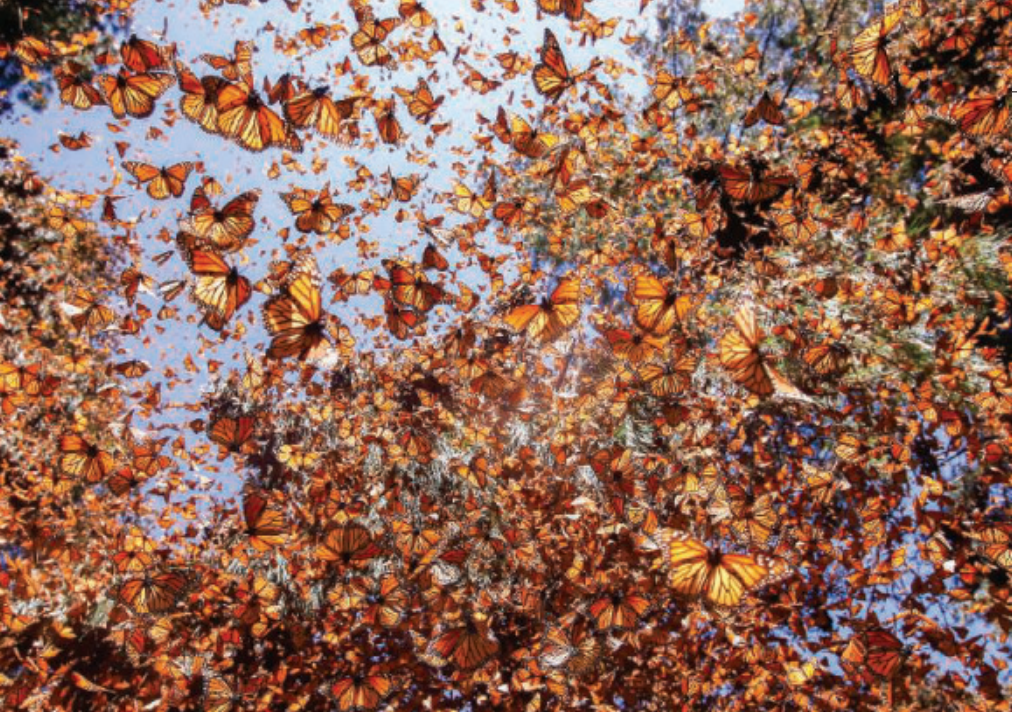
By **Elizabeth Pennisi**

Last month, the U.S. Fish and Wildlife Service (FWS) declared that one of North America's best known butterflies, the monarch, might be in trouble. But the agency put off protecting the insect under the federal Endangered Species Act, in part because it said its resources are limited and other species are in greater need of help. In the meantime, researchers are continuing to debate whether the species is really at risk, and the best way to tell.

In recent months dueling preprints and publications have intensified the debate. In one camp: researchers who have documented drastic declines in the number of monarchs in Mexico and other areas where some butterflies spend the winter. They believe the species needs immediate help, particularly by protecting and expanding the milkweed-filled meadows where its larvae feed. In another: scientists who have tallied surveys of butterfly numbers in areas they occupy during the warmer months and concluded there is less cause for alarm. As a species, monarchs "don't really need saving," says Andrew Davis, an ecologist at the University of Georgia, Athens.

Monarchs are important pollinators found around the world, but North America is home to the two migratory populations. A larger group, which accounts for an estimated 90% of all North American monarchs, occupies the eastern half of the continent. Once, hundreds of millions of these butterflies completed a 9600-kilometer migration loop that takes them to Mexico and back as far north as Canada each year. Monarchs in a second, smaller population in western North America travel only as far as Southern California to overwinter.

The insects face threats including habitat loss and pesticides, and there is broad consensus that the western population has suffered deep declines, with wintering numbers dropping as low as 2000 in 2020. But it is the condition of the larger eastern population that will determine whether monarchs get federal protection. And those



Monarch butterflies swarm trees in Mexico, where some of the insects spend the winter.

numbers have proved difficult to pin down.

One obstacle is the monarch's complex life cycle, which can involve lengthy migrations made relay race style by individuals from four different generations, each completing just one leg of the journey. As a result, population estimates can vary depending on "how and where you count the monarchs, and over what time period you look," says ecologist Joshua Puzey of the College of William & Mary.

Some researchers focus on the number of monarchs that arrive each year at wintering grounds in a small region in the highlands of central Mexico. The butterflies congregate on fir trees in such dense clusters that researchers estimate numbers by measuring the area of trees they cover. That area has shrunk over the past 2 decades. During the 2019–20 season, it dropped to 2.83 hectares, half its size the previous winter and down from 18 hectares in 1996–97. The U.S. Geological Survey (USGS) has estimated 6 hectares are required for monarchs to stay afloat in the long run. "Current monarch numbers are not sustainable," says ecologist Karen Oberhauser of the University of Wisconsin, Madison.

But a different picture emerges from data collected north of Mexico during other parts of the year, Davis and others say. Each season, scores of scientists and thousands of volunteers tally butterflies as they fly past recording stations, and count monarch eggs and caterpillars they find on milkweed, the larvae's only food source. When Davis and colleagues examined 20 of these data sets, covering time spans from 15 years to more than 100 years, they saw little evidence of drastic declines. Winter and spring populations had shrunk a little but summer and fall surveys showed few losses, they reported in October 2020 in a preprint posted on Preprints.org, which has not yet been peer reviewed.

Davis acknowledges his view that monarchs are not in danger of extinction is unpopular: "No one wants [it], ironically," he says. "They want to keep saving them."

And the preprint has drawn mixed reviews. Insect ecologist Anurag Agrawal of Cornell University calls it "important. … Some of these data have never been put together this way." But Leslie Ries, an ecologist at Georgetown University, rejects its conclusions. "The picture painted … includes many faulty conclusions based on the studies or data sets cited," she says.

Volunteer surveys, Ries says, "are invaluable," but "there are some issues that need to be addressed." For example, volunteers tend to count monarchs in places that are easy to reach and where they are likely to encounter butterflies, potentially skewing the numbers, notes ecologist Laura López-Hoffman of the University of Arizona. "If you don't look for butterflies where they used to be … you could wrongly conclude that monarchs aren't declining," she says.

Agrawal points to another source of confusion. Based on volunteer tallies of monarch numbers across their life cycle, he has found that each of the four generations in a year can expand or decline independently, presenting conflicting trends. Like Davis, he does not think the species faces extinction, but he does believe the North American population is declining. That "does not bode well," he says.

If the numbers are dropping, some researchers have argued for years that more milkweed could help. A number of studies have concluded that, since the 1990s, shifts in farming practices and the broad use of weed-killing chemicals have driven monarch declines by causing precipitous declines in the tall, weedy plant. By attaching tracking tags to butterflies, for example, the nonprofit Monarch Watch found that the size of the summer populations, which require milkweed to reproduce, determines the size of the overwintering populations. That suggests "increasing milkweed habitat, which has the potential of increasing the summer monarch population, is the conservation measure that will have the greatest impact," insect ecologist and Monarch Watch founder Orley Taylor of the University of Kansas, Lawrence, and colleagues concluded in their August 2020 study, which appeared in *Frontiers in Ecology and Evolution*.

Elise Zipkin, an ecologist at Michigan State University, and her colleagues agree, as they have unpublished data from six monitoring programs over 25 years. They, too, found a strong correlation between breeding and winter populations.

But some doubt the milkweed limitation hypothesis. "While more milkweed won't hurt the monarch … there is very compelling evidence … that milkweed is not necessarily limiting," Puzey says. For example, if milkweed was in short supply, monarch caterpillars should be defoliating the few plants that are left, and that has not happened, Ries says. Indeed, sometimes volunteers have to look hard to find monarch larvae even in fields full of milkweed.

Ries believes other factors, such as weather and long-term climate change, play a bigger role in determining monarch numbers. She notes that some studies have found the number of butterflies that head north in the spring to breed "is the biggest factor in how big the populations grow each year." So, a spring freeze or storm that kills many butterflies can have a yearlong ripple effect.

Given such uncertainties and the fact that conservation efforts are already underway, U.S. officials say the monarch is not yet a prime candidate for federal protection. But they plan to revisit a decision on the monarch's recommended status in 2024, FWS ecologist Lori Nordstrom explained last month at a virtual press conference.

The delay worries Tyler Flockhart, an adjunct ecologist at the University of Maryland Center for Environmental Science's Appalachian Laboratory who has been modeling monarch population dynamics. "We run the risk of studying this problem to death by not taking actions until we are completely certain." ■

PHOTO: SYLVAIN CORDIER/NPL/MINDEN PICTURES

EVOLUTION

Anemone shows mechanism of rapid evolution

Single genetic switch converts stinging cells into sticky ones that cling to surfaces

By **Elizabeth Pennisi**

Anyone who has been stung by a jellyfish might think they know more than enough about cnidocytes, the cells that deliver the sting. But Leslie Babonis has found that these cells have much more to tell, including insight into a simple evolutionary mechanism that may enable jellyfish, sea anemones, corals, and their relatives—collectively known as cnidarians—to quickly adapt to new environments. Babonis has found that a single genetic switch can transform cells that sting into cells that cling, enabling the animal to colonize new surfaces. The work suggests this kind of switch may have helped power evolutionary transformations for hundreds of millions of years.

The finding, reported last week at the virtual annual meeting of the Society for Integrative and Comparative Biology, is "an impressive biological discovery … [providing] powerful observations about how new cell types evolve and arrive in novel places" says Kristen Koenig, an evolutionary developmental (evodevo) biologist at Harvard University. Researchers have long known that some single genetic switches can cause one body part to develop as another in more complex organisms. But Babonis's finding suggests this simple mechanism for evolutionary change dates back to some of the earliest animals.

Cnidocytes have multiple guises, making them a tempting focus for biologists studying how new kinds of tissues evolved. The stinger cells (also called nematocytes) of jellyfish shoot tiny, toxin-laden harpoons, whereas some cnidocytes in sea anemones and corals shoot out threads of sticky material that help the animals anchor themselves in substrates like mud. "The cnidocytes are a great model system to study the evolution and diversification of novel cell types," revealing principles that can be applied to other animals, says Billie Swalla, an evodevo researcher at the University of Washington, Seattle.

Babonis, an evodevo biologist at Cornell University, looked at the starlet sea anemone *Nematostella vectensis*, a 5-centimeter, translucent creature common in Atlantic Ocean estuaries. She and her colleagues used the gene-editing tool CRISPR to knock out the anemone's *Sox2* gene, known to be important in neural development in many animals.

After disabling *Sox2*, the researchers closely examined the body wall and other parts of the anemone under a light microscope. Nematocytes in the tentacle tips developed crooked harpoons, Babonis found. The nematocytes normally found in the body wall were missing, replaced by fat cnidocytes called robust spirocytes, known for their stickiness. Those cells had never been seen in this species.

"You don't usually expect organisms to be capable of producing organs that they don't normally develop," says Nicole Webster, an evolutionary biologist at Clark University. "It's like a human growing a prehensile tail."

It seems the *Sox2* gene controls a switch. When it's working, stinger cells form. When it's not, spirocytes form, but apparently only in the body wall. (No one has yet studied whether *Sox2* is important for spirocyte formation in other anemones or cnidarians.) By transforming cells in just one part of the body, such developmental switching may have equipped early cnidarians to explore new habitats, Babonis suggested. For example, some sea anemones—equipped with plenty of robust spirocytes—can burrow into ice; one, *Edwardsiella andrillae*, has colonized the underside of the Antarctic ice shelf.

The study suggests "how the evolution of novel traits can exist on a small scale—different cell types—but can lead to larger consequences," Webster says.

Researchers have seen similar switches, called homeotic transformations, in the nervous systems of worms, flies, and fish, known as bilaterians because they have symmetrical left and right sides. Sea anemones are from a different branch of the animal tree; they have only two layers of cells and radial rather than bilateral symmetry. Thus the finding suggests that this kind of powerful evolutionary mechanism—a simple genetic switch—dates back at least 600 million years to the common ancestor of bilaterians and cnidarians, "before [the] sophisticated morphology of worms and flies came on the scene," Babonis says.

Marymeagan Daly, an integrative biologist at Ohio State University, Columbus, who studies the Antarctic sea anemones, cautions that the experimentally transformed cnidocytes need to be more closely examined to be sure they are bona fide spirocytes; Babonis agrees and notes other open questions, such as whether spirocytes or nematocytes evolved first and thus, whether burrowing or predation was cnidocytes' earliest function. Still, Daly says, the work "shows that big changes can be triggered by small differences in [gene] expression." ■



One genetic change governs whether certain cells of the starlet sea anemone shoot toxin-laden harpoons into prey or toss out sticky threads to anchor the organism in mud.

PHOTO: LESLIE BABONIS/UNIVERSITY OF FLORIDA



Medical workers take care of a COVID-19 patient at Union Hospital in Wuhan, China, in April 2020.

PHOTO: XINHUA/SHEN BOHAN/GETTY IMAGES

COVID-19

Pandemic could mark 'turning point' for Chinese science

Despite missteps and government control, early findings guided other countries' fight against the coronavirus

By **Dennis Normile**, *in Wuhan, China*

On 2 January 2020, a group of clinician-researchers at the Jinyintan Hospital here, along with colleagues at other institutions, launched a study of 41 patients suffering from a new, atypical pneumonia. The team assembled clinical data, laboratory results, and chest x-rays; tracked the production of immune system molecules called cytokines; and noted the use of antivirals, antibiotics, and corticosteroids. Thirteen of the patients required intensive care, and six died.

The group's observations, published online by *The Lancet* on 24 January 2020, were the first dispatch from the clinical front lines of the COVID-19 pandemic and gave clinicians around the world a detailed picture of what to brace for as the virus, then called 2019-nCoV, began to race across the globe. The paper also contained a clear warning: "We are concerned that 2019-nCoV could have acquired the ability for efficient human transmission," Chaolin Huang, a Jinyintan medical doctor, and colleagues wrote. They "strongly recommended" that health care workers use personal protective equipment.

China's initial handling of the pandemic, and the way it has shared information, has come under intense criticism. The government only reported the discovery of a novel coronavirus after *The Wall Street Journal* broke the news. It punished Chinese doctors who spoke out about the disease's early spread and a researcher who published the first sequence of the virus. It took until 20 January for China to confirm the potential for human-to-human transmission, which had been clear for weeks, and the country still strictly controls how scientists speak with media.

Yet at the pandemic's first anniversary, Chinese scientists can boast that they made major contributions to the science of SARS-CoV-2, as the virus was christened in February 2020, and taught the world vital lessons about how the outbreak might be contained.

The 10 most cited COVID-19 papers of the first 6 months of 2020, based on data from Elsevier's Scopus database, all came from China, according to an August study in *Scientometrics*; the *Lancet* paper topped the list. That's a sharp contrast to what happened during the global outbreak of severe acute respiratory syndrome (SARS) in 2003, when researchers here, stifled by prolonged political denial about the crisis, made few contributions. For SARS, "China's scientists were not so well prepared," says Wang Weibing, an epidemiologist at Fudan University. "This time was different."

Early on, the National Natural Science Foundation of China (NSFC) awarded more than 200 million yuan ($31 million) to some 100 projects under two rapid call programs. China has dragged its feet in some areas—most notably the origins of the virus, a politically explosive issue subject to conspiracy theories both in China and abroad. And research slowed down after March, for a happy reason: China ran out of cases.

Still, the response overall is a testament to China's rapid scientific development, says Edward Holmes, a virologist and evolutionary biologist at the University of Sydney who with Chinese colleagues published the first genome of the virus on 10 January 2020. "COVID-19 is perhaps a turning point for Chinese science: the point when their work really had global reach and they saw the value of sharing," Holmes says.

Much of the initial data came from Wuhan, by far the hardest hit city. Researchers at Huazhong University of Science and Technology published well over 400 COVID-19 articles and reviews from January through June. The bulk came from the university's Tongji Medical College, home to four authors of the *Lancet* paper, and its large clinical network. The studies covered clinical observations and outcomes, epidemiology, convalescent plasma therapy, blood glucose control for COVID-19 patients with diabetes, and the use of statins to reduce mortality. "Our doctors and nurses worked at the front line fighting against the epidemic," says Chen Jian-Guo, a pharmacologist and dean of the college, but they also felt a responsibility "to share their experiences and treatment plans with colleagues."

Existing international ties proved helpful. Tongji's Chaolong Wang teamed up with Xihong Lin, a biostatistician at Harvard University's T.H. Chan School of Public Health, where Wang had done a postdoc from 2012 to 2014. With others, they detailed how Wuhan's increasingly strict counter-measures—sealing the city, halting local travel, and quarantines—affected the course of the outbreak. They posted a paper on the impact of such "non-pharmaceutical interventions" on medRxiv on 6 March, in hopes "that our findings and experience could help other countries tailor their intervention strategies," Chaolong Wang now says.

A report released 1 week earlier by a joint mission of WHO and China had confirmed that countermeasures adopted in Wuhan and throughout the country were on the cusp of stopping the virus in its tracks—a feat many outside China found hard to believe. But the report presented epidemio-

Science's COVID-19 reporting is supported by the Pulitzer Center and the Heising-Simons Foundation.

logic curves showing new cases peaked in late January and rapidly tapered off after isolation of cases, quarantining of contacts, and harsh lockdowns in several cities. "We in New Zealand learnt that this pandemic virus could be successfully controlled," says Nick Wilson, a public health scientist at the University of Otago.

Despite political tensions, China and the United States collaborated more frequently on COVID-19–related papers than they had on papers in general in the previous 5 years, Jenny Lee and John Haupt of the University of Arizona reported in *The Journal of Higher Education* in November. "For scientists, advancing knowledge and improving the human condition, in this case, overcoming COVID-19, appears to be the greater goal," Lee says. A Chinese property development company bankrolled a $115 million COVID-19 research collaboration between researchers in Boston and China.

Yet China's remarkable success at taming its outbreak meant the focus of research there began to shift after a few months. "There are almost no cases, so it's very difficult for us to start a good cohort study," says Zhang Wenhong, an infectious disease specialist at Fudan University's Huashan Hospital.

Now, Zhang and others are trying to understand why COVID-19 has such a disproportional impact on the elderly and how long immunity, triggered by either natural infection or vaccination, lasts. Several groups are looking at the psychological impact of infection and the lockdown. Other studies focus on the long-term consequences of infection. Huang co-authored a study published online by *The Lancet* last week on the health status of 1733 COVID-19 patients discharged from Wuhan's Jinyintan Hospital between January and May 2020. Fatigue or muscle weakness afflicted 63% of the former patients; 26% had sleep difficulties, and 23% suffered from anxiety or depression.

Research on the origins of the virus and how it crossed into the human population has lagged, however. Early widespread speculation on social media both within and beyond China claimed the virus escaped from a laboratory, with the Chinese Academy of Sciences's Wuhan Institute of Virology (WIV) being the prime suspect, a notion that U.S. President Donald Trump and some other Western politicians have repeated. China, for its part, is claiming the virus originated elsewhere and was brought here by visiting U.S. servicemen or on frozen food shipments. The scientific consensus is that the virus probably evolved in nature, possibly from a bat-borne virus.

Shi Zhengli, a WIV virologist who has collected more than 2000 viral genetic sequence samples from bats in the wild, told *Science* in July that many groups in China are trying to pin down the origin of the virus (*Science*, 31 July 2020, p. 487). But few data have been released. And China has waffled on letting members of a long-awaited joint WHO-Chinese mission enter the country. As *Science* went to press, the mission was scheduled to begin on 14 January.

China expects to have a major impact this year with its vaccines, which were the first to work in monkey experiments and to enter human trials. Because the country has so few cases, they are being tested in more than a dozen countries in Central and South America, Southeast Asia, and the Middle East. On 30 December 2020, an affiliate of pharma giant Sinopharm said a phase III trial had shown its vaccine to have a 79% efficacy, although details are scant. China's drug regulator granted conditional marketing authorization the next day and Beijing initiated mass inoculation of priority groups on 1 January.

The United Arab Emirates and Bahrain had already approved the use of the vaccine earlier in December, based on studies in those countries, and Indonesia authorized the emergency use of another Chinese vaccine, produced by Sinovac Biotech, on 11 January. Both vaccines are based on inactivating the entire virus, a classic approach not used for leading candidate vaccines in the West. China plans to offer millions of doses to developing countries at a "fair and reasonable" price in what some are calling "vaccine diplomacy" (*Science*, 11 December 2020, p. 1263).

The pandemic has also highlighted opportunities for strengthening China's public health research. In particular, disease modeling needs an upgrade, Wang Weibing says. China's modeling groups are made up of a few people, in contrast to the dozens on teams overseas. And the country has no graduate-level training in disease modeling.

Another slug of funding for COVID-19 research is on its way through NSFC. And after demonstrating that "they are committed and talented team members of the international scientific community," Lin says, China's researchers seem unlikely to give up the momentum of the past year. ■

Ground zero for science

Two Wuhan institutes dominated COVID-19 papers published in the first 6 months of 2020.

Huazhong University of Science and Technology	442
Tongji Medical College	433
Harvard Medical School (United States)	395
INSERM (France)	327
University of Milan (Italy)	287

DATA: J. TEIXEIRA *ET AL.*, *SCIENTOMETRICS*, HTTPS://DOI.ORG/10.1007/S11192-020-03675-3, 2020

Q&A

How to market vaccination

Marketing expert Stacy Wood has studied how people respond to everything from online shopping to reality TV. Now, the professor at North Carolina State University's business school has turned to COVID-19, co-authoring a 6 January paper in *The New England Journal of Medicine* that uses marketing theory to explain how to persuade people to get vaccinated. The interview was edited for length and clarity. —*Warren Cornwall*

Q: When you look at how vaccination is being marketed now, what do you see?

A: I see public health officials approaching it in a very straightforward way that says, "All we need to do is educate people about why this is a good idea." But there's more nuance to the hesitancy than we realize. Someone says, "Hey, I know how pharmaceutical products are developed and tested, this went way too fast." Another person says, "You know, science is not the answer, we trust too much in science." So the communications towards these different groups have to be well targeted.

Q: How does a provider do that?

A: People are more compelled by stories than they are by statistics. If your patient says to you, "Hey, the lady down the street from me said her niece had a bad reaction. I'm the same age as her niece. I'm really worried about this." It's important not to say, "Well, let me show you a chart that will explain exactly how rare this is." It's more important to say, "I have a patient exactly your age who was in here last week, and they were one of the first people to get the vaccine, and they did great."

Q: Some people have a really big megaphone, like Anthony Fauci. What would you tell him?

A: People don't like to be lumped in with the average. You may say the average person is going to have no reaction. Well, how dare you imply I'm an average person, I am very special. I can see very clearly that someone who's unlike Dr. Fauci by age, or people of color, might say, "Well, look, that may be true for you, but for people in my situation …." He needs a couple of Fauci surrogates who meet these other communities a little closer.

Q: You suggest a visible marker that you've been vaccinated, like a Livestrong bracelet.

A: The gist of the strategy is that it's a visible sign of in-group/out-group. That's one that works really well for people who are in the "probables": I probably will get it or I probably won't. I don't know if observables would ever change someone who's in the hardcore "definitely, no." ■

PUBLIC HEALTH

COVID-19 measures also suppress flu—for now

In downside, trend could weaken immunity and complicate vaccine formulation

By **Kelly Servick**

Influenza forecasters are a cautious bunch. Flu cases can spike in late winter after months of low infection rates, making experts reluctant to predict a mild season too soon. But many are ready to declare that COVID-19 control measures have dramatically tamped down the flu and other respiratory viruses that would normally be ripping through the Northern Hemisphere.

The World Health Organization (WHO), based on global surveillance data collected through late last month, says flu activity in the Northern Hemisphere is at "interseasonal levels," meaning it's as low as in an ordinary summer. In the United States, the percentage of outpatient visits for influenzalike illness is at 1.6%, well below the 2.6% baseline used to define a seasonal epidemic. U.S. clinical labs have collected 925 positive samples since the end of September 2020, versus 63,975 at this point in the 2019–20 flu season.

"I'd be very surprised if we have a typical flu season now," says John McCauley, a virologist who directs the Worldwide Influenza Centre at the Francis Crick Institute in London. "To see nothing so far, it's difficult to see how it's going to come up in large numbers in January."

For now, that's a relief. Fearing a flu surge on top of the pandemic, many European countries ramped up fall immunization campaigns, says Cornelia Adlhoch, an epidemiologist at the European Centre for Disease Prevention and Control. In the United States, the Centers for Disease Control and Prevention reported record flu vaccine distribution; surveys showed adult vaccination climbed from 42% in 2019 to 53% in 2020.

"But I don't think it's the vaccine" that accounts for the mercifully light flu season, McCauley says. Instead, he and others point to COVID-19 measures such as mask wearing, social distancing, and travel restrictions. As in the Southern Hemisphere early last year (*Science*, 21 August 2020, p. 890), efforts that failed to fully control SARS-CoV-2 have brought less infectious seasonal viruses to heel—including influenza and respiratory syncytial virus (RSV), which causes serious illness in infants and the elderly.

For virologist Trevor Bedford of the University of Washington, Seattle, the unusual flu season means a challenge. His team analyzes flu virus genomes collected by WHO's surveillance network to identify emerging strains, which the next year's flu vaccine will have to protect against. "Generally, we have thousands of viruses to look at, and it's still challenging," he says. This season, just 127 sequences were collected between 1 September 2020 and 1 January 2021, versus 12,218 in that period the year before.

Many are a genetic variant of a flu virus that recently emerged in Cambodia, Bangladesh, and India and has caused a small seasonal outbreak, Bedford says. "That's the strain I suspect would be the one we'd pick [as a component of] the vaccine if we had to pick it today." WHO will convene a group in February to decide on the composition of the next vaccine for the Northern Hemisphere.

Natural immunity to flu might suffer from this anomalous season. Fewer infections one season can lead to a larger susceptible population and a bigger outbreak the next. "We saw cases go down, and as disease modelers, we knew … there might be a bit of a twist," says Rachel Baker, an epidemiologist at Princeton University. In a November 2020 study in the *Proceedings of the National Academy of Sciences*, Baker and colleagues simulated future flu and RSV outbreaks in more than 300 U.S. counties and Mexican states assuming a 20% reduction in transmission of those viruses this year. For some locations, their model predicted outbreaks in the winter of 2021–22 that were double the size of typical years'.

More susceptibility could also lead to outbreaks outside peak virus season, Baker says. She suspects that's happening in Australia: After unusually low rates of RSV in the Southern Hemisphere's winter, the country began to lift lockdowns. Some Australian states documented a spike in October 2020, as summer approached, and continue to report above-average levels.

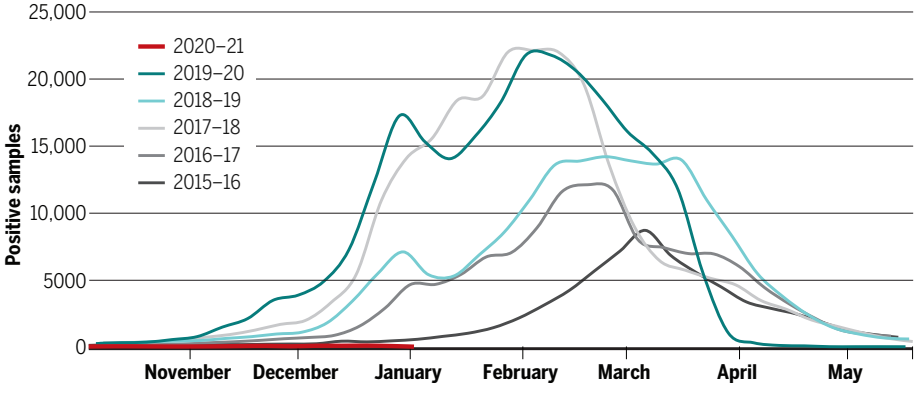
Flu outbreaks are less predictable, however, and might not rebound in the same way, Baker says; in her team's model, suppressing flu transmission one season didn't consistently boost incidence in the next. And if worries about a spike next year inspire more flu shots, "a larger outbreak might be thwarted," she says.

Bedford says a less welcome development might also mitigate a flu surge next year: a revival of COVID-19 and a reinstatement of any loosened control measures. "If we don't get enough people vaccinated over the course of the summer, mainly [because of] vaccine hesitancy," he says, "we'll get some smaller wave of COVID."

But even as the threat of COVID-19 subsides in future winters, mitigation measures might linger, says Benjamin Singer, a pulmonary and critical care physician at Northwestern University. "As we start thinking about the balance of all respiratory viruses—COVID, plus flu, plus the others—are we in the United States and in the West going to start thinking more about wearing masks in public in winter months?" he wonders. "It's an interesting sociologic kind of question: how our behavior will be impacted by our experience with COVID." ■

Flu away

The number of influenza-positive samples reported by U.S. clinical laboratories remains low in 2020–21 compared with past years, even though labs are testing tens of thousands of samples per week.



CREDITS: (GRAPHIC) N. DESAI/*SCIENCE*; (DATA) NATIONAL RESPIRATORY AND ENTERIC VIRUS SURVEILLANCE SYSTEM/CDC



FEATURES

On 1 December 2020, the 900-ton instrument platform of the Arecibo Observatory crashed into its dish, which is cradled in a natural sinkhole.

PHOTO: RICARDO ARDUENGO/AFP VIA GETTY IMAGES

FALLEN GIANT

Engineering failures and a harsh climate conspired in the sudden collapse of the Arecibo telescope. Now, researchers are planning a rebirth

By **Daniel Clery**

In the early morning of 10 August 2020, Sravani Vaddi, a postdoc astronomer at the Arecibo Observatory in Puerto Rico, was working from home, but her thoughts were at Arecibo's giant radio telescope. At 2 a.m., she had one precious hour to focus the 305-meter dish on NGC 7469, a distant galaxy. At its center, two supermassive black holes wheeled around each other, following an earlier galaxy merger. Vaddi wanted to see whether having two dark hearts instead of the usual one made the galaxy shine more brightly by stirring up gases and stoking starbirth. Radio emissions from the glowing gases would help her find out.

When she checked in near the end of her observations, computer servers suggested the telescope wasn't pointing at the galaxy anymore. She couldn't get an on-site telescope operator on the phone, so she gave up and went to bed.

She woke up to a full inbox. At 2:45 a.m., toward the end of her slot, an 8-centimeter-thick steel cable, one of 18 suspending a 900-ton instrument platform high above the dish, had pulled out of its socket at one end and fallen, slicing into the dish. "I was totally shocked. How could a cable break?" she says. Although she didn't know it at the time, the photons she gathered from NGC 7469 would be the last ones Arecibo would ever scoop up.

The rest of the story is now well known. A second support cable snapped 3 months later, on 6 November, and the National Science Foundation (NSF), which owns the observatory, said attempting repairs was too dangerous: Arecibo would be dismantled (*Science*, 27 November 2020, p. 1018). On 1 December, fate took control as more cables snapped and the platform, as heavy as 2000 grand pianos, came crashing down into the dish.

Hail and farewell

Built into the hills of Puerto Rico, the Arecibo Observatory was a force in radio astronomy for 57 years. But its design left it vulnerable to a harsh tropical climate. *Graphic by* **Chris Bickel**



Arecibo, Puerto Rico

Gregorian dome
Added in 1997, the dome focuses radio waves onto receivers covering a range of frequencies.

Cable anchor

Tower 8

Instrument platform
The platform weighs 900 tons, stressing the support cables.

Line feed
This antenna bounces radar beams off the ionosphere, a mirrorlike layer of charged particles in the atmosphere.

Suspension cables

View below

Tower 12

Access catwalk

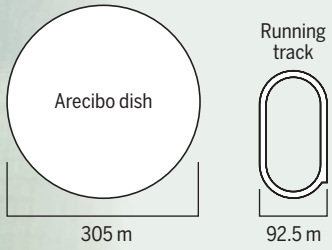
Tower 4

Karst terrain
Arecibo was built in a sinkhole in a Swiss cheese landscape of soft limestone rocks. The sinkhole supports the reflector dish and protects it from radio interference.

Reflector dish
A 1974 upgrade replaced a wire mesh with 38,000 aluminum panels.

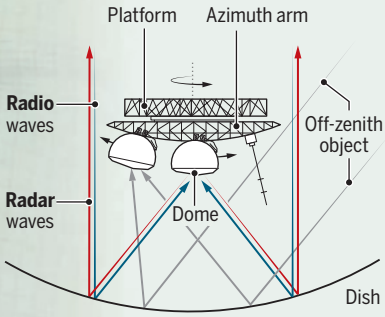
Big eye on the sky

Arecibo was the world's largest radio dish until it was surpassed in 2016 by a radio telescope in China. Size offers sensitivity to faint objects.



How Arecibo worked

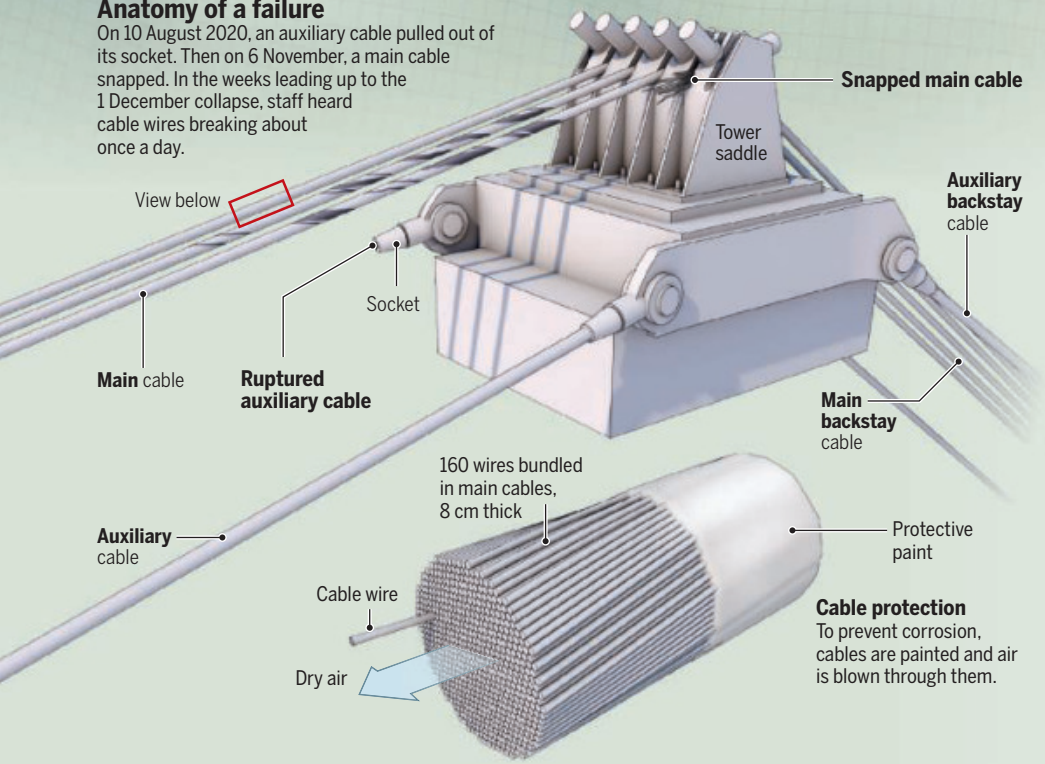
Radio astronomy
Arecibo's spherical dish allows it to see objects that aren't directly overhead; the telescope "points" by moving receivers on the platform.



Radar astronomy
In radar mode, the dish turns emitted waves into a collimated beam. The dish catches reflections from targets in the upper atmosphere or Solar System.

Anatomy of a failure

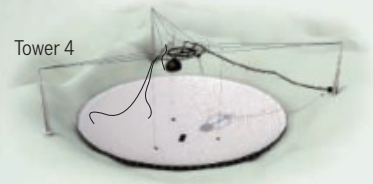
On 10 August 2020, an auxiliary cable pulled out of its socket. Then on 6 November, a main cable snapped. In the weeks leading up to the 1 December collapse, staff heard cable wires breaking about once a day.



Cable protection
To prevent corrosion, cables are painted and air is blown through them.

Fall from grace

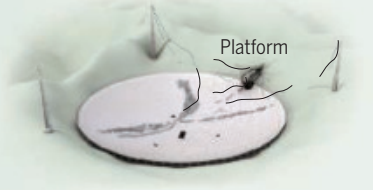
1. After two cables connected to Tower 4 broke, the remaining four shouldered extra loads.



2. On 1 December, those four cables snapped within seconds of each other.



3. The platform crashed through the dish and onto the hillside.



DATA: RHYS TAYLOR/WWW.RHYSY.NET

The loss dismayed scientists worldwide. Although 57 years old, Arecibo was still a scientific trailblazer. Its powerful radar could bounce radio waves off other planets and asteroids, revealing the contours of their surfaces. Other antennas could heat plasma in Earth's upper atmosphere, creating artificial aurorae for study. And for most of Arecibo's life, it was the biggest radio dish in the world, able to sense the faintest emissions, from the metronomic beats of distant stellar beacons called pulsars to the whisper of rarefied gases between galaxies.

The public, familiar with the majestic dish from films such as *Contact* and *GoldenEye*, also felt the loss. And it was a bitter blow to the people of Puerto Rico, who embraced hosting the technological marvel. Some 130 people work at the observatory, and many more derive indirect economic benefits from it. Every schoolchild on the island goes on a field trip to see the telescope, and those experiences often lead to science careers, says astrobiologist Abel Méndez of the University of Puerto Rico, Arecibo. With its fall, "Puerto Rico loses much more than any other place," he says.

Along with the grief have come sharper questions. After surviving numerous earthquakes and hurricanes, why did this scientific crown jewel collapse so unceremoniously on a calm winter morning? Some engineers and astronomers think manufacturing flaws or poor maintenance in a tropical, corrosive environment doomed the suspension cables. Others place blame at the feet of NSF's astronomy division, which for more than a decade tried to offload Arecibo so it could divert funds to operating newer telescopes. "Somehow, we lost a $300 million instrument, a magnificent, really expensive instrument, for a few million dollars," says Richard Behnke, an Arecibo staffer from 1970 to 1982 who went on to head the geospace science division at NSF. "Things should not collapse like that. It's not acceptable stewardship at all."

Meanwhile, astronomers are looking to the future. "First we mourned, then we had a wake, then we got down to work," says Joanna Rankin, an astronomer at the University of Vermont. Together with Arecibo staff, researchers last month delivered a white paper to NSF describing plans for a new $400 million telescope on the same site. Although any rebuilding effort faces major political and financial hurdles, the proposal aims for an instrument with even more dazzling capabilities than the one that was lost. "There's been a remarkable amount of commitment and energy," Rankin says.

ORIGINALLY, Arecibo had little to do with astronomy. The Pentagon's Advanced Research Projects Agency funded its construction in the early 1960s as part of an effort to detect and intercept incoming Soviet missiles. Researchers thought radars might be able to spot missile trails left in the ionosphere, the upper part of the atmosphere where the Sun's radiation ionizes air molecules. But little was known about the ionosphere at the time. Arecibo's large dish, built in a natural sinkhole in Puerto Rico's karst landscape, was meant to serve as a giant radar for probing it.

Upgrades after NSF took over the facility in 1969 made it alluring for more kinds of science. The original wire-mesh surface was replaced with aluminum panels that enabled observations at higher frequencies. NASA added a more powerful radar transmitter that could track Earth-threatening asteroids—and also used it to beam a message to possible civilizations among the stars. In the subsequent decades, a string of high-profile discoveries burnished the telescope's reputation: a binary pulsar system whose subtly slowing pulses provided the first indirect evidence of gravitational waves, radar maps of Venus's cloud-veiled surface that revealed evidence for volcanic repaving, and the very first planet outside our Solar System (albeit one orbiting a pulsar).

"First we mourned, then we had a wake, then we got down to work."
Joanna Rankin, University of Vermont

One of the telescope's quirks is that the curve of its dish is spherical rather than parabolic like most other radio telescopes. That shape enables the telescope to track objects that aren't directly overhead, even though the dish can't tilt. But it also focuses incoming rays to a line rather than a point, requiring elongated receivers. A 1997 upgrade added the igloo-shaped "Gregorian dome," which housed additional reflectors to focus the radio waves to a point where detectors and transmitters covering many frequencies could be mounted. "It became a completely different telescope and enabled it to stay on the cutting edge," says Robert Kerr, who was observatory director for two spells in the past 15 years.

The beefed-up scope won a starring role in the NANOGrav project, which in 2007 began to monitor pulsar beats for fluctuations caused by passing gravitational waves. Arecibo also aided the hunt for fast radio bursts, short and powerful blasts that have been one of radio astronomy's biggest mysteries of the past decade. In 2016, the telescope detected the first burst that repeated, showing that whatever produces the blasts is not destroyed in the process. (Highly magnetized neutron stars are the leading candidate.) "There was a new discovery every year," remembers astronomer Joan Schmelz, who was deputy director from 2015 to 2018.

ALTHOUGH THE 1997 upgrade kept Arecibo in the vanguard, it may also have contributed to its demise. The telescope's cables were designed with a safety factor of just over two, so everyday loads on the cables would be less than half of the load that would break them. That surprises Robert Lark, a civil engineer at Cardiff University, who says that bridge cables typically have safety factors of six or more.

The Gregorian dome and other new equipment added 300 tons to the platform. Although six auxiliary cables were added to bring the safety factor back to two, Kerr says it never quite got there. It was one of these auxiliary cables that failed in August. "One of the difficulties of adding or replacing cables is the accurate distribution of load," Lark says. "The new cable could have been bearing more than it should."

The end of the cable pulled free from its socket at the top of one of the platform's three support towers, says engineer Ramón Lugo, principal investigator for Arecibo at the University of Central Florida (UCF), which leads the consortium that now manages the observatory for NSF. Engineers make sockets by inserting the cable end into a cone-shaped steel cavity, splaying the cable's wires, and filling the cavity with molten metal such as zinc. The zinc adheres to the wires and forms a plug that locks them in place.

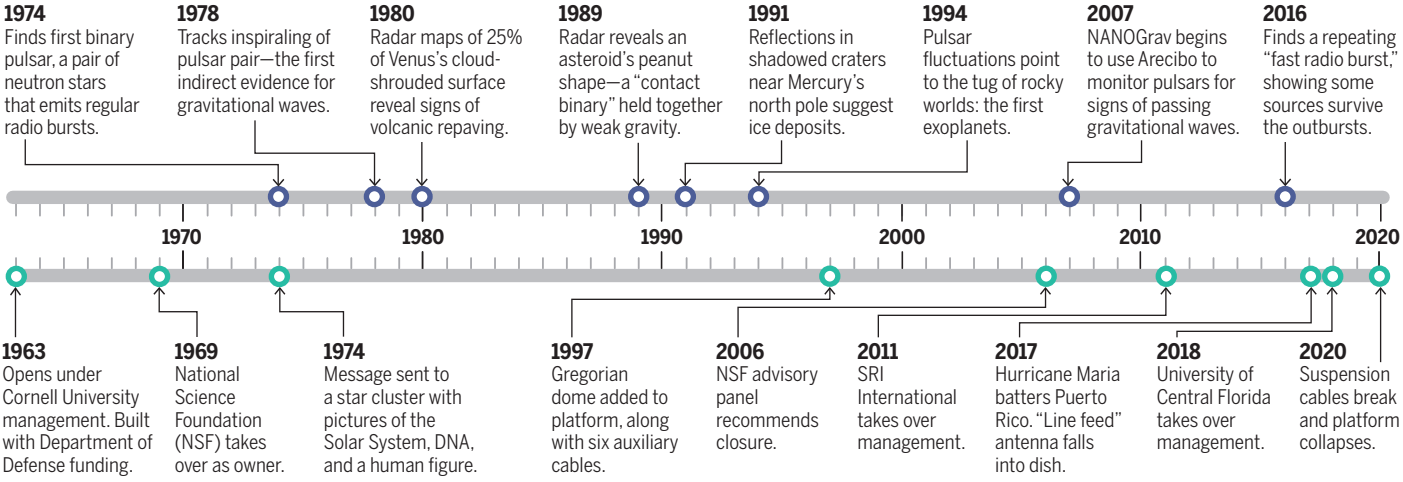
Engineers from Cornell University, which managed Arecibo from its construction until 2011, got an unexpected glimpse into one of Arecibo's sockets in the early 1980s, after an old cable was replaced and shipped to Cornell for inspection. Engineer Leigh Phoenix, who was on the team that carried out the postmortem, says the socket appeared to be faulty. The zinc was distributed unevenly and was poorly adhered to the splayed wires. "It provided an avenue for water to get in," Phoenix says. The team also found broken and cracked wires in the socket. "It would be alarming if it had been allowed to continue," he says.

After the August failure of the auxiliary cable, UCF brought in three engineering firms to assess the situation. Their suspicion was that similar manufacturing faults in this cable's socket were to blame, Lugo says. They did not think the entire structure was at risk—even though staff were hearing individual wires break at a rate of about one per day across all of the telescope's cables. The wires were known to

Big dish, big science

For most of its 57 years, the 305-meter-wide dish of the Arecibo Observatory was the largest in the world. Researchers used it to study Earth's upper atmosphere, the rocks and planets of the Solar System, and more distant astrophysical objects. Here are some of its milestones.

SCIENCE



HISTORY

corrode in the tropical environment, but with 160 of them bundled into each main cable, the breakage didn't cause immediate alarm.

The lead engineering firm, Thornton Tomasetti, built a full structural model of the telescope. It showed that the four main cables running to the platform from the crippled tower, known as Tower 4, were now bearing a load equal to about 60% of their breaking strength: a safety factor of 1.67. After inspecting the structure, all three firms concluded it was stable and that the loss of another cable wouldn't cause a collapse.

Thornton Tomasetti recommended replacing all the auxiliary cables because the socket failure made all of them suspect—and because inspections showed some other cables had slipped as much as 1 centimeter from their sockets. Lugo says Arecibo staff wrote up a 500-page proposal for the repairs in 2 weeks. NSF approved the $10.5 million request, and orders were placed for new cables. Then, on 6 November, the second cable broke: a main cable, with just six visible broken wires. And this time, it did not separate from its socket: It snapped.

The mission to save the telescope was now urgent. The engineers had to reduce the load on the three main cables still attached to Tower 4, now shouldering more than 75% of their breaking load, but they couldn't risk putting people on the towers or platform. They looked at using helicopters to install extra cables or sever platform components to reduce its weight. They even considered sacrificing the entire 110 tons of the Gregorian dome, but the violent recoil of the platform after the dome was cut loose would have been "a bad thing," Lugo says. There was no good option.

One firm—Wiss, Janney, Elstner Associates—favored stabilizing the telescope by relaxing the backstays that stretch from the towers to the ground, installing extra support cables, and removing mass from the platform before starting restoration work. But Thornton Tomasetti and the third firm, WSP, concluded that, after two cables had broken well below their design strength, none of them could be trusted. "Although it saddens us to make this recommendation, we believe the structure should be demolished in a controlled way as soon as pragmatically possible," principal engineer John Abruzzo of Thornton Tomasetti said in his report. So, at a 19 November press briefing, NSF called time on the telescope. "We understand how much Arecibo means to [the scientific] community and to Puerto Rico," said Sean Jones, head of the Directorate for Mathematical and Physical Sciences. "There is no path forward that allows us to do so safely."

On 1 December, less than 2 weeks later, Lugo, who had temporarily relocated to Puerto Rico, stopped to buy breakfast before driving up to the observatory. Just after 8 a.m., he got a call telling him the platform had collapsed. "I felt like throwing up," he says. One hour later he was on-site talking to staff who had heard and felt the crash. "There were a lot of glazed over expressions, they were all crying," he says. Cameras on a drone had caught the remaining Tower 4 cables snapping within seconds of each other while a fixed camera watched the platform fall. Arecibo's giant telescope was no more.

SO WHY DID CABLES that had held up the platform for decades suddenly fail so spectacularly? Decades earlier, staff noted cable wires snapping and suspected that corrosion from water was to blame. In 1976, managers tackled the problem by painting the cables to seal them off from the elements and installing fans to blow dry air through the length of the cables. Phoenix says that reduced the rate of wire breaks, but it's unclear how long those practices were maintained. Kerr says the fans weren't in use when he took over in 2007, nor was he aware of when the cables were last painted. "Someone may have dropped the ball," he says.

Lugo insists procedures were continued since UCF took over in 2018. "We were doing what was being done prior," he says. "It was not poorly maintained," Rankin agrees. "The Puerto Rico staff are incredible: They did every possible thing."

Natural disasters hastened the end, Lugo says. Hurricane Maria battered Puerto Rico in 2017 (*Science*, 29 September 2017, p. 1336). Phoenix says it was "an opportunity for trouble," because the storm's winds could have picked up seawater, whose salt makes it especially corrosive, and dumped some on the telescope. The observatory was also shaken by a series of earthquakes in December 2019 and January 2020.

Others say the NSF astronomy division's efforts to hand off the telescope didn't help. In 2006, the division convened an independent panel of astronomers for one of its "senior reviews" of existing facilities. To pay for planned new telescopes, such as the Atacama Large Millimeter/submillimeter

GRAPHIC: M. ATAROD/*SCIENCE*

Array in Chile and the Daniel K. Inouye Solar Telescope in Hawaii, economies were needed. Among other measures, the panel recommended closing Arecibo by 2011 unless partners were found to share operating costs. The astronomy division began to ramp down its roughly $10 million annual spending on Arecibo. NSF's atmospheric and geospace division increased its funding from $2 million to $4 million and NASA chipped in a few million dollars for tracking near-Earth asteroids. But Arecibo wasn't out of the woods.

Following an open competition, management of the observatory was transferred in 2011 from Cornell to a collaboration led by SRI International, a nonprofit research institute. NSF's astronomy division still wanted more savings, however (*Science*, 11 November 2016, p. 693). In 2018, UCF stepped up to take over management, with support from Puerto Rico's Metropolitan University and the company Yang Enterprises, on the understanding that the astronomy division would gradually reduce its contribution to $2 million annually.

Two management changes in 7 years and the slow dwindling of funds took a toll, supporters say. "People would leave or retire when there are no raises. The best people would go elsewhere," says planetary scientist Michael Nolan of the University of Arizona, who was Arecibo director from 2008 to 2011. And when old hands move on, something goes with them, Phoenix says. "Knowledge gets lost without that continuity." In response to questions from *Science*, an NSF spokesperson says, "Funding from NSF covered scheduled maintenance for the facility and should not have negatively affected the observatory's ability to maintain the 305-meter telescope."



The 110-ton Gregorian dome, added to Arecibo in 1997, boosted capabilities but the added weight may have hastened the platform's collapse.

Although Kerr is convinced neglect was a factor, he believes the collapse had no single cause. "We drove that telescope hard. It's an old piece of steel in the tropics, too heavy, it failed." But he does think the 1997 upgrade, although scientifically valuable, was a mistake. "If it had not been upgraded, it would still be standing."

AFTER THE SHOCK of last month's collapse wore off, observatory managers gave a group of staff and outside researchers 3 weeks to come up with a plan to replace the telescope. "We need something concrete to put in front of people," Lugo says. "We want to develop a system that will be relevant for another 50 years." The planners are aiming for a replacement that would surpass the capabilities of the original, be more flexible, and satisfy the needs of planetary and atmospheric scientists as well as astronomers. And they are trying to do that for less than $400 million—roughly the cost of making a Hollywood blockbuster.

The researchers first considered a new fixed dish, along with an array of independently steerable smaller ones. But in the white paper delivered to NSF last month, they went with something more ambitious: a flat, 300-meter-wide, rigid platform, bridging the sinkhole, and studded with more than 1000 closely packed 9-meter dishes. The dishes would not steer but the disk would, with hydraulics tilting it more than 45° from the horizontal. At such an extreme tilt, one edge of the disk would be higher than Arecibo's existing support towers. Steering "will be a great mechanical challenge," says Anish Roshi, head of astrophysics at the observatory.

In this design, modern receivers built into each dish could cover a broader frequency range than its predecessor and, fired synchronously, the collective radar of 1000 dishes could send out a more powerful beam than a single transmitter. Dubbed the Next Generation Arecibo Telescope, it would be nearly twice as sensitive and have four times the radar power of the original. The steerable platform would enable it to see more than twice as much of the sky as its predecessor, while the field of view of its 1000 dishes would cover a swath 500 times larger.

The extreme tilt was designed to bring an important target within view: the supermassive black hole that sits in the galactic center. The 2020 Nobel Prize in Physics was awarded in part to astronomers who peered through a haze of dust and gas at the heart of the Galaxy to painstakingly track a star following a tortuous orbit in the grip of the black hole. If radio astronomers could discover a pulsar in a similar orbit, its steady clock would allow them to study the behemoth's gravitational field in fine detail. "It would be a better probe than anything that exists now," Roshi says.

But some think the plan is a pipe dream. When choosing major projects, NSF and funders in Congress traditionally follow the recommendations of the decadal survey in astrophysics, a priority-setting exercise that at the turn of each decade asks the field what it wants to do next. The current one is already complete and will report in the coming months. "If you skip to the front of the line, those other projects would be furious," Behnke says.

In theory, Congress could choose to set aside extra funds for a pet project, as happened after the 90-meter telescope at Green Bank Observatory collapsed in 1988. West Virginia's influential senator pushed through funding for a replacement, resulting in the Robert C. Byrd Green Bank Telescope, inaugurated in 2000 and the world's largest steerable dish. But Puerto Rico, with only a nonvoting representative in Congress, has little clout, even though it could use a leg up after being battered by earthquakes and hurricanes. "In terms of economy, [Puerto Rico] needs it," Méndez says.

Lugo says advocates for a new telescope are talking to private foundations. And late last month Puerto Rico Governor Wanda Vázquez Garced allocated $8 million to clean up the site and design a replacement. Lugo says the money will go to a feasibility study of the new design. "We have to be optimistic that we will make this happen."

But for researchers who relied on data gathered by Arecibo's big eye, it won't happen soon enough, leaving them to cast around for other, less capable instruments to continue their work. "I had so many projects in mind," Vaddi says. "Along with the cable, this broke all my projects." ■

With additional reporting by Rodrigo Pérez Ortega.

PHOTO: DAVID PARKER/SCIENCE SOURCE



PERSPECTIVES

CORONAVIRUS

Herd immunity by infection is not an option

Difficult lessons are learned from a largely uncontrolled COVID-19 epidemic in Manaus, Brazil

By **Devi Sridhar** *and* **Deepti Gurdasani**

Herd immunity is expected to arise when a virus cannot spread readily, because it encounters a population that has a level of immunity that reduces the number of individuals susceptible to infection. On page 288 of this issue, Buss *et al.* (*1*) describe the extent of the largely uncontrolled severe acute respiratory syndrome coronavirus 2 (SARS-CoV-2) epidemic in Manaus, the capital of Amazonas state in Brazil. Their data show the impact on mortality rates of a largely unmitigated outbreak where even with an estimated 76% of the population being infected, herd immunity was not achieved. Manaus provides a cautionary example of unmitigated spread across a population, showing that herd immunity is likely not achieved even at high levels of infection and that it comes with unacceptably high costs.

Buss *et al.* used data on the occurrence of SARS-CoV-2–specific antibodies (seroprevalence) in blood donors, adjusted for waning antibody responses over time, to calculate an estimated attack rate for COVID-19 of 66% in June, rising to 76% in October, in Manaus. The attack rate is the proportion of at-risk people who develop infection after exposure in a period of time. This attack rate resulted in a factor of 4.5 excess mortality in 2020 relative to previous years. The infection fatality rate was estimated to be between 0.17% and 0.28%, consistent with the population being predominantly young and at reduced risk of death from COVID-19. Manaus recorded 2642 [1193/million inhabitants (mil)] confirmed deaths from COVID-19 and 3789 (1710/mil) deaths from severe acute respiratory syndrome likely to have been caused by SARS-CoV-2 infection. These figures are starkly different from the fatality rates during the same period (until 1 October) in the United Kingdom (620/mil), France (490/mil), and the United States (625/mil), and orders of magnitude higher than in Australia (36/mil), Taiwan (0.3/mil), and New Zealand (5/mil). Despite such a high proportion of the population being infected, transmission in Manaus has continued, even in the presence of nonpharmaceutical interventions (NPIs), with the effective reproduction rate (R) near 1.

These data have numerous implications. In particular, the herd immunity threshold (HIT), the proportion of the population that needs to be immune to reduce the number of susceptible individuals sufficiently to reverse epidemic growth, is likely to be high for SARS-CoV-2. If the basic reproduction

Usher Institute of Population Health Sciences and Informatics, Edinburgh Medical School, University of Edinburgh, Edinburgh EH8 9AG, UK. Email: devi.sridhar@ed.ac.uk

PHOTO: BRUNO KELLY/REUTERS



Gravediggers bury a deceased COVID-19 patient at the Parque Taruma cemetery, Manaus, Brazil, where the disease has caused a huge number of deaths.

number (R_0)—that is, the average number of secondary infections resulting from an index case in a fully susceptible population—is 2.5 to 3, as estimated within Manaus, the expected attack rate would be 89 to 94% and the HIT is expected to be 60 to 70% for a homogeneous population (*2*). Although the epidemic was largely unmitigated in Manaus at the outset, the subsequent introduction of behavioral change (such as social distancing) and NPIs (such as masks), together with nonhomogeneous population mixing, may explain the lower than expected attack rate. However, even with an estimated 76% of the population being infected, it appears the HIT was not reached. It is unclear whether this is due to waning immunity after infection, to a higher HIT than previously anticipated, or possibly a lower attack rate than estimated. Accruing data on reinfection with SARS-CoV-2 suggests that primary infection may not consistently confer long-term immunity to all infected, although the frequency of reinfection and the correlates of an effective immune response remain poorly understood. If immunity wanes over time, exposed individuals may revert to becoming susceptible, providing a new susceptible population that may then contribute to transmission.

These findings also suggest that the majority of people who are unexposed are susceptible to this virus. Although some have suggested that there may be a degree of preexisting cross-reactive T cell and humoral (antibody-related) immunity against SARS-CoV-2 (*3*, *4*) and that a lower proportion of infection of only 10 to 40% of the population could achieve herd immunity (*5*), the study of Buss *et al.* shows that there is no meaningful level of any such immunity.

Additionally, given that seroprevalence is under 20% in most countries (*6*), these data suggest that without strict control measures, the epidemic would continue to accelerate for many months ahead, with an unacceptably high cost. The deaths that would accrue in pursuit of naturally acquired herd immunity would be catastrophic. Manaus has a particularly young population. In populations with a higher proportion of older people, the overall infection fatality rates would be higher, between 0.46% and 0.72% as seen in São Paulo (*1*). Applying age-specific infection fatality rates estimated from the Manaus data, a 76% attack rate would mean 350,000, 386,000, and 1.58 million deaths in the United Kingdom, France, and the United States, respectively.

Buss *et al.* reported similar seroprevalence estimates across the age groups studied, which suggests that spread appears to have occurred relatively uniformly across the population and was not limited to specific subsets of people who may have been more exposed. This is consistent with other global evidence suggesting that it is practically impossible to "shield" the vulnerable or to carry out "focused protection" given the difficulty of identifying and separating the healthy from the vulnerable (*7*). Inevitably, with unmitigated transmission, infection will spread to vulnerable populations, with attendant costs (*8*).

Even in a younger population, SARS-CoV-2 is harmful and deadly. The growing evidence of long COVID and its long-lasting multisystem effects indicates that there may be substantial morbidity after infection (*9*, *10*). Although the risk of long COVID seems to increase with age, recent reports of multisystem disease and long COVID among children suggest that the risk in younger age groups cannot be overlooked (*11*). This highlights the risks associated with exposing large swaths of the population to a virus that is still not fully understood. Strategies for suppression of COVID-19 should not focus only on older people or those with comorbidities, but rather on the entire population, given the substantial impact of unmitigated infection on the health of all groups and the economic impacts of poor health among these groups on society as a whole.

There remain major unknowns about how long immunity to SARS-CoV-2 lasts and the risk of reinfection (*12*). Seasonal coronaviruses, which cause common colds, are known to induce short immunity, and reinfections occur commonly within 12 months of infection (*13*), although immunity to SARS-CoV and MERS-CoV, which cause more severe disease, can last several years (*14*). T cell immunity might be longer-lasting, but it is unclear whether this would fade within 1 to 2 years (*3*). If immunity does fade, this would mean that recurrent epidemic cycles are likely, especially if new strains that can escape immune detection emerge.

What the findings of Buss *et al.* definitively show is that pursuing herd immunity through naturally acquired infection is not a strategy that can be considered. Achieving herd immunity through infection will be very costly in terms of mortality and morbidity, with little guarantee of success. Although the duration and effectiveness of immunity in reducing transmission with vaccination is unclear, experience across several infectious diseases suggests that immunity can be boosted safely through vaccination, if required. Even a mitigation strategy whereby the virus is allowed to spread through the population with the objective of keeping admissions just below health care capacity, as is done for influenza virus, is clearly misguided for SARS-CoV-2. Like SARS-CoV and MERS-CoV, this virus is optimally addressed with an aggressive suppression strategy (*15*). Governments need to focus on more precise NPIs, robust test/trace/isolate systems, border control measures, mass testing, better treatments, and development and delivery of vaccines (*15*). This is the most sustainable path for countries out of this pandemic. ■

REFERENCES AND NOTES

1. L. F. Buss *et al.*, *Science* **371**, 288 (2021).
2. P. Fine, K. Eames, D. L. Heymann, *Clin. Infect. Dis.* **52**, 911 (2011).
3. N. Le Bert *et al.*, *Nature* **584**, 457 (2020).
4. Y. Zhu *et al.*, *Sci. Adv.* **6**, eabc9999 (2020).
5. J. Lourenço *et al.*, *medRxiv* 20154294 (2020).
6. R. K. Arora *et al.*, *Lancet Infect. Dis.* 10.1016/S1473-3099(20)30631-9 (2020).
7. N. A. Alwan *et al.*, *Lancet* **396**, e71 (2020).
8. C. S. Richmond *et al.*, *medRxiv* 20210294 (2020).
9. C. Galeotti, J. Bayry, *Nat. Rev. Rheumatol.* **16**, 413 (2020).
10. I. G. Long, *BMJ* **371**, m4470 (2020).
11. C. Diorio *et al.*, *Blood Adv.* **4**, 6051 (2020).
12. A. Iwasaki, *Lancet Infect. Dis.* 10.1016/S1473-3099(20)30783-0 (2020).
13. A. W. D. Edridge *et al.*, *Nat. Med.* **26**, 1691 (2020).
14. A. T. Huang *et al.*, *Nat. Commun.* **11**, 4704 (2020).
15. E. Han *et al.*, *Lancet* **396**, 1525 (2020).

10.1126/science.abf7921

NUCLEAR PHYSICS

From nuclear clusters to neutron stars

Measurements of α cluster formation in nuclear "skins" can improve neutron star models

By **Or Hen**

When neutron stars are formed, their massive gravitational pressure "crushes" most of their protons and electrons into neutrons. Understanding the interaction between the remaining protons (~5%) and neutrons in the star's core is required to model the neutron star equation of state, which relates its pressure and density and determines many of its macroscopical properties. These proton-neutron interactions are governed by the extremely complex strong nuclear force that challenges direct EOS calculations. This problem is traditionally overcome by using effective mean-field models. Although overall instructive, the important impact of nucleon-nucleon correlations and nuclear clusters are usually not explicitly included in these calculations. On page 260 of this issue, Tanaka *et al.* (*1*) now report precise measurements of α cluster (helium-4 nuclei) formation in the outer neutron "skin" of a wide range of neutron-rich tin isotopes that should help constrain models.

A neutron star is born when a massive star runs out of nuclear fuel. After all of the matter at the very center of the star has been transformed into iron or similar elements through nuclear fusion, it collapses under its own gravitational pressure and leaves an extremely compact remnant (*2*). A typical neutron star is about as big as Manhattan (~10 km radius) but has about 1.4 times the mass of the Sun (~10^6 times the mass of Earth). The density inside their core ranges from about two to five times that of atomic nuclei.

In the mean-field models often used to study nuclei and neutron stars, individual interactions between particles (neutrons and protons) are averaged and replaced by the average potential experienced by each particle in the system. Such models contain tunable parameters whose values are chosen to reproduce known properties of atomic nuclei. However, these parameters could depend on the neutron-proton asymmetry and system density, both of which are far higher in the star's core than in normal atomic nuclei.

Neutron-proton asymmetry effects are described by the nuclear symmetry energy, $E_{sym}(\rho)$, that describes the difference in the energy between symmetric nuclear matter (in which the number of protons equals the number of neutrons) and pure neutron matter at density ρ. The density dependence of the symmetry energy is then described by its slope, $L(\rho) = 3\rho\, dE_{sym}(\rho)/d\rho$. The symmetry energy is well constrained at the density of terrestrial atomic nuclei (ρ_0), but its density dependence $L(\rho_0)$ is not (*3*, *4*).

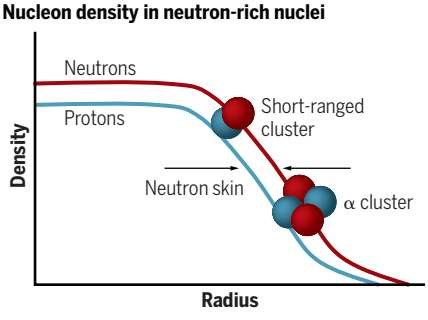
Determining L would greatly improve modeling of the matter inside the cores of neutron stars. Usually, the method used to constrain L is to measure nuclear neutron skins, which are the differences between the radii of the neutron and proton distributions in neutron-rich nuclei (*2*, *5*). This method is based on the density decrease of atomic nuclei near their surface; neutrons are pushed out to a larger radius depending on L. This structural model is based on mean-field calculations, which show a strong correlation between calculated neutron skins and the density dependence of the symmetry energy (*5*) but usually neglect the effects of nucleon-nucleon correlations and nuclear clusters.

Because protons are electrically charged, the proton distribution radius of many nuclei has been measured with electromagnetic probes (*6*, *7*). By contrast, neutrons are electrically neutral, and measuring their distribution radii has proven to be an extremely challenging task. The experiment of Tanaka *et al.* used a 392 MeV proton beam to knock out α clusters from the nuclear surface. The measured cross sections, which decreased with increasing mass number, are directly sensitive to the abundance of α clusters. Their dependence on the proton-neutron asymmetry of the measured isotopes showed excellent agreement with the mean-field models that include cluster effects (*8*, *9*). The same calculations also show that cluster formation affects the correlation between the neutron skin and the density dependence of the symmetry energy. This finding is supported by the recent chiral dynamics study of Miller *et al.* (*10*), which found that a different type of clustering—two-nucleon short-range correlations (*11*, *12*)—can also potentially affect the thickness of the neutron skin.

The impact of such cluster correlations was previously considered but deemed to be negligible compared with the large experimental uncertainties in the determination of the neutron skin. This assumption is now being challenged by a new generation of high-precision experiments. Most notably, the PREX (^{208}Pb Radius Experiment) collaboration (*13*) at the U.S. Jefferson Lab accelerator uses parity-violating elastic electron scattering to directly measure the neutron radius of lead and recently reported achieving 1% accuracy. Along with precision measurements made with pion photoproduction reactions (*14*) by the Crystal Ball collaboration at the German Mainz Microtron (MAMI) accelerator, future measurements may reach 0.5% accuracy. The results of Tanaka *et al.* call for new precision theoretical calculations that directly account for nuclear correlations and clusters. Such theoretical advances are in progress (*15*) and will enable a precise extraction of the density dependence of the symmetry energy from the neutron skin measurements. ■

Probing neutron skins

The neutron skin, the region where neutron density exceeds proton densities in nuclei, is affected by a cluster formation in the outer low-density regions (as measured by Tanaka *et al.*) and short-ranged clusters at higher-density regions.



GRAPHIC: N. DESAI/SCIENCE

Department of Physics, Massachusetts Institute of Technology, Cambridge, MA 02139, USA. Email: hen@mit.edu

REFERENCES AND NOTES

1. J. Tanaka *et al.*, *Science* **371**, 260 (2021).
2. J. M. Lattimer, M. Prakash, *Science* **304**, 536 (2004).
3. J. M. Lattimer, Y. Lim, *Astrophys. J.* **771**, 51 (2013).
4. B. A. Li, X. Han, *Phys. Lett. B* **727**, 276 (2013).
5. X. Roca-Maza *et al.*, *Phys. Rev. Lett.* **106**, 252501 (2011).
6. I. Angeli, K. P. Marinova, *At. Data Nucl. Data Tables* **99**, 69 (2013).
7. R. F. Garcia Ruiz *et al.*, *Nat. Phys.* **12**, 594 (2016).
8. S. Typel, G. Ropke, T. Klahn, D. Blaschke, H. H. Wolter, *Phys. Rev. C Nucl. Phys.* **81**, 015803 (2010).
9. S. Typel, *Phys. Rev. C Nucl. Phys.* **89**, 064321 (2014).
10. G. Miller *et al.*, *Phys. Lett. B* **793**, 360 (2019).
11. O. Hen *et al.*, *Rev. Mod. Phys.* **89**, 045002 (2017).
12. R. Subedi *et al.*, *Science* **320**, 1476 (2008).
13. S. Abrahamyan *et al.*, PREX Collaboration, *Phys. Rev. Lett.* **108**, 112502 (2012).
14. C. M. Tarbert *et al.*, (Crystal Ball at MAMI and A2 Collaboration), *Phys. Rev. Lett.* **112**, 242502 (2014).
15. G. Hagen *et al.*, *Nat. Phys.* **12**, 186 (2015).

10.1126/science.abf2427

COMPUTER SCIENCE

The language of a virus

Viral fitness and its immune escape can be modeled by using concepts of natural language

By **Yoo-Ah Kim** *and* **Teresa M. Przytycka**

Uncovering connections between seemingly unrelated branches of science might accelerate research in one branch by using the methods developed in the other branch as stepping stones. On page 284 of this issue, Hie *et al.* (*1*) provide an elegant example of such unexpected connections. The authors have uncovered a parallel between the properties of a virus and its interpretation by the host immune system and the properties of a sentence in natural language and its interpretation by a human. By leveraging an extensive natural language processing (NLP) toolbox (*2*, *3*) developed over the years, they have come up with a powerful new method for the identification of mutations that allow a virus to escape from recognition by neutralizing antibodies.

In 1950, Alan Turing predicted that machines will eventually compete with men in "intellectual fields" and suggested that one possible way forward would be to build a machine that can be taught to understand and speak English (*4*). This was, and still is, an ambitious goal. It is clear that language grammar can provide a formal skeleton for building sentences, but how can machines be trained to infer the meanings? In natural language, there are many ways to express the same idea, and yet small changes in expression can often change the meaning. Linguistics developed a way of quantifying the similarity of meaning (semantics). Specifically, it was proposed that words that are used in the same context are likely to have similar meanings (*5*, *6*). This distributional hypothesis became a key feature for the computational technique in NLP, known as word (semantic) embedding. The main idea is to characterize words as vectors that represent distributional properties in a large amount of language data and then embed these sparse, high-dimensional vectors into more manageable, low-dimensional space in a distance-preserving manner. By the distributional hypothesis, this technique should group words that have similar semantics together in the embedding space.

Hie *et al.* proposed that viruses can also be thought to have a grammar and semantics. Intuitively, the grammar describes which sequences make specific viruses (or their parts). Biologically, a viral protein sequence should have all the properties needed to invade a host, multiply, and continue invading another host. Thus, in some way, the grammar represents the fitness of a virus. With enough data, current machine learning approaches can be used to learn this sequence-based fitness function.

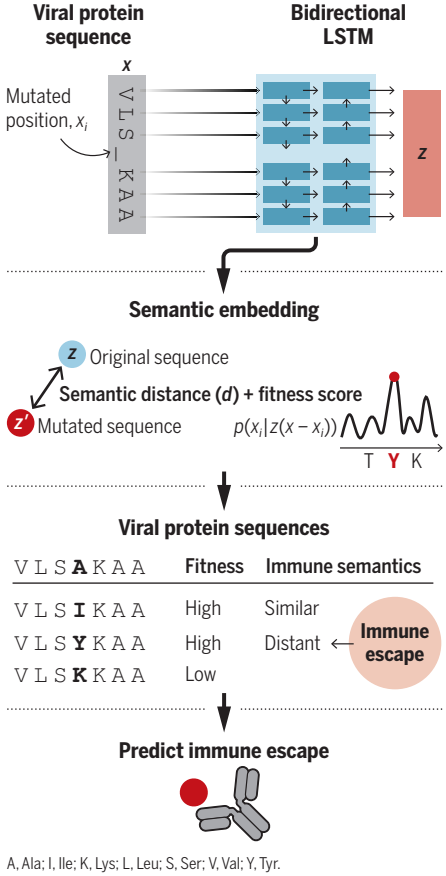
But what would be the meaning (semantics) of a virus? Hie *et al.* suggested that the semantics of a virus should be defined in terms of its recognition by immune systems. Specifically, viruses with different semantics would require a different state of the immune system (for example, different antibodies) to be recognized. The authors hypothesized that semantic embeddings allow sequences that require different immune responses to be uncovered. In this context, words represent protein sequences (or protein fragments), and recognition of such protein fragments is the task performed by the immune system. To escape immune responses, viral genomes can become mutated so that the virus evolves to no longer be recognized by the immune system. However, a virus that acquires a mutation that compromises its function (and thus fitness) will not survive. Using the NLP analogy, immune escape will be achieved by the mutations that change the semantics of the virus while maintaining its grammaticality so that the virus will remain infectious but escape the immune system. On the basis of this idea, Hie *et al.* developed a new approach, called constrained semantic change search (CSCS).

Computationally, the goal of CSCS is to identify mutations that confer high fitness and substantial semantic changes at the same time (see the figure). The immune escape scores are computed by combining the two quantities. The search algorithm builds on a powerful deep learning technique for language modeling, called long short-term memory (LSTM), to obtain semantic embeddings of all mutated sequences and rank the sequences according to their immune escape scores in the embedded space. The semantic changes correspond to the distance of the mutated sequences to the original sequence in the semantic embedding, and its "grammaticality" (or fitness) is estimated by the probability that the mutation appears in viral sequences. The immune escape scores can then be computed by simultaneously considering both the semantic distance and fitness probability.

Hie *et al.* confirmed their hypothesis for the correspondence of grammaticality and semantics to fitness and immune response in three viral proteins: influenza A hemagglutinin (HA), HIV-1 envelope (Env), and severe acute respiratory syndrome coronavirus 2 (SARS-CoV-2) Spike. For the analogy of semantics to immune response, they found that clusters of semantically similar viruses were in good correspondence with virus subtypes, host, or both, confirming

Predicting immune escape

The constrained semantic change search algorithm obtains semantic embeddings of all mutated protein sequences using bidirectional long short-term memory (LSTM). The sequences are ranked according to the combined score of the semantic change (the distance of a mutation from the original sequence) and fitness (the probability that a mutation appears in viral sequences).



A, Ala; I, Ile; K, Lys; L, Leu; S, Ser; V, Val; Y, Tyr.

National Center of Biotechnology Information, National Library of Medicine, NIH, Bethesda, MD, USA.
Email: przytyck@ncbi.nlm.nih.gov

GRAPHIC: V. ALTOUNIAN/SCIENCE

that the language model can extract functional meanings from protein sequences. The clustering patterns also revealed interspecies transmissibility and antigenic similarity. The correspondence of grammaticality to fitness was assessed more directly by using deep mutational scans evaluated for replication fitness (for HA and Env) or binding (for Spike). The combined model was tested against experimentally verified mutations that allow for immue escape. Scoring each amino acid residue with CSCS, the authors uncovered viral protein regions that are significantly enriched with escape potential: the head of HA for influenza, the V1/V2 hypervariable regions for HIV Env, and the receptor-binding domain (RBD) and amino-terminal domain for SARS-CoV-2 Spike.

The language of viral evolution and escape proposed by Hie *et al.* provides a powerful framework for predicting mutations that lead to viral escape. However, interesting questions remain. Further extending the natural language analogy, it is notable that individuals can interpret the same English sentence differently depending on their past experience and the fluency in the language. Similarly, immune response differs between individuals depending on factors such as past pathogenic exposures and overall "strength" of the immune system. It will be interesting to see whether the proposed approach can be adapted to provide a "personalized" view of the language of virus evolution. ■

"...immune escape will be achieved by the mutations that change the semantics of the virus while maintaining its grammaticality so that the virus will remain infectious..."

REFERENCES AND NOTES

1. B. Hie, E. Zhong, B. Berger, B. Bryson, *Science* **371**, 284 (2021).
2. L. Yann, Y. Bengio, G. Hinton, *Nature* **521**, 436 (2015).
3. T. Young, D. Hazarika, S. Poria, E. Cambria, *IEEE Comput. Intell. Mag.* **13**, 55 (2018).
4. A. Turing, *Mind LIX*, 433 (1950).
5. Z. S. Harris, *Word* **10**, 146 (1954).
6. J. R. Firth, in *Studies in Linguistic Analysis* (1957), pp. 1–32.

ACKNOWLEDGMENTS

The authors are supported by the Intramural Research Programs of the National Library of Medicine at the National Institutes of Health, USA.

10.1126/science.abf6894

METABOLISM

Targeting metabolism to influence aging

Inhibition of glutamine metabolism promotes death of senescent cells and improves healthy life span in mice

By **Christopher Pan** *and* **Jason W. Locasale**

Glutamine has a host of metabolic functions, including biosynthesis, redox maintenance, and chromatin biology. Drugs are currently available to target glutamine and related metabolism. However, the use of these compounds has been limited by finding appropriate applications because the role of glutamine in health and disease is still poorly understood. Some studies have pointed to a limited role of glutamine metabolism in vivo; others have found specific roles in critical areas of biomedical interest, such as the potentiation of immune responses in cancer. On page 265 of this issue, Johmura *et al.* (*1*) report a role for glutamine in maintaining the viability of senescent cells and the senescence-associated secretory phenotype, which may be a major factor in the aging process. Thus, targeting glutamine and associated metabolic processes could be an attractive, clinically feasible way to modify the aging process.

It was noted in the 1950s that culture of cell lines such as mouse fibroblasts and human HeLa cells requires copious amounts of glutamine, which was counter to its identification as a nonessential amino acid (*2*). Almost 70 years later, glutamine continues to be the most abundant amino acid in many formulations of cell culture media (*3*). Glutamine metabolism has many functions, including the use of the carbon atoms of glutamine to fuel the biosynthetic tricarboxylic acid (TCA) cycle in mitochondria, a process called anaplerosis (*4*). Furthermore, nearly all other functions of glutamine have been found to have some role in supporting cell proliferation. Moreover, many of the major oncogenes and tumor suppressor genes, such as *KRAS*, *MYC*, and *TP53*, can influence the activity of glutamine metabolism (*5*). Other studies have indicated that tumor glutamine metabolism and cancer phenotypes could be affected by dietary glutamine (*6*).

Department of Pharmacology and Cancer Biology, Duke University School of Medicine, Durham, NC, USA. Email: dr.jason.locasale@gmail.com

Drug development efforts to target glutamine metabolism have focused on glutaminase 1 (GLS1), the enzyme that converts glutamine to glutamate and ammonia as the initial step in the breakdown of glutamine (glutaminolysis). For example, CB-839, a small molecule derived from the parent compound bis-2-(5-phenylacetamido-1,3,4-thiadiazol-2-yl)ethyl sulfide (BPTES), and the compound IACS-6274 have been administered in humans with, for example, renal cell carcinoma (*4*). Additionally, analogs and derivatives of glutamine involving 6-diazo-5-oxo-L-norleucine (DON) have been developed as agents that have pleiotropic effects on glutamine metabolism (*7*).

The role of glutamine metabolism has had its controversies. One study concluded that the use of glutamine, particularly in the TCA cycle, in vivo was less than anticipated in certain mouse cancer models, which suggested that the importance of glutamine may have been overemphasized in part owing to stronger effects in cell culture that result from high concentrations of glutamine in culture media (*8*). Nevertheless, several studies have found an essential role for glutamine in mice, including situations that have clinical application, such as combining GLS1 inhibition with immunotherapies in mice (*7*).

Aging can be defined by a progressive decline in tissue function and is a risk factor for many pathologies, including fibrosis and cancer. There is emerging evidence suggesting that cellular senescence, which has been studied in cancer, is a key biological process that links multiple pathologies of aging. Cellular senescence is characterized by a stable cell cycle arrest that is thought to occur after exposure to stress, including oxidative, mitochondrial, and replicative stress (*9*). Senescent cells secrete a myriad of proinflammatory chemokines and cytokines, called the senescence-associated secretory phenotype (SASP). SASP alters the surrounding microenvironment and may propagate tissue senescence though paracrine signaling. Senescent cells have been proposed to accumulate during aging and underlie chronic inflammation mediated by SASP, eventually leading to tissue dysfunc-

tion and the onset of various age-associated pathologies. Recent observations in mice support the idea that removal of senescent cells can extend healthy life span (*10*, *11*). These findings have led to the exploration of pharmacological approaches to induce selective death in senescent cells (senolysis).

Although it has been found that metabolism can influence cellular senescence, a general understanding of the links between metabolism, senescence, and aging is still in its early stages (*12*). Johmura *et al.* reveal that glutamine metabolism may contribute to the pathogenesis of age-related disorders (see the figure). They found that *GLS1* expression was up-regulated in multiple cell types in response to diverse senescent stimuli, and its depletion induced senolysis and improved various age-associated organ dysfunctions in mice. As a possible mechanism, the authors present evidence that senescent cells utilize glutamine to neutralize the intracellular acidosis that results from senescence-associated lysosomal dysfunction. Indeed, supplementation of ammonia could ablate the senolytic activity of GLS1 inhibition. A number of interpretations are consistent with this finding, including the anabolic functions of ammonia that could then couple to the activity of the TCA cycle. More analysis of metabolic pathway activity in the presence of ammonia and supplementation with other nutrients might address this. These possibilities could be separate or interconnected metabolic mechanisms from those that involve nicotinamide adenine dinucleotide (NAD^+), which along with mitochondrial metabolism are perhaps the most studied molecular features associated with aging (*13*). Given the pleotropic roles of glutamine metabolism, more work is needed to better define the metabolic requirements of senescent cells.

The general molecular traits of senescent cells and their contribution to aging and related diseases remain open questions (*14*). The identification of GLS1 as a senolytic target confirms metabolism as a major regulator of aging, thus providing some rationale for how therapeutics that target metabolism might achieve specificity for senescent cells as anti-aging agents. GLS1 is an attractive target for anti-aging therapies because clinical studies for cancer indications have so far established safety (*4*). Much attention has been focused on the use of dietary supplementation or possibly metformin or rapamycin use to manipulate aging. These efforts have included increasing NAD^+ concentrations and altering mitochondrial metabolism, which, although promising, may not be the entire picture (*13*). The findings of Johmura *et al.* suggest a complementary strategy, although more research is needed. ■

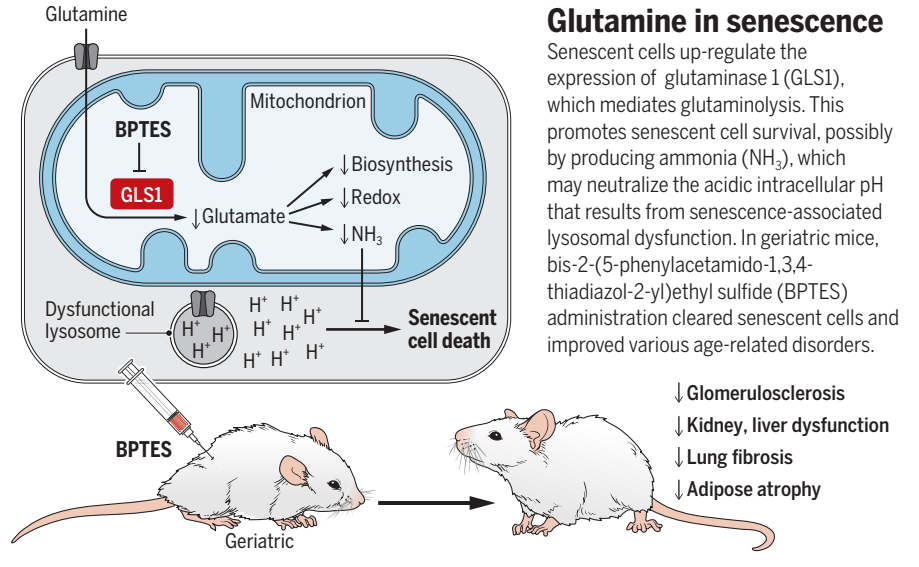
REFERENCES AND NOTES

1. Y. Johmura *et al.*, *Science* **371**, 265 (2021).
2. H. Eagle, V. I. Oyama, M. Levy, C. L. Horton, R. Fleischman, *J. Biol. Chem.* **218**, 607 (1956).
3. J. Vande Voorde *et al.*, *Sci. Adv.* **5**, eaau7314 (2019).
4. B. J. Altman, Z. E. Stine, C. V. Dang, *Nat. Rev. Cancer* **16**, 749 (2016).
5. A. J. Levine, A. M. Puzio-Kuter, *Science* **330**, 1340 (2010).
6. M. B. Ishak Gabra *et al.*, *Nat. Commun.* **11**, 3326 (2020).
7. R. D. Leone *et al.*, *Science* **366**, 1013 (2019).
8. S. M. Davidson *et al.*, *Cell Metab.* **23**, 517 (2016).
9. J. Campisi, *Annu. Rev. Physiol.* **75**, 685 (2013).
10. J. N. Farr *et al.*, *Nat. Med.* **23**, 1072 (2017).
11. J. Chang *et al.*, *Nat. Med.* **22**, 78 (2016).
12. J. Kaplon *et al.*, *Nature* **498**, 109 (2013).
13. T. Nacarelli *et al.*, *Nat. Cell Biol.* **21**, 397 (2019).
14. V. Gorgoulis *et al.*, *Cell* **179**, 813 (2019).

ACKNOWLEDGMENTS

J.W.L. advises Restoration Foodworks, Nanocare Technologies, and Raphael Pharmaceuticals.

10.1126/science.abf6368



GRAPHIC: KELLIE HOLOSKI/*SCIENCE*

Glutamine in senescence

Senescent cells up-regulate the expression of glutaminase 1 (GLS1), which mediates glutaminolysis. This promotes senescent cell survival, possibly by producing ammonia (NH_3), which may neutralize the acidic intracellular pH that results from senescence-associated lysosomal dysfunction. In geriatric mice, bis-2-(5-phenylacetamido-1,3,4-thiadiazol-2-yl)ethyl sulfide (BPTES) administration cleared senescent cells and improved various age-related disorders.

CULTURAL EVOLUTION

Behavioral convergence in humans and animals

Local ecology combines with culture to produce behavioral variation in hunter-gatherers

By **Kim Hill** *and* **Robert Boyd**

Over the 20th century, the social sciences developed without taking much notice of humans' nature as products of evolution. In the 1970s this attitude was challenged by behavioral biologists (*1*, *2*) who asserted that general principles concerning the behavior of life forms must also be relevant to understanding human behavior. They argued that because human cognition and emotions had evolved by natural selection, these behavior-generating mechanisms should generally shape behavior so that it maximizes biological fitness. Not all social scientists agreed. Cultural anthropologists, in particular, were mostly aghast at the rigidly scientific and overtly biological nature of this perspective, viewing it as blatantly flawed (*3*). They claimed that differences between and within human societies were mainly due to variant cultural belief systems. On page 292 of this issue, Barsbai *et al.* (*4*) show that adaptation to local ecological conditions is an important determinant of variation in human behavior in traditional societies.

The sample analyzed by Barsbai *et al.* consists of 339 hunter-gatherer societies that are most appropriate for comparison because their members' lives and livelihoods are intimately constrained by the natural world. The authors show that variation in hunter-gatherer patterns for 15 behavioral variables statistically converges on the same characteristics that are most common in birds and mammals in the same local regions of the world. These traits include diet composition, mobility patterns, paternal invest-

School of Human Evolution and Social Change, Institute of Human Origins, Arizona State University, Tempe, AZ 85287, USA. Email: kim.hill@asu.edu, robert.t.boyd@gmail.com

ment, divorce rates, social group size, and social stratification. In other words, in places where hunter-gatherers are more polygynous, there also tend to be more polygynous bird and mammal species. These patterns appear to be driven by ecological and habitat similarity, not by locational proximity per se. Not only are hunter-gatherers behaviorally similar in similar ecologies, but even mammals and birds in those ecologies tend to exhibit the same behavioral regularities as do the human populations. Hence, the study appears to validate the basic premise of the evolutionary perspective called "human behavioral ecology" (*5*, *6*).

However, it is a mistake to conclude from this that culture is unimportant. Beginning in the 1980s, researchers in human behavioral sciences developed a sophisticated, scientific, evolutionary theory accounting for the role of culture in human behavior (*7*, *8*). These scientists provided both theoretical and empirical evidence that social learning was a prime determinant of human behavioral variation. The affective and cognitive mechanisms that underpin social learning are adaptations and are in large part responsible for our species' spectacular ecological success, but they also create historical patterns absent in other species and lead to outcomes not predicted by theories developed for noncultural creatures.



Penan hunter-gatherers from Borneo extracting sago palm starch, their dietary staple. The Penan were one of 339 societies around the world showing convergence in behavioral patterns with bird and mammal species living in the same habitats (Barsbai *et al.*, this issue).

Barsbai *et al.* show convincingly that ecological factors explain much variation in human behavior, but so too does cultural history. For example, Mathew and Perreault (*9*) studied the causes of variation among 172 native American groups in western North America. Like Barsbai *et al.*, they found that ecological factors explained a substantial amount of variation, particularly in behaviors related to subsistence and technology. But the variation in subsistence-related behaviors was equally well explained by the linguistic distance between groups, which proved to be an even better explanation than ecological factors for the variation in political organization, religious practice, and kinship organization. Moreover, the effect of cultural history seems to persist for hundreds or even thousands of years.

Cultural evolution can also lead to outcomes not predicted by the evolutionary mechanisms applied to other species. Barsbai *et al.* show that variation in human residential group size has the same relationship to ecology as in other species. However, human foragers are much more cooperative than other primates (*10*), and sometimes they cooperate in groups numbering hundreds of individuals in communal foraging, construction of shared capital facilities, and warfare (*11*). No other vertebrate cooperates on these scales. Exactly why this is the case is controversial, but it seems likely that culturally transmitted social norms play an important role.

Culture and genes are linked in a tight coevolutionary embrace, and this leads to complex patterns of genetic and cultural coadaptation. For example, Henrich has recently argued (*12*) that the extent to which people are embedded in networks of kin obligation is a function of both ecological factors (cooperative intensive agriculture) and cultural history (church edicts against kin marriage and collective property institutions), and that variations in the intensity of kin-network embeddedness ultimately transformed human psychology into that observed today in "WEIRD" (Western, educated, industrialized, rich, democratic) societies, where individualism is paramount, rather than the psychology of traditional societies, where collectivism and kin-group favoritism predominate. Experiments show that the cognitive, emotional, and psychological effects of these different cultural histories are profound, and imply that findings from Western modern societies may often be irrelevant to predicting behavior in non-Western and traditional societies. Likewise, the spread of monogamy in modern societies, despite increasing wealth stratification, appears to be a puzzle that requires both adaptive modeling (*13*) and a recognition that monogamous social norms substantially increased cooperation with societies, and this norm can spread by group competition and cultural imitation (*12*). Coevolution between genes and culture in different ecologies may lead to uniquely human patterns not anticipated by animal studies. These examples illustrate just how complex human behavioral studies will become when the social sciences fully integrate an adaptive evolutionary view with a view of human behavioral variation in terms of cultural social norms. So far, a complete theory that predicts when culture will override fitness maximizing ecological adaptation and vice versa is not available. That will be the challenge for the next generation of social scientists, as an "either/or" view is replaced with an integrated evolutionary theory of human behavior. ■

REFERENCES AND NOTES

1. E. O. Wilson, *Sociobiology* (Harvard Univ. Press, 1976).
2. R. Alexander, *Darwinism and Human Affairs* (Univ. of Washington Press, 1979).
3. M. Sahlins, *The Use and Abuse of Biology* (Univ. of Michigan Press, 1976).
4. T. Barsbai, D. Lukas, A. Pondorfer, *Science* **371**, 292 (2021).
5. B. Winterhalder, E. Smith, *Evol. Anthropol.* **9**, 51 (2000).
6. M. Borgerhoff Mulder, *Behav. Ecol.* **24**, 1042 (2013).
7. R. Boyd, P. Richerson, *Culture and the Evolutionary Process* (Univ. of Chicago Press, 1985).
8. L. Cavalli-Sforza, M. Feldman, *Cultural Transmission and Evolution* (Princeton Univ. Press, 1981).
9. S. Mathew, C. Perreault, *Proc. R. Soc. B* **282**, 20150061 (2015).
10. K. Hill, *Hum. Nat.* **13**, 105 (2002).
11. R. Boyd, *A Different Kind of Animal* (Princeton Univ. Press, 2018).
12. J. Henrich, *The WEIRDest People in the World* (Farrar, Straus and Giroux, 2020).
13. C. Ross *et al.*, *J. R. Soc. Interface* **15**, 144 (2018).

10.1126/science.abf7572

PHOTO: YVAN COHEN/LIGHTROCKET/GETTY IMAGES

VIEWPOINT: COVID-19

Bioactive lipids in antiviral immunity

Lipids may influence viral entry, replication, and clearance and modulate immune responses

By **Katherine N. Theken**[1,2] *and* **Garret A. FitzGerald**[1,2,3]

Severe acute respiratory syndrome coronavirus 2 (SARS-CoV-2) has brought focus to attempts to limit viral replication and manage the immunological response to infection. Lipids modulate host receptor binding, facilitate viral fusion, and fuel viral replication; thus, modulation of viral-host lipid interactions may have therapeutic utility (*1*). Indeed, the spike (S) glycoprotein on the surface of SARS-CoV-2 tightly binds the free fatty acid linoleic acid, stabilizing it and reducing its interaction with the host angiotensin-converting enzyme 2 (ACE2) receptor that facilitates viral cell entry (*2*). However, in the case of many viral infections, including COVID-19, it is the overexuberant host immune response that results in life-threatening consequences of infection. Therefore, therapies that modulate bioactive lipids that regulate the host immune response to respiratory viral infections may be beneficial.

Viruses may release lipids as they transiently disrupt membrane integrity during cell entry or by causing cell lysis. Oxidized phospholipids (oxPLs) are generated enzymatically—for example, by 15-lipoxygenase in immune cells—yielding specific enantiomers (*3*), or they are produced nonenzymatically when reactive oxygen species react with unsaturated fatty acids in membrane phospholipids (see the figure). The effects of oxPLs are context- and site-specific. They can function as damage associated molecular patterns (DAMPs) to amplify the host innate immune response and contribute to the pathogenesis of acute lung injury by activating Toll-like receptor 4 (TLR4) signaling (*4*) with a potency similar to that of endotoxin (produced by Gram-negative bacteria). However, lower concentrations of oxPLs can have protective effects by enhancing pulmonary endothelial barrier function and inducing expression of antioxidant genes. Autoantibodies directed against PLs and PL binding proteins may worsen the severity of COVID-19 because they may stimulate the formation of neutrophil extracellular traps, which are extruded DNA "nets" that can promote venous thrombosis (blood clots). Cleavage of isoprostanes—free radical oxidized prostaglandin (PG) isomers—from membrane lipids affords an accessible index in biological fluids as biomarkers of lipid peroxidation.

Sphingosine-1-phosphate (S1P) is formed by phosphorylation of the lipid sphingosine by one of two sphingosine kinases (SK1 and SK2), and its concentrations in blood are tightly regulated through irreversible cleavage by S1P lyase (SPL) and lipid phosphate phosphatases (LPPs). It acts intracellularly or through one of five membrane G protein–coupled receptors ($S1PR_1$ to $S1PR_5$) in immune cells, resulting in diverse effects on innate immune function. S1PR antagonists are approved for treatment of autoimmune diseases. S1P signaling in the lung decreases dendritic cell (DC) migration and expansion and recruitment of $CD8^+$ T cells in response to influenza A virus (IAV) infection. Antigen presentation to lymphocytes by DCs thus links the innate and adaptive immune systems. S1PR activation in endothelial cells early (i.e., 1 hour) in IAV infection in mice tempers the hyperinflammatory response and improves survival, whereas deletion of *S1pr1* in endothelial cells decreases survival and worsens lung pathology after IAV infection (*5*). It remains to be seen if S1PR agonists would be similarly beneficial if administered at later stages of infection, as would be more common in clinical settings. SK2 is also a rational drug target because it facilitates viral persistence by restraining T cell immune pathology during lymphocytic choriomeningitis virus clone 13 infection in mice (*6*).

Eicosanoids are metabolites of arachidonic acid, the fatty acid present in membrane phospholipids. Eicosanoids include PGs and thromboxane—together, prostanoids—formed by the cyclooxygenases COX-1 and COX-2; the leukotrienes formed by the lipoxygenase (LOX) enzymes; and epoxyeicosatrienoic acids (EETs) and 20-hydroxyeicosatetraenoic acid (20-HETE) formed by cytochrome P450 (CYP) enzymes. These bioactive lipids can modulate antiviral immune responses differently.

The first step in prostanoid synthesis is the conversion of arachidonic acid to prostaglandin H_2 (PGH_2) by COX-1 or COX-2. PGH_2 is further metabolized to the bioactive prostanoids prostaglandin E_2 (PGE_2), prostaglandin D_2 (PGD_2), prostacyclin (PGI_2), prostaglandin $F_{2\alpha}$ ($PGF_{2\alpha}$), and thromboxane A_2 (TxA_2), which can then bind to their receptors to elicit biological effects. The role of COX-1 in viral infections has not been well described, although mortality after H3N2 IAV infection was higher in mice in which COX-1 was deleted or inhibited. By contrast, COX-2 expression is up-regulated in response to viral infection and suppression of COX-2–derived PGs or deletion of *Ptgs2* (which encodes COX-2) before H3N2 IAV infection in mice tempers the inflammatory response, attenuates weight loss, and improves survival. This is coincident with a reduction in the numbers of neutrophils, macrophages, and the cytokines tumor necrosis factor–α (TNF-α), interleukin-1β (IL-1β), IL-6, and interferon-γ (IFN-γ) in bronchoalveolar lavage fluid (BALF) (*7*).

Treatment of mice with COX inhibitors before IAV infection similarly reduced inflammation and improved survival. COX-2 inhibition may also enhance the response to viral infection in the setting of a chronic inflammatory state such as that induced by obesity (*8*). Obese mice have higher amounts of cytokines and chemokines in lung homogenates at baseline and display poor induction of the type 1 IFN response that is critical to viral clearance. PG suppression restores type 1 IFN induction and improves survival in response to infection in obese, but not in lean, mice (*8*). Overall, genetic deletion and pharmacological inhibition of the COXs give concordant results where available, but these enzymes produce prostanoids with contrasting effects on immune function and hemostasis.

Downstream of the COXs, attention has focused on PGE_2, given its well-recognized immunomodulatory effects. Deletion or blockade of microsomal PGE synthase 1 (mPGES-1), the major source of PGE_2, or of the E prostanoid receptors, EPr2 or EPr4, suppresses the immune response to viral infection. *Ptges* deletion improves survival, lowers viral load, and promotes pulmonary infiltration of macrophages, monocytes, and DCs after H1N1 IAV infection in mice (*9*). Furthermore, *Ptges* deletion enhanced adaptive immune responses, with higher numbers of $CD4^+$ and $CD8^+$ T cells in lymph nodes, BALF, and lungs of mice. Pharmacologic inhibition of mPGES-1 or of EPr2 and EPr4 signaling in vivo improves

[1]Department of Systems Pharmacology and Translational Therapeutics, University of Pennsylvania Perelman School of Medicine, Philadelphia, PA, USA. [2]Institute for Translational Medicine and Therapeutics, University of Pennsylvania Perelman School of Medicine, Philadelphia, PA, USA. [3]Department of Medicine, University of Pennsylvania, Perelman School of Medicine, Philadelphia, PA, USA. Email: garret@upenn.edu

survival after IAV infection, and this benefit is lost in mice lacking the type I IFN-α/β receptor.

PGD_2 is the predominant COX-2 product of mast cells and acts through its two receptors, DPr1 and DPr2. DPr1 signaling delays migration of DCs to lung and lymph nodes by down-regulating the expression of C-C chemokine receptor type 7 (CCR7) on respiratory DCs in response to infection. DPr1 inhibition enhances DC migration and, in turn, T cell proliferation, which increased survival in older but not younger mice after SARS-CoV infection (*10*). In a neonatal mouse model of severe respiratory syncytial virus (RSV)–induced bronchiolitis, treatment with a DPr2 inhibitor decreased viral load and improved morbidity by up-regulating IFN-γ expression. This effect was recapitulated by treatment with a DPr1 agonist, suggesting that these two receptors for PGD_2 have opposing roles in the regulation of the antiviral response (*11*).

$PGF_{2\alpha}$, prostacyclin, and TxA_2 may contribute to the systemic effects of respiratory viral infection. For example, $PGF_{2\alpha}$ and prostacyclin promote or restrain, respectively, pulmonary fibrotic reactions to viral infection in mice. Antagonism of the thromboxane receptor (TPr) prevents acute respiratory distress syndrome (ARDS) in an endotoxin model in sheep (*12*). Suppression of TxA_2 formation may have the added benefit of inhibiting platelet-dependent thrombosis. Thus, early administration of well-tolerated TPr antagonists may limit progress to severe COVID-19.

Of the leukotriene eicosanoids, the expression of LTB_4 and cysteinyl leukotrienes (cysLTs) is up-regulated in nasal or lung lavage fluids from animals and humans infected with viruses. They promote inflammation, vascular leakiness, and bronchoand vasoconstriction. However, evidence for modulation by leukotrienes of the immune response to viral infection is conflicting. Administration of zileuton, an inhibitor of 5-lipoxygenase (5-LO, which produces a precursor of LTB_4), before RSV infection in mice improved virus-inflicted airway constriction and reduced inflammatory cells in the lungs and weight loss (*13*).

However, leukotriene signaling may support tolerance to IAV infection. In the lungs of IAV-infected mice, interstitial macrophages deficient in LTB_4 receptor signaling failed to produce type I IFN to suppress activated inflammatory monocyte-derived macrophages, which was one of the main drivers of tissue injury and death from uncontrolled immune responses (*14*). Similarly, CysLT1 receptor blockade reduced the susceptibility of alveolar macrophage–deficient mice to IAV and decreased airway hyper-responsiveness in mice challenged with RSV. However, treatment of respiratory symptoms of post-RSV bronchiolitis in humans with montelukast, a CysLT receptor antagonist, was inconclusive.

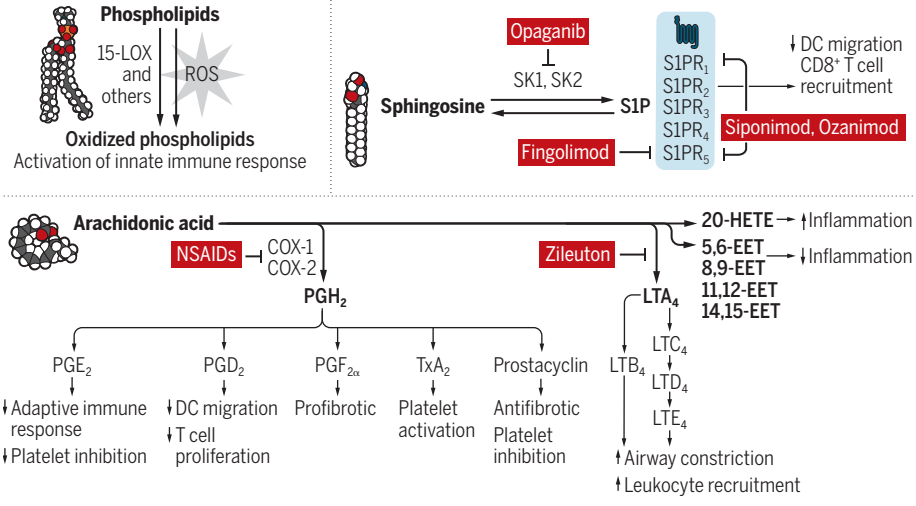
CYP-derived eicosanoids also possess immunomodulatory properties, but their role in regulating the host response to viral infection has not been studied to date. The EETs attenuate cytokine-induced nuclear factor κB (NF-κB) activation and leukocyte adhesion to the vascular wall. Soluble epoxide hydrolase (sEH) rapidly hydrolyzes EETs to the less biologically active dihydroxyeicosatrienoic acids (DHETs), and inhibition of sEH has been studied as a therapeutic strategy to decrease inflammation in vivo. Conversely, 20-HETE activates NF-κB signaling and induces expression of cellular adhesion molecules and cytokines, thereby promoting inflammation.

The role of bioactive lipids in inflammation is complex, and additional studies in humans and model organisms are essential to elucidate their importance in regulating the immune response to viral infection, particularly SARS-CoV-2. Further, genomic, transcriptomic, and serial lipidomic analyses in individuals with COVID-19 may reveal specific lipid pathways that contribute to pathology, as well as identify whether these pathways predict or mediate the heterogeneous response to viral infection.

In the current pandemic, there may be utility in targeting eicosanoids and other bioactive lipids with existing drugs. These approaches would likely be most effective early in the disease before the development of ARDS, where cytokines and chemokines dominate. However, even in that setting, leukotrienes and related compounds may serve as important amplifying signals, which has prompted suggestions to combine approved 5-LO inhibitors with CysLT antagonists in the treatment of severe COVID-19 (*15*). Given the thrombotic complications of COVID-19, early intervention in patients with increased hemostatic markers with low-dose aspirin (which inhibits platelet COX1), TPr antagonists, or prostacyclin receptor (IPr) agonists are among the therapeutic possibilities that might be explored. Although nonsteroidal anti-inflammatory drugs (NSAIDs, such as ibuprofen) should be avoided in patients with renal compromise in ARDS owing to the importance of vasodilator PGs in the maintenance of renal blood flow, more discrete modulation of selective, downstream biosynthetic enzymes and/or receptors—for example, with mPGES-1 inhibitors or EPr antagonists—may have therapeutic utility in the treatment of viral disease. ■

Immunomodulatory lipids

Oxidized phospholipids, S1P, and eicosanoids derived from arachidonic acid can affect antiviral immune responses. Drugs (red boxes) target some of these pathways and may have application in treating COVID-19.



15-LOX, 15-lipoxygenase; COX, cyclooxygenase; DC, dendritic cell; EET, epoxyeicosatrienoic acid; 20-HETE, 20-hydroxyeicosatetraenoic acid; IFN, interferon; LT, leukotriene; NSAID, nonsteroidal anti-inflammatory drug; PG, prostaglandin; ROS, reactive oxygen species; S1P, sphingosine-1-phosphate; S1PR, S1P receptor; SK, sphingosine kinase; TxA_2,thromboxane A_2.

REFERENCES AND NOTES

1. E. Ketter, G. Randall, *Annu. Rev. Virol.* **6**, 319 (2019).
2. C. Toelzer *et al.*, *Science* **370**, 725 (2020).
3. V. B. O'Donnell *et al.*, *Sci. Signal.* **12**, eaau2293 (2019).
4. Y. Imai *et al.*, *Cell* **133**, 235 (2008).
5. A. Cartier *et al.*, *Science* **366**, eaar5551 (2019).
6. C. J. Studstill *et al.*, *J. Clin. Invest.* **130**, 6523 (2020).
7. M. A. Carey *et al.*, *J. Immunol.* **175**, 6878 (2005).
8. A. J. X. Zhang *et al.*, *J. Infect. Dis.* **219**, 795 (2019).
9. F. Coulombe *et al.*, *Immunity* **40**, 554 (2014).
10. J. Zhao *et al.*, *J. Clin. Invest.* **121**, 4921 (2011).
11. R. B. Werder *et al.*, *Sci. Transl. Med.* **10**, eaao0052 (2018).
12. P. G. Kühl *et al.*, *Am. J. Physiol.* **254**, R310 (1988).
13. R. C. Welliver 2nd *et al.*, *J. Infect. Dis.* **187**, 1773 (2003).
14. E. Pernet *et al.*, *Nat. Microbiol.* **4**, 1389 (2019).
15. C. D. Funk *et al.*, *Front. Pharmacol.* **11**, 1214 (2020).

10.1126/science.abf3192

GRAPHIC: A. KITTERMAN/SCIENCE



POLICY FORUM

Collembola, such as this *Acanthanura sp.* in North Queensland, Australia, can be useful indicators of soil quality and also the focus of nature conservation measures.

PHOTO: ANDY MURRAY/CHAOSOFDELIGHT.ORG

BIODIVERSITY

Tracking, targeting, and conserving soil biodiversity

A monitoring and indicator system can inform policy

By **Carlos A. Guerra, Richard D. Bardgett, Lucrezia Caon, Thomas W. Crowther, Manuel Delgado-Baquerizo, Luca Montanarella, Laetitia M. Navarro, Alberto Orgiazzi, Brajesh K. Singh, Leho Tedersoo, Ronald Vargas-Rojas, Maria J. I. Briones, François Buscot, Erin K. Cameron, Simone Cesarz, Antonis Chatzinotas, Don A. Cowan, Ika Djukic, Johan van den Hoogen, Anika Lehmann, Fernando T. Maestre, César Marín, Thomas Reitz, Matthias C. Rillig, Linnea C. Smith, Franciska T. de Vries, Alexandra Weigelt, Diana H. Wall, Nico Eisenhauer**

Nature conservation literature and policy instruments mainly focus on the impacts of human development and the benefits of nature conservation for oceans and aboveground terrestrial organisms (e.g., birds and plants) and processes (e.g., food production), but these efforts almost completely ignore the majority of terrestrial biodiversity that is unseen and living in the soil (*1*). Little is known about the conservation status of most soil organisms and the effects of nature conservation policies on soil systems. Yet like "canaries in the coal mine," when soil organisms begin to disappear, ecosystems will soon start to underperform, potentially hindering their vital functions for humankind. Soil biodiversity and its ecosystem functions thus require explicit consideration when establishing nature protection priorities and policies and when designing new conservation areas. To inform such efforts, we lay out a global soil biodiversity and ecosystem function monitoring framework to be considered in the context of the post-2020 discussions of the Convention on Biological Diversity (CBD). To support this framework, we suggest a suite of soil ecological indicators based on essential biodiversity variables (EBVs) (*2*) (see the figure and table S3) that directly link to current global targets such as the ones established under the CBD, the Sustainable Development Goals (SDGs), and the Paris Agreement (table S1).

Soils not only are a main repository of terrestrial biodiversity, harboring roughly one-quarter of all species on Earth, but also provide a wide variety of functions (e.g., nutrient cycling, waste decomposition) and benefits (e.g., climate regulation, pathogen resistance); they regulate the diversity and functioning of aboveground systems, including their contributions to human well-being (*3*). If we do not protect soils for the next generations, future aboveground biodiversity and food production cannot be guaranteed. Nonetheless, recent calls to expand nature protection (*4*), as well as many other initiatives aimed to shape future environmental policies (*5*), do not consider the specific requirements of soil biodiversity and associated ecosystem functions (*6*, *7*).

Discussions and data concerning soils and their sustainability have long focused on either their vulnerability to physical impacts (e.g., soil erosion) or improvements to their food production potential (e.g., through fertilization). These narrow perspectives, often missing tangible indicators and disconnected from environmental monitoring, limit a wider discussion on the ecological importance of soil biodiversity and its role in maintaining ecosystem functioning beyond food production systems. The prevailing emphasis has also prevented soils from becoming a more mainstream nature conservation priority. Although initiatives to provide a more holistic representation of soils as ecosystem services providers exist [e.g., (*8*)], standardized and timely information to track policy targets related to soils is missing, particularly at global scales. These information gaps have precluded the delivery of a robust scientific message supporting the importance of soil biodiversity and have delayed the inclusion of soil biodiversity in nature conservation debates.

Unlike for physical and chemical soil properties, the high-resolution and molecular tools needed to investigate soil biodiversity and function have only recently been developed, and harmonized static datasets are just starting to emerge (*7*). Because of this, and because soil biodiversity monitoring is not prioritized at a national level, there is a lack of knowledge on soil biodiversity compared with above-ground plants and animals. In fact, most of the 196 Parties of the CBD do not have national targets (for 2011–2020) that explicitly consider soils, with very few specifically considering soil conservation and biodiversity.

CHALLENGES AND OPPORTUNITIES

Soil organisms, including nematodes, collembola, fungi, and bacteria, are responsible for a cascade of intricate soil functions (*3*) that underpin essential ecosystem services (e.g., climate regulation, soil fertility). As such, they require specific protection measures that go beyond protecting aboveground systems or reducing the application of surplus fertilizers and fungicides. Positive measures include the identification of soil biodiversity hotspots, endemisms, and priority habitats; the assessment of relevant drivers of soil biodiversity change; and the development of dedicated nature conservation policies. Additionally, most management decisions in conservation areas are not soil-specific or, when they exist, are focused on soil physical properties (e.g., reducing soil erosion) with no specific soil biodiversity conservation targets. With-

Author affiliations are listed in the supplementary materials. Email: carlos.guerra@idiv.de

out such measures, nature conservation has limited effects on the protection of soil organisms and their functions. For example, although expansion of protected areas has demonstrated benefits for protecting birds and mammals, there is little to no benefit to belowground diversity (*1*). To prioritize soils for nature conservation worldwide, policymakers require up-to-date data as well as transparent, reliable, and unbiased policy-ready indicators that are critical to providing a measure of success or failure of policy agendas (*4*, *5*). Recent efforts to describe the macroecological drivers and patterns of soil biodiversity (*9*), the general lack of comparable temporal data (*7*), the limitations to the development of coordinated large-scale monitoring efforts (*2*, *7*), and the enormous number of undescribed soil-dwelling species have all impeded the production of reliable assessments of soil biodiversity change (*9*). As a consequence, to date, most policies are informed by sparse information on soil chemistry (e.g., soil carbon) or on impacts to soils (e.g., soil erosion), and until recently we did not have the right instruments to inform policy-makers on soil ecological changes and impacts. With recent advancements in DNA technology, methods to integrate diversity and functional data, and international agreements for soil research [e.g., the recently endorsed resolution by the Food and Agriculture Organization (FAO) 27th Session of the Committee on Agriculture on the international exchange of soil samples for research purposes], we now have the resources, initiative, and technology to support the large-scale generation of this soil ecological knowledge.

Excluding soil biodiversity and associated ecosystem functions from nature conservation targets means that policies may fail to represent them and may render soil biodiversity and critical ecosystem functions more vulnerable to global change. Below- and aboveground diversity do not necessarily follow similar ecological patterns (*6*), which suggests that even when the focus is on restoring wild areas or increasing carbon sequestration (*10*)—both seen as positive outcomes of nature conservation—such practices might not have the same positive effects on soil organisms and their associated functions (*1*). Moreover, although constrained by current knowledge and logistic limitations (*7*), available studies already show the scale at which climate and land-use change, pollution, and other types of threats directly affect soil systems (*11*), pointing to the urgent need for policies to be based on a more comprehensive view of these terrestrial ecosystems (*7*, *9*).

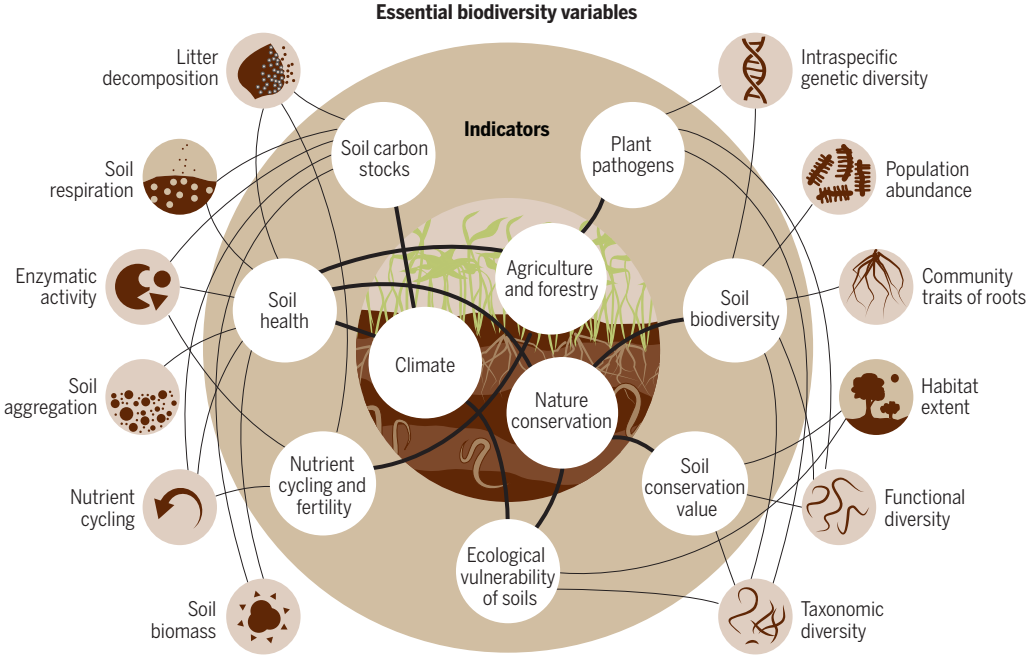
WORLDWIDE MONITORING

To fully comprehend the role of terrestrial biodiversity in the context of climate change, sustainable development, and nature conservation, we must invest in understanding what lies belowground. This requires a holistic system approach (see the figure) that includes definitions of a wide variety of soil-related EBVs, as well as standardized international monitoring systems (*12*) to track the state and dynamics of global soil biodiversity and ecosystem functioning over time. These EBVs encompass four complementary dimensions of soil systems (soil physics, soil chemistry, soil biodiversity, and soil ecosystem functions) and relate to specific ecological indicators (see the figure, inner ring, and table S3). This effort will be facilitated by existing mechanisms designed to mainstream the use of data and derived indicators to inform decision-making and policy-making, such as the Biodiversity Indicator Partnership and the U.N. System of Environmental Economic Accounting.

To this end, the global soil research community has started to organize itself to respond to the challenge. Efforts such as the International Initiative for the Conservation and Sustainable Use of Soil Biodiversity, the Global Soil Biodiversity Initiative, the Global Soil Partnership (GSP) of the Food and Agriculture Organization, and the Status of the World's Soil Resources Report reflect how the international community has started to pay greater attention to the loss of biodiversity in agricultural soils. Indicators related to soil health have also emerged, although these mostly rely only on physical and chemical parameters without any functional or biodiversity aspect explicitly included (*13*). The recent Global Soil Biodiversity Assessment for the CBD and the updated plan of action for the International Initiative for the Conservation and Sustainable Use of Soil Biodiversity are two other recent steps to elevate the policy status of soil biodiversity and increase soil literacy. However, all these initiatives rely on static fragmented soil biodiversity data without any temporal resolution or coordination.

Linking soil biodiversity to policy

Links between global soil essential biodiversity variables (EBVs) (outer ring) are prioritized by the Soil Biodiversity Observation Network (SoilBON) and policy sectors (center) through the use of soil ecological indicators (inner ring; table S3). Thin lines correspond to links between EBVs and soil indicators; thicker lines refer to links between each soil indicator and specific policy sectors. The EBVs for soil systems are proposed as a holistic system approach (table S2), where soil organisms are intertwined with relevant soil chemical, physical, and functional properties, contributing to overall societal well-being. See table S1 for further information on links to specific policy targets and policies. See table S2 for details of the EBVs.



GRAPHIC: MELISSA THOMAS BAUM/*SCIENCE*

We therefore must move beyond snapshots of soil biodiversity data and relay concrete input for temporally and spatially explicit soil biodiversity and ecosystem function indicators. As an example, in the context of the post-2020 discussions of the CBD, there is a focus on the protection of critical ecosystems. By assessing the state and trends of soil conservation value (see the figure and table S3), inherently including soil biodiversity information, we would be able to directly determine the extent to which countries are in line with this target. More important, we can support the identification of critical ecosystems that include soil communities.

In response to this need, we established the first global Soil Biodiversity Observation Network (SoilBON; https://geobon.org/bons/thematic-bon/soil-bon) under the umbrella of the Group on Earth Observations Biodiversity Observation Network (GEOBON) to systematically collect and sample observational data worldwide on the condition of soil biodiversity and functions. With the aim of including researchers working on all continents, we have proposed a plan to overcome legal limitations (e.g., centralizing requirements to comply with the Nagoya Protocol) and operational limitations (e.g., by providing funds to support researchers across the world) (*7*) to produce the first globally standardized time series on the condition of soil biodiversity and ecosystem functions (see the figure). Using lessons learned from and integrating methods used in other initiatives [e.g., (*2*, *12*, *14*)] and co-funded by multiple institutions around the world, this program will implement standard protocols across the entire monitoring infrastructure (see table S2) to systematically assess both soil biodiversity and soil ecosystem functions in both protected and nonprotected areas (*6*).

Although a global network will not have the resolution to distinguish among specific management practices, it can call attention to good examples of nature conservation focusing on soils and can be used as a global reference for comparison across regions and countries, thereby contributing to more effective soil conservation policies (see the figure and table S1). By identifying connections between soil ecological indicators and various reporting needs related to policy targets (see table S1), we provide a road map for researchers and policy-makers (see the figure and tables S1 and S2) on the priorities for data collection and on how to integrate such information into policy design.

Effective soil monitoring is needed to increase our capacity to mitigate ongoing global environmental changes (*11*) and inform policy sectors as different as nature conservation (e.g., SDG Target 15.1), land degradation (SDG Target 15.3), climate mitigation and adaptation (e.g., Paris agreement 2015), forestry (e.g., United Nations Decade on Ecosystem Restoration), and food security (e.g., SDG Target 2 and European Union Common Agricultural Policy) (table S1). Such a global initiative will not be possible without a wide network of local partners that cover different ecosystems and environmental conditions. This includes providing support to colleagues working in developing countries and establishing a centralized global analysis network across different volunteering institutions that allows for a high level of standardization and analytical power, and that can be extended to potential new partners or initiatives following the same standards [e.g., with regional or thematic focus (*14*), or focusing on data harmonization and synthesis]. In addition to increasing the quantity and quality of available soil ecological data worldwide, locally produced data and information will also become comparable between countries and projects thanks to the emerging collaboration with the Global Soil Laboratory Network of the GSP.

This program must include a strong commitment to capacity-building and knowledge-sharing mechanisms (Post-2020 CDB Goal D), as well as an open world archive of soil biodiversity resources. It provides a multi-tiered approach (globally coordinated sampling and harmonization using reference laboratories, cross-laboratory standardization and protocols, data aggregation using a clear set of EBVs and policy-relevant indicators, cross-initiative and cross-time validation and reporting) on which other networks, countries, and regions can build to create a comparable global patchwork of soil biodiversity and functional assessments. The goal is to create a program that builds on available assessments [e.g., the Global Soil Biodiversity Assessment (*15*)] to deliver valuable information on the state and trends of soil biodiversity and functions to support current policy-making and help reshape it to bring soils and their biodiversity to the center stage of global sustainability thinking. A first example is under way in Europe, where a partnership between SoilBON and several research institutions aims to provide essential biodiversity data to inform current and future European policy (e.g., the European Biodiversity Strategy for 2030; see the figure).

We aim for a future where the conservation value of giant earthworms [e.g., *Rhinodrilus alatus* (Righi 1971)] or endemic fungi [e.g., *Lactarius indigo* (Schwein 1822)] is recognized and their ecology is properly protected by nature conservation measures (e.g., establishing no-tillage areas or promoting environmental compensation schemes that explicitly include soil-related measures such as deadwood management plans that favor soil invertebrates and fungi). Local soil biodiversity should be considered when designing conservation areas and highlighted when implementing appropriate management efforts. To do this, we propose a complementary set of ecological indicators that considers the multiple facets of soil ecology (between biodiversity and key ecosystem functions) and provides a comprehensive overview of soil systems. These indicators were developed to address specific societal needs (e.g., soil health, nutrient cycling and fertility, or plant pathogens) but also to extend the use of soil ecological data to other policy realms [e.g., nature conservation (soil conservation value, soil biodiversity); climate action and land degradation neutrality (ecological vulnerability of soils, soil carbon stocks)]. If considered across the policy spectrum (table S1), these indicators will provide baseline data and methodologies to map and assess the current state and temporal trends of global soil biodiversity and functions, and to identify the regions that are more vulnerable to abrupt ecosystem shifts in the context of future climate and land-use change.

An international soil monitoring program based on EBVs and holistic indicators such as those presented here will provide the tools to assess how far we are from conservation targets in the next decades, acting as an early warning system of how current nature conservation measures are succeeding or failing in the conservation of soil biodiversity and functions. ■

REFERENCES AND NOTES

1. M. Ciobanu, N. Eisenhauer, I.-A. Stoica, S. Cesarz, *Appl. Soil Ecol.* **135**, 166 (2019).
2. L. M. Navarro *et al.*, *Curr. Opin. Environ. Sustain.* **29**, 158 (2017).
3. R. D. Bardgett, W. H. van der Putten, *Nature* **515**, 505 (2014).
4. P. Visconti *et al.*, *Science* **364**, 239 (2019).
5. S. Díaz *et al.*, *Summary for Policymakers of the Global Assessment Report on Biodiversity and Ecosystem Services of the Intergovernmental Science-Policy Platform on Biodiversity and Ecosystem Services* (IPBES, 2019).
6. E. K. Cameron *et al.*, *Conserv. Biol.* **33**, 1187 (2019).
7. C. A. Guerra *et al.*, *Nat. Commun.* **11**, 3870 (2020).
8. Food and Agriculture Organization of the United Nations, *Voluntary Guidelines for Sustainable Soil Management* (2017).
9. M. Delgado-Baquerizo *et al.*, *Nat. Clim. Chang.* **10**, 550 (2020).
10. J.-F. Bastin *et al.*, *Science* **365**, 76 (2019).
11. M. C. Rillig *et al.*, *Science* **366**, 886 (2019).
12. F. T. Maestre, N. Eisenhauer, *Soil Org.* **91**, 73–85 (2019).
13. J. Lehmann *et al.*, *Nat. Rev. Earth Environ.* **1**, 544–553 (2020).
14. A. Orgiazzi, C. Ballabio, P. Panagos, A. Jones, O. Fernández-Ugalde, *Eur. J. Soil Sci.* **69**, 140–153 (2018).
15. Food and Agriculture Organization of the United Nations, *State of Knowledge of Soil Biodiversity: Status, Challenges and Potentialities* (2020).

ACKNOWLEDGMENTS

N.E. and D.H.W. contributed equally to this work.

SUPPLEMENTARY MATERIALS

science.sciencemag.org/content/371/6526/239/suppl/DC1

10.1126/science.abd7926



Young climate activists, like those who participated in the 2019 Global Climate Strike, give Mann hope.

PHOTO: EZRA ACAYAN/STRINGER/GETTY IMAGES

CLIMATE SCIENCE

Fighting the good fight

Fossil fuel advocates may have added strategic inaction to their arsenal, but there is reason for climate optimism

By **Adrienne Hollis**

In Michael Mann's latest book, *The New Climate War*, the reader is afforded a unique perspective on the struggle for climate action and climate protection. This perspective, covering the span of a few centuries and ending in the present, weaves together the missteps, manipulations, and misrepresentations that have occurred throughout the so-called climate war between those who believe that human actions play a role in climate change and those who do not. The book ends on a hopeful note with a call to action and recommended steps for climate advocates.



The New Climate War: The Fight to Take Back Our Planet
Michael E. Mann
PublicAffairs, 2021. 272 pp.

The "new" climate war Mann refers to in the book's title introduces a previously untapped element in the climate battle—strategic inaction, as perpetuated by entities he describes as "inactivists." According to Mann, this new approach—used to greatest effect by those charged with advancing fossil fuel interests—is intended to deflect blame, divide the public, and delay action so that business can continue as usual. Climate inaction differs from climate change denial, a strategy used in past climate arguments that was ultimately unsuccessful. Although I understand Mann's reasoning, I disagree that we are in a new climate war. It is, I believe, the same war, albeit with higher stakes.

Mann describes various attacks that have been leveraged against climate advocates, including himself: attacks on scientific data, terminology, and hypotheses; attempted character assassinations; and the use of outright trickery and deceit to mislead the scientific community and the public. Such efforts, he argues, were meant to deflect attention away from fossil fuel interest groups and their supporters.

At the same time, the book ties together every action and every inaction that has affected the fight to protect Earth from the adverse consequences of climate change. Mann is transparent about times when those who fight for climate action have fallen short, for example, describing incidents in which climate change advocates have failed to refute false narratives perpetuated by climate deniers. The notion that individuals should be responsible for addressing the adverse effects of climate change is one such narrative, which, he rightly argues, deflects attention away from the fossil fuel industry.

Climate change is a "threat multiplier," a term that has different meanings in different contexts, notes Mann. From a national security perspective, for example, it may contribute to political instability and terrorist activity by exacerbating existing stressors such as agricultural deficits and water shortages. It can also imperil a country's civil infrastructure. Meanwhile, from a public health perspective, climate change can exacerbate health disparities in communities that are already disproportionately affected by environmental pollution. Here, Mann describes how adverse effects from climate change rendered regions such as Puerto Rico, where health care infrastructure was severely compromised as a result of Hurricane Maria, unable to adequately respond to the COVID-19 pandemic.

In the book's closing pages, Mann reveals that he is "cautiously optimistic" about tackling the climate crisis. His reasons stem from the fact that a great deal of attention has been focused on climate change of late, both as a result of the numerous extreme weather events that have occurred recently and because we have had to grapple with the COVID-19 crisis, which has highlighted just how unprepared and vulnerable we are to global threats.

Mann is most heartened, however, by the current revival of environmental activism, particularly, as he states, "by children across the world," which he argues has helped to show that climate change is the "defining challenge of our time." As such, this book is a must read not just for people currently working to address climate change but also for those who are new to the climate fight, the latter of whom will learn much about past challenges, struggles, and attacks that have been aimed at climate champions.

There is good reason to hope for change, Mann argues. He points to the sustainability efforts that many cities, states, corporations, and nations are embracing, and he emphasizes that although we need to recognize and accept that damage has already been done as a result of climate change, it is not too late to take action. ■

The reviewer is the senior climate justice and health scientist at the Union of Concerned Scientists, Washington, DC 20006, USA. Email: ahollis@ucsusa.org

10.1126/science.abf6346

ECONOMICS

Deflating the opaque online ad bubble

A lightweight book aims a heavyweight punch at the digital advertising ecosystem

By **Steve Tadelis**

General Motors and Ford, the two largest U.S. automakers, are together worth about US$100 billion. The combined value of Google and Facebook is about $2 trillion—20 times higher. What makes these companies worth so much? Ads. In *Subprime Attention Crisis: Advertising and the Time Bomb at the Heart of the Internet*, Tim Hwang suggests that the digital advertising industry may be on the brink of a global collapse. And if it is not, he argues, then we should push it off the cliff.

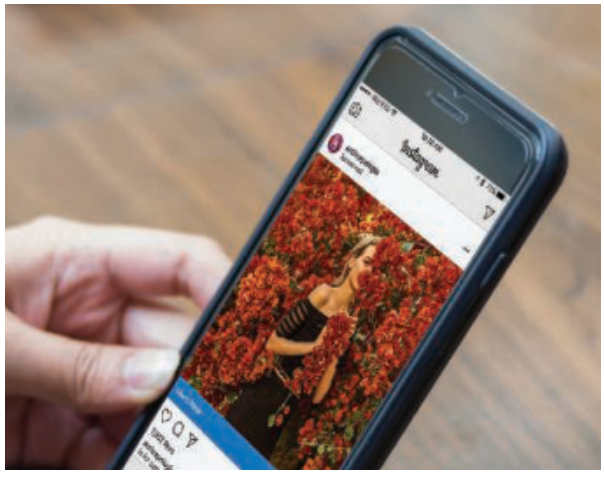
Many folks do not realize that the ads they see on their screens are sold through automated real-time auctions that resemble algorithmic trading in financial markets. Buyers bid for attention, and sellers offer eyeballs through which the attention is supplied. The market for online ads managed to grow to its current size because the underlying technology created standard ways in which attention is measured and sold. Attention has been "commoditized" in order for it to be easily traded.

Those who shaped these platforms were inspired by financial markets, Hwang argues, and indeed—under the hood—the industry resembles a stock- or commodity-trading market. The ad-tech industry, he cautions, exhibits strong parallels to the mortgage-backed financial markets that caused the 2008 global financial crisis.

Hwang describes what experts refer to as the "opacity" problem, arguing that companies do not know exactly what they are getting for their ad spend and that they considerably overvalue online ads, just as the market overvalued mortgage-backed securities in the mid-2000s. The book is thin on supporting evidence, but there is indeed a growing academic literature that demonstrates the severity of the opacity problem and the degree to which digital advertising is overvalued (*1*–*3*).

The opacity problem is exacerbated by the "subprime" nature of attention, suggests Hwang. Over the past decade or so, the value of attention has deteriorated as a result of fatigue, ad blockers, and outright fraud in the ad-tech space. Combine these factors with companies that want to spend tons of money on a shiny new advertising medium, and you have a bubble waiting to burst.

Opacity and overvaluations are clearly rampant in advertising. A recent study showed that television ads are significantly less influential than the industry claims (*4*), and another revealed that ad exchanges promise targeting that they cannot deliver, successfully predicting a viewer's gender only about half the time—just as good as a random guess (*5*). Still, marketing expenses continue to grow across the board. Why? Because many of us place more weight on unfounded convictions than on scientific evidence. And, as the past year (or four) have shown, falsehood-driven behaviors are widespread.



Overvaluation is rampant in online advertising, argues Hwang.

Ad industry insiders will insist that without robust spending on brand advertising and digital ads, a company's brand will deteriorate. Tell that to Costco, a company that spends practically nothing on advertising.

Hwang's conclusion is that we should stick a needle in the digital advertising bubble, or better yet, let the air out slowly, lest a crash cause serious turmoil to the global economy. To do so, he proposes creating independent (possibly not-for-profit) research centers that will keep the industry honest and help ad buyers correct their expectations about the benefits of digital ads.

Subprime Attention Crisis: Advertising and the Time Bomb at the Heart of the Internet
Tim Hwang
FSG Originals, 2020. 176 pp.



There is much to enjoy in this short book, and I highly recommend it to those who are interested in this topic. But the notion that we are headed toward a market collapse comparable to the one that occurred in 2008 is one I have trouble buying. Globally, stock markets are valued at around US$100 trillion. The global ad-tech industry is worth maybe $5 trillion and, unlike mortgage-backed securities, is not intertwined with other financial assets. Indeed, if advertisers substantially lower their ad spending, this will hurt the ad-tech industry but will likely also increase profits for the companies in question. Unlike financial markets, there is no contagion.

Will the internet shut down completely or shrink drastically if revenues plummet in the ad-tech industry? In 2019, Google's 118,899 employees generated $162 billion in revenue ($1.3 million per employee), while Facebook's 44,942 employees generated $70 billion ($1.6 million per employee). Meanwhile, the ad-free classified-listings site Craigslist is estimated to have raked in about $1 billion in revenues with only 50 employees ($20 million per employee). A deflated ad-tech industry may mean a smaller workforce and a lot less revenue, but I am confident that we would still be able to enjoy most of what the internet has to offer (with fewer ads). ■

The reviewer is at the Haas School of Business, University of California, Berkeley, Berkeley, CA 94720, USA. Email: stadelis@berkeley.edu

REFERENCES AND NOTES

1. T. Blake, C. Nosko, S. Tadelis, *Econometrica* **83**, 155 (2015).
2. R. A. Lewis, J. M. Rao, *Q. J. Econ.* **130**, 1941 (2015).
3. B. R. Gordon, F. Zettelmeyer, N. Bhargava, D. Chapsky, *Marketing Sci.* **38**, 193 (2019).
4. B. Shapiro, G. J. Hitsch, A. Tuchman, "Generalizable and robust TV advertising effects" (NBER Working Paper No. 27684, August 2020).
5. N. Neumann, C. E. Tucker, T. Whitfield, *Marketing Sci.* **38**, 918 (2019).

10.1126/science.abe8306

PHOTO: PIXELLOVER RM 3/ALAMY STOCK PHOTO



Some positive COVID-19 test results reflect researchers' exposure to non-infectious nucleic acids rather than a true infection.

PHOTO: BRITTA PEDERSEN/PICTURE ALLIANCE/GETTY IMAGES

Edited by **Jennifer Sills**

Anomalous COVID-19 tests hinder researchers

Universities conduct a large proportion of the community surveillance testing for severe acute respiratory syndrome coronavirus 2 (SARS-CoV-2) (*1*). At the same time, they have shifted focus to SARS-CoV-2 research to address critical needs during this pandemic. There are now multiple reports of asymptomatic researchers who worked with or near non-infectious SARS-CoV-2 nucleic acids and subsequently tested positive during SARS-CoV-2 surveillance screening (*2*, *3*). Such positive test results and the resulting isolation and quarantine are deleterious to the health of researchers, their research programs, and their close contacts. Universities and labs should take steps to identify and prevent misleading test results among their researchers.

Because health departments cannot distinguish positive test results reflecting exposure to non-infectious nucleic acids from those revealing true active SARS-CoV-2 infections, affected U.S. researchers are removed from the testing pool for 90 days, a period during which true infections could be missed (*4*). Additional false positives could result when monitoring of wastewater for viral outbreaks detects DNA products that are washed down the drain as non-biohazardous waste (*5*). As polymerase chain reaction tests, other DNA amplification tests (*6*, *7*), and the recently approved at-home nucleic acid tests (*8*) become more widespread, these cases will likely become more frequent among researchers.

To mitigate harm from misleading results, we recommend the implementation of extra safety controls (*2*) in addition to standard practices for handling nucleic acids (*9*). Genetic loci should be chosen with care to not interfere with any available tests. Incorporation of deoxyuridine triphosphate, codon optimization, and DNA watermarks can prevent detection of a laboratory-generated nucleic acid and differentiate it from circulating pathogens (*10*, *11*). DNA products should be treated with bleach or other DNA-damaging agents before disposal. The best policies and practices for preventing laboratory contamination should take place before initiating research: Once a space is contaminated with DNA, it is extremely difficult to decontaminate (*2*). These policies should accommodate the specific needs of the research and the institutions and not place undue burden on the essential work of studying these pathogens.

For individuals who are asymptomatic, have no history of SARS-CoV-2 exposure, and are affected by anomalous surveillance test results, we propose verification with orthogonal follow-up testing. At an institutional level, administrators, environmental health and safety personnel, and departments of public health should collaborate to determine who is at risk for anomalous tests and coordinate immediate follow-up testing. Alternate providers using orthogonal tests should be established before surveillance testing and/or research initiation.

Community-wide COVID-19 surveillance testing directly improves human health (*12*). Given the extensive development in testing infrastructure amassed during this short period, viral testing will likely extend to other pathogens, endemic or emergent. Sensible policies governing the stewardship of nucleic acids will help protect this vital asset.

Lindsey R. Robinson-McCarthy[1], Alexander J. Mijalis[1], Gabriel T. Filsinger[3], Helena de Puig[2,4], Nina M. Donghia[2], Thomas E. Schaus[2], Robert A. Rasmussen[2], Raphael Ferreira[1,2], Jeantine E. Lunshof[2,5,6], George Chao[1], Dmitry Ter-Ovanesyan[2], Oliver Dodd[1,2], Erkin Kuru[1,2], Adama M. Sesay[2], Joshua Rainbow[2,7], Andrew C. Pawlowski[1,2], Timothy M. Wannier[1], Peng Yin[2,3], James J. Collins[2,4,8,9,10,11], Donald E. Ingber[2,12,13,14], George M. Church[1,2,11], Jenny M. Tam[1,2]*

[1]Department of Genetics, Blavatnik Institute, Harvard Medical School, Boston, MA 02115, USA. [2]Wyss Institute for Biologically Inspired Engineering, Harvard University, Boston, MA 02115, USA. [3]Department of Systems Biology, Harvard Medical School, Boston, MA 02115, USA. [4]Institute for Medical Engineering and Science, Massachusetts Institute of Technology (MIT), Cambridge, MA 02139, USA. [5]Department of Global Health and Social Medicine, Harvard Center for Bioethics, Harvard Medical School, Boston, MA 02115, USA. [6]Department of Genetics, University Medical Center Groningen, University of Groningen, Netherlands. [7]Department of Electrical and Electronic Engineering, University of Bath, Bath, BA2 7AY, UK. [8]Department of Biological Engineering, MIT, Cambridge, MA 02139, USA. [9]Synthetic Biology Center, MIT, Cambridge, MA 02139, USA. [10]Infectious Disease and Microbiome Program,

Broad Institute of MIT and Harvard, Cambridge, MA 02142, USA. [11]Harvard–Massachusetts Institute of Technology Program in Health Sciences and Technology, Cambridge, MA 02139, USA. [12]Vascular Biology Program, Department of Surgery, Boston Children's Hospital, Boston, MA 02115, USA. [13]Harvard Medical School, Boston, MA 02115, USA. [14]Harvard John A. Paulson School of Engineering and Applied Sciences, Cambridge, MA 02138, USA. *Corresponding author.
Email: jenny.tam@wyss.harvard.edu

REFERENCES AND NOTES

1. Massachusetts Department of Public Health, "Massachusetts Department of Public Health COVID-19 dashboard—Dashboard of public health indicators" (2020), p. 22; www.mass.gov/doc/covid-19-dashboard-december-20-2020/download.
2. L. R. Robinson-McCarthy *et al.*, *OSF Preprints*, 10.31219/osf.io/9svjq (2020).
3. K. J. Wu, "These researchers tested positive. But the virus wasn't the cause," *The New York Times* (2020).
4. Centers for Disease Control and Prevention, "Duration of isolation and precautions for adults with COVID-19," (2020); www.cdc.gov/coronavirus/2019-ncov/hcp/duration-isolation.html.
5. "Status of environmental surveillance for SARS-CoV-2 virus" (World Health Organization, 2020).
6. B. A. Rabe, C. Cepko, *Proc. Natl. Acad. Sci. U.S.A.* **117**, 24450 (2020).
7. J. Joung *et al.*, *N. Engl. J. Med.* **383**, 1492 (2020).
8. U.S. Food and Drug Administration, "Lucira COVID-19 all-in-one test kit" letter of authorization (2020); www.fda.gov/media/143810/download.
9. "Dos and Don'ts for molecular testing" (World Health Organization, 2018).
10. D. C. Jupiter *et al.*, *PLOS Pathog.* **6**, e1000950 (2010).
11. M. C. Longo, M. S. Berninger, J. L. Hartley, *Gene* **93**, 125 (1990).
12. A. M. Neilan *et al.*, *Clin. Infect. Dis.* 10.1093/cid/ciaa1418 (2020).

COMPETING INTERESTS

L.R.R.-M., A.J.M., G.T.F., R.F., O.D., D.T.-O., G.M.C., and J.M.T. are co-inventors of MAP-Dx, a COVID diagnostic platform. J.J.C. is a co-founder and director of Sherlock Biosciences. G.M.C.'s tech transfer, advisory roles, and funding sources can be found at http://v.ht/PHNc.

10.1126/science.abf8873

Data-driven solutions to U.S. polarization

In their Policy Forum "Political sectarianism in America" (30 October 2020, p. 533), E. J. Finkel *et al.* summarize research on the multiple sources of the decades-long U.S. march to toxic polarization. However, the mitigation tactics they offer seem piecemeal and insufficient. To reverse a 50-year trajectory of runaway division (*1*), we need an evidence-based strategy tailored to structural change.

Research on how deeply divided societies change course (*2*) suggests that how leaders approach entrenched problems, especially early on in their tenure (*3*), can make the difference. Transformations are most likely to occur when leaders take office after a major political shock—like the COVID-19 pandemic or the 6 January storming of the Capitol by political extremists—has destabilized the status quo (*4*) and lead in a way that differs dramatically from the leadership that instigated the divisions (*5*). Moreover, in societies where distrust and suspicion reign (*6*), changes in political strategies are often best introduced with a public declaration of intention.

The Biden-Harris administration could apply such research by announcing a two-pronged strategy to defeat toxic division in America. First, given that many Americans feel left behind, the new leaders should begin by launching a listening tour during which they partner with local, trusted community groups to elicit grievances and proposed remedies (*4*). Research has shown that when members of disenfranchised groups feel heard by those in power, it can lead to constructive shifts in attitudes (*7*). Large-scale initiatives like these, when transparent and brought to completion, can begin healing (*8*).

Second, the new administration should seek to strengthen our national immune system. Research on international peacebuilding finds that many of the more sustainable initiatives helping communities transition out of intergroup strife come from within (*9*). These local initiatives (*8*) emerge in response to community challenges and manage to thrive under difficult circumstances. Today, there are thousands of bridge-building groups (*10*) across the United States that fit this bill, whose impact could be scaled up through federal funding, recognition, and coordination. They fight against the pathologies of hate and can help citizens build bipartisan alliances that take on the structural incentives that divide us. This is critical. We will never talk our way out of this division (*11*); we must aim for structural change (*12*).

Peter T. Coleman
Columbia University, New York, NY 10027, USA.
Email: pc84@columbia.edu

REFERENCES AND NOTES

1. Pew Research Center, "Political polarization in the American public" (2014).
2. R. R. Vallacher *et al.*, *Attracted to Conflict: Dynamic Foundations of Destructive Social Relations* (Springer-Verlag, 2013).
3. M. Macy *et al.*, *Sci. Adv.* **5**, eaax0754 (2019).
4. C. Gersick, *Acad. Manag. Rev.* **16**, 10.5465/amr.1991.4278988 (1991).
5. C. Gersick, *J. Change Manag.* **20**, 7 (2019).
6. S. Lindskold, M. G. Collins, *J. Conflict Resol.* **22**, 679 (1978).
7. E. G. Bruneau, R. R. Saxe, *J. Exp. Soc. Psych.* **48**, 855 (2012).
8. J. Rothman, *Ohio State J. Dispute Resol.* **22**, 105 (2006).
9. A. Munroe, "'Positive deviants' point the way in peacebuilding master's program" (U.S. Institute of Peace, 2013).
10. Morton Deutsch International Center for Cooperation and Conflict Resolution, "Organizations Transforming Polarization & Division" (2020); https://icccr.tc.columbia.edu/resources/organizations-bridging-divides/.
11. E. Badger, K. Quealy, "These Americans tried to listen to one another. A year later, here's how they're voting," *The New York Times* (2020).
12. M. J. Barber, *J. Polit.* **78**, 296 (2016).

10.1126/science.abg1730

China is pivotal to the ocean's future

Since the 1980s, China has developed into the most important player in global capture fisheries; the country now catches about 15% of the global total (*1*). As scientists and environmental groups called for an end to harmful fishing subsidies (*2*, *3*), China spent US$5.89 billion in 2018—more than twice that of the European Union—on subsidies that increase fisheries capacity (*4*). However, China has indicated a willingness to make commitments that would move the nation toward a more sustainable path. We call on the country to take these steps. Without China's action, attaining international fisheries sustainability will be unachievable.

China has discussed both domestic and international steps forward. The country pledged to reduce fuel subsidies for its domestic fishing fleet by 60% between 2014 and 2019 (*5*), and in 2016 it stated its intention to cap its distant water fishing fleet at 3000 vessels by the end of 2020 (6). In addition, China has taken part in the World Trade Organization (WTO) fishery subsidy negotiations (*7*), and the country's domestic fisheries behavior indicates that it may be poised to ratify the Agreement on Port State Measures (*8*) to prevent, deter, and eliminate illegal, unreported, and unregulated (IUU) fishing. China is also participating in the UN conference for an international, legally binding instrument to protect biodiversity beyond national jurisdiction (*9*) and has agreed to implement the 2030 Agenda, including Sustainable Development Goal 14. By committing to these international efforts and acting to eliminate harmful subsidies, end IUU fishing, and protect marine biodiversity, China could mark a profound turnaround. Currently the nation with the largest and most heavily subsidized distant water fishing fleet (*4*) and the most fishing vessels on the global IUU list (*10*), China has the opportunity to transform into a global leader in ocean sustainability.

In its position paper on WTO Reform in 2019 (*11*), China's refusal to give up its "developing country" status—despite being the world's second-largest economy—has exacerbated fears that the WTO subsidy negotiations may mean little for the world leader in international fishing. Such sidestepping has also been seen in China's distant water fishing growth strategy, which has slowed in terms of vessel numbers but increased in individual vessel size and capacity (*12*), posing a serious and continued threat to fish stocks globally

and signaling a continued unwillingness to collaborate in ocean conservation outside of its domestic waters. The WTO subsidy negotiations missed the December 2020 deadline to end harmful fishing subsidies (*7*). The agreement, now likely to be finalized in early 2021, will be one of the biggest global milestones in international fisheries to date, but meaningful change will depend on China's cooperation.

Andrew F. Johnson[1,2]* and Susanna Lidström[3,4]
[1]MarFishEco Fisheries Consultants Ltd., Edinburgh, UK. [2]Marine Sustainability, Policy & Conservation Evidence (Marine SPACE) group, The Lyell Centre, Institute of Life and Earth Sciences, School of Energy, Geoscience, Infrastructure and Society, Heriot-Watt University, Edinburgh, EH14 4AS, UK. [3]Division of History of Science, Technology and Environment, KTH Royal Institute of Technology, 100 44, Stockholm, Sweden. [4]Scripps Institution of Oceanography, University of California San Diego, La Jolla, CA 92037, USA.
*Corresponding author.
Email: andrew@marfisheco.com

REFERENCES AND NOTES

1. Food and Agriculture Organization of the United Nations, "The state of world fisheries and aquaculture: Sustainability in action" (Rome, 2020).
2. World Wildlife Fund, "Ending harmful fisheries subsidies: It's vital for the WTO to take action now" (2019).
3. U. R. Sumaila, D. Pauly, *Nature* **450**, 945 (2007).
4. U. R. Sumaila *et al*., *Mar. Pol.* **109**, 103695 (2019).
5. L. Cao, *Proc. Natl. Acad. Sci. U.S.A.* **114**, 435 (2017).
6. Ministry of Agriculture and Rural Affairs, "Thirteenth five-year national ocean fishery development plan" (2017); www.moa.gov.cn/gk/ghjh_1/201712/t20171227_6128624.htm [in Chinese].
7. WTO, "Negotiations on fisheries subsidies" (2017).
8. Food and Agriculture Organization of the United Nations, "Illegal, Unreported and Unregulated (IUU) fishing, Agreement on Port State Measures (PSMA)" (2020); www.fao.org/iuu-fishing/international-framework/psma/en/.
9. UN Intergovernmental Conference on Marine Biodiversity of Areas Beyond National Jurisdiction (2020).
10. Trygg Mat Tracking, "Combined IUU list" (2020); www.tm-tracking.org/combined-iuu-list.
11. WTO, "China's Proposal on WTO Reform" (2019); http://images.mofcom.gov.cn/sms/201905/20190514094326217.pdf.
12. H. Zhang, *Mar. Pol.* **68**, 65 (2016).

COMPETING INTERESTS

S.L. was funded by the Swedish research council Formas (grant no. 942-2015-1643).

10.1126/science.abf8888

TECHNICAL COMMENT ABSTRACTS

Comment on "Boosted molecular mobility during common chemical reactions"

Jan-Philipp Günther, Lucy L. Fillbrook, Thomas S. C. MacDonald, Günter Majer, William S. Price, Peer Fischer, Jonathon E. Beves

The apparent "boosted mobility" observed by Wang *et al*. (Reports, 31 July 2020, p. 537) is the result of a known artifact. When signal intensities are changing during a nuclear magnetic resonance (NMR) diffusion measurement for reasons other than diffusion, the use of monotonically increasing gradient amplitudes produces erroneous diffusion coefficients. We show that no boosted molecular mobility is observed when shuffled gradient amplitudes are applied.

Full text: dx.doi.org/10.1126/science.abe8322

Response to Comment on "Boosted molecular mobility during common chemical reactions"

Huan Wang, Myeonggon Park, Ruoyu Dong, Junyoung Kim, Yoon-Kyoung Cho, Tsvi Tlusty, Steve Granick

Günther *et al*. report that their control experiment using randomized magnetic field gradient sequences disagreed with findings we had reported using linear gradients. However, we show that measurements in our laboratory are consistent using both methods.

Full text: dx.doi.org/10.1126/science.abe8678

ERRATA

Erratum for the Research Article "Identification of Integrator-PP2A complex (INTAC), an RNA polymerase II phosphatase" by H. Zheng *et al*., *Science* **371**, eabg4122 (2020). Published online 15 January 2021; 10.1126/science.abg4122



CALL FOR PAPERS

SPJ
SCIENCE PARTNER JOURNALS

北京理工大學
BEIJING INSTITUTE OF TECHNOLOGY

中国空间技术研究院
China Academy of Space Technology
中国航天



Space: Science & Technology

Space: Science & Technology is an online-only, Open Access journal published in affiliation with **Beijing Institute of Technology (BIT)** and distributed by the **American Association for the Advancement of Science (AAAS)**. BIT cooperates with China Academy of Space Technology (CAST) in managing the journal. The journal aims to promote the exploration and research of space worldwide, to lead the rapid integration and technological breakthroughs of interdisciplinary sciences in the space field, and to build a high-level academic platform for discussion, cooperation, technological progress and information dissemination among professional researchers, engineers, scientists and scholars.

Submit your research to *Space: Science & Technology* today!

Learn more at **spj.sciencemag.org/space**

The Science Partner Journal (SPJ) program was established by the American Association for the Advancement of Science (AAAS), the nonprofit publisher of the *Science* family of journals. The SPJ program features high-quality, online-only, Open Access publications produced in collaboration with international research institutions, foundations, funders and societies. Through these collaborations, AAAS furthers its mission to communicate science broadly and for the benefit of all people by providing top-tier international research organizations with the technology, visibility, and publishing expertise that AAAS is uniquely positioned to offer as the world's largest general science membership society.

Visit us at **spj.sciencemag.org**

@SPJournals **@SPJournals**

OPEN ACCESS

ARTICLE PROCESSING CHARGES WAIVED UNTIL JULY 2023

RESEARCH

IN *SCIENCE* JOURNALS

Edited by **Michael Funk**



PLANT SCIENCE

Diterpenoids inhibit lipid biosynthesis

Plants make a variety of molecules that serve to protect them against hungry insects. Li *et al*. analyzed the balance between plants defending themselves and plants poisoning themselves. In wild tobacco (*Nicotiana attenuata*), two cytochrome P450 enzymes work within the biosynthetic pathway of 17-hydroxygeranyllinalool diterpene glycosides to help prevent the accumulation of toxic diterpene derivatives. Those same diterpene derivatives are formed in an insect herbivore after ingestion and cause toxicity by inhibiting sphingolipid biosynthesis in both plant and insect. —PJH *Science*, this issue p. 255

Toxic compounds in tobacco leaves fend off tobacco hornworms but can also be harmful to the plant if they accumulate.

PLASMONIC CHEMISTRY

Coaxing unreactive sites

Optical excitation of localized surface plasmon resonances can confine light and create electromagnetic (EM) "hotspots" that can increase catalytic reaction rates. Sytwu *et al.* show how optical excited plasmons can also control the location of the active site. A crossed-bar gold-palladium hydride (Au-PdH_x) plasmonic antenna-reactor system localized EM radiation away from the more reactive PdH_x tips. Using in situ environmental transmission electron microscopy, the authors show that changing the illumination wavelength and intensity, along with the surrounding hydrogen gas pressure, could shift dehydrogenation away from the sharp PdH_x nanorod tips to the flat middle faces. —PDS

Science, this issue p. 280

ARCHAEOLOGY

Early cave art from Sulawesi

Although less well known than the cave art of Paleolithic Europe, the karst landscapes of Island Southeastern Asia, especially Sulawesi, have large numbers of painted caves of greater antiquity. Using uranium-series isotope analysis at the site of Leang Tedongnge, Brumm *et al.* dated the image of a Sulawesi warty pig, defined by its characteristic head crest and preorbital facial warts, to a minimum age of more than 45,000 years ago. Not only is this the earliest art known from the region, but it is also the earliest known drawing of a recognizable animal in the world. The authors speculate that art of this style was an important cultural element of the first groups of anatomically modern *Homo sapiens* to enter this region. —MSA

Sci. Adv. 10.1126/sciadv.abd4648 (2021).



A painted image of a Sulawesi warty pig is possibly the earliest known human representation of an animal.

RNA SPLICING

A tight couple makes messenger RNAs

Gene expression in eukaryotes first requires transcription of DNA to an RNA copy and then splicing to form the final, processed messenger RNA (mRNA). Zhang *et al.* investigated how gene transcription and RNA splicing are physically coupled. Using cryo–electron microscopy, they resolved the molecular structure of a complex of the transcription enzyme RNA polymerase II with part of the splicing

PHOTOS (TOP TO BOTTOM): GRANT HEILMAN PHOTOGRAPHY/ALAMY STOCK PHOTO; MAXIME AUBERT

machinery, the U1 small nuclear ribonucleoprotein particle. The results provide important details for our understanding of coupled mRNA production. —DJ

Science, this issue p. 305

IMMUNOLOGY

GPER1 in utero to the rescue!

Several common pathogens, including influenza A virus (IAV), can activate systemic type I interferon (IFN) signaling during pregnancy. Such infections would be expected to cause birth defects and fetal mortality, but maternal IAV infections rarely produce such effects, suggesting the presence of a protective mechanism in fetal tissues. Harding *et al.* used a CRISPR screen to uncover IFN regulators that can mediate differential IFN control across tissues in human cell lines. They found that G protein–coupled estrogen receptor 1 (GPER1), which is expressed in fetal tissues, acts as a protective suppressor of IFN responses in the placenta during maternal infection. In a mouse model, pharmacological activation of GPER1 shielded fetuses from maternal inflammation. Activation of GPER1 might be promising therapeutically to protect the fetus from both maternal and fetal infections. —STS

Science, this issue p. 271

STRUCTURAL BIOLOGY

A key complex in B cell activation

A core component of the immune system are B cells, which are activated by infection and then mature to provide long-lived immunity. Activation is initiated when a cell surface B cell receptor, in association with its coreceptor, recognizes an antigen. Susa *et al.* report a structure of the B cell receptor CD81 in complex with its coreceptor, CD19. CD81 alone binds to cholesterol, but the conformational changes associated with binding to CD19 occlude the cholesterol-binding pocket. Regulating cholesterol binding could play a role in the activation mechanism. The structure also provides a basis for the design of immunotherapies. —VV

Science, this issue p. 300

QUANTUM GASES

Making a quantum pump

Most nonequilibrium, many-particle systems eventually reach a thermal state. However, some one-dimensional quantum systems do not thermalize, although they may settle into a long-term equilibrium state. Kao *et al.* studied such a system consisting of dipolar dysprosium atoms confined in an optical potential shaped like a two-dimensional array of elongated tubes. The authors cycled the contact interaction between the atoms in a prescribed way, creating increasingly excited nonthermal quantum many-body states. —JS

Science, this issue p. 296

BIOCHEMISTRY

SARS-CoV-2: From entry to autophagy?

Severe acute respiratory syndrome coronavirus 2 (SARS-CoV-2) enters cells upon binding to cell surface receptors such as angiotensin-converting enzyme 2 (ACE2) and potentially others such as integrins. Mészáros *et al.* identified short linear motifs (SLiMs) in the cytoplasmic tails of ACE2 and various integrins. Kliche *et al.* not only confirmed that many of these predicted SLiMs interacted with target peptides in various components of the endocytosis and autophagy machinery but also found that these interactions were regulated by the phosphorylation of amino acids adjacent to SLiMs. These findings could lead to new ways of preventing viral infection. —LKF

Sci. Signal. **14**, eabd0334, eabf1117 (2021).

IN OTHER JOURNALS

Edited by **Caroline Ash** *and* **Jesse Smith**

FISHING

Corporations dominate the high seas

Fishing in the high seas (regions outside of countries' exclusive economic zones) is often likened to the Wild West. It is a vast area that has been challenging to monitor—and to fish. But as technologies have improved, the high seas have become more accessible, a worrying trend for maintaining biodiversity in this region, which covers much of the planet. Monitoring technologies have also improved, however, and Carmine *et al.* used satellite and vessel ownership data to identify fishing activity and determine who was conducting it. They found that ~1000 corporations owned the >2000 vessels, but one-third of the identified vessels were owned by 100 corporations, revealing a pattern of conglomeration. Knowledge of the corporate actors, and how and where they fish, is an essential step toward sustainable high-seas fishing. —SNV

One Earth **3**, P730 (2020).



About a third of fishing vessels on the high seas are owned by large corporations.

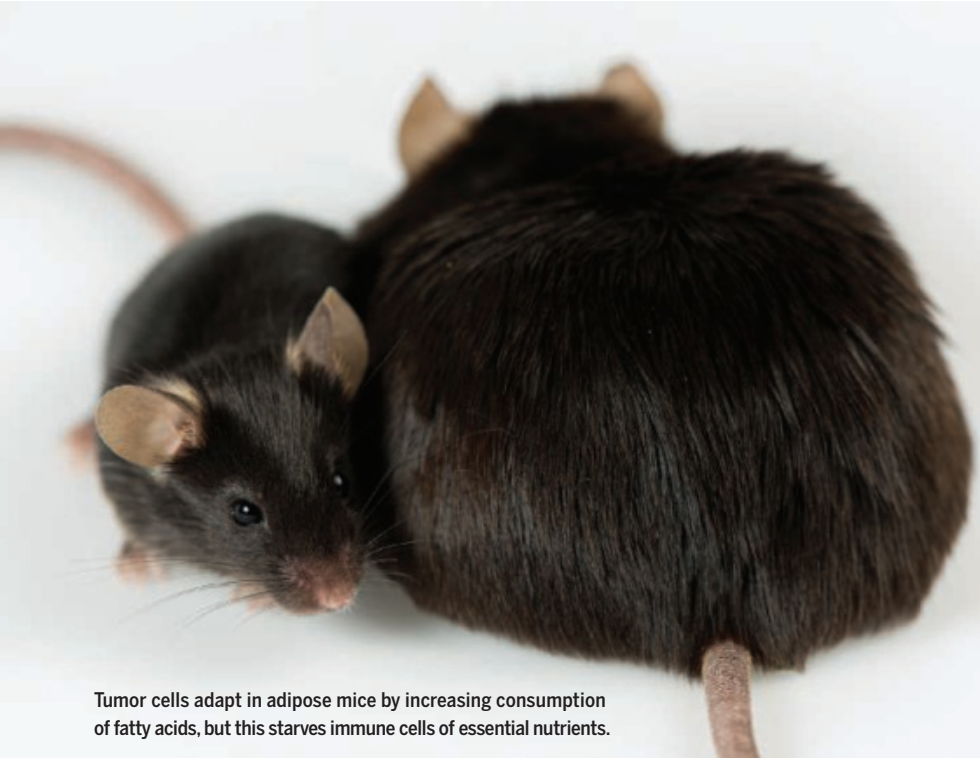
FRAMEWORK MATERIALS

Modulating structural diversity

Although most combinations of metal-organic framework (MOF) nodes and linkers lead to one topology, some nodes such as Zr_6 support a wide range of connectivities and even form different topologies with the same linker. Chen *et al.* report on controlling the formation of four different MOF topologies of this node with the 1,4-dibromo-2,3,5,6-tetrakis(4-carboxyphenyl) benzene ($H_4TCPB\text{-}Br_2$) linker by changing two solvents and two modulators that competitively bind to the nodes. All syntheses were performed under the same conditions, but the solvent (*N,N*-dimethylformamide versus *N,N*-diethylformamide), the modulator (formic acid versus acetic acid), and their concentrations were changed. The different frameworks displayed different sorption properties for organic molecules, and one had a new topology with a five-connection Zr node. —PDS

J. Am. Chem. Soc. **142**, 21428 (2020).

PHOTO: CHRIS GOMERSALL/ALAMY STOCK PHOTO



Tumor cells adapt in adipose mice by increasing consumption of fatty acids, but this starves immune cells of essential nutrients.

CANCER

Fatty acids all around, but none to eat

Obesity is a major risk factor for developing cancer. Although tumor cells have distinct adaptations to an adipose environment, a high-fat diet in mice impairs $CD8^+$ T cell function. That is the challenge that Ringel *et al.* found for $CD8^+$ T cells trying to fight colorectal adenocarcinoma cells in a mouse model. The interaction of metabolic alterations with cancer progression is complicated, particularly in the tumor microenvironment. Tumor cells responded to a high-fat diet by enhancing the uptake of fatty acids. Enhanced consumption of fatty acids appeared to leave insufficient amounts to support the $CD8^+$ T cells that would normally help to eliminate the cancer. In mice, preventing tumor cells from hogging fatty acids by metabolic reprogramming improved the antitumor T cell response. —LBR

Cell **183**, P1848 (2020).

MINERALOGY

A new structure for an old mineral

The rare mineral kaliophilite, discovered in 1839, has the simple formula of $KAlSiO_4$, but this is a surprisingly challenging crystal structure to nail down. Mugnaioli *et al.* determined the structure using a combination of techniques including electron and x-ray diffraction. Kaliophilite has a complex and intriguing framework structure with several different silicate tetrahedra–based rings and the potential for very large cavities. This discovery opens the door to developing other useful topologies for applications such as catalysis, photonics, and more. —BG

IUCrJ **7**, 1070 (2020).

HUMAN GENOMICS

Portable polygenic risk

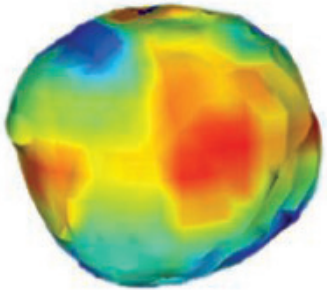
Most genome-wide association studies (GWASs) have been performed on individuals of European descent. This imbalance has led to questions regarding how useful the findings of such studies, such as a polygenic risk score (PRS), are for individuals from other populations. Amariuta *et al.* examined 707 cell type–specific epigenetic regulatory annotations that had been identified in 111 GWASs investigating polygenic diseases and traits at transcription factor–binding sites in individuals of European and East Asian origin. Their method allowed them to prioritize those variants that affect gene regulation and improve transancestry PRS. Although population-specific causal effect sizes could not be determined, the results of this study indicate that information regarding functional genetic variation associated with disease and gene regulation is transferable across human populations. —LMZ

Nat. Genet. **52**, 1346 (2020).

X-RAY IMAGING

Stabilizing rock and roll

Coherent diffraction imaging with x-rays is a powerful characterization technique for nanoparticles. Piecing together the two-dimensional Bragg diffraction patterns through slices of the sample provides a three-dimensional picture of the structure and strain. However, for nanoparticles, the x-ray beam can induce mechanical instabilities in the sample; the rotation, rocking, and rolling that occur tend to limit the resolution of the information obtained. Björling *et al.* adapted a diffractive volume assembly algorithm that mitigates for the uncontrolled mechanical instabilities and demonstrate that it can be used to reconstruct sharper images of shape-controlled 60-nanometer-sized gold nanoparticles. —ISO



Surface strain fields on a gold nanoparticle rotating under the influence of a focused coherent x-ray beam

Phys. Rev. Lett. **125**, 246101 (2020).

METABOLISM

Communicating stress

Gap junctions are channels that connect the cytoplasm of adjacent cells and are composed of connexin subunits. Tirosh *et al.* found that gap junctions comprising connexin 43 (CX43) are increased when hepatocytes undergo endoplasmic reticulum stress (ERS), which is associated with obesity-induced insulin resistance. Hepatocytes from obese mice could intercellularly transmit ERS to hepatocytes from lean mice when they were cocultured. Moreover, ablation of CX43 prevented mice from developing diet-induced ERS, insulin resistance, and liver injury. Although the factor (or factors) that allows transmission of ERS between cells remains unknown, this study illuminates tissue bystander effects that can have systemic effects on glucose homeostasis. —GKA

Cell Metab. 10.1016/j.cmet.2020.11.009 (2020).

CREDITS (TOP TO BOTTOM): ISTOCK.COM/GEORGEJASON; A. BJÖRLING *ET AL., PHYS. REV. LETT.* **125**, 246101 (2020)

REVIEW SUMMARY

PHYLODYNAMICS

Phylodynamics for cell biologists

T. Stadler*, O. G. Pybus*, M. P. H. Stumpf*

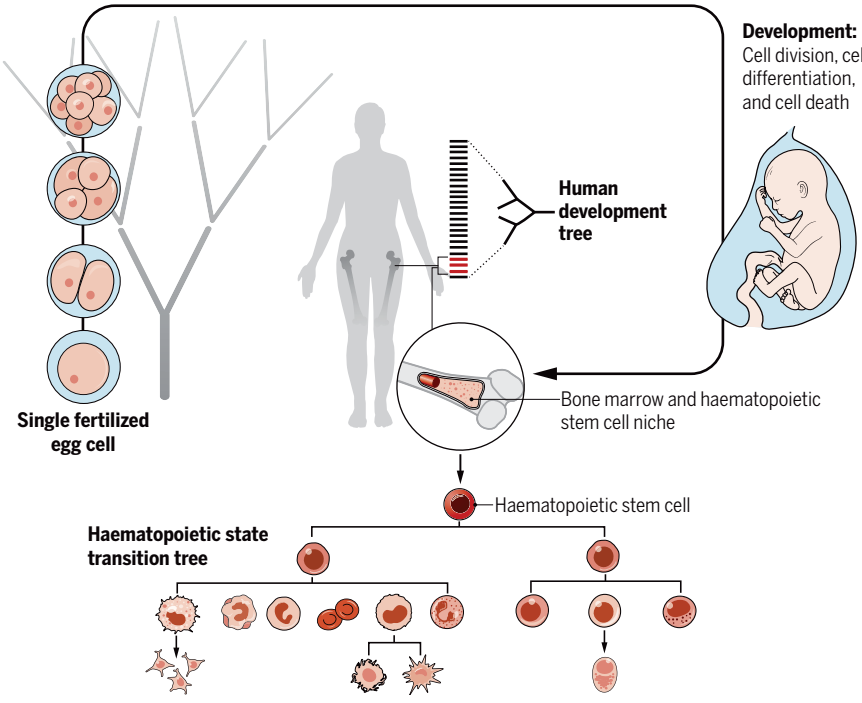
BACKGROUND: The birth, death, and diversification of individuals are events that drive biological processes across all scales. This is true whether the individuals in question represent nucleic acids, cells, whole organisms, populations, or species. The ancestral relationships of individuals can be visualized as branching trees or phylogenies, which are long-established representations in the fields of evolution, ecology, and epidemiology. Molecular phylogenetics is the discipline concerned with the reconstruction of such trees from gene or genome sequence data. The shape and size of such phylogenies depend on the past birth and death processes that generated them, and in phylodynamics, mathematical models are used to infer and quantify the dynamical behavior of biological populations from ancestral relationships.

New technological advances in genetics and cell biology have led to a growing body of data about the molecular state and ancestry of individual cells in multicellular organisms. Ideas from phylogenetics and phylodynamics are being applied to these data to investigate many questions in tissue formation and tumorigenesis.

ADVANCES: Trees offer a valuable framework for tracing cell division and change through time, beginning with individual ancestral stem cells or fertilized eggs and resulting in complex tissues, tumors, or whole organisms (see the figure). They also provide the basis for computational and statistical methods with which to analyze data from cell biology. Our Review explains how "tree-thinking" and phylodynamics can be beneficial to the interpretation of empirical data pertaining to the individual cells of multicellular organisms.

We summarize some recent research questions in developmental and cancer biology and briefly introduce the new technologies that allow us to observe the spatiotemporal histories of cell division and change. We provide an overview of the various and sometimes confusing ways in which graphical models, based on or represented by trees, have been applied in cell biology. To provide conceptual clarity, we outline four distinct graphical representations of the history of cell division and differentiation in multicellular organisms. We highlight that cells from an organism cannot be always treated as statistically independent observations but instead are often correlated because of phylogenetic history, and we explain how this can cause difficulties when attempting to infer dynamical behavior from experimental single-cell data. We introduce simple ecological null models for cell populations and illustrate some potential pitfalls in hypothesis testing and the need for quantitative phylodynamic models that explicitly incorporate the dependencies caused by shared ancestry.

OUTLOOK: We expect the rapid growth in the number of cell-level phylogenies to continue, a trend enhanced by ongoing technological advances in cell lineage tracing, genomic barcoding, and in situ sequencing. In particular, we anticipate the generation of exciting datasets that combine phenotypic measurements for individual cells (such as through transcriptome sequencing) with high-resolution reconstructions of the ancestry of the sampled cells. These developments will offer new ways to study developmental, oncogenic, and immunological processes but will require new and appropriate conceptual and computational tools. We discuss how models from phylogenetics and phylodynamics will benefit the interpretation of the data sets generated in the foreseeable future and will aid the development of statistical tests that exploit, and are robust to, cell shared ancestry. We hope that our discussion will initiate the integration of cell-level phylodynamic approaches into experimental and theoretical studies of development, cancer, and immunology. We sketch out some of the theoretical advances that will be required to analyze complex spatiotemporal cell dynamics and encourage explorations of these new directions. Powerful new statistical and computational tools are essential if we are to exploit fully the wealth of new experimental data being generated in cell biology. ■



Multicellular organisms develop from a single fertilized egg. The division, apoptosis, and differentiation of cells can be displayed in a development tree, with the fertilized egg being the root of the tree. The development of any particular tissue within an organism can be traced as a subtree of the full developmental tree. Subtrees that represent cancer tumors or B cell clones may exhibit rapid growth and genetic change. Here, we illustrate the developmental tree of a human and expand the subtree representing haematopoiesis (blood formation) in the bone marrow. Stem cells in the bone marrow differentiate, giving rise to the numerous blood cell types in humans. The structure of the tree that underlies haematopoiesis and the formation of all tissues is unclear. Phylogenetic and phylodynamic tools can help to describe and statistically explore questions about this cell differentiation process.

The list of affiliations is available in the full article online.
*Corresponding author. Email: tanja.stadler@bsse.ethz.ch (T.S.); oliver.pybus@zoo.ox.ac.uk (O.G.P.); mstumpf@unimelb.edu.au (M.P.H.S.)
Cite this article as T. Stadler *et al.*, *Science* **371**, eaah6266 (2021). DOI: 10.1126/science.aah6266

READ THE FULL ARTICLE AT
https://doi.org/10.1126/science.aah6266

RESEARCH ARTICLE SUMMARY

ANTIFUNGAL IMMUNITY

Aberrant type 1 immunity drives susceptibility to mucosal fungal infections

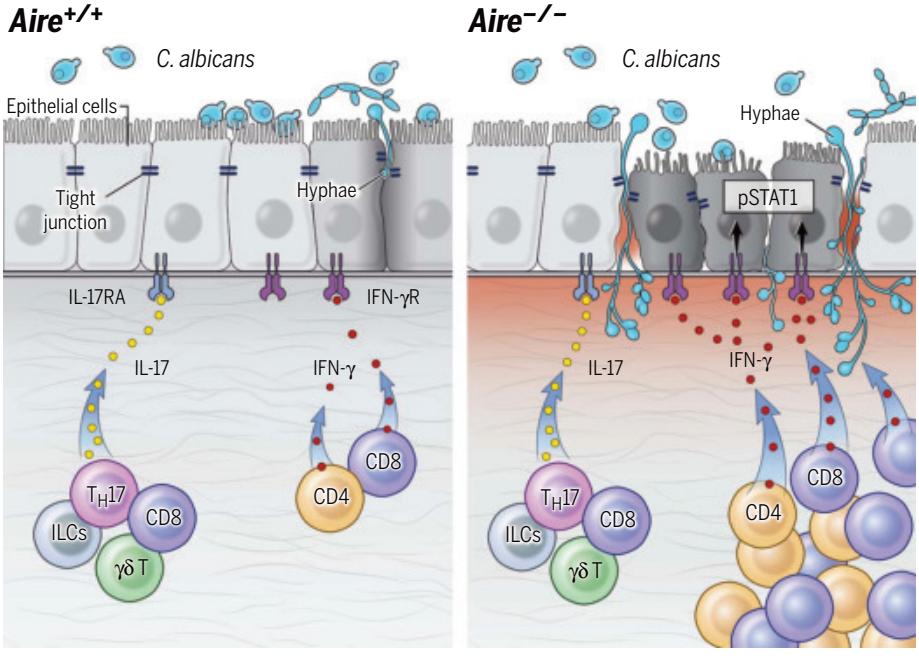
Timothy J. Break*, Vasileios Oikonomou*, Nicolas Dutzan, Jigar V. Desai, Marc Swidergall, Tilo Freiwald, Daniel Chauss, Oliver J. Harrison, Julie Alejo, Drake W. Williams, Stefania Pittaluga, Chyi-Chia R. Lee, Nicolas Bouladoux, Muthulekha Swamydas, Kevin W. Hoffman, Teresa Greenwell-Wild, Vincent M. Bruno, Lindsey B. Rosen, Wint Lwin, Andy Renteria, Sergio M. Pontejo, John P. Shannon, Ian A. Myles, Peter Olbrich, Elise M. N. Ferré, Monica Schmitt, Daniel Martin, Genomics and Computational Biology Core, Daniel L. Barber, Norma V. Solis, Luigi D. Notarangelo, David V. Serreze, Mitsuru Matsumoto, Heather D. Hickman, Philip M. Murphy, Mark S. Anderson, Jean K. Lim, Steven M. Holland, Scott G. Filler, Behdad Afzali, Yasmine Belkaid, Niki M. Moutsopoulos, Michail S. Lionakis†

INTRODUCTION: Studies of monogenic diseases have uncovered the importance of immune pathways in human tissue-specific immunity and antimicrobial defense. In particular, human inborn errors of the interleukin-17 (IL-17) receptor signaling pathway and corroborating mouse studies have established the critical contribution of type 17 responses in mucosa-specific fungal surveillance. The yeast *Candida albicans* is the signature pathogen in autoimmune polyendocrinopathy–candidiasis–ectodermal dystrophy (APECED), an inherited autoimmune disease caused by loss-of-function mutations in the autoimmune regulator (*AIRE*) gene. Fungal disease in APECED is limited to chronic mucocutaneous candidiasis (CMC) without dissemination, suggesting a central defect in barrier immunity.

RATIONALE: *AIRE* deficiency impairs central immune tolerance, resulting in the generation of pathogenic autoreactive T cells and autoantibodies directed against many tissue-specific antigens and certain cytokines, including "type 17" cytokines. However, although a majority of APECED patients with CMC have type 17 cytokine–targeted autoantibodies, whether type 17 or other local mucosal immune responses are affected in *AIRE* deficiency has not been determined. Here, we broadly investigated oral mucosal immune responses both in a model of oropharyngeal candidiasis in $Aire^{-/-}$ mice and in a large cohort of APECED patients.

RESULTS: Type 17 immune responses at the oral mucosa were unexpectedly intact in mice and humans with AIRE deficiency. To define alternative mechanisms of fungal susceptibility, we investigated $Aire^{-/-}$ mice, which exhibited oral mucosa-specific susceptibility to candidiasis without dissemination and controlled experimental challenges with viruses and bacteria normally, thereby phenocopying the infection predisposition observed in APECED patients. Notably, $Aire^{-/-}$ $CD4^+$ and $CD8^+$ T cells accumulated in increased numbers and displayed an activated and proliferative phenotype within the oral mucosa and were both necessary and sufficient to drive mucosal fungal infection in *Aire* deficiency. Enhanced production of interferon-γ (IFN-γ) by $Aire^{-/-}$ mucosal $CD4^+$ and $CD8^+$ T cells resulted in exacerbated IFN-γ/STAT1-mediated responses in the oral mucosa, which promoted IFN-γ–dependent epithelial barrier disruption and mucosal fungal susceptibility. Genetic and pharmacologic inhibition of IFN-γ or JAK-STAT signaling ameliorated mucosal fungal disease in $Aire^{-/-}$ mice. Aberrant type 1 responses were also observed in the oral mucosa of APECED patients.

CONCLUSION: We identify a T cell–dependent interferonopathy as a critical local mucosal mechanism underlying CMC in APECED. Although type 17 mucosal immunity is critical for host defense against barrier infection, mucosal type 17 responses were intact in patients with APECED and in a mouse model of the disease. These findings show that, in contrast to the known protective roles of T cells in antifungal host defense, aberrant type 1–associated T cell responses can be detrimental to antifungal mucosal immunity. They also support a paradigm by which exaggerated immunopathology may facilitate susceptibility to mucosal fungal infection by impairing the integrity of the epithelial barrier. Finally, they pave the way for investigating type 1 mucosal responses in other CMC-manifesting diseases and for the prevention and treatment of CMC in APECED patients using FDA-approved therapies that target IFN-γ or JAK-STAT signaling. ■



Aberrant type 1 mucosal immunity underlies mucosal fungal susceptibility. Left: Type 17 mucosal responses promote mucosal fungal clearance. Right: In *AIRE* deficiency, T cells drive enhanced IFN-γ/STAT1-dependent mucosal responses that disrupt the epithelial barrier and promote fungal susceptibility in the setting of intact type 17 mucosal responses. AIRE, autoimmune regulator; pSTAT1, phosphorylated signal transducer and activator of transcription 1; ILCs, innate lymphoid cells.

The list of author affiliations is available in the full article online.
*These authors contributed equally to this work.
†Corresponding author. Email: lionakism@mail.nih.gov
Cite this article as T. J. Break *et al.*, *Science* **371**, eaay5731 (2021). DOI: 10.1126/science.aay5731

READ THE FULL ARTICLE AT
https://doi.org/10.1126/science.aay5731

RESEARCH ARTICLE SUMMARY

SIGNAL TRANSDUCTION

Noncanonical transnitrosylation network contributes to synapse loss in Alzheimer's disease

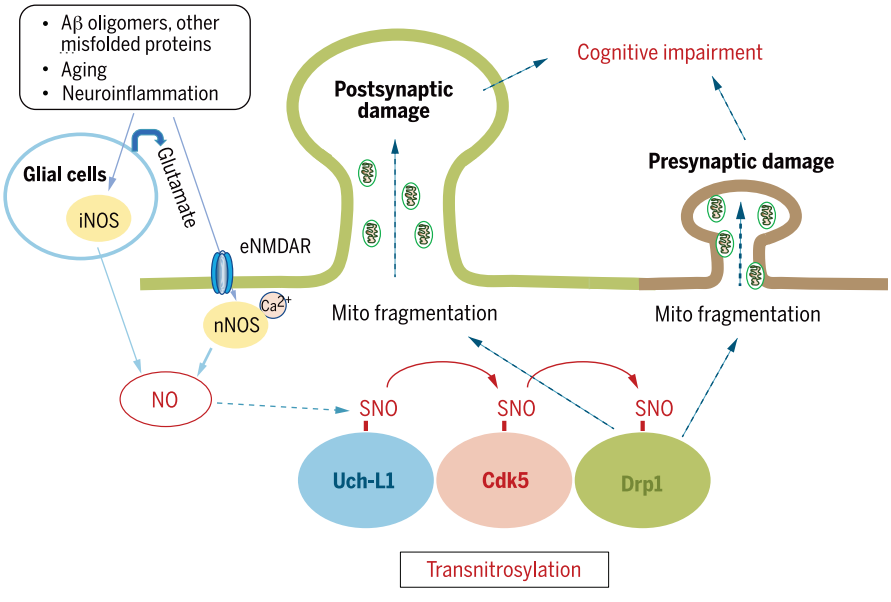
Tomohiro Nakamura*, Chang-ki Oh, Lujian Liao, Xu Zhang, Kevin M. Lopez, Daniel Gibbs, Amanda K. Deal, Henry R. Scott, Brian Spencer, Eliezer Masliah, Robert A. Rissman, John R. Yates III, Stuart A. Lipton*

INTRODUCTION: Contributing to the pathogenesis of Alzheimer's disease (AD), oligomerized amyloid-β peptide (Aβ), neuronal hyperexcitability, and aging-associated neuroinflammation trigger the production of excessive nitric oxide (NO) with resultant aberrant S-nitrosylation of multiple proteins. In this chemical redox reaction, NO [possibly in the form of nitrosonium cation (NO^+)] reacts with cysteine thiol [or, more precisely, thiolate anion ($R\text{-}S^-$, where R is a protein)]. The reaction mechanism for transnitros(yl)ation (transfer of an NO^+ group from one protein to another) involves thiolate anion, as a nucleophile, performing a reversible nucleophilic attack on a nitroso nitrogen to form an SNO-protein adduct. Such reactions are known to contribute to synaptic damage in AD. For example, S-nitrosylation of the mitochondrial fission enzyme Drp1 (forming SNO-Drp1) stimulates its activity, leading to excessive mitochondrial fragmentation and bioenergetic compromise, with consequent synapse loss. Because synapse loss is closely correlated with cognitive decline in AD, this nitrosylation reaction represents an important potential contributor to disease pathogenesis. Here we explore the origin of formation of SNO-Drp1, revealing a previously unknown network of transnitrosylation reactions in AD, culminating in synaptic damage and dementia.

RATIONALE: In general, biochemical reactions are thought to develop through evolutionary selection pressure that gives an advantage to the organism. However, in the case of S-nitrosylation of Drp1, this reaction is clearly deleterious. Although prior studies in our laboratory have demonstrated that S-nitrosylated Cdk5 is upstream from Drp1, transferring NO to Drp1 to form SNO-Drp1 via a reaction termed transnitrosylation, additional members of this pathological cascade are yet to be determined. Characterizing this aberrant series of NO-transfer reactions is important to assess its contribution to AD pathogenesis and to examine its potential therapeutic implications.

RESULTS: Using both in vitro and in vivo models of AD plus postmortem brains of humans with AD, we found that enzymes with disparate catalytic activities from different biochemical pathways can form an alternative biochemical network consisting of a concerted transnitrosylation cascade that contributes to synapse loss in AD. We demonstrate that the deubiquitinylating enzyme, Uch-L1, contributes to this transnitrosylation cascade, leading to transfer of an NO group from Uch-L1 to Cdk5 to Drp1. We show that these reactions are kinetically and thermodynamically favored. Moreover, we develop a quantitative method based on the Nernst equation for thermodynamic assessment of the reactions at steady state, as might be expected to occur in a chronic disease. This analysis revealed Gibbs free energies that predict the spontaneous forward reaction of the transnitrosylation cascade. Although other potential members of the cascade remain to be determined, this work shows that noncanonical pathways mediating a series of aberrant transnitrosylation reactions can contribute to the pathogenesis of neurodegenerative disorders. One reason that this second noncanonical function of transnitrosylation may occur is that the catalytic sites of many types of enzymes contain cysteine residues, and their thiol groups (thiolates) are nucleophiles that can perform a reversible nucleophilic attack on the nitroso nitrogen via an S-nitrosylation reaction scheme.

CONCLUSION: We conclude that enzymes with distinct primary reaction mechanisms can form a completely separate network for protein transnitrosylation. Because this network operates in the aging-associated postreproductive period that is fraught with neurodegenerative disorders, natural selection pressure may be lessened on this aberrant alternative activity. Moreover, aberrant redox signaling pathways, as exemplified by NO transfer from Uch-L1 to Cdk5 to Drp1, may represent a potential therapeutic target for AD and possibly other diseases associated with nitrosative stress. ■



Concerted transnitrosylation reactions in the pathophysiology of synapse loss in AD. Oligomerized Aβ, neuronal hyperexcitability, and aging-associated neuroinflammation trigger NO production via neuronal or inducible NO synthase (nNOS or iNOS), resulting in S-nitrosylated Uch-L1 (SNO-Uch-L1). Transnitrosylation from Uch-L1 to Cdk5 to Drp1 results in aberrant SNO-Drp1 formation, causing excessive stimulation of Drp1 and consequent mitochondrial fragmentation. The resulting bioenergetic failure contributes to synaptic damage underlying cognitive decline. eNMDAR, extrasynaptic *N*-methyl-D-aspartate–type glutamate receptor.

The list of author affiliations is available in the full article online.
*Corresponding author. Email: tnakamura@scripps.edu (T.N.); slipton@scripps.edu (S.A.L.)
Cite this article as T. Nakamura *et al.*, *Science* **371**, eaaw0843 (2021). DOI: 10.1126/science.aaw0843

READ THE FULL ARTICLE AT
https://doi.org/10.1126/science.aaw0843

RESEARCH ARTICLE SUMMARY

CORONAVIRUS

Transmission heterogeneities, kinetics, and controllability of SARS-CoV-2

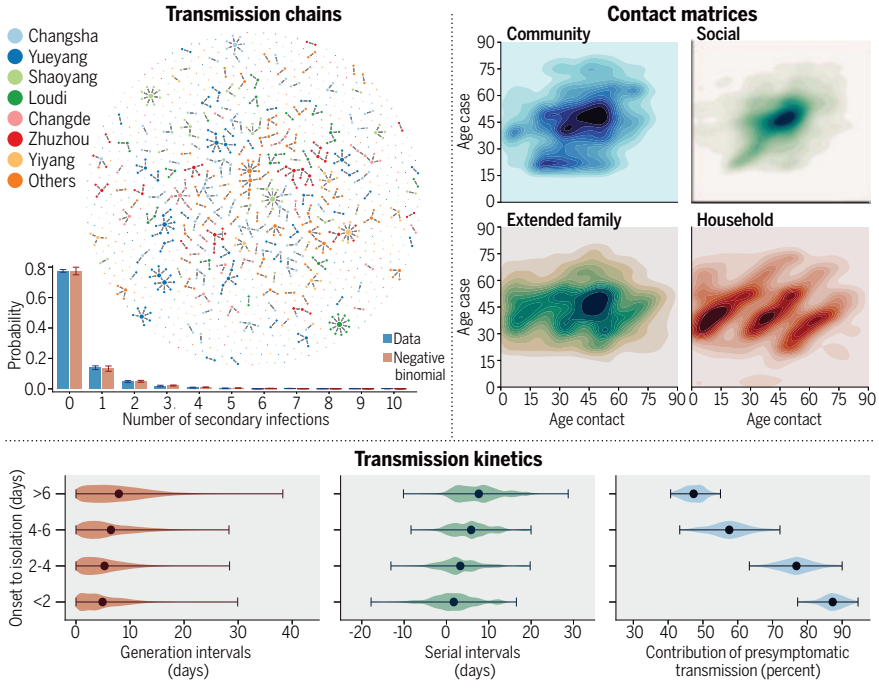
Kaiyuan Sun*†, Wei Wang†, Lidong Gao†, Yan Wang, Kaiwei Luo, Lingshuang Ren, Zhifei Zhan, Xinghui Chen, Shanlu Zhao, Yiwei Huang, Qianlai Sun, Ziyan Liu, Maria Litvinova, Alessandro Vespignani, Marco Ajelli, Cécile Viboud‡, Hongjie Yu*‡

INTRODUCTION: The role of transmission heterogeneities in severe acute respiratory syndrome coronavirus 2 (SARS-CoV-2) dynamics remains unclear, particularly those heterogeneities driven by demography, behavior, and interventions. To understand individual heterogeneities and their effect on disease control, we analyze detailed contact-tracing data from Hunan, a province in China adjacent to Hubei and one of the first regions to experience a SARS-CoV-2 outbreak in January to March 2020. The Hunan outbreak was swiftly brought under control by March 2020 through a combination of nonpharmaceutical interventions including population-level mobility restriction (i.e., lockdown), traveler screening, case isolation, contact tracing, and quarantine. In parallel, highly detailed epidemiological information on SARS-CoV-2–infected individuals and their close contacts was collected by the Hunan Provincial Center for Disease Control and Prevention.

RATIONALE: Contact-tracing data provide information to reconstruct transmission chains and understand outbreak dynamics. These data can in turn generate valuable intelligence on key epidemiological parameters and risk factors for transmission, which paves the way for more-targeted and cost-effective interventions.

RESULTS: On the basis of epidemiological information and exposure diaries on 1178 SARS-CoV-2–infected individuals and their 15,648 close contacts, we developed a series of statistical and computational models to stochastically reconstruct transmission chains, identify risk factors for transmission, and infer the infectiousness profile over the course of a typical infection. We observe overdispersion in the distribution of secondary infections, with 80% of secondary cases traced back to 15% of infections, which indicates substantial transmission heterogeneities. We find that SARS-CoV-2 transmission risk scales positively with the duration of exposure and the closeness of social interactions, with the highest per-contact risk estimated in the household. Lockdown interventions increase transmission risk in families and households, whereas the timely isolation of infected individuals reduces risk across all types of contacts. There is a gradient of increasing susceptibility with age but no significant difference in infectivity by age or clinical severity. Early isolation of SARS-CoV-2–infected individuals drastically alters transmission kinetics, leading to shorter generation and serial intervals and a higher fraction of presymptomatic transmission. After adjusting for the censoring effects of isolation, we find that the infectiousness profile of a typical SARS-CoV-2 patient peaks just before symptom onset, with 53% of transmission occurring in the presymptomatic phase in an uncontrolled setting. We then use these results to evaluate the effectiveness of individual-based strategies (case isolation and contact quarantine) both alone and in combination with population-level contact reductions. We find that a plausible parameter space for SARS-CoV-2 control is restricted to scenarios where interventions are synergistically combined, owing to the particular transmission kinetics of this virus.

CONCLUSION: There is considerable heterogeneity in SARS-CoV-2 transmission owing to individual differences in biology and contacts that is modulated by the effects of interventions. We estimate that about half of secondary transmission events occur in the presymptomatic phase of a primary case in uncontrolled outbreaks. Achieving epidemic control requires that isolation and contact-tracing interventions are layered with population-level approaches, such as mask wearing, increased teleworking, and restrictions on large gatherings. Our study also demonstrates the value of conducting high-quality contact-tracing investigations to advance our understanding of the transmission dynamics of an emerging pathogen. ■



Transmission chains, contact patterns, and transmission kinetics of SARS-CoV-2 in Hunan, China, based on case and contact-tracing data from Hunan, China. (Top left) One realization of the reconstructed transmission chains, with a histogram representing overdispersion in the distribution of secondary infections. (Top right) Contact matrices of community, social, extended family, and household contacts reveal distinct age profiles. (Bottom) Earlier isolation of primary infections shortens the generation and serial intervals while increasing the relative contribution of transmission in the presymptomatic phase.

The list of author affiliations is available in the full article online.
*Corresponding author. Email: kaiyuan.sun@nih.gov (K.S.); yhj@fudan.edu.cn (H.Y.)
†These authors contributed equally to this work.
‡These authors contributed equally to this work.
This is an open-access article distributed under the terms of the Creative Commons Attribution license (https://creativecommons.org/licenses/by/4.0/), which permits unrestricted use, distribution, and reproduction in any medium, provided the original work is properly cited.
Cite this article as K. Sun *et al.*, *Science* **371**, eabe2424 (2021). DOI: 10.1126/science.abe2424

READ THE FULL ARTICLE AT
https://doi.org/10.1126/science.abe2424

RESEARCH ARTICLE

PLANT SCIENCE

Controlled hydroxylations of diterpenoids allow for plant chemical defense without autotoxicity

Jiancai Li[1], Rayko Halitschke[1], Dapeng Li[1], Christian Paetz[2], Haichao Su[1], Sven Heiling[1]*, Shuqing Xu[3]†, Ian T. Baldwin[1]†

Many plant specialized metabolites function in herbivore defense, and abrogating particular steps in their biosynthetic pathways frequently causes autotoxicity. However, the molecular mechanisms underlying their defense and autotoxicity remain unclear. Here, we show that silencing two cytochrome P450s involved in diterpene biosynthesis in the wild tobacco *Nicotiana attenuata* causes severe autotoxicity symptoms that result from the inhibition of sphingolipid biosynthesis by noncontrolled hydroxylated diterpene derivatives. Moreover, the diterpenes' defensive function is achieved by inhibiting herbivore sphingolipid biosynthesis through postingestive backbone hydroxylation products. Thus, by regulating metabolic modifications, tobacco plants avoid autotoxicity and gain herbivore defense. The postdigestive duet that occurs between plants and their insect herbivores can reflect the plant's solutions to the "toxic waste dump" problem of using potent chemical defenses.

Plants produce a vast array of specialized metabolites that help them solve ecological challenges, such as attacks from herbivores and pathogens, and optimize their Darwinian fitness in the harsh conditions of nature (*1*–*3*). These small molecules that function as defenses typically target specialized tissues of the attackers, tissues that plants lack, such as the nervous and cardiovascular systems. By targeting these specialized tissues, plants avoid the autotoxicity problem of using potent chemicals for defense. Nicotine, the plant-produced neurotoxin that targets nicotinic acetylcholine receptors of neuromuscular junctions, is one of many examples of neurotoxins that are well tolerated by a variety of plants, including those that do not produce nicotine (*4*). However, many small-molecule defenses target fundamental cellular processes shared by all organisms, including plants (*5*). To avoid autotoxicity, many plant defense compounds are stored in nonactive glycosylated forms, which release toxic aglycones in response to attack (*6*, *7*). Although abrogating the glycosylation step of these compounds frequently results in autotoxicity (*8*–*10*), whether defense functions and autotoxicity share the same mechanism is largely unknown. To address this question, the metabolite's direct targets must be known. However, the vast number of potential targets and the metabolic complexity that arises postingestively during herbivore consumption make this a challenging task (*11*). Understanding these mechanisms could open avenues for the use of plant specialized metabolites in human health and agriculture (*12*, *13*).

We used the 17-hydroxygeranyllinalool diterpene glycosides (17-HGL-DTGs) of the coyote tobacco, *Nicotiana attenuata*, a native of the Great Basin Desert in the southwestern United States, to study the relationship between autotoxicity and defense. 17-HGL-DTGs are abundant metabolites in *N. attenuata*'s above-ground tissues [~6 mg g^{-1} fresh mass (*14*)], with proven defensive function against a native specialist herbivore, *Manduca sexta* larvae (*15*, *16*). However, the mechanism responsible for the metabolites' defensive function is unknown. The biosynthetic pathway of 17-HGL-DTGs is typical for terpenoids, including the condensation of the five-carbon units dimethylallyl diphosphate and isopentenyl diphosphate to form geranylgeranyl pyrophosphate (GGPP) by GGPP synthase (GGPPS); the conversion of GGPP to a terpene alcohol (geranyllinalool) by a terpene synthase [geranyllinalool synthase (GLS)]; hydroxylation of the terpene alcohol to the diterpenoid aglycone (17-HGL) by uncharacterized cytochrome P450s (CYPs); glycosylation of the aglycone by uridine diphosphate glucosyltransferase (UGT74P) and rhamnosyltransferase (UGT91T1); and the acylation of the glycosides by an acyltransferase [malonyltransferase (MaT)] (*16*–*19*) (Fig. 1A). This pathway produces a diversity of 17-HGL-DTGs in *N. attenuata* with different glycosylation and malonylation decorations (*20*), with lyciumoside IV (Lyc4) and its malonylated derivatives, nicotianoside I (monomalonylated) and nicotianoside II (dimalonylated), being the most abundant (*14*). All known diterpene glycosides in *N. attenuata* share the identical aglycone, 17-HGL, which indicates the importance of a precise hydroxylation at the C-17 position of geranyllinalool. Silencing genes involved in glycosylation (*NaUGT74P*) or malonylation (*NaMaT1*) resulted in autotoxicity, whereas silencing of *NaGLS* did not, pointing to the likely phytotoxicity of 17-HGL or upstream biosynthetic intermediates (*18*, *19*).

Abrogating geranyllinalool 17-hydroxylation results in autotoxicity

To investigate whether 17-HGL is responsible for the autotoxicity, we sought to identify and manipulate the CYPs involved in the biosynthesis of 17-HGL. Coexpression analysis of all 163 *N. attenuata* CYP candidate genes in the transcriptomes of different tissues and treatment groups revealed four CYP candidates to be coexpressed with characterized 17-HGL-DTG biosynthetic genes (fig. S1). The candidate genes were ectopically expressed in yeast, together with an *N. attenuata* NADPH (reduced form of nicotinamide adenine dinucleotide phosphate)–cytochrome P450 oxidoreductase gene, to evaluate their catalytic functions. Two proteins, NaCYP736A304 and NaCYP736A305, showed activity in oxidizing geranyllinalool to 17-HGL (Fig. 1B) and evolved by duplication of their ancestor, NaCYP736A303 (fig. S2), which lacks the activity (fig. S3) and does not coexpress with the other biosynthetic genes (fig. S4A).

We evaluated the functions of the two active NaCYP736As in vivo by silencing their expression together in *N. attenuata* using virus-induced gene silencing (VIGS). VIGS reduced transcripts of *NaCYP736A304* and *NaCYP736A305* by 89 and 91%, respectively (fig. S4B). The abundance of 17-HGL-DTGs was reduced to a low level in control and methyl jasmonate (MeJA)–treated leaves (Fig. 1C and fig. S5), a treatment known to amplify 17-HGL-DTG production (*16*). Consistently, the substrate of the NaCYP736As, geranyllinalool, accumulated in VIGS-*CYP736A* plants (Fig. 1D and fig. S6). Thus, NaCYP736A304 and NaCYP736A305 mediate the 17-hydroxylation of geranyllinalool in the biosynthesis of 17-HGL-DTGs in *N. attenuata*.

Contrary to the expectation that 17-HGL is phytotoxic, VIGS-*CYP736A* plants also exhibited strong phytotoxic symptoms, despite their lack of 17-HGL accumulation. The phytotoxic effects were seen in early elongation stages, in which rosette growth and stalk elongation were retarded (fig. S7). In early flowering stages, VIGS-*CYP736A* plants produced numerous small inflorescences that usually aborted before fertilization (Fig. 1E and fig. S8A). In older plants, the few flowers that were produced were severely deformed, with unexpanded corollas and

[1]Department of Molecular Ecology, Max Planck Institute for Chemical Ecology, Hans-Knoell-Strasse 8, D-07745 Jena, Germany. [2]Department of Biosynthesis/NMR, Max Planck Institute for Chemical Ecology, Hans-Knoell-Strasse 8, D-07745 Jena, Germany. [3]Institute for Evolution and Biodiversity, University of Münster, Hüfferstrasse 1, D-48161 Münster, Germany.
*Present address: Institute for Clinical Chemistry and Laboratory Diagnostics and Integrated Biobank Jena, University Hospital Jena, Am Klinikum 1, 07745 Jena, Germany.
†Corresponding author. Email: shuqing.xu@uni-muenster.de (S.X.); baldwin@ice.mpg.de (I.T.B.)

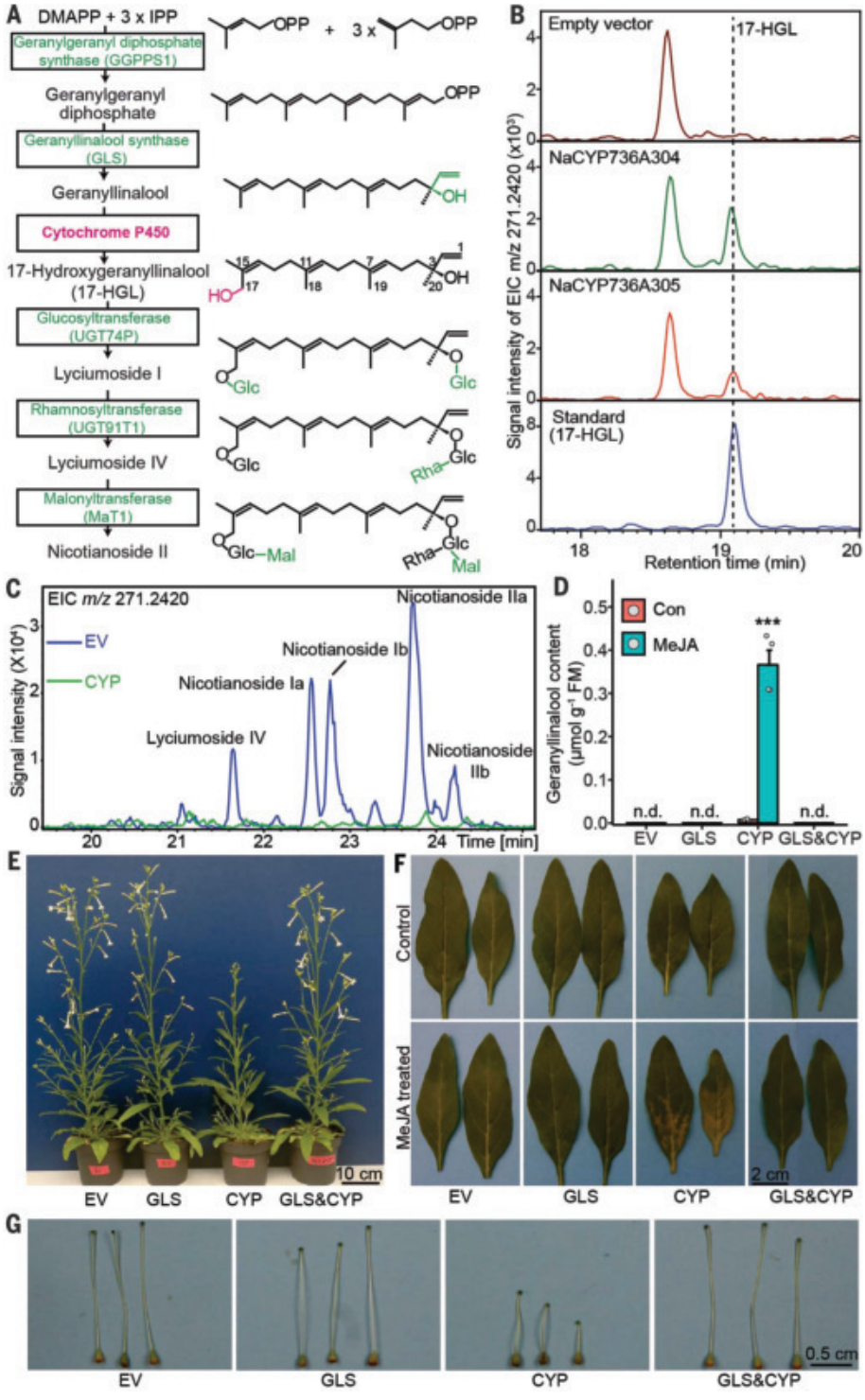


Fig. 1. Abrogating 17-hydroxylation of geranyllinalool results in severe developmental defects. (**A**) The 17-HGL-DTG pathway, including enzymes, biosynthetic intermediates, and products, is shown. DMAPP, dimethylallyl diphosphate; Glc, glucose; IPP, isopentenyl diphosphate; Mal, malonyl; OPP, diphosphate ester; Rha, rhamnose. (**B**) Liquid chromatography–quadrupole time of flight–mass spectrometry chromatograms of a 17-HGL standard and products of yeast expressing the indicated *CYP736A* genes. EIC, extracted-ion chromatogram; *m/z*, mass-to-charge ratio. (**C**) Overlay of chromatograms of 17-HGL-DTGs in the leaves of VIGS-*CYP736A* (CYP) or EV plants. (**D**) Geranyllinalool contents (+SE, $n = 4$) in leaves that were treated with lanolin [control (Con)] or lanolin with MeJA (MeJA) for 3 days. Asterisks indicate significant differences (***$P < 0.001$, Student's *t* test). FM, fresh mass; n.d., not detected. (**E** to **G**) Representative plants (61 days old), leaves, and pistils in which the expression of *NaCYP736A*s (CYP) and *NaGLS* (GLS) was silenced individually or in combination (GLS&CYP), with EV plants used as controls.

truncated pistils, resulting in plant sterility (Fig. 1G and fig. S8). Although the MeJA-induced high 17-HGL-DTG levels did not result in any morphological or developmental changes in the leaves of empty vector (EV) plants, this elicitation treatment resulted in leaf necrosis in VIGS-*CYP736A* plants (Fig. 1F). To evaluate whether the phytotoxicity was mediated by the targeted perturbation of 17-HGL-DTG biosynthesis or by some other unknown functions of the NaCYP736As, we silenced *NaCYP736A*s expression in plants, which were abrogated in the biosynthesis of geranyllinalool. The phytotoxic phenotypes were greatly attenuated when VIGS-*CYP736A* was performed on 17-HGL-DTG–deficient plants, in which the upstream *NaGGPPS1* was silenced by RNA interference with an inverted repeat (ir) construct (irGGPPS) (*16*) (fig. S9). Co-silencing of the *NaCYP736A* genes with *NaGLS* also abolished the phytotoxic and infertility phenotypes, although silencing *NaGLS* alone did not obviously affect plant growth and morphology (Fig. 1, D to F, and figs. S7 and S8). These results suggest that the accumulation of geranyllinalool is responsible for the observed autotoxicity. A similar phytotoxic effect was observed in the cyanobacterium

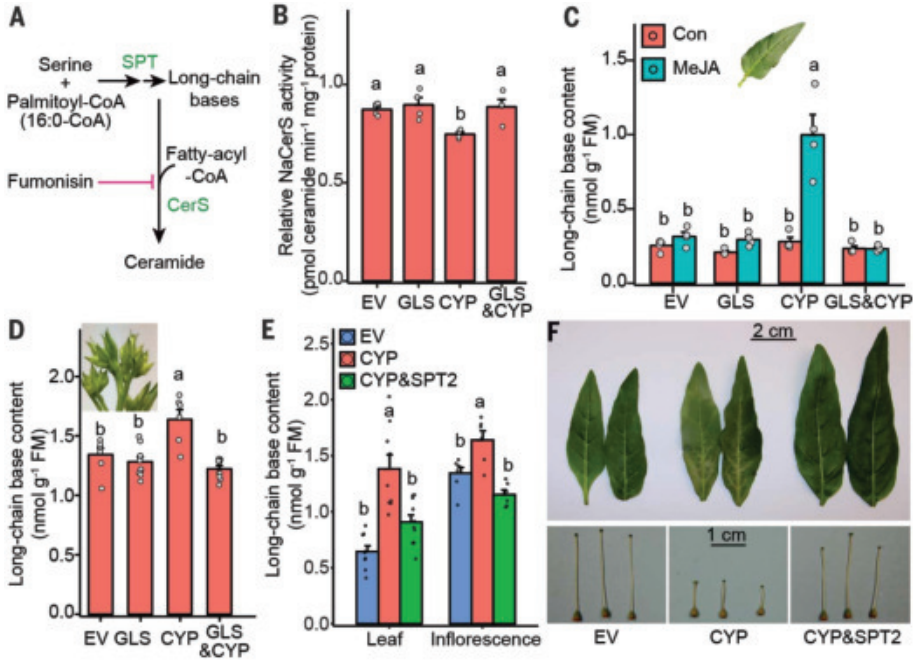


Fig. 2. Plant autotoxicity results from excessive accumulation of LCBs and CerS inhibition. (**A**) Part of the sphingolipid biosynthesis pathway. CoA, coenzyme A. (**B**) NaCerS in vitro enzyme activity assays were performed with the crude aqueous extract of MeJA-treated leaves. (**C** and **D**) Contents (+SE; n = 4 or 7) of LCBs in (C) control and MeJA-treated leaves and (D) inflorescences. (**E** and **F**) Co-silencing *NaSPT2* affected the (E) accumulation of LCBs (+SE; n = 9) and (F) phenotypes of MeJA-treated leaves and pistils. Different letters indicate significant differences [$P < 0.05$, one-way analysis of variance (ANOVA) with Tukey's post hoc test].

Synechocystis overexpressing *NaGLS* (*21*) and *Arabidopsis thaliana* overexpressing the *GLS* homolog (*AtGES*) (*22*), indicating the involvement of a general mechanism.

Ceramide synthase inhibition is responsible for the autotoxicity

To investigate the mechanism underlying this autotoxicity, a whole-genome microarray analysis was performed on MeJA-treated leaves from VIGS-*GLS*, VIGS-*CYP736A*, and VIGS-*GLS*&*CYP736A* plants in comparison with VIGS-EV plants. Whereas VIGS-*GLS* and VIGS-*GLS*&*CYP736A* plants showed moderate differences, VIGS-*CYP736A* plants showed a greater number of differentially expressed genes (DEGs) (fig. S10A). Pathway analysis identified lipid metabolism as an assembly point of the specific DEGs of VIGS-*CYP736A* plants (fig. S10B), and sphingolipid biosynthesis was the largest contributor to the differentially regulated lipid metabolism (fig. S10C). Sphingolipids are structural elements of the eukaryotic cell lipid bilayer that contribute to the dynamic nature of the membrane and control major cell events such as apoptosis (*23*). A detailed analysis of the expression of sphingolipid biosynthetic genes revealed that the genes upstream of ceramide synthase (CerS) were up-regulated, whereas the genes controlling two steps directly downstream of CerS were down-regulated (fig. S11), suggesting that the inhibition of CerS activity is the target responsible for the observed autotoxicity. Inhibition of CerS activity by mycotoxins such as fumonisin that mimic the CerS substrate sphinganine causes programmed cell death (PCD) and leaf necrosis (*24*), the symptoms that were also observed in MeJA-treated VIGS-*CYP736A* plants. This fumonisin-induced PCD is related to the excessive accumulation of CerS substrates, long-chain bases (LCBs), and decreasing LCBs through silencing their upstream gene *serine palmitoyltransferase* (*SPT*) (Fig. 2A) attenuates PCD and increases the plant's tolerance to fumonisin (*25*).

To test whether the phytotoxicity in *NaCYP736A*-silenced plants is mediated by inhibited CerS activity, we first compared the effects of the crude MeJA-treated leaf extracts of VIGS plants on *N. attenuata* CerS activity. The in vitro NaCerS enzyme inhibition assay showed that only the extracts of MeJA-treated VIGS-*CYP736A* leaves reduced CerS catalytic activity (Fig. 2B). However, geranyllinalool, which is accumulated in VIGS-*CYP736A* plants, did not inhibit plant CerS activity over a large concentration range (fig. S12). Then, we quantified LCBs in these VIGS plants. In comparison with EV, only VIGS-*CYP736A* plants accumulated higher levels of LCBs in MeJA-treated leaves (Fig. 2C and fig. S13) and inflorescences (Fig. 2D and fig. S14). To further evaluate whether the observed autotoxicity in VIGS-*NaCYP736A* plants is associated with the excess of LCBs, we manipulated levels of LCBs in plants by silencing their biosynthetic gene, *NaSPT2*, using VIGS (fig. S15). Although the strong silencing of *NaSPT2* resulted in severe developmental defects similar to those observed in the *A. thaliana spt* mutant (*26*), plants moderately silenced in *NaSPT2* grew only slightly smaller than EV plants but developed and flowered normally and showed reduced LCB accumulation in the inflorescence (fig. S16). When *NaSPT2* was moderately co-silenced with *NaCYP736A*s, the overaccumulated LCBs were reduced to the levels found in EV plants (Fig. 2E and figs. S17 to S19). Moreover, the previously observed *NaCYP736A*-associated autotoxicity was abolished, and the plants developed and flowered normally (Fig. 2F and fig. S20). Together, these results demonstrate that the autotoxicity from silencing *NaCYP736A*s is due to the overaccumulation of LCBs that resulted from inhibited NaCerS activity.

17-HGL-DTG derivatives mediate herbivore defense

Through controlled hydroxylation and further modifications, tobacco plants channel geranyllinalool into 17-HGL-DTGs, a class of defense compounds (*15*, *16*). The larvae of *M. sexta* fed on 17-HGL-DTG–deficient irGGPPS plants attained masses fourfold larger than larvae fed on EV plants (Fig. 3A). Considering the ubiquitous occurrence of sphingolipids in plants and animals and the essential function of CerS for insect growth (*27*), we hypothesized that sphingolipid metabolism in herbivores could be the target mediating the defensive function of plant 17-HGL-DTGs. To test this hypothesis, we first quantified the LCBs in the midguts of *M. sexta* larvae. EV-fed caterpillars accumulated twofold higher levels of saturated LCBs compared with larvae fed on irGGPPS plants (Fig. 3B and fig. S21). To examine the defensive function of 17-HGL-DTGs, we isolated 17-HGL-DTGs from *N. attenuata* wild-type plants and added them into an *M. sexta* artificial diet. 17-HGL-DTGs did not affect caterpillar growth at all (Fig. 3C). Furthermore, *M. sexta* CerS inhibition assays showed that plant 17-HGL-DTGs did not affect herbivore CerS activity in vitro (Fig. 3D). Because storing toxic defense compounds in the form of inactive conjugates is a common strategy to protect plants from autotoxicity (*28*),

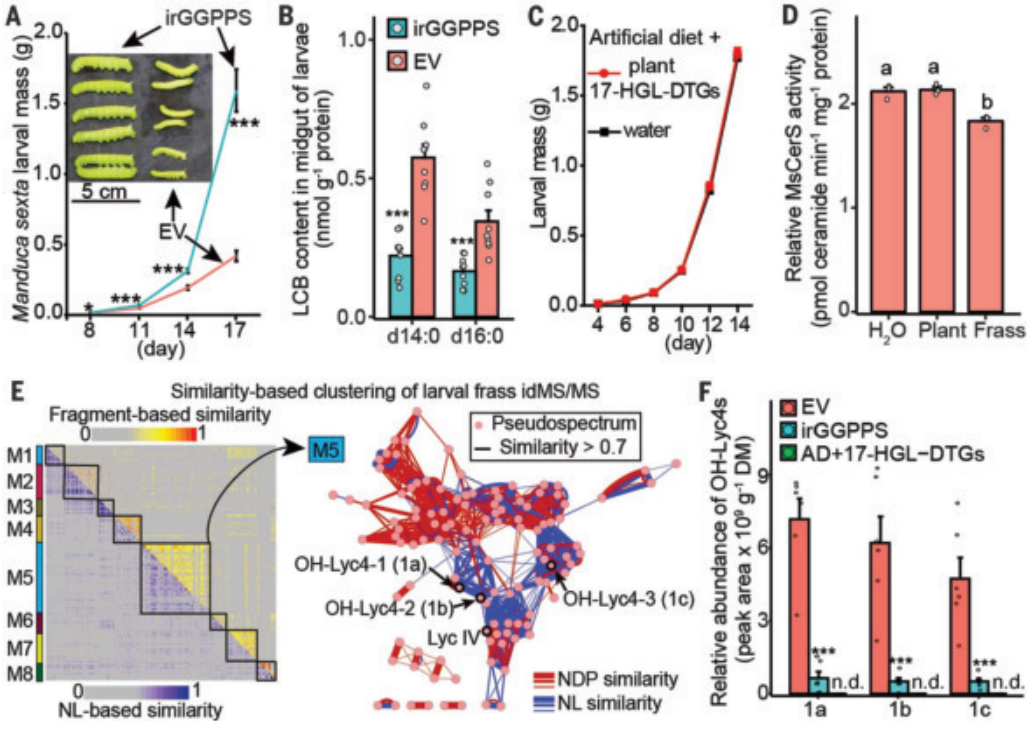


Fig. 3. Derivatives of 17-HGL-DTGs in *M. sexta* mediate plant defense function by inhibiting herbivores' CerS activity. (**A**) Representative image and mass (+SE; n = 20 to 25) of *M. sexta* larvae. (**B**) Contents (+SE; n = 9) of LCBs in midguts of *M. sexta* larvae. (**C**) Larval mass (+SE; n = 12 to 15) of *M. sexta* fed on artificial diet containing 2 mg g^{-1} 17-HGL-DTGs (plant 17-HGL-DTGs) or water as control (water). (**D**) Effect of 2 mg ml^{-1} 17-HGL-DTGs isolated from plant (plant) and 5 mg ml^{-1} crude frass extract (frass) on *M. sexta* CerS (MsCerS) activity. (**E**) Biclustering analysis of *M. sexta* frass metabolites. idMS/MS, indiscriminant tandem mass spectrometry; NDP, normalized dot products (fragment-based); NL, neutral loss. (**F**) Relative contents (+SE, n = 6) of OH-Lyc4s in the frass of *M. sexta* larvae that fed on EV plants, irGGPPS plants, or artificial diet (AD) with 2 mg g^{-1} 17-HGL-DTGs. Compounds 1a, 1b, and 1c are identified in (E). DM, dry mass. Significant differences are indicated by asterisks (*P < 0.05 and ***P < 0.001, Student's t test) or different letters (P < 0.05, one-way ANOVA with Tukey's post hoc test).

glycosylated 17-HGL-DTGs could be inactive and only show activity after ingestion by the herbivore. Therefore, we extracted metabolites from larval frass to test their inhibitory effect on CerS activity. In vitro *M. sexta* CerS activity assays showed that crude frass extracts inhibited *M. sexta* CerS catalytic activity (Fig. 3D), suggesting that the CerS inhibitory effect of 17-HGL-DTGs is activated by ingestion.

To identify the active compounds responsible for the inhibition of herbivore CerS activity, we performed a frass metabolomics ("frassomics") analysis using an indiscriminant tandem mass spectrometry pipeline (*29*). The metabolites in *M. sexta* frass were clustered into eight modules according to their fragment- and neutral loss–based similarities. Module 5 contained the most 17-HGL-DTG–related compounds, several of which contain an additional hydroxylation on the 17-HGL (Fig. 3E). Three abundant compounds corresponded to 17-HGL-hydroxylated Lyc4 (OH-Lyc4), whose predicted precursor Lyc4 is the most abundant 17-HGL-DTG in *N. attenuata*–fed *M. sexta* frass (*15*) (figs. S22 and S23). The amounts of OH-Lyc4s in the frass of *M. sexta* that had fed on irGGPPS plants were less than 10% of that in the frass of larvae fed on EV plants (Fig. 3F). Consistent with the lost defensive effect of 17-HGL-DTGs in artificial diet, OH-Lyc4s were not detected in the frass of *M. sexta* larvae that fed on an artificial diet containing 17-HGL-DTG (Fig. 3F and fig. S24). These data suggest that some unknown oxidizing compound(s) or enzyme(s) from ingested plant material are responsible for the hydroxylation of 17-HGL-DTGs in caterpillar guts and further conveyed the defensive function.

Hydroxylated aglycones inhibit CerS in plants and herbivores

To gain more understanding of the structures and functions of these postingestive metabolites, we purified the putative OH-Lyc4s from *M. sexta* frass. The structures of these compounds were elucidated by nuclear magnetic resonance analysis. In addition to the extra hydroxyl moiety, the double bonds adjacent to the hydroxylated carbon were shifted to neighboring positions (Fig. 4A and fig. S25). All three isomers of OH-Lyc4 inhibited *M. sexta* CerS activity (Fig. 4B). When added to artificial diets, the two tested isomers of OH-Lyc4 significantly inhibited *M. sexta* larval growth, even at concentrations one-third of those of Lyc4, which did not inhibit growth at the tested concentration (Fig. 4C). These results show that the postingestively hydroxylated 17-HGL-DTGs directly inhibit CerS activity and provide herbivore defense.

Considering the inhibitory effect of hydroxylated 17-HGL-DTGs on insect CerS activity and the inhibition of *N. attenuata* CerS activity by geranyllinalool-related intermediates, we hypothesize that hydroxylated geranyllinalools are also the toxic compounds in planta. By mining the metabolomics data of VIGS plants, we detected multiple peaks corresponding to mono- and di-hydroxylated geranyllinalool in the MeJA-treated leaves of *NaCYP736A*-silenced plants but not in the co-silenced VIGS-*GLS&CYP736A* plants (fig. S26), which is consistent with the phytotoxic phenotypes. The inflorescences of VIGS-*CYP736A* plants also accumulated significantly more di-hydroxylated geranyllinalool than other genotypes (fig. S27). Considering the similar phytotoxic phenotypes of VIGS-*CYP736A* observed in this work and the VIGS-*UGT74P* plants impaired in 17-HGL glycosylation (*18*), we analyzed hydroxylated geranyllinalool derivatives in plants individually silenced in all 17-HGL-DTG biosynthetic genes. Consistent with the phytotoxic phenotypes, the inflorescences of VIGS-*CYP736A*, VIGS-*UTG74P* (*18*), and VIGS-*MaT1* (*19*) plants all accumulated di-hydroxylated geranyllinalool or hydroxylated 17-HGL (OH-17-HGLs) (fig. S28). We detected large amounts of similar nonglycosylated OH-17-HGLs in *M. sexta* frass after prolonged storage; these are likely the hydrolysis products of the hydroxylated 17-HGL-DTGs described above. We confirmed the identity of the frass-derived OH-17-HGLs and the metabolites detected in VIGS-*UGT74P* plants by comparisons of mass spectra and retention times (fig. S29). The large accumulations in aged frass provided the opportunity to purify the OH-17-HGLs for structure verification and bioassays (Fig. 4D and fig. S30). Similar to the inhibition of herbivore CerS activity by OH-Lyc4s, OH-17-HGLs inhibited the catalytic activity of *N. attenuata* CerS (Fig. 4E). The two

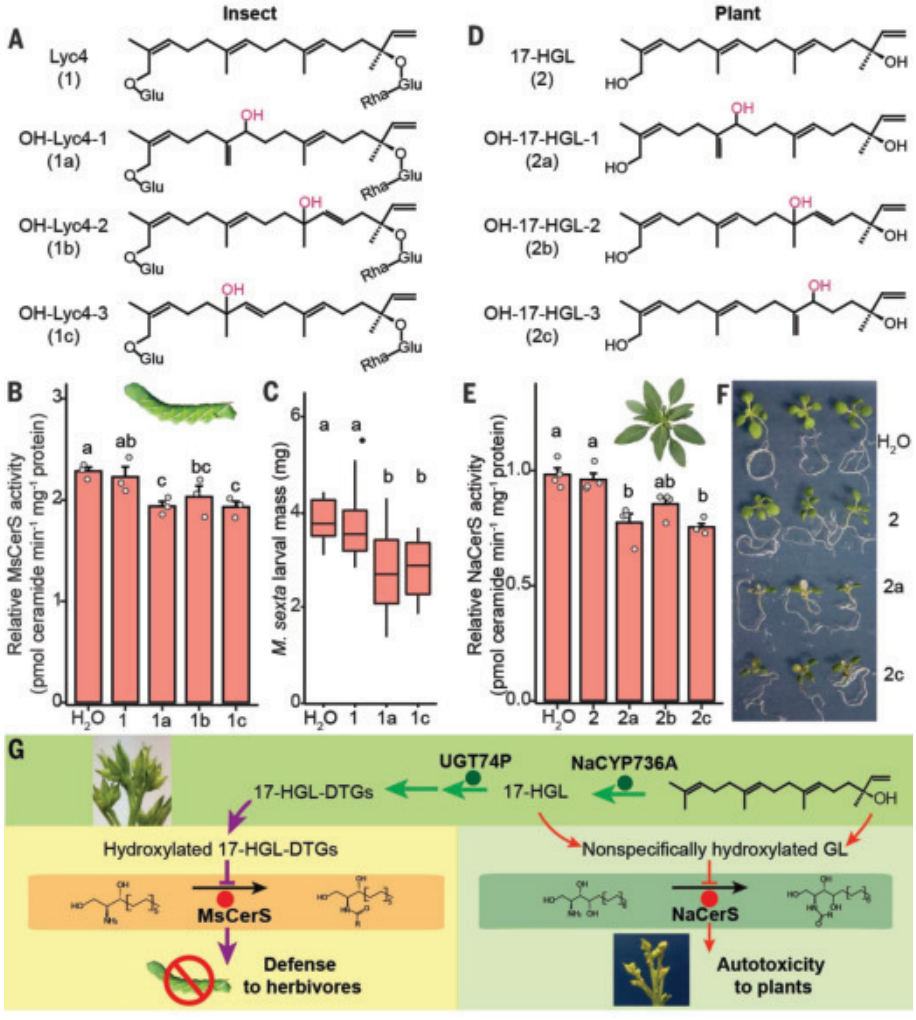


Fig. 4. Hydroxylated diterpene backbone inhibits activity of CerS from plants and herbivores. (**A**) Structures of Lyc4 and OH-Lyc4s found in *M. sexta* frass. (**B**) Effects (+SE; n = 4) of Lyc4 and OH-Lyc4s (100 μM) on *M. sexta* CerS in vitro enzyme activity. (**C**) Mass (+SE; n = 9 to 12) of 6-day-old *M. sexta* larvae that fed on AD with 3 mg g^{-1} Lyc4, 1 mg g^{-1} OH-Lyc4s, or water as control (H_2O). For (B) and (C), compounds 1, 1a, 1b, and 1c are defined in (A). (**D**) Structures of 17-HGL and OH-17-HGLs found in *NaUGT74P*-silenced plants. (**E** and **F**) The effects of 17-HGL and OH-17-HGLs (100 μM) on (E) *N. attenuata* CerS in vitro enzyme activity and (F) *N. attenuata* seedlings. Compounds 2, 2a, 2b, and 2c are defined in (D). (**G**) Proposed model of the function of diterpene hydroxylation responsible for plant autotoxicity and herbivore defense, including the processes that occur in wild-type plants (green background), biosynthetic pathway–abrogated plants (light green background), and caterpillars (yellow background). Different letters indicate significant differences (P < 0.05, one-way ANOVA with Tukey's post hoc test).

tested isomers of OH-17-HGL showed phytotoxic effects on *N. attenuata* plants, whereas 17-HGL did not, at the tested concentration (Fig. 4F). Comparing these structures, we infer that these nonspecific hydroxyl moieties, rather than the C-17 hydroxyl moiety, were essential for the CerS inhibition. Thus, the phytotoxic effects in plants with altered 17-HGL-DTG biosynthesis can also be attributed to the inhibition of CerS activity.

Wild tobacco plants produce diterpene glycosides through a regulated biosynthetic pathway. Normally, geranyllinalool is oxidized at the 17-carbon by CYP736A, glycosylated by UGT74P, and further decorated to produce a bouquet of 17-HGL-DTGs, in which additional modifications of the aglycone are prevented. When ingested by herbivores, these 17-HGL-DTGs are converted to a class of toxic compounds, hydroxylated 17-HGL-DTGs, that inhibit the biosynthesis of essential structural components of herbivore cell membranes (sphingolipids) to achieve their defensive functions. However, if part of the biosynthetic pathway is abrogated, as in plants silenced in *NaCYP736A*s or *NaUGT74P* expression, accumulated geranyllinalool or 17-HGL will flow into nonspecific hydroxylated derivatives that also inhibit the plant's own sphingolipid biosynthesis and result in autotoxicity (Fig. 4G). Considering that sphingolipid metabolism is universal among all eukaryotic cells and is implicated in diabetes, cancers, and some neurodegenerative diseases such as Alzheimer's disease (*30*), the intrinsic chemical and molecular interactions between terpenes and sphingolipid metabolism highlight the medical and agricultural potential of the highly diverse terpenes of plants (*31*).

This work completes the biosynthetic pathway for 17-HGL-DTGs and identifies a common mechanism by which the autotoxic and defensive properties emerge from a natural product pathway by identifying the universal target, the sphingolipid pathway. Native tobacco plants retain the defensive function of their 17-HGL-DTGs while avoiding autotoxicity through precisely regulated terpenoid aglycone modifications. This study also reveals how the postdigestive duet that occurs between plants and their herbivores can reflect the plant's solutions to the "toxic waste dump" problem of chemical defense and that exploring the metabolomics of excreta (i.e., "frassomics") in other plant-consumer systems might point to how plant natural products can be used more strategically in medicine and agriculture.

REFERENCES AND NOTES

1. A. Kessler, I. T. Baldwin, *Science* **291**, 2141–2144 (2001).
2. L. Chae, T. Kim, R. Nilo-Poyanco, S. Y. Rhee, *Science* **344**, 510–513 (2014).
3. A. C. Huang *et al.*, *Science* **364**, eaau6389 (2019).
4. I. T. Baldwin, P. Callahan, *Oecologia* **94**, 534–541 (1993).
5. P. Bednarek, P. Schulze-Lefert, in *Annual Plant Reviews, Molecular Aspects of Plant Disease Resistance*, vol. 34, J. Parker, Ed. (Wiley, 2008), pp. 220–260.
6. P. Jones, T. Vogt, *Planta* **213**, 164–174 (2001).
7. A. V. Morant *et al.*, *Phytochemistry* **69**, 1795–1813 (2008).
8. P. Mylona *et al.*, *Plant Cell* **20**, 201–212 (2008).
9. M. Itkin *et al.*, *Plant Cell* **23**, 4507–4525 (2011).
10. C. K. Blomstedt *et al.*, *Plant Cell Physiol.* **57**, 373–386 (2016).
11. R. S. Rattan, *Crop Prot.* **29**, 913–920 (2010).
12. F. S. Li, J. K. Weng, *Nat. Plants* **3**, 17109 (2017).
13. J. Singh, A. N. Yadav, Eds., *Natural Bioactive Products in Sustainable Agriculture* (Springer, 2020).
14. S. Poreddy *et al.*, *Nat. Commun.* **6**, 8525 (2015).
15. A. R. Jassbi, K. Gase, C. Hettenhausen, A. Schmidt, I. T. Baldwin, *Plant Physiol.* **146**, 974–986 (2008).
16. S. Heiling *et al.*, *Plant Cell* **22**, 273–292 (2010).
17. V. Falara, J. M. Alba, M. R. Kant, R. C. Schuurink, E. Pichersky, *Plant Physiol.* **166**, 428–441 (2014).
18. S. Heiling *et al.*, bioRxiv 2020.08.26.267690 [Preprint]. 27 August 2020; https://doi.org/10.1101/2020.08.26.267690.
19. J. Li *et al.*, *eLife* **7**, e38611 (2018).
20. S. Heiling *et al.*, *Plant J.* **85**, 561–577 (2016).
21. C. Formighieri, A. Melis, *Appl. Microbiol. Biotechnol.* **101**, 2791–2800 (2017).
22. M. Herde *et al.*, *Plant Cell* **20**, 1152–1168 (2008).
23. L. V. Michaelson, J. A. Napier, D. Molino, J. D. Faure, *Biochim. Biophys. Acta* **1861**, 1329–1335 (2016).
24. W. Wang *et al.*, *Proc. Natl. Acad. Sci. U.S.A.* **93**, 3461–3465 (1996).
25. L. Shi *et al.*, *Cell Res.* **17**, 1030–1040 (2007).
26. M. Chen, G. Han, C. R. Dietrich, T. M. Dunn, E. B. Cahoon, *Plant Cell* **18**, 3576–3593 (2006).
27. R. Bauer *et al.*, *EMBO J.* **28**, 3706–3716 (2009).
28. B. A. Halkier, J. Gershenzon, *Annu. Rev. Plant Biol.* **57**, 303–333 (2006).
29. D. Li, I. T. Baldwin, E. Gaquerel, *Proc. Natl. Acad. Sci. U.S.A.* **112**, E4147–E4155 (2015).

30. S. M. Turpin-Nolan, J. C. Brüning, *Nat. Rev. Endocrinol.* **16**, 224–233 (2020).
31. J. Bohlmann, C. I. Keeling, *Plant J.* **54**, 656–669 (2008).
32. S. Xu, Li et al_Science_source_data. Figshare (2020); https://doi.org/10.6084/m9.figshare.13414670.v1.

ACKNOWLEDGMENTS

We thank T. G. Köllner (Max Planck Institute for Chemical Ecology) for sharing yeast and plasmids; M. Wang and K. Luck (Max Planck Institute for Chemical Ecology) for technical support; and J. Gershenzon, S. O'Connor, E. Gaquerel, and M. Huber for their helpful comments on the manuscript. **Funding:** This work was supported by the Max Planck Society, the University of Münster, the Advanced Grant (no. 293926) of the European Research Council to I.T.B., and the Deutsche Forschungsgemeinschaft (SFB 1127/2 ChemBioSys – 239748522). **Author contributions:** J.L., R.H., S.X., and I.T.B. conceived and designed the project. J.L., D.L., C.P., H.S., and S.H. performed the experiments. J.L., R.H., D.L., C.P., S.X., and I.T.B. analyzed data. J.L., R.H., S.X., and I.T.B. wrote the manuscript, with contributions from all authors. **Competing interests:** The authors declare that they have no competing interests. **Data and materials availability:** Microarray files are available from the NCBI database (GEO number: GSE160453). Source data are deposited in the Figshare repository (*32*). All other data are available in the manuscript or the supplementary materials.

SUPPLEMENTARY MATERIALS

science.sciencemag.org/content/371/6526/255/suppl/DC1
Materials and Methods
Figs. S1 to S30
Tables S1 and S2
References (*33*–*57*)
MDAR Reproducibility Checklist
Data S1 and S2

31 August 2020; accepted 16 November 2020
10.1126/science.abe4713

REPORTS

NUCLEAR PHYSICS

Formation of α clusters in dilute neutron-rich matter

Junki Tanaka[1,2,3]*, Zaihong Yang[3,4]*, Stefan Typel[1,2], Satoshi Adachi[4], Shiwei Bai[5], Patrik van Beek[1], Didier Beaumel[6], Yuki Fujikawa[7], Jiaxing Han[5], Sebastian Heil[1], Siwei Huang[5], Azusa Inoue[4], Ying Jiang[5], Marco Knösel[1], Nobuyuki Kobayashi[4], Yuki Kubota[3], Wei Liu[5], Jianling Lou[5], Yukie Maeda[8], Yohei Matsuda[9], Kenjiro Miki[10], Shoken Nakamura[4], Kazuyuki Ogata[4,11], Valerii Panin[3], Heiko Scheit[1], Fabia Schindler[1], Philipp Schrock[12], Dmytro Symochko[1], Atsushi Tamii[4], Tomohiro Uesaka[3], Vadim Wagner[1], Kazuki Yoshida[13], Juzo Zenihiro[3,7], Thomas Aumann[1,2,14]

The surface of neutron-rich heavy nuclei, with a neutron skin created by excess neutrons, provides an important terrestrial model system to study dilute neutron-rich matter. By using quasi-free α cluster–knockout reactions, we obtained direct experimental evidence for the formation of α clusters at the surface of neutron-rich tin isotopes. The observed monotonous decrease of the reaction cross sections with increasing mass number, in excellent agreement with the theoretical prediction, implies a tight interplay between α-cluster formation and the neutron skin. This result, in turn, calls for a revision of the correlation between the neutron-skin thickness and the density dependence of the symmetry energy, which is essential for understanding neutron stars. Our result also provides a natural explanation for the origin of α particles in α decay.

Correlations and clustering are universal phenomena in composite systems for all scales of the material world, which range from the largest structures in the Universe to minute hadronic systems made of quarks. The atomic nucleus is a many-body quantum system that consists of nucleons, namely protons and neutrons. It can be described in the first approximation as nucleons moving independently in an attractive mean field generated by all nucleons. Their fermionic nature leads to the development of a shell structure with well-defined single-particle levels (*1*, *2*). This is the basis of the nuclear shell model that can take pairing and other residual interactions additionally into account (*1*–*3*). Correlations among nucleons play a decisive role in understanding the properties of atomic nuclei, nuclear matter, and giant objects in the Universe such as neutron stars (*4*). In nuclear matter, nucleons form light nuclear clusters that comprise deuterons (^{2}H), tritons (^{3}H), helions (^{3}He), and α particles (^{4}He) at densities sufficiently below the saturation density of nuclei (*5*). Deuteron-like clusters can also be found as short-range correlated pairs at higher densities (*6*–*8*). The α particle, as a compact four-nucleon correlation, plays a particular role because its strong binding is beneficial for the cluster formation.

Following the prediction of α-cluster formation (*9*, *10*) as reported in the 1930s for light self-conjugate nuclei (*11*), such as ^{8}Be, ^{12}C, and ^{16}O, microscopic theories on α clustering (*12*) have been developed that presume strong correlations between nucleons in clusters and weak intercluster correlations. In light nuclei, cluster structures are experimentally known to exist in their ground state as well as in excited states (*13*, *14*), specifically for states at energies in the vicinity of the cluster emission threshold (*15*). A prominent example is the Hoyle state (*16*) in ^{12}C with a three–α cluster structure at an excitation energy of 7.65 MeV (*17*). The existence of this state is crucial for the fusion of the three α clusters into a carbon nucleus in stars. This occurs at a rate that ensures a sufficient abundance of carbon, which is necessary for organic life, including human life (*18*).

Conversely, providing a consistent description of α clusters and nucleons on the same footing in heavy nuclei is challenging from a theoretical perspective (*19*). Although the formation of α clusters in heavy nuclei may be suggested from α decay according to the postulated model of Gamow (*19*, *20*), direct experimental evidence has not yet been reported. Theoretical studies have suggested that, similar to dilute nuclear matter, there exists a certain probability that α clusters can form in the ground state of heavy nuclei at the very surface of the nucleus—that is, the region outside the saturated nuclear core—with densities below the α-cluster dissolution threshold (the Mott density) (*5*, *21*, *22*). This feature could potentially explain the origin of α particles in the α-decay process. This surface α-clustering phenomenon also occurs in neutron-rich heavy nuclei that feature a neutron skin created by the excess neutrons and are generally stable against α decay (*4*, *23*). In this case, however, there is a close interplay between this surface α-clustering effect and the neutron-skin thickness, as suggested by recent generalized relativistic density functional (gRDF) calculations (*5*, *23*). This model predicts a reduction of the neutron-skin thickness in comparison to theoretical calculations without considering the α-clustering effect, which will further affect our understanding of the nuclear equation of

[1]Technische Universität Darmstadt, Fachbereich Physik, Institut für Kernphysik, Schlossgartenstraße 9, 64289 Darmstadt, Germany. [2]GSI Helmholtz Center for Heavy Ion Research GmbH, Planckstraße 1, 64291 Darmstadt, Germany. [3]RIKEN Nishina Center for Accelerator-Based Science, 2-1 Hirosawa, Wako 351-0198, Japan. [4]Research Center for Nuclear Physics, Osaka University, 10-1 Mihogaoka, Ibaraki 567-0047, Japan. [5]State Key Laboratory of Nuclear Physics and Technology, School of Physics, Peking University, Beijing 100871, China. [6]Université Paris-Saclay, CNRS/IN2P3, IJCLab, 91405 Orsay, France. [7]Department of Physics, Kyoto University, Kitashirakawa-Oiwake, Sakyo, Kyoto 606-8502, Japan. [8]Faculty of Engineering, University of Miyazaki, 1-1 Gakuen, Kibanadai-nishi, Miyazaki 889-2192, Japan. [9]Cyclotron and Radioisotope Center, Tohoku University, 6-3 Aoba, Aramaki, Aoba-ku, Sendai 980-8578, Japan. [10]Department of Physics, Tohoku University, Sendai 980-8578, Japan. [11]Department of Physics, Osaka City University, Osaka 558-8585, Japan. [12]Center for Nuclear Study, The University of Tokyo, 2-1 Hirosawa, Wako 351-0198, Japan. [13]Advanced Science Research Center, Japan Atomic Energy Agency, Tokai, Ibaraki 319-1195, Japan. [14]Helmholtz Research Academy Hesse for FAIR, Schlossgartenstraße 9, 64289 Darmstadt, Germany.
***Corresponding author. Email: zhyang@ribf.riken.jp (Z.Y.); junki.tanaka@riken.jp (J.T.)**

state (*5*, *23*). As a result of this interplay, the formation of α clusters also gets hindered by the development of a neutron skin in heavy nuclei. The tin isotopic chain with a proton magic number $Z = 50$ provides an ideal testing ground to study this intriguing interplay. The bulk and surface properties of these nuclei are not strongly dependent on the details of the nuclear structure and can be well described by relativistic mean-field theories (*23*) [see fig. S1 and table S5 for the comparison between theoretical calculated radii (*23*) and the experimental data]. According to the gRDF calculation, the probability of α-cluster formation gradually decreases along the tin isotopic chain when progressing from the stable ^{112}Sn to the very neutron-rich ^{132}Sn, which is accompanied by a steady increase in the neutron-skin thickness (*23*). Therefore, we performed an experiment with tin isotopes to examine the probability of finding α clusters [hereafter defined as "the effective number of α clusters (*23*)"] in stable heavy nuclei and to study its isotopic dependence. Our experiment covers stable nuclides from ^{112}Sn to ^{124}Sn (see table S2 for detailed properties of the target materials), with neutron numbers from $N = 62$ to 74.

The most direct access to α clustering in the ground state of nuclei is the proton-induced α-knockout reaction (p, $p\alpha$). Quasi-free knockout reactions of the type (e, ep) and (p, pp) are well-established methods to investigate the single-particle structures of nuclei (*24*); quasi-free (p, $p\alpha$) reactions were also used extensively in the 1970s and 1980s to study α clustering in light- and medium-mass stable nuclei (*25*–*27*). By measuring the momenta and angles of the light particles involved in the scattering process, the intrinsic momentum of the knocked-out particle and its binding energy in the nucleus can be reconstructed from the conservation of energy and momentum. For the (p, $p\alpha$) experiment reported herein, the experimental setup was designed according to the quasi-free scattering kinematics of protons on α particles bound in tin isotopes. For this investigation, we selected a large center-of-mass scattering angle, i.e., a large momentum is transferred to the α particle at the instance of the reaction and the residue can be regarded safely as a spectator (see fig. S2). Therefore, the observed α particles in the final state, detected in coincidence with the scattered protons, directly reflect the probability of finding α clusters in the target nucleus. By measuring the (p, $p\alpha$) cross sections under quasi-free kinematic conditions, the change in the effective number of α clusters in the tin isotopic chain can be obtained as a function of the neutron number.

The experiment was performed at the nuclear experimental facility in the Research Center for Nuclear Physics (RCNP), Osaka University. Figure 1 shows the experimental setup. A 392-MeV proton beam with an intensity of 100 nA, provided by a ring cyclotron, impinged on a tin target. Information on the targets and beam intensities is specified in Table 1. After the (p, $p\alpha$) reaction, the scattered protons were analyzed by using the Grand Raiden magnetic spectrometer (*28*). It was set at 45.3° with respect to the proton beam, and the energies and momenta were deduced from the position and angles measured at the focal plane. The coincident α particles were detected at 60° by the large acceptance spectrometer (LAS) (*29*). The acceptance was mainly determined by using a slit with a well-defined rectangular aperture at the entrance of the Grand Raiden spectrometer. Each type of particle was identified in the corresponding focal-plane detectors for the Grand Raiden and LAS instruments, as shown in Fig. 1.

Figure 2A presents the coincident timing spectrum of the recorded proton-α pair in the

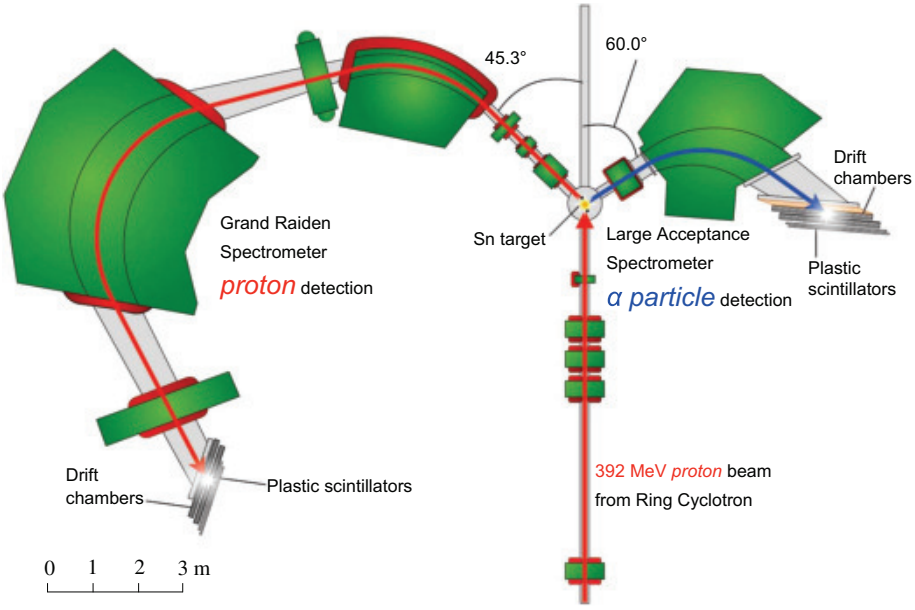


Fig. 1. Schematic illustration of the experimental setup. A 392-MeV proton beam from the ring cyclotron accelerator impinges on a tin target. After a ^{A}Sn(p, $p\alpha$)$^{A-4}$Cd reaction, a scattered proton is detected by the focal-plane detectors, drift chambers, and plastic scintillators after traversing the Grand Raiden spectrometer at an angle of 45.3° with respect to the proton beam. A knocked-out α particle is detected by the focal-plane detectors behind the LAS spectrometer at an angle of 60.0° with respect to the proton beam.

Table 1. Experimental and theoretical values of the tin isotope parameters. Target thicknesses and enrichments of the tin-isotope targets, the experimental and theoretical cross sections, the effective number of α clusters, and the theoretical neutron-skin thicknesses Δr_{np} from the gRDF prediction (*23*). The calculations were performed with the DD2 parameters (*5*) for the effective interaction without and with the α clusters. In the last column, the value is the percentage by which Δr_{np} is reduced when α clusters are included. nb, nanobarn.

Tin isotope	Target thickness (mg/cm^2)	Isotopic enrichment (%)	Experimental cross sections (nb)	Theoretical cross sections (nb)	Effective number of α clusters	Theoretical Δr_{np} without α (fm)	Theoretical Δr_{np} with α (fm)	Relative Δr_{np} change (%)
^{112}Sn	40.2(4)	95.1(1)	0.157(12)	0.160	0.3876	0.0495	0.0277	−44
^{116}Sn	39.3(4)	97.8(2)	0.129(16)	0.127	0.3304	0.0843	0.0580	−31
^{120}Sn	39.9(4)	99.6(1)	0.090(13)	0.095	0.2668	0.1179	0.0912	−23
^{124}Sn	40.7(4)	97.4(2)	0.073(10)	0.065	0.1958	0.1505	0.1275	−15

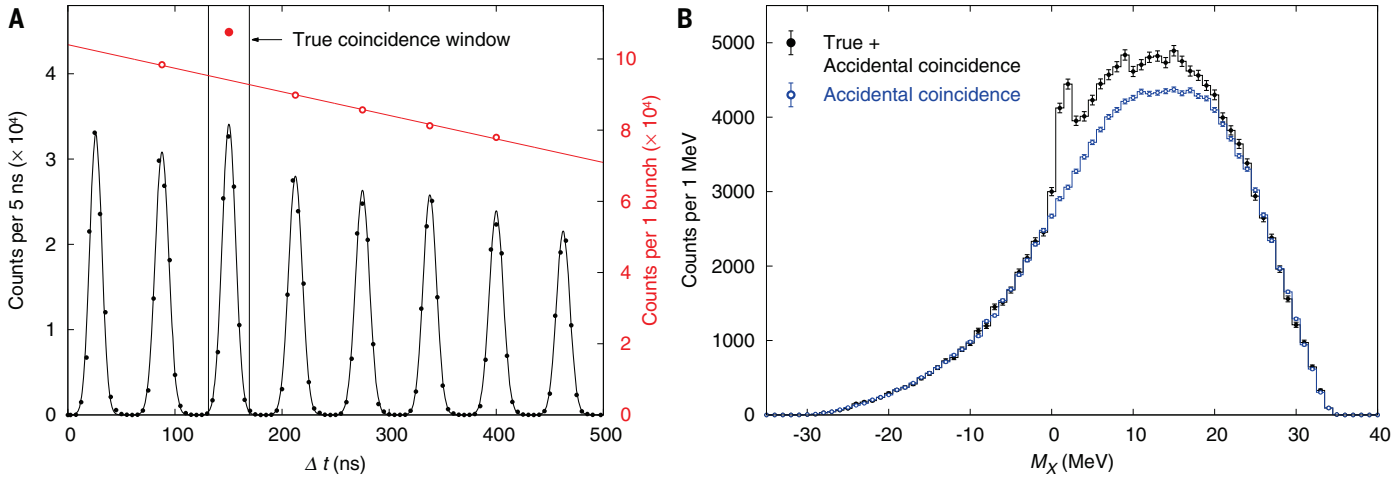


Fig. 2. Accidental-coincidence background distributions from the coincident timing spectrum and missing-mass spectrum for the ^{112}Sn target. (**A**) Coincident time spectrum of the protons and α particles in the time window of the 500-ns coincidence gate. (**B**) Missing-mass spectrum (black: true and accidental-coincidence events; blue: only accidental-coincidence events. The error bars are statistical only. In (B), the amplitude of the accidental-coincidence background within the true-coincidence time window is determined from the linear fitting [the red line in (A)] of the statistics of the accidental-coincidence peaks. Similar plots for the other three tin isotope targets are presented in fig. S5.

time window of the 500-ns coincidence gate. It includes seven peaks separated by time intervals of 62.5 ns, which correspond to the time structure of the beam bunches from the cyclotron. Although accidental-coincidence events are dominant, an enhancement in the third bunch, which arises from true-coincidence events, is observed. From the measured kinetic energies of the protons, T_p, and α particles, T_α, in the coincident bunch, the missing-mass spectrum, M_X = 392 MeV − T_p − T_α, is constructed (black points in Fig. 2B). The blue points in Fig. 2B correspond to the background spectrum resulting from the accidental-coincidence bunches after proper normalization. The spectrum from the true-coincidence bunch shows a prominent peak on top of the background.

We subtracted the "accidental-coincidence" background from the "true-coincidence" spectrum. The error bars presented in Fig. 3, A to D, include the effect of this subtraction. The missing-mass spectra for the targets—^{112}Sn, ^{116}Sn, ^{120}Sn, and ^{124}Sn—were obtained with a resolution of 0.83(3) MeV (standard deviation) and fitted using the Gaussians for the ground-state peaks and the simulated shapes of the continuum (fitting parameters in table S3). The peak positions of the ground state for the different targets agree well with the known α-separation energies. This result clearly indicates the preformation of α particles in these tin isotopes. The observed momentum distribution of the α particles (fig. S3) is also in good agreement with the theoretical prediction (*23*), reaffirming that the formation of α particles indeed occurs in the low-density surface region of heavy nuclei as predicted by the gRDF calculation (*23*).

To study the isotopic dependence of the α-formation probability, we then deduced the cross sections from the reaction yields by integrating the ground-state peaks (the black dashed-dotted line in Fig. 3, A to D), which are given in Table 1. Note that the instrumental ("accidental-coincidence") background has already been removed as discussed above. Figure 3E displays the results of the isotopic dependence of the (p, $p\alpha$) cross sections. The associated errors are dominated by the statistical errors but also include the systematical errors (~1.6%). (Details are given in the methods.) We observe a gradual decrease in the cross section with increasing mass numbers. The cross section for ^{112}Sn is larger by a factor of 2.2(3) as compared to that for ^{124}Sn. This is in line with the predicted isotopic dependence of the effective numbers of the α clusters (Table 1 and Fig. 3F). The radial density distributions of the α clusters in the gRDF approach were incorporated into a distorted-wave reaction model in the impulse approximation with a proton optical potential (*30*) and an elastic proton-α cross section (*31*) (see methods). These were used to obtain the theoretical (p, $p\alpha$) cross sections while considering the experimental conditions of the angular and momentum acceptances. Although the α particles were emitted in the direction opposite to the core nuclei after the reactions under the selected kinematic condition in the experiment, the absorption of the α particles was considered by introducing a proper optical potential (*32*, *33*). The imaginary potential depth was rescaled to obtain theoretical cross sections that almost match with the experimental ones, but the scaling factor was kept identical for all Sn nuclei. The points of origin of the α particles were sampled according to the probability of finding them on the surface of the target nuclei in the gRDF calculation (*23*). The scaling factor of 0.148 for the imaginary potential depth is rather small. This indicates that the α particle is hardly absorbed by the residual nucleus after being hit by the incident proton. The dependence of the (p, $p\alpha$) reaction cross section on the mass number A of the target nucleus is depicted in Fig. 3E. The isotopic trend of the theoretical cross sections is very robust against variations in the optical potential radius R and the diffuseness parameter a. This was explored in trial calculations by varying R and a by about 15%, which covers the typical range of these quantities. The theoretical isotopic dependence closely follows the experimentally determined one; in fig. S6, the linear relationship between the theoretical cross sections and the experimental cross sections is clearly observed [Pearson's correlation coefficient (r) = 0.9934, P = 0.0066]. We emphasize that the reduction of the cross section by a factor of about two when going from ^{112}Sn to ^{124}Sn cannot be attributed to the systematic change of the proton optical potential (*32*) with the mass number or that of the α-particle optical potential (*33*), because the volume integrals of the imaginary part vary by only 15.3 and 8.9%, respectively. This is reaffirmed by the experimental and theoretical σ/N_α ratios of all the isotopes used in the experiment, given in Fig. 3G, where σ is the experimental cross section and N_α is the number of α particles. An almost flat distribution is obtained for σ/N_α, demonstrating that the decline in the measured cross sections with an increasing mass number is indeed predominantly caused by the decrease in N_α. Note that the

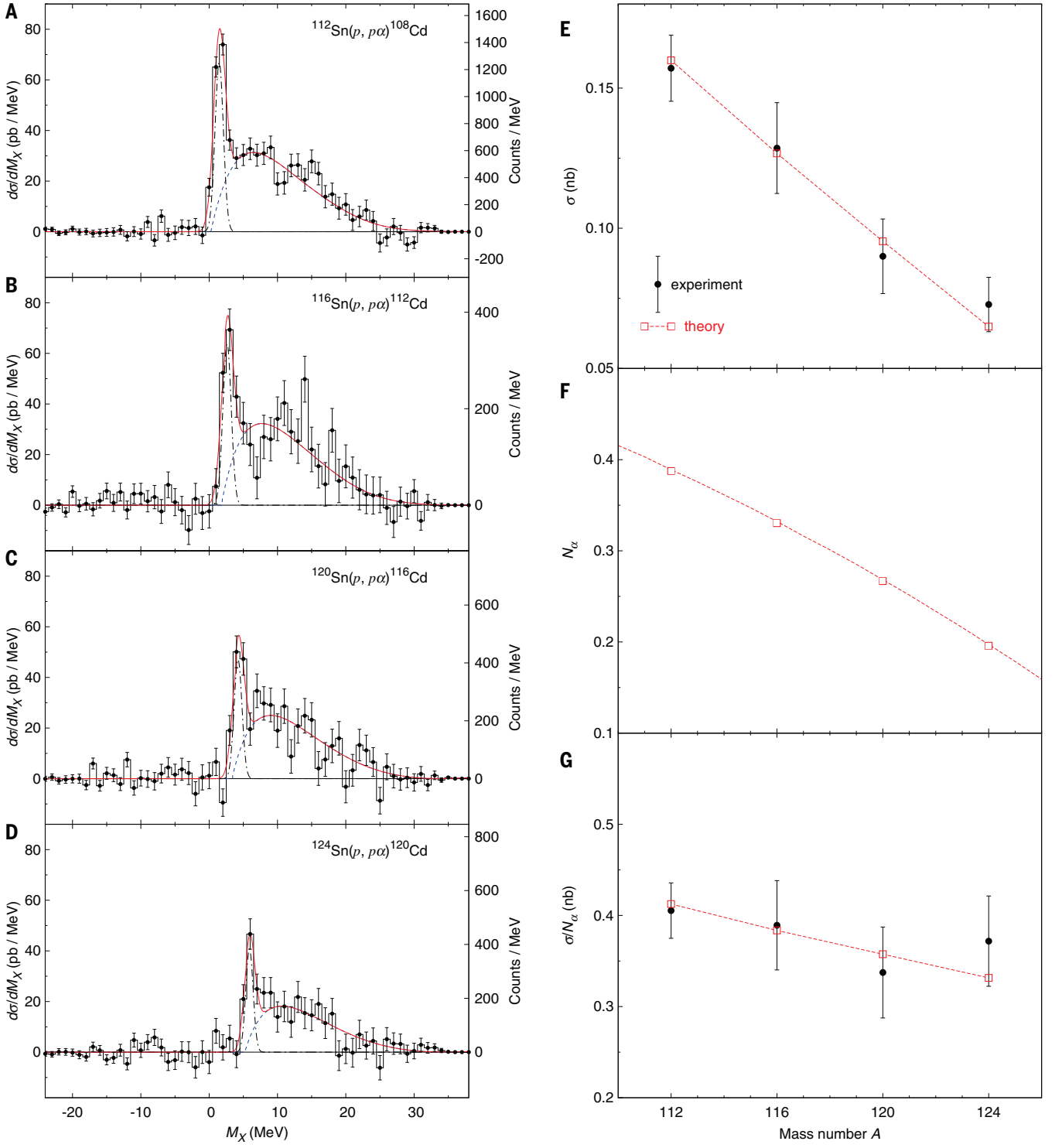


Fig. 3. Missing-mass spectra for the α-knockout reactions, the isotopic dependence of the (p, $p\alpha$) cross sections, and a comparison with the theoretical calculations. (**A** to **D**) Missing-mass spectra for the α-knockout reactions for tin targets (A) ^{112}Sn, (B) ^{116}Sn, (C) ^{120}Sn, and (D) ^{124}Sn. The effect of a small dip between the ground state peak and the broad continuous bump in (B) on the count of the peak is within the fitting error and does not change the conclusions of this study. The red lines in (A) to (D) represent the results of the fits with the Gaussians for the ground-state peaks (the black dashed-dotted lines) and the simulated shapes of the continuum (the blue dashed lines). They include the experimental acceptances of the momenta and the geometric cuts. (**E**) Isotopic dependence of the cross sections, as determined experimentally (black points) and theoretically (red line). (**F**) Dependence of the effective number of α clusters, N_α, on the mass number A of the tin nuclei in the calculation using the gRDF approach (*23*) with the DD2 parameters (*5*). (**G**) Ratios of the cross sections σ and N_α. In (A) to (D), the error bars are statistical only; in (E) and (G), the error bars are dominated by the statistical errors but also include the systematical errors (~1.6%). (Details are given in the methods.) In (E) and (G), the correlated normalization uncertainty of the theoretical values is not presented because it is canceled out when we discuss the isotopic dependence of σ and σ/N_α.

decrease of σ and N_α is also correlated with the increase of the α-particle binding energy with the mass number A. Because the α-particle density distribution, in particular the shape and position, and the binding energy are determined self-consistently in the gRDF calculations, only a change of the parametrization of the interaction can help to lift this correlation, which is beyond the scope of the present work. However, the change of the α-particle density distribution and the α-particle binding energy should have a minor contribution to the reduction of the cross section, as is evident from the almost constant σ/N_α ratio. Hence, the observed reduction of the cross section with increasing mass number reflects the decrease of the effective number of α particles N_α, depicted in Fig. 3F.

The neutron-skin thickness Δr_{np} is defined as the difference between the root-mean-square radius of the neutron density distribution r_n and that of the proton density distribution r_p, $\Delta r_{np} = r_n - r_p$. For heavy nuclei, it is closely related to the density dependence of the symmetry energy in the nuclear equation of state (EOS) (*34*). The correlation between Δr_{np} and the slope parameter L (neutron-matter pressure) in the EOS (*35*) is a linear function when the results of many mean-field model calculations are compiled (*36*). Therefore, L can be deduced from Δr_{np}. According to the gRDF framework, the existence of α clusters on the nuclear surface will reduce the size of the neutron skin (*23*). The theoretical Δr_{np} for the tin isotopes used in this experiment with and without considering the α-cluster effect are given in Table 1, which indicates a reduction of 15 to 44%. This effect necessitates a correction to the relationship between Δr_{np} and L (*35*) that goes beyond the mean-field calculations without considering the formation of α clusters. Knowledge of the EOS for neutron-rich matter is of fundamental importance in nuclear physics and for understanding the properties of neutron stars (*4*). The result reported herein supports the close correlation between the surface α clustering and the neutron-skin thickness in heavy nuclei as predicted by the gRDF calculations (*23*). The Δr_{np} of tin isotopes can be better reproduced by relativistic mean-field calculations after considering the α-clustering effect. (A comparison between the experimental data and the theoretical calculations can be found in fig. S4.) The existence of α clusters on the nuclear surface needs to be considered for determining L from Δr_{np}. It is worthwhile to mention that short-range correlated pairs in neutron-rich nuclei (*6*, *7*) may have similar effects in reducing the neutron-skin thickness (*37*). Recent ab initio many-body calculations of ^{48}Ca also show the necessity to refine nuclear density functionals and to reassess the correlation of the neutron skin thickness with isovector properties of the nuclear EOS (*38*). We expect that such ab initio calculations will be extended to even heavier nuclei and will explicitly take into account the effect of nuclear clustering in the future.

We have measured the cross sections for the proton-induced quasi-free α-cluster knockout reactions along the tin isotopic chain, $^{A}\mathrm{Sn}(p, p\alpha)^{A-4}\mathrm{Cd}$. Our results provide direct evidence for the formation of α clusters in the dilute neutron-rich matter such as the surface of neutron-rich heavy nuclei. The measured cross sections along the isotopic chain decrease smoothly, but substantially, with the neutron number. The theoretical analysis attributes this decrease to the interplay between α-cluster formation and the neutron skin, which further affects our understanding of the nuclear EOS (*4*, *5*, *23*). Extensive efforts across the world are ongoing to measure the neutron-skin thicknesses of nuclei with sufficient precision (*35*). In particular, parity-violating electron scattering experiments at Jefferson Lab are expected to provide more accurate measurements of the neutron-skin thickness of ^{208}Pb and ^{48}Ca (*39*, *40*). To accurately constrain the nuclear EOS, our result also suggests the necessity of considering the effect of nuclear clustering when deducing constraints for the EOS parameters from the observed parity-violating asymmetry and neutron-skin thickness. The formation of α-clusters at the surface of heavy nuclei can be a natural explanation for the "α-particle preformation factor" that is postulated in the theory of α decay (*19*, *20*). Future experiments with radioactive α emitters, which are produced as high-energy secondary beams with radioactive-beam facilities such as the Radioactive Isotope Beam Factory (RIBF) , GSI Helmholtzzentrum für Schwerionenforschung GmbH (GSI), and Facility for Antiproton and Ion Research (FAIR) could elucidate this relationship.

REFERENCES AND NOTES

1. P. Ring, P. Schuck, *The Nuclear Many-Body Problem* (Springer, 1980).
2. T. Otsuka, A. Gade, O. Sorlin, T. Suzuki, Y. Utsuno, *Rev. Mod. Phys.* **92**, 015002 (2020).
3. D. J. Dean, M. Hjorth-Jensen, *Rev. Mod. Phys.* **75**, 607–656 (2003).
4. M. Oertel, M. Hempel, T. Klähn, S. Typel, *Rev. Mod. Phys.* **89**, 015007 (2017).
5. S. Typel, G. Röpke, T. Klähn, D. Blaschke, H. H. Wolter, *Phys. Rev. C* **81**, 015803 (2010).
6. O. Hen, G. A. Miller, E. Piasetzky, L. B. Weinstein, *Rev. Mod. Phys.* **89**, 045002 (2017).
7. O. Hen *et al*., *Science* **346**, 614–617 (2014).
8. R. Subedi *et al*., *Science* **320**, 1476–1478 (2008).
9. H. A. Bethe, R. F. Bacher, *Rev. Mod. Phys.* **8**, 82–229 (1936).
10. W. Wefelmeier, *Z. Phys.* **107**, 332–346 (1937).
11. H. Morinaga, *Phys. Rev.* **101**, 254–258 (1956).
12. H. Margenau, *Phys. Rev.* **59**, 37–47 (1941).
13. J. P. Ebran, E. Khan, T. Nikšić, D. Vretenar, *Nature* **487**, 341–344 (2012).
14. M. Freer, H. Horiuchi, Y. Kanada-En'yo, D. Lee, U.-G. Meißner, *Rev. Mod. Phys.* **90**, 035004 (2018).
15. K. Ikeda, N. Takigawa, H. Horiuchi, *Prog. Theor. Phys. Suppl.* **E68**, 464–475 (1968).
16. F. Hoyle, *Astrophys. J. Suppl. Ser.* **1**, 121 (1954).
17. C. W. Cook, W. A. Fowler, C. C. Lauritsen, T. Lauritsen, *Phys. Rev.* **107**, 508–515 (1957).
18. H. O. U. Fynbo *et al*., *Nature* **433**, 136–139 (2005).
19. C. Qi, R. J. Liotta, R. A. Wyss, *Prog. Part. Nucl. Phys.* **105**, 214–251 (2018).
20. G. Gamow, *Z. Phys.* **51**, 204–212 (1928).
21. D. S. Delion, R. J. Liotta, *Phys. Rev. C* **87**, 041302(R) (2007).
22. K. Hagel *et al*., *Phys. Rev. Lett.* **108**, 062702 (2012).
23. S. Typel, *Phys. Rev. C* **89**, 064321 (2014).
24. G. Jacob, Th. A. J. Maris, *Rev. Mod. Phys.* **38**, 121–142 (1966).
25. T. A. Carey, P. G. Roos, N. S. Chant, A. Nadasen, H. L. Chen, *Phys. Rev. C* **23**, 576–579 (1981).
26. N. S. Chant, P. G. Roos, *Phys. Rev. C* **15**, 57–68 (1977).
27. P. G. Roos *et al*., *Phys. Rev. C* **15**, 69–83 (1977).
28. M. Fujiwara *et al*., *Nucl. Instrum. Meth. A* **422**, 484–488 (1999).
29. T. Wakasa, K. Ogata, T. Noro, *Prog. Part. Nucl. Phys.* **96**, 32–87 (2017).
30. M. Toyokawa, K. Minomo, M. Yahiro, *Phys. Rev. C* **88**, 054602 (2013).
31. K. Yoshida, K. Minomo, K. Ogata, *Phys. Rev. C* **94**, 044604 (2016).
32. S. Hama, B. C. Clark, E. D. Cooper, H. S. Sherif, R. L. Mercer, *Phys. Rev. C* **41**, 2737–2755 (1990).
33. M. Nolte, H. Machner, J. Bojowald, *Phys. Rev. C* **36**, 1312–1316 (1987).
34. B. A. Brown, *Phys. Rev. Lett.* **85**, 5296–5299 (2000).
35. X. Roca-Maza, N. Paar, *Prog. Part. Nucl. Phys.* **101**, 96–176 (2018).
36. X. Roca-Maza, M. Centelles, X. Viñas, M. Warda, *Phys. Rev. Lett.* **106**, 252501 (2011).
37. G. A. Miller *et al*., *Phys. Lett. B* **793**, 360–364 (2019).
38. G. Hagen *et al*., *Nat. Phys.* **12**, 186–190 (2016).
39. S. Abrahamyan *et al*., *Phys. Rev. Lett.* **108**, 112502 (2012).
40. C. J. Horowitz, K. S. Kumar, R. Michaels, *Eur. Phys. J. A* **50**, 48 (2014).
41. J. Tanaka *et al*., Numerical data for "Formation of α clusters in dilute neutron-rich matter." Zenodo (2020); https://doi.org/10.5281/zenodo.4290691.

ACKNOWLEDGMENTS

We thank RCNP staff for their hospitality and acknowledge experimental support from RCNP ring cyclotron operational staff and Grand Raiden supporting scientific staff. We thank the local technical staff at the RCNP for aid during the preparation of the experiment. We thank the GSI target laboratory for the preparation of the targets. **Funding:** This work was partially supported by the Deutsche Forschungsgemeinschaft (DFG, German Research Foundation) Project-ID 279384907 - SFB 1245, by the GSI-TU Darmstadt cooperation agreement, by the BMBF (project 05P19RDFN1), and in part by Grants-in-Aid of the Japan Society for the Promotion of Science (grant no. JP16K05352). Z.Y. acknowledges support from the Foreign Postdoctoral Researcher program of RIKEN. **Author contributions:** T.A., S.T., T.U., and Z.Y. proposed the experiment. Z.Y. and J.Z. designed the experimental setup and led the test experiments. Z.Y. and J.T. conducted the necessary experimental preparations and also executed the experiment. J.T. and Z.Y. performed the data reduction and analysis presented here. J.T., S.T., T.A., and Z.Y. prepared the draft of the manuscript. All authors read the manuscript, gave comments, suggested changes, and agreed with the final version. S.T. provided the original theoretical idea and performed the reaction calculations with contributions from K.O. and K.Y. A.T. and N.K., along with the Grand Raiden and LAS support team, took responsibility for the operation of the spectrometers. Y.Mat. and A.T. upgraded the drift chambers of the LAS spectrometer with the help of staff at RIKEN, RCNP, and Konan University. D.S., S.A., V.P., V.W., Y.K., W.L., S.Hu., Y.J., and J.L. prepared the experimental setup with the local group. P.v.B., Y.F., S.He., A.I., Y.J., M.K., N.K., J.H., S.B., K.M., Y.Mae., S.N., H.S., F.S., and P.S. supervised the experiment and verified that the data were acquired correctly. **Competing interests:** The authors declare that they have no competing financial interests. **Data and materials availability:** The data that support the findings of this study have been presented in the main text and supplementary materials. The data underlying the figures are accessible at Zenodo (*41*).

SUPPLEMENTARY MATERIALS

science.sciencemag.org/content/371/6526/260/suppl/DC1
Materials and Methods
Figs. S1 to S6
Tables S1 to S5
References (*42*–*47*)

24 August 2020; accepted 30 November 2020
10.1126/science.abe4688

AGING

Senolysis by glutaminolysis inhibition ameliorates various age-associated disorders

Yoshikazu Johmura[1]*, Takehiro Yamanaka[1]†, Satotaka Omori[1]†, Teh-Wei Wang[1]†, Yuki Sugiura[2], Masaki Matsumoto[3]‡, Narumi Suzuki[1], Soichiro Kumamoto[1], Kiyoshi Yamaguchi[4], Seira Hatakeyama[4], Tomoyo Takami[3], Rui Yamaguchi[5], Eigo Shimizu[5], Kazutaka Ikeda[6], Nobuyuki Okahashi[6], Ryuta Mikawa[7], Makoto Suematsu[2], Makoto Arita[6,8], Masataka Sugimoto[7], Keiichi I. Nakayama[3], Yoichi Furukawa[4], Seiya Imoto[9], Makoto Nakanishi[1]*

Removal of senescent cells (senolysis) has been proposed to be beneficial for improving age-associated pathologies, but the molecular pathways for such senolytic activity have not yet emerged. Here, we identified glutaminase 1 (*GLS1*) as an essential gene for the survival of human senescent cells. The intracellular pH in senescent cells was lowered by lysosomal membrane damage, and this lowered pH induced kidney-type glutaminase (KGA) expression. The resulting enhanced glutaminolysis induced ammonia production, which neutralized the lower pH and improved survival of the senescent cells. Inhibition of KGA-dependent glutaminolysis in aged mice eliminated senescent cells specifically and ameliorated age-associated organ dysfunction. Our results suggest that senescent cells rely on glutaminolysis, and its inhibition offers a promising strategy for inducing senolysis in vivo.

Accumulation of senescent cells (SnCs) is associated with age-related pathologies (*1*, *2*), which can be alleviated by senolytic compounds (*3*–*7*). However, because of the heterogeneity of senescence in vivo, molecular targets that induce mortality in various types of SnCs have not yet been identified. To identify senolytic compounds, we developed a method for long-term culturing of human SnCs (hSnCs) of high purity (*8*) (fig. S1A). Senescent human fibroblast cell line hHCA2 induced by transient p53 activation with nutlin3a (n-Sen) showed high expression of p16, cluster of differentiation 26 (CD26), interleukin-6 (*IL-6*), and *IL-8* (fig. S1, B and C), and the purity appeared to be nearly 100%, as evidenced by senescence-associated β-galactosidase (SA–β-gal) positivity (fig. S1D). p16 expression and the SA–β-gal–positive population were higher in n-Sen hHCA2 cells than in other senescent hHCA2 cells [DNA damage-induced (d-Sen), oxidative-induced (ox-Sen), and replicative (r-Sen)] (fig. S1E). The transcriptome signature of n-Sen hHCA2 cells was similar to that of other hSnCs (fig. S1F). Immunocytochemical analysis revealed reduced lamin B1 and high-mobility group box 1 (HMGB1), which are senescent hallmarks (*9*, *10*), in all hSnCs (fig. S2).

Using n-Sen hHCA2 cells and short hairpin RNA (shRNA) libraries, we identified shRNAs that induce mortality (data S1). Among the top hits was glutaminase 1 (GLS1) (Fig. 1A and fig. S3A), the expression of which was increased in n-Sen hHCA2 cells compared with uninduced cells (fig. S3B). Protein absolute quantification analysis revealed that GLS1 expression was induced in n-Sen hHCA2 cells, among the ~100 proteins involved in metabolic regulation (Fig. 1B and data S2). Furthermore, the abundance of glutamate dehydrogenase (GDH), glutamine synthetase (GS), and excitatory amino acid transporter 3 (EAAT3) implicated in glutamine metabolism was increased in n-Sen hHCA2 and d-Sen hIMR-90 cells (fig. S3, C and D). Induction of GLS1 was also observed in d-Sen hIMR-90 cells (fig. S3D). GLS1 activity was increased in n-Sen hHCA2 cells (fig. S3E). The activation of glutaminolysis and its inhibition by BPTES [bis-2-(5-phenylacetamido-1,3,4-thiadiazol-2-yl)ethyl sulfide], an inhibitor of GLS1, in n-Sen hHCA2 cells were confirmed by isotope tracing using $^{13}C_5$, $^{15}N_2$ L-glutamine (fig. S4). GLS1 depletion (fig. S5A) and BPTES treatment (Fig. 1C and fig. S5B) showed that GLS1 was essential for the survival of n-Sen, d-Sen, r-Sen hHCA2, and oncogene-induced senescent (o-Sen) hIMR-90 cells as well as that of all other d-Sen cells tested (hIMR-90, hRPE-1, and mouse embryo fibroblasts) (fig. S5, B and C). Although glutamine metabolism is affected by culture conditions, GLS1 up-regulation and BPTES-induced mortality were independent of culture conditions in n-Sen hHCA2 cells (fig. S5, D and E). Other GLS1 inhibitors, C968 and CB-839, had similar inhibitory effects on n-Sen hHCA2 survival (fig. S5F). Overexpression of GLS1 failed to induce a senescent phenotype in uninduced hHCA2 cells (fig. S5G).

We tried to clarify the mechanism of GLS1 induction in SnCs. Kidney-type glutaminase (KGA)–type GLS1 was induced in n-Sen, d-Sen, and r-Sen hHCA2 cells (Fig. 1D and fig. S6A). The *KGA* transcript contains an AU-rich element (ARE) at the 3′ untranslated region (3′UTR) (*11*), which increases mRNA stability through HuC binding (*12*) under acidic conditions (*13*). HuC was essential for the induction of the *KGA* transcript and protein in n-Sen and r-Sen hHCA2 cells, respectively (fig. S6, B and C). The *KGA*-L transcript was stable in n-Sen hHCA2 cells but unstable in uninduced cells and HuC-depleted n-Sen hHCA2 cells (Fig. 1E and fig. S6D). HuC specifically bound to the *KGA*-L transcript (fig. S6E). HuC depletion reduced survival of n-Sen hHCA2 cells (fig. S6F). These results suggest that the induction of KGA arises from HuC-mediated stabilization of its transcript under acidic conditions in SnCs. This notion was further supported by the finding that incubation of n-Sen hHCA2 cells in alkaline medium (pH 8.5) reduced KGA expression (fig. S6G).

Glutaminolysis produces three important metabolites: α-ketoglutarate (α-KG), glutathione (GSH), and ammonia. Supplying dimethyl-α-KG (DM-α-KG) and/or GSH reduced ethyl ester (GSH-MEE) or N-acetyl-cysteine (NAC) as a source of cysteine or sulfur in culture medium failed to prevent the BPTES-induced death of n-Sen hHCA2 cells (Fig. 1F and fig. S6, H and I), although the contribution of glutaminolysis to total oxygen consumption was higher in n-Sen hHCA2 cells than in uninduced cells (figs. S6, J and K). By contrast, addition of ammonia to the medium (Fig. 1G) and incubation with alkaline medium (pH 8.5) (Fig. 1H and figs. S5F and S6, L and M) prevented the death of n-Sen hHCA2 cells caused by BPTES, C968, CB-839, or GLS1 depletion. Although glutamate is a precursor of nonessential amino acids (NEAAs), inhibition of glutaminolysis by BPTES did not affect NEAA amounts in n-Sen hHCA2 cells, suggesting that NEAAs were scavenged rather

[1]Division of Cancer Cell Biology, Institute of Medical Science, The University of Tokyo, 4-6-1 Shirokanedai, Minato-ku, Tokyo 108-8639, Japan. [2]Department of Biochemistry, Keio University School of Medicine, 35 Shinanomachi, Shinjyuku-ku, Tokyo 160-8582, Japan. [3]Department of Molecular and Cellular Biology, Medical Institute of Bioregulation, Kyushu University, 3-1-1 Maidashi, Higashi-ku, Fukuoka 812-8582, Japan. [4]Clinical Genome Research, Institute of Medical Science, The University of Tokyo, 4-6-1 Shirokanedai, Minato-ku, Tokyo 108-8639, Japan. [5]Human Genome Center, Institute of Medical Science, The University of Tokyo, 4-6-1 Shirokanedai, Minato-ku, Tokyo 108-8639, Japan. [6]RIKEN Center for Integrative Medical Sciences, Suehiro-cho, Tsurumi-ku, Yokohama, Kanagawa 230-0045, Japan. [7]Research Institute, National Center for Geriatrics and Gerontology, 7-430 Morioka-cho, Obu, Aichi 474-8511, Japan. [8]Division of Physiological Chemistry and Metabolism, Graduate School of Pharmaceutical Sciences, Keio University, Shibakoen, Minato-ku, Tokyo 105-0011, Japan. [9]Health Intelligence Center, Institute of Medical Science, The University of Tokyo, 4-6-1 Shirokanedai, Minato-ku, Tokyo 108-8639, Japan.
*Corresponding author. Email: mkt-naka@ims.u-tokyo.ac.jp (M.N.); johmuray@ims.u-tokyo.ac.jp (Y.J.) †These authors contributed equally to this work. ‡Present address: Department of Omics and Systems Biology, Niigata University Graduate School of Medical and Dental Sciences, 1-757 Asahimachi-douri, Chuo-ku, Niigata, Niigata 951-8510, Japan.

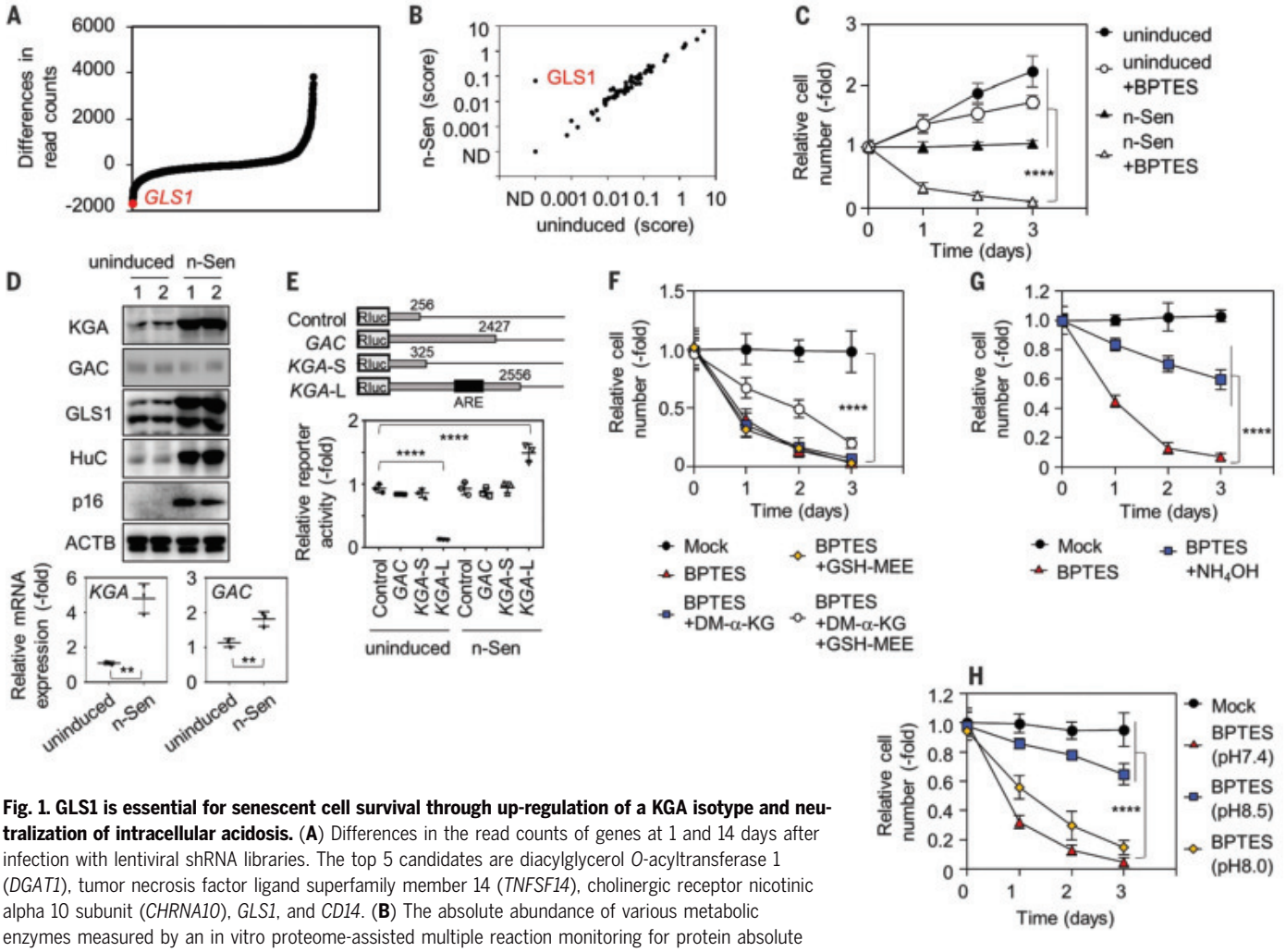


Fig. 1. GLS1 is essential for senescent cell survival through up-regulation of a KGA isotype and neutralization of intracellular acidosis. (**A**) Differences in the read counts of genes at 1 and 14 days after infection with lentiviral shRNA libraries. The top 5 candidates are diacylglycerol *O*-acyltransferase 1 (*DGAT1*), tumor necrosis factor ligand superfamily member 14 (*TNFSF14*), cholinergic receptor nicotinic alpha 10 subunit (*CHRNA10*), *GLS1*, and *CD14*. (**B**) The absolute abundance of various metabolic enzymes measured by an in vitro proteome-assisted multiple reaction monitoring for protein absolute quantification (iMPAQT) method in uninduced and n-Sen hHCA2 (n-Sen) cells. The average values of three independent samples are plotted. ND, not detected. (**C**) The relative numbers of the indicated cells in the presence or absence of BPTES (10 μM). (**D**) Immunoblotting using the indicated antibodies (top) and quantitative PCR (qPCR) using the indicated primers from the indicated cells (bottom). GAC, glutaminase C; ACTB, actin β. (**E**) Dual luciferase reporters containing the indicated 3′UTR (top) and a luciferase (luc) assay of the indicated cells expressing reporters (bottom). (**F** to **H**) The relative numbers of the indicated cells (F) in the presence or absence of BPTES (10 μM) with or without DM-α-KG (7 mM) and GSH-MEE (2 mM), (G) with or without NH_4OH (5 mM) in the presence of BPTES (10 μM), and (H) in different pH-adjusted media at the indicated times. Data are presented as means ± SD of three independent experiments. Unpaired two-tailed Student's *t* test (D) and one-way analysis of variance (ANOVA) with Dunnett's multiple comparisons post hoc test [(C) and (E) to (H)] were performed. $^{**}P < 0.01$; $^{****}P < 0.0001$.

than de novo synthesized (fig. S7A). Among amino acid transporters, only EAAT3 was highly expressed in n-Sen and d-Sen hHCA2 cells compared with uninduced cells (figs. S3, C and D, and S7B). Macropinocytosis, but not autophagy, was activated, and inhibition of macropinocytosis suppressed the survival of n-Sen hHCA2 cells (fig. S7, C and D). Supplying NEAAs in culture medium failed to prevent senescent cell death by BPTES (fig. S7E). In addition, the abundance of solute carrier family 7 member 11 (SLC7A11), the overexpression of which promotes glutaminase sensitivity, was comparable between uninduced and n-Sen hHCA2 cells (fig. S7F). Together with the finding that lowering of cysteine concentration in the medium did not alter the sensitivity of SnCs to BPTES (fig. S5D), this suggests that the mortality of SnCs after inhibition of glutaminolysis presumably occurs due to the failure in neutralizing intracellular acidosis.

Intracellular acidosis induces cell death through activation of the BCL2 and adenovirus E1B 19-kDa-interacting protein 3 (BNIP3) and mitochondrial permeability transition pore (mPTP) axis (*14*, *15*). Depletion of BNIP3 or inhibition of mPTP by decylubiquinone (DUB) or cyclosporine A (CsA) reduced the mortality of n-Sen hHCA2 cells by BPTES, C968, CB-839, or GLS1 depletion (fig. S8, A to F). Although BNIP3 colocalized with voltage-dependent anion-selective channel 1 (VDAC1), a marker of mitochondria, without BPTES (fig. S8G), in the presence of BPTES, only n-Sen hHCA2 cells showed a tight mitochondrial association with BNIP3 after alkaline treatment (fig. S8H). These data imply that mPTP activation by BNIP3 caused the cell mortality in SnCs under BPTES treatment. The amount of mitochondria-bound BNIP3 was specifically reduced in n-Sen hHCA2 cells cultured under pH 8.5 (fig. S8I). Overexpression of dominant-negative BNIP3 lacking a transmembrane domain (BNIP3-ΔTM) protected n-Sen hHCA2 cells from death after BPTES treatment or GLS1 depletion (fig. S8, J to M). BPTES-induced mortality of n-Sen hHCA2 cells was not affected by treatment with benzyloxycarbonyl-Val-Ala-Asp(OMe)-fluoromethylketone (Z-VAD-FMK), ferrostatin-1, or Nec1s (fig. S8N). The amount

of ammonium production in n-Sen hHCA2 cells and medium was high in the presence of DUB and dropped after treatment with BPTES, C968, CB-839, or GLS1 depletion (fig. S9, A to C), resulting in a lowering of the intracellular pH.

Insoluble macromolecules in lysosomes cause lysosomal membrane damage, resulting in leaking intralysosomal H^+ and subsequent intracellular acidosis (*16*). Many foci of galectin-3, a marker of membrane damage, colocalized with lysosomal-associated membrane

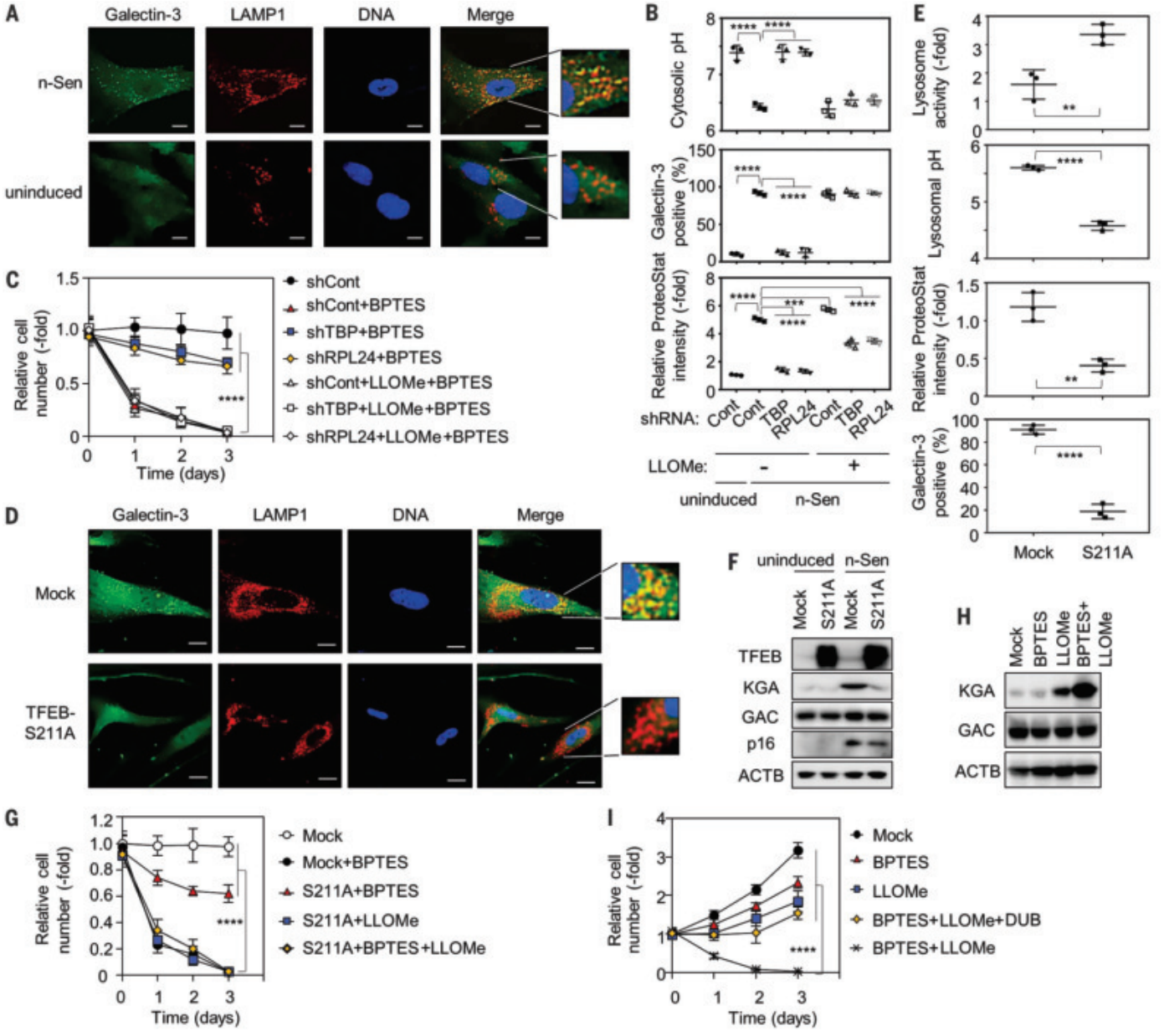


Fig. 2. Protein aggregates cause lysosomal membrane damage that provokes intracellular acidosis in SnCs. (**A**) Immunostaining of uninduced and n-Sen hHCA2, using anti–galectin-3 (green) and anti-LAMP1 (red) antibodies and Hoechst 33342 (DNA, blue). Magnified images show the colocalization between galectin-3 and LAMP1 foci. Scale bars, 20 μm. (**B**) The cytosolic pH, relative population of galectin-3–positive cells (cells with more than five galectin-3–positive foci colocalized with LAMP1: n = 200), and ProteoStat intensity of n-Sen hHCA2 cells expressing the indicated shRNA with or without LLOMe (1 mM). Cont, control. (**C**) The relative number of n-Sen hHCA2 cells expressing the indicated doxycycline (Dox)–inducible shRNA with Dox (1 μg/ml) with or without BPTES (10 μM) and LLOMe (1 mM) at the indicated times. (**D**) Immunostaining of n-Sen hHCA2 cells expressing mock or TFEB-S211A, as described in (A). Scale bars, 20 μm. (**E**) Lysosomal activity, the lysosomal pH, the ProteoStat signal, and the relative population of galectin-3–positive cells (n = 200) among the indicated n-Sen hHCA2 cells. (**F**) Immunoblotting of uninduced and n-Sen hHCA2 cells expressing mock or TFEB-S211A using the indicated antibodies. (**G**) The relative number of n-Sen hHCA2 cells expressing mock or TFEB-S211A with or without BPTES (10 μM) and LLOMe (1 mM) at the indicated times. (**H**) Immunoblotting of uninduced hHCA2 cells with or without LLOMe (1 mM and/or BPTES (10 μM) for 2 hours using the indicated antibodies. (**I**) The relative number of uninduced hHCA2 cells with or without BPTES (10 μM), LLOMe (1 mM), and/or DUB (100 μM) at the indicated times. Data are presented as means ± SD of three independent experiments. Unpaired two-tailed Student's t test (E) and one-way ANOVA with Dunnett's multiple comparisons post hoc test [(B), (C), (G), and (I)] were performed. $^{**}P < 0.01$; $^{***}P < 0.001$; $^{****}P < 0.0001$.

protein 1 (LAMP1), a marker of lysosomes, in n-Sen hHCA2 cells but not in uninduced cells (Fig. 2A). The lysosomal pH was higher in n-Sen hHCA2 cells, suggesting leaking of intralysosomal H^+ to the cytosol (fig. S10A). ProteoStat staining revealed the presence of many aggregates in lysosomes of n-Sen hHCA2 cells (fig. S10B). Amounts of endoplasmic reticulum stress markers—C/EBP homologous protein (CHOP), activating transcription factor 4 (ATF4), and ATF6—were not different between n-Sen and uninduced hHCA2 cells (fig. S10, C and D). mRNA and protein syntheses were higher in d-Sen and r-Sen hHCA2 cells than in uninduced cells (fig. S10, E and F). Suppression of RNA or protein syntheses by depletion of TATA-box binding protein 1 (TBP1) (*17*) or ribosomal protein L24 (RPL24) (*18*), respectively, reduced protein aggregates, ameliorated lysosomal membrane damage, ameliorated the extent of intracellular acidosis, and improved the survival of n-Sen hHCA2 cells in the presence of BPTES (Fig. 2, B and C, and fig. S10, F and G). Artificial lysosomal membrane damage by L-leucyl-L-leucine methyl ester (LLOMe) treatment, which induced galectin-3 foci and intracellular acidosis in uninduced hHCA2 cells when applied alone or combined with BPTES (fig. S10H), reversed the effects of TBP1 and RPL24 depletion (Fig. 2, B and C). However, mechanisms underlying high rates of RNA and protein syntheses in SnCs remain elusive.

Overexpressing constitutively active transcription factor EB (TFEB-S211A) (*19*), which promoted the expression of lysosome biogenesis-related genes (fig. S11A), reduced the levels of galectin-3 foci, protein aggregates, and intralysosomal pH and increased lysosomal activity in n-Sen hHCA2 cells (Fig. 2, D and E). Induction of KGA, stabilization of the *KGA* transcript, intracellular acidosis, and cell mortality in BPTES-treated n-Sen hHCA2 cells were suppressed by TFEB-S211A expression (Fig. 2, F and G, and fig. S11, B to D). The increased survival of cells expressing TFEB-S211A with BPTES was reversed by LLOMe treatment and by incubation with acidic medium (pH 6.2) (Fig. 2G and fig. S11E). Even in uninduced hHCA2 cells, lysosomal membrane damage by LLOMe induced KGA expression and increased mortality in the presence of BPTES (Fig. 2, H and I). The induction of KGA by LLOMe was reduced under an alkaline condition (pH 8.5), whereas incubation with acidic medium (pH 6.2) increased KGA expression in uninduced hHCA2 cells (fig. S11F).

Using comprehensive RNA sequencing (RNA-seq) data of human skin fibroblasts (*20*), we found that the amount of the *KGA* transcript was correlated with aging (Fig. 3A). As reported previously (*21*), a high expression of CD26 was observed in senescent hHCA2 cells induced by all stimuli tested (fig. S12, A to C). The CD26-positive population in lung mesenchymal cells

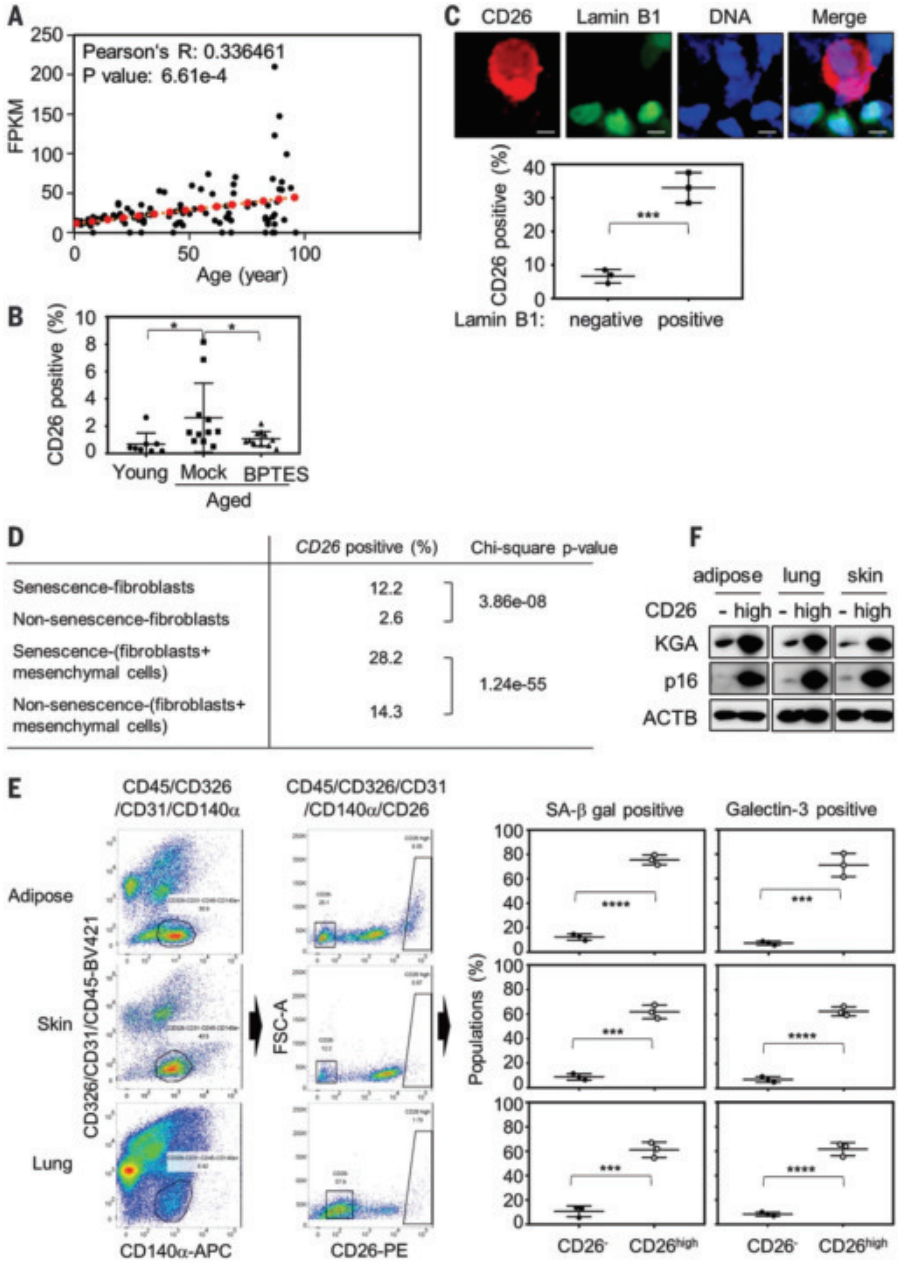


Fig. 3. GLS1 is highly expressed in in vivo SnCs from adipose tissue, skin, and lung. (**A**) Dots for each individual showing the *KGA* fragments per kilobase of exon per million reads mapped (FPKM) value from published RNA-seq data for human dermal fibroblasts versus true age (men; $n = 99$), with a line of best fit overlaid. The Pearson's correlation coefficient (R) value and P value are shown. (**B**) Relative populations of CD26-positive lung mesenchymal populations from young (12-week-old C57BL/6 male) ($n = 8$) and aged (80-week-old C57BL/6 male) mice with ($n = 11$) or without ($n = 11$) BPTES. Smirnov-Grubbs test indicated no outlier in the samples. (**C**) In situ immunostaining of intra-abdominal adipose tissues from 96-week-old aged mice ($n = 3$) with the indicated antibodies and Hoechst 33342 (DNA) (top) and the CD26-positive cell population in lamin B1–positive and –negative cells ($n = 200$ per each animal, bottom). Scale bars, 10 μm. (**D**) Single-cell RNA-seq analysis of the CD26-positive population in mouse fibroblasts with or without mesenchymal cells. (**E**) Anti-CD26 FACS of mouse mesenchymal populations ($CD45^-CD326^-CD31^-CD140\alpha^+$) and CD26-negative or CD26-high cells from the indicated tissues. The relative populations of SA–β-gal–positive cells and galectin-3–positive cells ($n = 200$ per each animal, total three animals) in the indicated population are shown. (**F**) Immunoblotting of CD26-high (high) and CD26-negative (–) mouse cells using the indicated antibodies. Data are presented as means ± SD of three independent experiments. Unpaired two-tailed Student's t test [(C) and (E)] and two-way ANOVA with a Fisher's least significant difference test (B) were performed. *$P < 0.05$; ***$P < 0.001$; ****$P < 0.0001$.

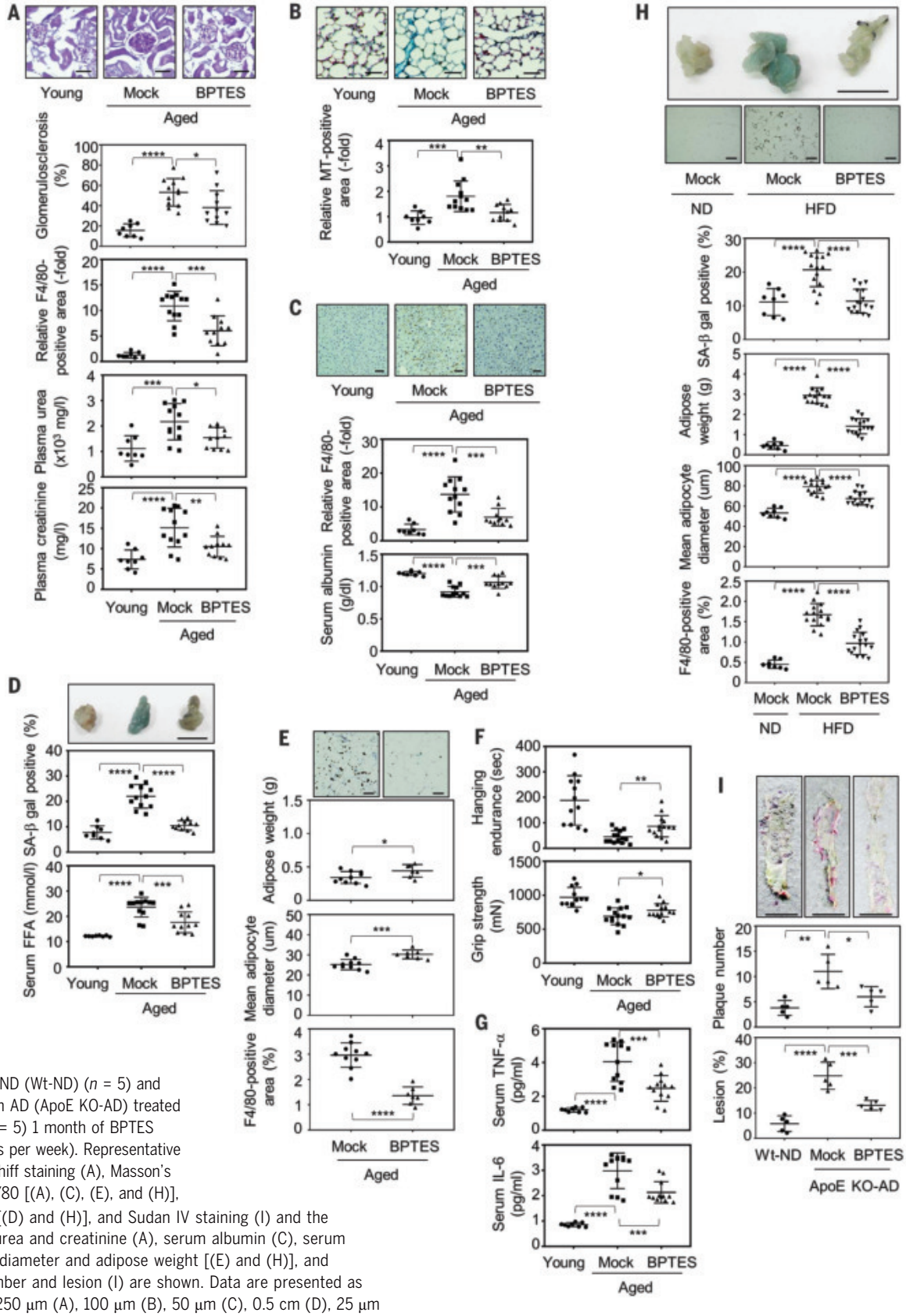


Fig. 4. BPTES treatment ameliorates age- and senescence-associated organ dysfunctions by eliminating SnCs in vivo. (**A** to **D**) Kidney (A), lung (B), liver (C), and adipose (D) tissue from 12-week-old (young) (n = 8) and 80-week-old (aged) C57BL/6 male mice with (n = 12) or without (n = 11) 1 month of repeated BPTES injection (three doses per week). (**E**) Intra-abdominal adipose tissues from 100-week-old C57BL/6 male (aged) mice with (n = 7) or without (n = 10) BPTES. (**F**) Quantification of hanging endurance (top) and grip strength (bottom) from 12-week-old (young) (n = 12) and 100-week-old (aged) C57BL/6 male mice with (n = 14) or without (n = 14) BPTES. (**G**) Quantification of serum tumor necrosis factor–α (TNF-α) (top) and IL-6 (bottom) from 12-week-old (young) (n = 8) and 80-week-old (aged) C57BL/6 male mice with (n = 12) or without (n = 11) BPTES. (**H**) Intra-abdominal adipose tissues from 48-week-old C57BL/6 male mice fed a normal diet (ND) (n = 4) or HFD for 8 weeks with (n = 8) or without (n = 8) BPTES. (**I**) Thoracic aorta from 16-week-old C57BL/6 male wild-type mice fed a ND (Wt-ND) (n = 5) and ApoE knockout mice fed an AD (ApoE KO-AD) treated with (n = 5) or without (n = 5) 1 month of BPTES administration (three doses per week). Representative images of periodic acid Schiff staining (A), Masson's trichrome staining (B), F4/80 [(A), (C), (E), and (H)], SA–β-gal staining in situ [(D) and (H)], and Sudan IV staining (I) and the quantification of plasma urea and creatinine (A), serum albumin (C), serum FFA (D), mean adipocyte diameter and adipose weight [(E) and (H)], and thoracic aorta plaque number and lesion (I) are shown. Data are presented as means ± SD. Scale bars, 250 μm (A), 100 μm (B), 50 μm (C), 0.5 cm (D), 25 μm (E), 0.5 cm [(H), top], 200 μm [(H), bottom], and 500 μm (I). Unpaired two-tailed Student's t test (E) and one-way ANOVA with Dunnett's multiple comparisons post hoc test [(A) to (D) and (F) to (I)] were performed. *P < 0.05; **P < 0.01; ***P < 0.001; ****P < 0.0001.

was higher in aged mice than in young mice and was reduced after 1 month of BPTES injection (Fig. 3B). More than 30% of lamin B1–negative cells were CD26-positive in aged mouse adipose tissues (Fig. 3C). Using a comprehensive single-cell RNA-seq dataset (*22*), SnCs were defined as *p21*-positive, *Lmnb1*-negative, and *IL-6*–positive because reads of *p16* were extremely low and could not be distinguished from those of alternate reading frame protein (ARF), excluding the possibility of using *p16* as a senescent marker for single-cell analysis. Higher proportions of senescent mouse fibroblasts and mesenchymal cells were CD26-positive as compared with nonsenescent cells (Fig. 3D). Fluorescence-activated cell sorting (FACS) using a mesenchymal population ($CD45^-CD326^-CD31^-CD140a^+$) of adipose, skin, and lung from 80-week-old mice revealed that 1 to 10% of cells were CD26-positive (Fig. 3E). The mouse CD26-high population had a higher proportion of SA–β-gal–positive cells, more galectin-3–positive cells, and higher expression of KGA and p16 than did the CD26-negative population (Fig. 3, E and F), suggesting that SnCs predominantly expressed KGA in vivo through lysosomal membrane damage-mediated acidosis. *p16* and *p21* were commonly upregulated CDK inhibitor genes in CD26-positive mouse SnCs from all the organs tested (fig. S12D). Senescence-associated secretory phenotype patterns varied among mouse CD26-positive SnCs from these organs (fig. S12E), consistent with previous reports (*23*).

We examined the effects of BPTES administration in aged mice (80-week-old males) on organ dysfunction. BPTES administration ameliorated age-associated glomerulosclerosis, macrophage invasion in kidney, and kidney dysfunction, which was reflected by abnormal levels of plasma creatinine and urea (Fig. 4A). As with a NADPH oxidase 4 inhibitor or with combining dasatinib and quercetin (*24*, *25*), BPTES administration improved lung fibrosis, macrophage invasion in the liver, and serum albumin concentration (Fig. 4, B and C). Senescence of adipogenic progenitor cells and the subsequent atrophy and macrophage infiltration in adipose tissue are features of natural aging (*26*, *27*). BPTES treatment eliminated the SA–β-gal–positive population and improved serum free fatty acids (FFAs) in the aged mice (Fig. 4D). It alleviated adipose tissue atrophy and macrophage invasion in adipose tissue in aged mice (100-week-old males) (Fig. 4E). Additionally, BPTES treatment improved age-associated weakness of grip strength and short hanging endurance as well as cytokinemia (Fig. 4, F and G). Consistent with the pathophysiological improvement of aging phenotypes, BPTES reduced the expression of *p16*, *KGA*, and *IL-6* transcripts and KGA protein in all tissues tested (fig. S13, A to F). Elimination of SnCs in vivo was confirmed by a reduction in lamin B1–negative populations in adipose tissue from the aged mice (100-week-old males) (fig. S13G).

Targeting SnCs with senolytic drugs was reported to alleviate obesity-induced disorders (*28*, *29*). High-fat diet (HFD)–induced adipocyte hypertrophy, increased SA–β-gal–positive population, and macrophage invasion in adipose tissue were improved by 1 month of BPTES injection in obese mice (48-week-old mice on HFD) (Fig. 4H), accompanied by an increase in the lamin B1–positive population and a reduction in the expression of *IL-6*, *KGA*, and *p16* (fig. S14A). BPTES treatment also improved glucose tolerance and insulin sensitivity in the obese mice (fig. S14B). Atherosclerosis of thoracic aorta in apolipoprotein E (ApoE) knockout mice (16-week-old mice) fed an atherogenic diet (AD) was alleviated by BPTES treatment with a reduced plaque numbers and lesions, accompanied by reduction in the expression of *p16*, *KGA*, and *IL-6* in abdominal aorta of the same mice (Fig. 4I and fig. S14C). In a nonalcoholic steatohepatitis model (16-week-old males), BPTES treatment also improved liver function, showing reduced concentrations of serum hydroxyproline and aspartate aminotransferase (fig. S14D). However, BPTES injection also modestly suppressed the rate of dorsal skin wound healing in mice (8-week-old males) (fig. S14E) (*30*). Overall, in addition to the clearance of SnCs, protection from senescence improved age- and senescence-associated pathogenesis.

Dysregulation of lysosomes had been proposed to be one of the senescent hallmarks. Mechanisms controlling both the quality and quantity of proteins play a pivotal role in the regulation of aging in vivo and in vitro, but precisely how the accumulation of unfolded proteins causes aging phenotypes both in cells and in the body remains enigmatic. Our results provide insights into the mechanisms underlying the relationship between protein quality control and aging in vivo. We developed a strategy for senolysis targeting a specific metabolic feature of SnCs. Elimination of SnCs and protection from senescence by inhibition of glutaminolysis in the aged body may ameliorate tissue microinflammation, prevent age-associated disorders, and even extend life span and rejuvenate an aging individual.

REFERENCES AND NOTES

1. B. G. Childs, M. Durik, D. J. Baker, J. M. van Deursen, *Nat. Med.* **21**, 1424–1435 (2015).
2. S. He, N. E. Sharpless, *Cell* **169**, 1000–1011 (2017).
3. M. Xu *et al.*, *Nat. Med.* **24**, 1246–1256 (2018).
4. M. P. Baar *et al.*, *Cell* **169**, 132–147.e16 (2017).
5. J. Chang *et al.*, *Nat. Med.* **22**, 78–83 (2016).
6. J. N. Justice *et al.*, *EBioMedicine* **40**, 554–563 (2019).
7. R. Yosef *et al.*, *Nat. Commun.* **7**, 11190 (2016).
8. Y. Johmura *et al.*, *Mol. Cell* **55**, 73–84 (2014).
9. A. R. Davalos *et al.*, *J. Cell Biol.* **201**, 613–629 (2013).
10. A. Freund, R. M. Laberge, M. Demaria, J. Campisi, *Mol. Biol. Cell* **23**, 2066–2075 (2012).
11. H. Ibrahim, Y. J. Lee, N. P. Curthoys, *Kidney Int.* **73**, 11–18 (2008).
12. G. Ince-Dunn *et al.*, *Neuron* **75**, 1067–1080 (2012).
13. J. M. Schroeder, H. Ibrahim, L. Taylor, N. P. Curthoys, *Am. J. Physiol. Renal Physiol.* **290**, F733–F740 (2006).
14. C. Vande Velde *et al.*, *Mol. Cell. Biol.* **20**, 5454–5468 (2000).
15. L. A. Kubasiak, O. M. Hernandez, N. H. Bishopric, K. A. Webster, *Proc. Natl. Acad. Sci. U.S.A.* **99**, 12825–12830 (2002).
16. M. L. Skowyra, P. H. Schlesinger, T. V. Naismith, P. I. Hanson, *Science* **360**, eaar5078 (2018).
17. P. Kotsantis *et al.*, *Nat. Commun.* **7**, 13087 (2016).
18. R. A. J. Signer, J. A. Magee, A. Salic, S. J. Morrison, *Nature* **509**, 49–54 (2014).
19. G. Napolitano, A. Ballabio, *J. Cell Sci.* **129**, 2475–2481 (2016).
20. J. G. Fleischer *et al.*, *Genome Biol.* **19**, 221 (2018).
21. K. M. Kim *et al.*, *Genes Dev.* **31**, 1529–1534 (2017).
22. Tabula Muris Consortium, *Nature* **583**, 590–595 (2020).
23. C. D. Wiley *et al.*, *Cell Metab.* **23**, 303–314 (2016).
24. L. Hecker *et al.*, *Sci. Transl. Med.* **6**, 231ra47 (2014).
25. M. Ogrodnik *et al.*, *Nat. Commun.* **8**, 15691 (2017).
26. D. J. Baker *et al.*, *Nature* **530**, 184–189 (2016).
27. M. De Cecco *et al.*, *Nature* **566**, 73–78 (2019).
28. A. K. Palmer *et al.*, *Aging Cell* **18**, e12950 (2019).
29. B. G. Childs *et al.*, *Science* **354**, 472–477 (2016).
30. M. Demaria *et al.*, *Dev. Cell* **31**, 722–733 (2014).

ACKNOWLEDGMENTS

We are grateful to A.-B. Shyu and S. A. Stewart for reagents and to C. Konishi, T. Ando, and T. Kanai for technical assistance. **Funding:** This study was supported by MEXT/JSPS KAKENHI under grant numbers JP26250027 (M.N.), JP22118003 (M.N.), JP16K15239 (M.N.), JP18H05026m (Y.J.), JP16H06148 (Y.J.), and JP16K15238 (Y.J.) and by AMED under grant numbers JP17cm0106122 (M.N.), JP17fk0310111 (M.N.), JP17gm5010001 (M.N.), and JP19gm5010003 (Y.S.), as well as by Ono Medical Research Foundation (M.N.), Princess Takamatsu Cancer Research Fund (M.N.), and Relay for Life Japan Cancer Society (M.N.). **Author contributions:** M.N. and Y.J. conceived the idea of the project; Y.J., T.Y., T.-W.W., Y.S., M.M., K.Y., R.Y., M.Sug., K.I.N., Y.F., S.I., and M.N. planned the experiments; Y.J., S.O., T.-W.W., Y.S., M.M., T.Y., N.S., S.K., K.Y., S.H., T.T., R.Y., E.S., K.I., N.O., R.M., M.Sue., and M.Sug. performed the experiments; Y.J., T.Y., T.-W.W., Y.S., M.M., K.Y., U.Y., M.Sue., M.Sug., M.A., K.I.N., Y.F., S.I., and M.N. analyzed the results; and M.N. and Y.J. wrote the manuscript with editing by all the other authors. **Competing interests:** M.N. and Y.J. are co-inventors on provisional patent application serial no. PCT/JP2019/043570: "Method for removing senescent cell, and method for preparing senescent cell." Y.J. is a shareholder and S.O. is a shareholder and CEO of Elixir Biotechnologies. All other co-authors declare that they have no competing interests. **Data and materials availability:** shRNA screening and RNA-seq data have been deposited in the Gene Expression Omnibus (GEO) under accession numbers GSE145414 and GSE138508, respectively. In vitro proteome-assisted multiple reaction monitoring for protein absolute quantification (iMPAQT) data have been deposited in the Japan Proteome Standard Repository (jPOSTrepo) under accession number JPST000730. All other data needed to evaluate the conclusions in the paper are presented in the paper and/or the supplementary materials. All materials are available from the corresponding authors.

SUPPLEMENTARY MATERIALS

science.sciencemag.org/content/371/6526/265/suppl/DC1
Materials and Methods
Figs. S1 to S14
Tables S1 to S3
References (*31*–*45*)
MDAR Reproducibility Checklist
Data S1 and S2

5 March 2020; resubmitted 14 September 2020
Accepted 13 November 2020
10.1126/science.abb5916

IMMUNOLOGY

GPER1 is required to protect fetal health from maternal inflammation

Alfred T. Harding[1], Marisa A. Goff[2], Heather M. Froggatt[1], Jean K. Lim[2], Nicholas S. Heaton[1,3]*

Type I interferon (IFN) signaling in fetal tissues causes developmental abnormalities and fetal demise. Although pathogens that infect fetal tissues can induce birth defects through the local production of type I IFN, it remains unknown why systemic IFN generated during maternal infections only rarely causes fetal developmental defects. Here, we report that activation of the guanine nucleotide–binding protein–coupled estrogen receptor 1 (GPER1) during pregnancy is both necessary and sufficient to suppress IFN signaling and does so disproportionately in reproductive and fetal tissues. Inactivation of GPER1 in mice halted fetal development and promoted fetal demise, but only in the context of maternal inflammation. Thus, GPER1 is a central regulator of IFN signaling during pregnancy that allows dynamic antiviral responses in maternal tissues while also preserving fetal health.

When pathogenic infections occur during pregnancy, the maternal immune system must respond and suppress pathogen replication without targeting the genetically heterologous fetus (*1*, *2*). In some cases, however, including during in utero infections, consequential fetal inflammation cannot be avoided, leading to birth defects and fetal demise (*3*–*5*). In particular, fetal type I interferon (IFN) signaling can be a major driver of developmental abnormalities (*4*, *5*). Many infections that are common during pregnancy, such as influenza A virus (IAV), induce systemic type I IFN and could cause fetal IFN signaling without local viral replication (*6*, *7*). Yet maternal IAV infections are rarely linked to birth defects (*8*, *9*). Thus, a mechanism may exist that allows IFN signaling in infected tissues while preventing maternal type I IFN from initiating signaling in the fetus.

To identify IFN regulators that could mediate differential IFN control across tissues, we performed genome-wide CRISPR-Cas9 screens in a human epithelial cell line with an IFN response reporter (fig. S1). After IFN treatment of the reporter cells and removal of the cytokine, we collected cells that aberrantly maintained fluorescence to identify the proteins required to down-regulate IFN signaling (Fig. 1A). Through bioinformatic analysis, we identified a number of genes that were enriched above the nontargeting sgRNA controls, including, as expected, proteasomal subunits that directly prevent green fluorescent protein degradation (Fig. 1B and table S1).

We used screen-enriched single-guide RNAs (sgRNAs) to target nine genes selected from among our top hits and saw that the targeting of six genes significantly prolonged IFN signaling (table S2). One of the validated screen hits, guanine nucleotide–binding protein–coupled estrogen receptor 1 (*GPER1*, also known as *GPR30*), is a nonclassical estrogen receptor (*10*) that was likely activated by fetal calf serum–derived estrogen during our screen. Because estrogen concentrations increase greatly during pregnancy (*11*, *12*), GPER1 had the potential to link pregnancy hormone levels to regulation of the IFN response. Because our initial *GPER1* validation was performed with a polyclonal population, we next verified our IFN reporter results with a clonal line (Fig. 1, C and D). We then made use of a GPER1-specific inhibitor, G15, which competitively blocks estrogen binding (*13*). In a dose-dependent manner, treatment with the inhibitor prevented appropriate down-regulation of the IFN response reporter (Fig. 1, E and F) as well as endogenous IFN-stimulated gene (ISG) mRNA transcripts (Fig. 1G). As expected, in our clonal GPER1 sgRNA line, G15 treatment did not significantly alter IFN signaling (Fig. 1H).

To determine whether GPER1 activity is sufficient to suppress IFN signaling, we overexpressed GPER1 (Fig. 2A). Without major alterations to cell viability (Fig. 2B and fig. S2), the IFN response was suppressed as measured by the IFN reporter as well as endogenous ISG RNA and protein levels (Fig. 2, C to H). We also used the GPER1 agonist G1, which specifically activates GPER1 (*14*). At a concentration that did not induce apparent cellular toxicity, G1 significantly reduced IFN signaling across a range of IFN treatment concentrations (Fig. 2, I and J). Finally, we tested individual estrogens to elucidate which natural GPER1 ligands can suppress IFN signaling. Consistent with previous reports describing GPER1 activation (*15*), estradiol (E2) and, to a much smaller extent, estrone (E1) could suppress the IFN response reporter, whereas estriol (E3) could not (Fig. 2K).

To determine which tissues might have biologically relevant GPER1 activity, we performed GPER1 protein immunoblots on tissues from pregnant mice. Consistent with the reports of GPER1 distribution in humans (*16*), expression was highest in the reproductive and fetal tissues, including the placenta (Fig. 3A). Because type I IFN signaling in the placenta has been implicated as a key determinant of fetal fate, we performed immunohistochemical analysis for the localization of GPER1 in the placenta. Although GPER1 was expressed in all of the major placental zones, we observed high expression in the cells that line the vascular labyrinth (Fig. 3B). Despite differences in blood supply architecture, GPER1 was also highly expressed in the cells that contact the maternal blood supply in human placental samples (fig. S3).

Elevated estrogen concentrations during pregnancy, combined with differential GPER1 expression across the maternal periphery and fetal tissues, suggested that GPER1 may mediate tissue-specific regulation of IFN signaling during pregnancy. We therefore used a murine pregnancy model of IAV infection, administering either the GPER1 inhibitor G15 or a vehicle control (Fig. 3C). Presumably because of relatively lower GPER1 expression in the respiratory tract, drug treatment had no major effects on maternal morbidity, the infectious viral titer, the lung transcriptional response, or the pulmonary inflammatory cytokine signature (Fig. 3, D to F, and figs. S4 and S5). Influenza disease in nonpregnant mice, at least in the C57BL/6 background, was similarly unaffected by G15 treatment (fig. S6).

By contrast, the placental response to maternal IAV infection (fig. S7) was significantly altered by G15 inhibition of GPER1 (Fig. 3G). These transcriptional changes were not attributable to G15 treatment allowing for viral dissemination from the respiratory tract (Fig. 3H). Instead, the inhibition of GPER1 during maternal infection led to the up-regulation of many, but not all, canonical ISGs and IFN-induced cytokines (*17*) such as CCL3 and CCL5, but not *Ifnb* itself (Fig. 3I and fig. S8). Our inability to detect the up-regulation of all ISGs was likely due to constitutive type III IFN responses in some regions of the placenta (*18*). Additionally, IFN treatment of primary human placental explants with and without G15 also led to increased ISG expression (fig. S9). Many non-IFN–regulated genes were also affected during G15 treatment and infection. Gene ontology of the suppressed genes revealed the enrichment of pathways involved in blood vessel development and angiogenesis (figs. S10 and S11), consistent with the reports of type I IFN signaling suppressing angiogenesis (*19*). As expected from the transcriptional data, we also observed an obvious attenuation or degradation of the placental endothelium when G15 was

[1]Department of Molecular Genetics and Microbiology, Duke University School of Medicine, Durham, NC 27710, USA. [2]Department of Microbiology, Icahn School of Medicine at Mount Sinai, New York, NY 10029, USA. [3]Duke Human Vaccine Institute, Duke University School of Medicine, Durham, NC 27710, USA.
*Corresponding author. Email: nicholas.heaton@duke.edu

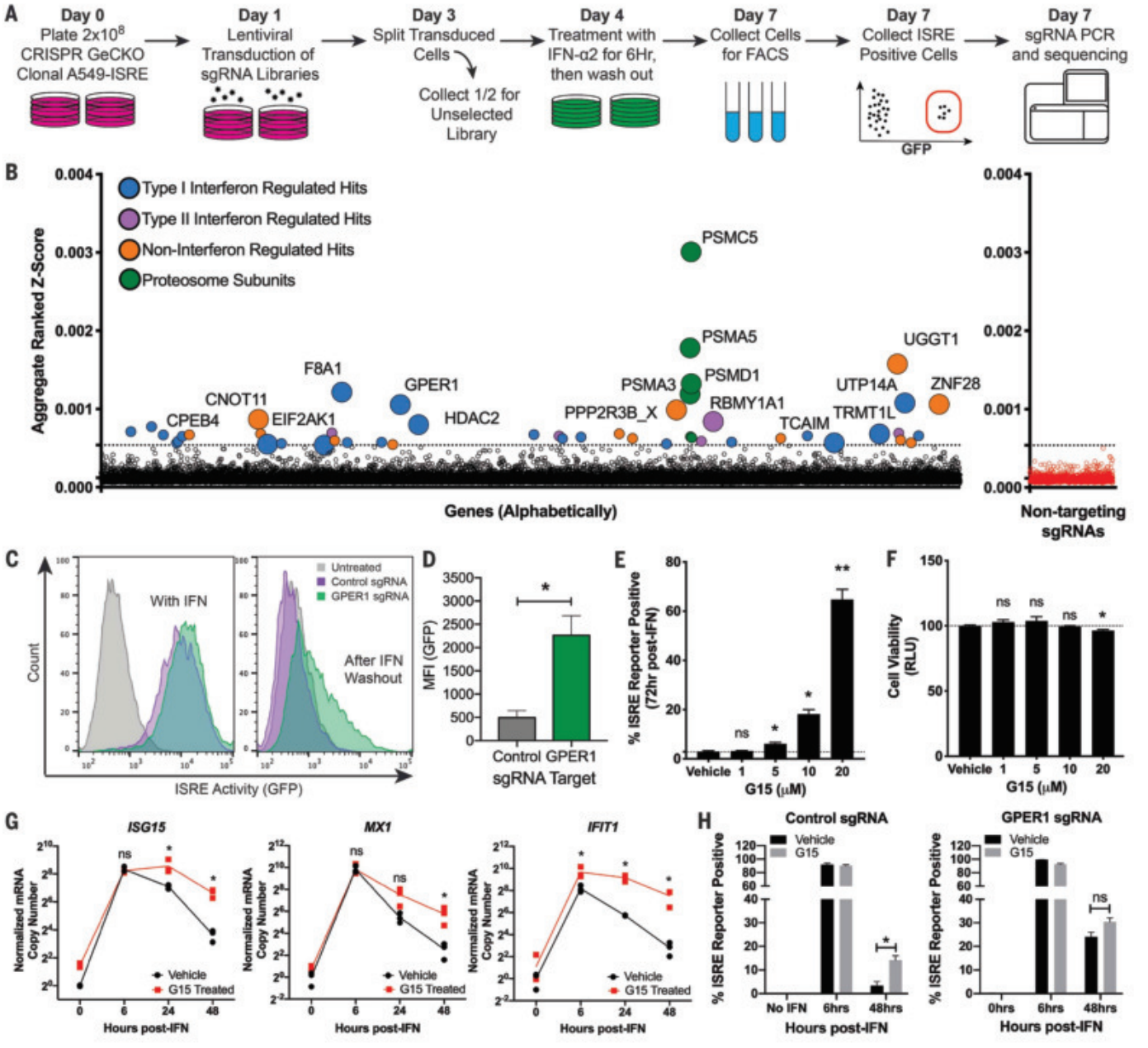


Fig. 1. A CRISPR screen identifies GPER1 as a negative regulator of the type I IFN response. (**A**) Schematic of the CRISPR genome-wide knockout screens. FACS, fluorescence-activated cell sorting; PCR, polymerase chain reaction. (**B**) Graphical representation of the screening results with candidate regulators (left) and the nontargeting controls (right). (**C**) Representative flow cytometry histograms of the IFN response during IFN-α2 treatment (left) and 48 hours after IFN-α2 removal (right) in the indicated cell lines. (**D**) Quantification of the mean fluorescence intensity from (C) at 48 hours after IFN-α2 treatment, sample size $n = 3$. GFP, green fluorescent protein; MFI, mean fluorescence intensity. (**E**) Percentage of IFN-stimulated response element (ISRE)–reporter–positive cells 72 hours after IFN-α2 treatment with the indicated concentrations of the GPER1 antagonist G15, $n = 3$. (**F**) Normalized cellular viability of the treatments in (E), $n = 3$. RLU, relative luciferase units. (**G**) Quantitative reverse transcription PCR (qRT-PCR) analysis of the indicated ISGs in vehicle- or G15-treated A549 cells after treatment with IFN-α2, $n = 3$. (**H**) Percent of the indicated cell lines that were ISRE reporter–positive at the indicated times after IFN-α2 treatment with or without G15 treatment, $n = 3$. All data are representative of at least two independent experiments. For all panels, error bars indicate the SEM, and statistical analyses were performed by means of unpaired Student's *t* tests. $^{*}P \leq 0.05$; $^{**}P \leq 0.001$; ns, not significant.

administered during IAV infection (Fig. 3, J and K, and fig. S12).

Next, we asked whether neonatal viability would be affected by these placental changes (Fig. 4A). Although again, there was no observable difference in maternal disease (Fig. 4, B and C), pup birth weight was modestly reduced by either viral infection or G15 treatment alone (Fig. 4D), which is consistent with a role for GPER1 in normal uterine function (*20*) and the effects of maternal influenza on fetal birth weight (*12*). However, the most severe reduction in birth weight was observed when G15 treatment occurred in the presence of IAV infection (Fig. 4D). Furthermore,

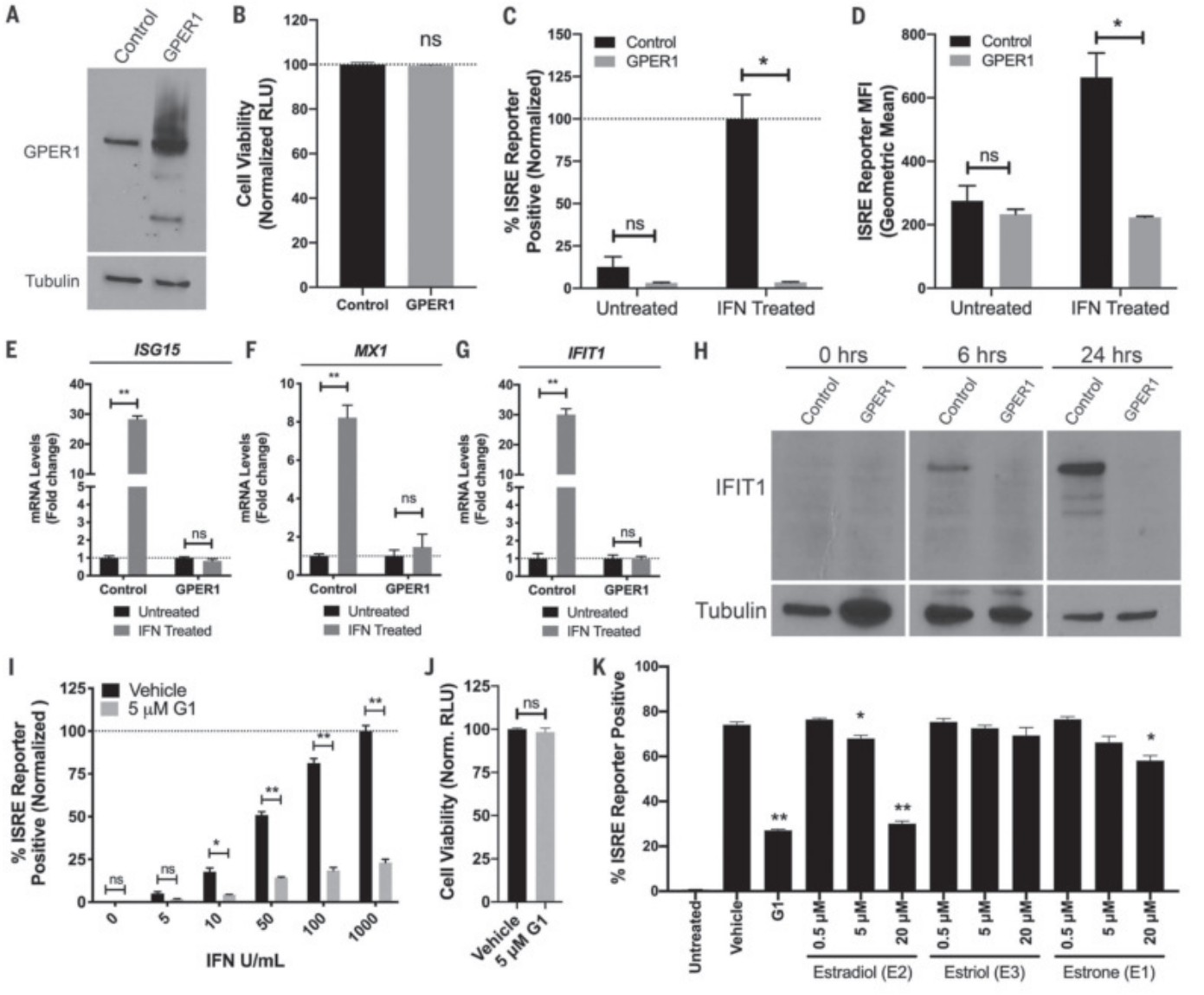


Fig. 2. GPER1 activity is sufficient to suppress the type I IFN response. (**A**) Protein immunoblots of GPER1 and tubulin in control or GPER1-overexpressing 293T cells. (**B**) Viability of 293T cells 18 hours after transfection with either a control or GPER1 expression plasmid, $n = 3$. (**C**) Percentage of 293T cells positive for the ISRE reporter after expression of the indicated protein, $n = 3$. (**D**) Quantification of the mean fluorescence intensity from (C). (**E** to **G**) qRT-PCR analysis of the indicated ISGs after IFN-α2 treatment of 293T cells expressing GPER1 or a control protein, $n = 3$. (**H**) Protein immunoblots of IFIT1 and tubulin after IFN-α2 treatment in 293T cells. (**I**) Percentage of reporter-positive ISRE-A549 cells after IFN-α2 and vehicle or G1 treatment, $n = 3$. (**J**) Cellular viability from (I), $n = 3$. (**K**) Percent of reporter-positive ISRE-A549 cells after treatment with IFN-α2 and the indicated concentrations of estradiol, estriol, or estrone, $n = 3$. All data are representative of at least two independent experiments. For all panels, error bars indicate SEM, and statistical analyses were performed by means of unpaired Student's t tests. $^*P \le 0.05$; $^{**}P \le 0.001$; ns, not significant.

although the number of pups in each litter was similar across treatment groups, only those pups born to IAV-infected, G15-treated dams were predominantly stillborn (Fig. 4, E to G). Analogous experiments using *Gper1*$^{-/-}$ mice revealed similar viability phenotypes (fig. S13).

Making use of immunocompetent Zika virus (*21*) and influenza B virus mouse pregnancy models, we again observed that G15 treatment exacerbated virus-induced fetal developmental defects (figs. S14 and S15). As a nonviral approach to induce systemic inflammation, we also treated pregnant dams with the viral RNA mimic polyinosinic:polycytidylic acid poly(I:C). Although this treatment by itself negatively affected fetal development, we could exacerbate the effects with G15 and, conversely, promote neonatal viability with the GPER1 agonist G1 (fig. S16). Finally, to experimentally link GPER1 activity to control of IFN signaling, we treated pregnant mice with poly(I:C) in the presence of either control or IFN alpha and beta receptor (IFNAR)–blocking antibodies (Fig. 4H). Administration of the IFNAR-blocking antibody mostly suppressed the negative effects of poly(I:C) and G15 on fetal development (Fig. 4, I and J). Thus, GPER1 activity is largely dispensable even when maternal inflammation is present, provided that type I IFN signaling has been blocked.

We propose a model whereby GPER1 is a central regulator of type I IFN signaling during pregnancy that protects fetal health without compromising peripheral maternal IFN responses. The effects of systemic or "nonlocal" type I IFN have not generally been

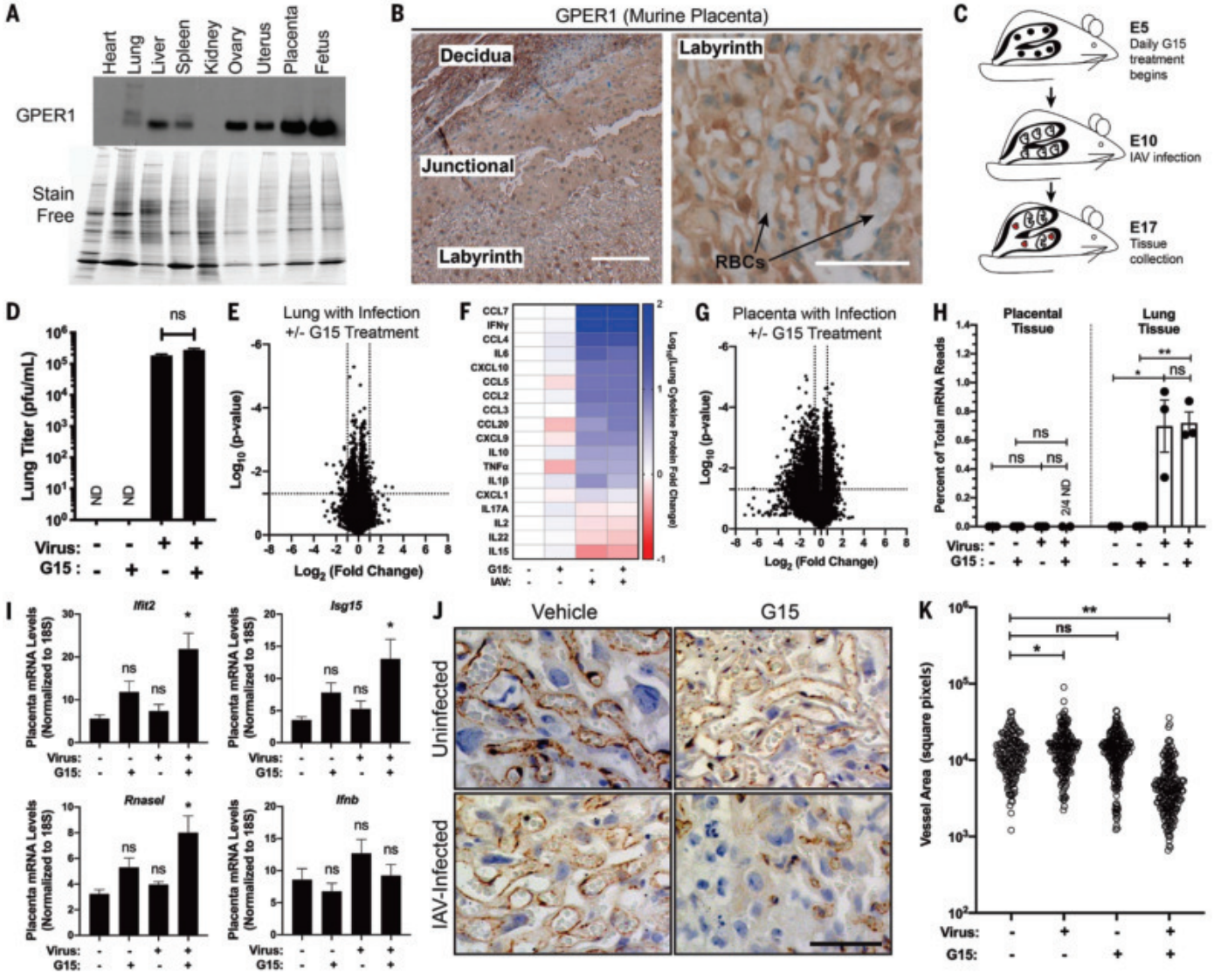


Fig. 3. GPER1 mediates placenta tissue–specific IFN regulation during an influenza virus infection. (**A**) Protein immunoblot for GPER1 on the indicated samples collected from one animal, representative of two mice. (**B**) Representative (n = 4) immunohistochemical staining for GPER1 expression in the mouse placenta. Scale bars, 200 μm (left) and 75 μm (right). RBC, red blood cell. (**C**) Experimental diagram related to panels (D) to (K). E5, embryonic day 5. (**D**) Lung IAV titers from pregnant dams, treated as indicated, 7 days after infection, n = 3. (**E**) Volcano plot of RNA sequencing from the lungs of infected pregnant dams ± G15 treatment. (**F**) Heatmap comparing the relative protein levels of cytokines in lungs described in (D). (**G**) Volcano plot of RNA sequencing from the placentas of infected pregnant dams ± G15 treatment. (**H**) Percent of total RNA sequencing reads that align to the A/Puerto Rico/8/1934 genome from the indicated tissues and treatments, $n \geq 3$ samples analyzed. (**I**) qRT-PCR analysis of ISG mRNA from the placental samples used for RNA sequencing, $n \geq 3$. (**J**) Representative images of CD31 staining of the placental labyrinth from the indicated treatments. Scale bar, 50 μm. (**K**) Quantification of the blood vessel area from the CD31 staining described in (J), $n \geq 180$. For panels (A) and (B), data are representative of at least two independent experiments. In panels (D) to (F) and (H), samples were collected from $n \geq 3$ independently treated animals per group and analyzed or sequenced once. In panels (G to K), $n \geq 3$ placentas were collected from multiple pregnancies and analyzed or sequenced once. For all panels, error bars indicate SEM, and statistical analyses were performed by means of unpaired Student's t tests except for panel (K), which used one-way analysis of variance (ANOVA) and post hoc Dunnett's multiple comparisons test. $^*P \leq 0.05$; $^{**}P \leq 0.001$; ND, not detected; ns, not significant.

appreciated as an important mediator of fetal disease. Our data argue that without GPER1-mediated suppression of IFN signaling, many maternal infections would have notable consequences for fetal health. Recent studies have highlighted the deleterious consequences for placental vasculature and syncytiotrophoblast formation after fetal type I IFN signaling (*4*, *5*). Our findings expand upon those results by identifying a regulatory mechanism for fetal IFN signaling.

Nevertheless, a number of important questions remain unresolved. First, the mechanism by which GPER1 prevents IFN signaling remains unknown. GPER1 activation has been reported to alter cyclic adenosine monophosphate levels, mediate extracellular signal–regulated kinase (ERK) 1/2 activation through epidermal growth factor receptor (EGFR) signaling, and activate the phosphatidylinositol 3-kinase (PI3K)–Akt pathways (*22*). At least in our in vitro system, treatment with the well-characterized EGFR and PI3K inhibitors erlotinib and LY294002 failed to reverse the G1-mediated

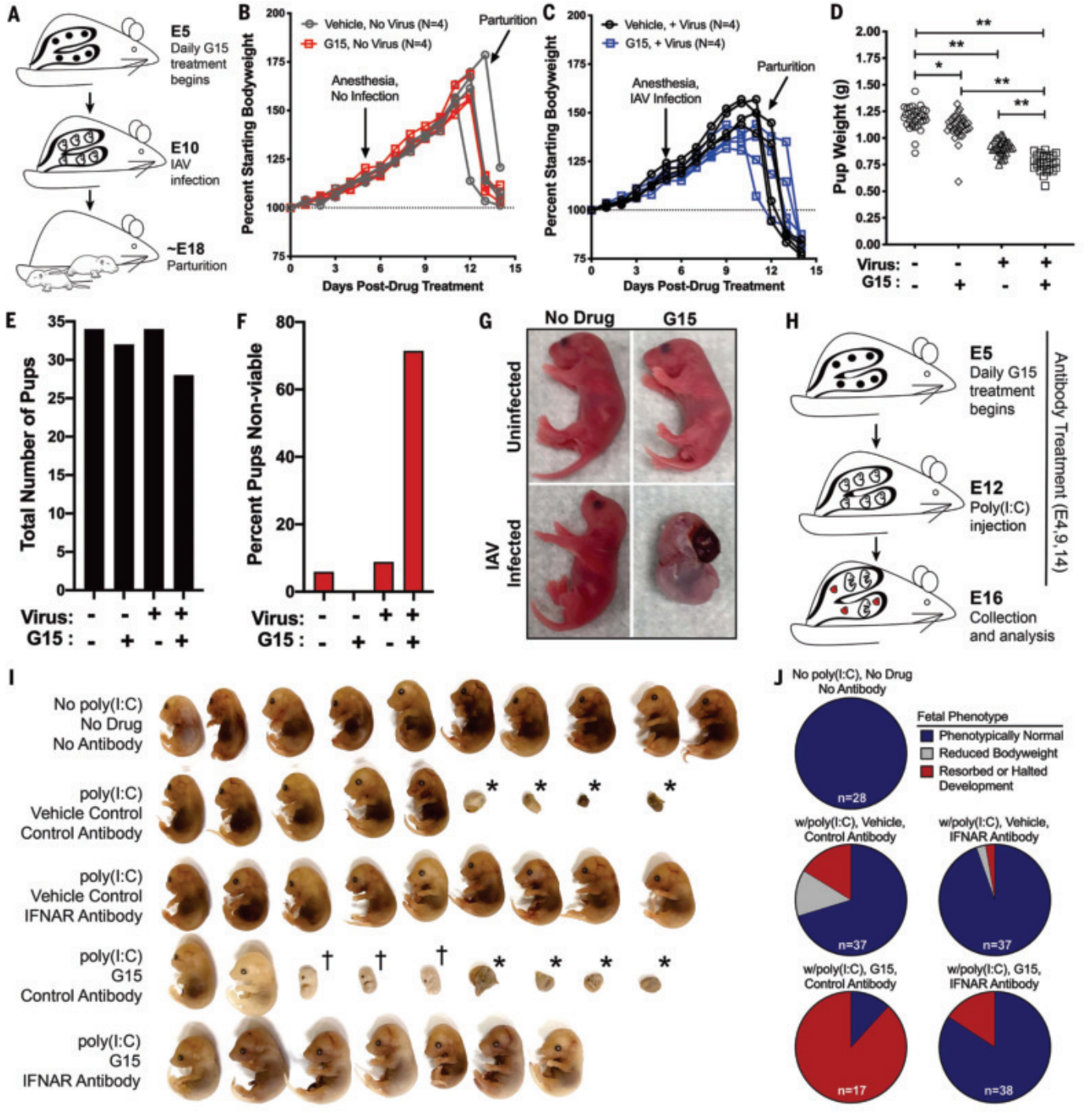


Fig. 4. GPER1 protects fetal development through its regulation of the type I IFN signaling pathway. (**A**) Experimental diagram related to panels (B) to (G). (**B** and **C**) Bodyweight changes of vehicle- or G15-treated, uninfected (B) or IAV-infected (C) pregnant dams. (**D**) Weight in grams of pups immediately after birth from the indicated treatment groups, $n \geq 25$, $^{*}P \leq 0.05$, $^{**}P \leq 0.001$ as per one-way ANOVA and post hoc Tukey's multiple comparisons test. (**E**) Total number of pups from (B) and (C). (**F**) Percentage of pups scored nonviable from (E). (**G**) Images of representative pups from each of the indicated treatment groups. (**H**) Experimental diagram related to panels (I) to (J). (**I**) One representative litter from each of the indicated treatment groups collected on E16. Resorbed fetuses are marked with * and developmentally halted fetuses with †. (**J**) Pie charts indicating the total number of fetuses analyzed and the developmental phenotypes, related to panel (I). All results are representative of at least two independent experiments.

suppression of IFN signaling, potentially implicating other pathways downstream of GPER1 (fig. S17). Also, alterations in GPER1 activity may induce changes in classical estrogen receptor signaling, which could then ultimately influence IFN regulation. Additionally, it will be important to understand why the GPER1-mediated suppression of IFN signaling is insufficient to protect from damage during infection with pathogens that replicate in fetal tissues (*23*). Future studies will be required to definitively answer this question, but we

hypothesize that GPER1 activity can be overwhelmed by relatively high concentrations of IFN at the sites of active pathogen replication.

Finally, on the basis of our experiments with G1, one might speculate that the therapeutic activation of GPER1 signaling could be used to protect fetal health. Although activation of the classical estrogen receptors can influence adult influenza disease (*24*), GPER1 can be targeted independently of the other estrogen receptors (*13*, *14*). Thus, without compromising maternal immunity, the induction of GPER1 activity may be able to prevent a range of developmental conditions linked to maternal infection and/or fetal inflammation (*25*), independent of their underlying etiologies, by targeting the commonality of inappropriate type I IFN signaling.

REFERENCES AND NOTES

1. K. Racicot, J. Y. Kwon, P. Aldo, M. Silasi, G. Mor, *Am. J. Reprod. Immunol.* **72**, 107–116 (2014).
2. G. Mor, I. Cardenas, V. Abrahams, S. Guller, *Ann. N. Y. Acad. Sci.* **1221**, 80–87 (2011).
3. C. B. Coyne, H. M. Lazear, *Nat. Rev. Microbiol.* **14**, 707–715 (2016).
4. L. J. Yockey *et al.*, *Sci. Immunol.* **3**, eaao1680 (2018).
5. J. Buchrieser *et al.*, *Science* **365**, 176–180 (2019).
6. Y. Nagaoka *et al.*, *Dis. Markers* **2017**, 2594231 (2017).
7. M. T. McClain *et al.*, *Clin. Exp. Immunol.* **183**, 441–451 (2016).
8. C. Hansen *et al.*, *J. Infect. Dis.* **206**, 1260–1268 (2012).
9. S. A. McNeil *et al.*, *Am. J. Obstet. Gynecol.* **204**, S54–S57 (2011).
10. C. M. Revankar, D. F. Cimino, L. A. Sklar, J. B. Arterburn, E. R. Prossnitz, *Science* **307**, 1625–1630 (2005).
11. R. De Hertogh, K. Thomas, J. J. Hoet, I. Vanderheyden, *Diabetologia* **12**, 455–461 (1976).
12. M. A. Pazos, T. A. Kraus, C. Muñoz-Fontela, T. M. Moran, *PLOS ONE* **7**, e40502 (2012).
13. M. K. Dennis *et al.*, *Nat. Chem. Biol.* **5**, 421–427 (2009).
14. C. G. Bologa *et al.*, *Nat. Chem. Biol.* **2**, 207–212 (2006).
15. P. Thomas, Y. Pang, E. J. Filardo, J. Dong, *Endocrinology* **146**, 624–632 (2005).
16. M. Uhlén *et al.*, *Science* **347**, 1260419 (2015).
17. M. Nakano *et al.*, *Clin. Exp. Immunol.* **170**, 94–100 (2012).
18. A. Bayer *et al.*, *Cell Host Microbe* **19**, 705–712 (2016).
19. Y. A. Sidky, E. C. Borden, *Cancer Res.* **47**, 5155–5161 (1987).
20. T. Tropea *et al.*, *PLOS ONE* **10**, e0141997 (2015).
21. M. J. Gorman *et al.*, *Cell Host Microbe* **23**, 672–685.e6 (2018).
22. E. R. Prossnitz, M. Barton, *Prostaglandins Other Lipid Mediat.* **89**, 89–97 (2009).
23. B. J. Stegmann, J. C. Carey, *Curr. Womens Health Rep.* **2**, 253–258 (2002).
24. D. P. Robinson, M. E. Lorenzo, W. Jian, S. L. Klein, *PLOS Pathog.* **7**, e1002149 (2011).
25. L. J. Yockey, A. Iwasaki, *Immunity* **49**, 397–412 (2018).

ACKNOWLEDGMENTS

We thank B. Heaton and B. Cullen for reagents and helpful discussion. We also thank B. Hughes, K. Weaver, B. Antczak, and the staff of the Carolina Cord Blood Bank. Additionally, we acknowledge support from the Duke Pathology Core, the Duke Cancer Institute Flow Cytometry Core, the Duke Light Microscopy Core Facility, and the Duke Sequencing and Genomic Technologies Core. **Funding:** A.T.H. was supported by an NIH training grant (T32-CA009111). M.A.G. was supported by an NIH training grant (T32-AI07647). J.K.L. is partially supported by the National Institute of Allergy and Infectious Disease (R21AI139593, R21AI144844, and R01AI150837). N.S.H. is partially supported by the National Institute of Allergy and Infectious Disease (R01AI37031), the National Heart Lung and Blood Institute (R01HL142985), and an Individual Biomedical Research Award from The Hartwell Foundation. **Author contributions:** A.T.H., N.S.H., and J.K.L. designed experiments; A.T.H., M.A.G., H.M.F., and J.K.L. performed experiments and collected data; N.S.H., A.T.H., and J.K.L. analyzed data; and A.T.H. and N.S.H. wrote the manuscript. **Competing interests:** The authors declare no competing interests. **Data and materials availability:** Raw sequencing files and mapped read counts are available at NCBI GEO under accession number GSE143432. The plasmids for encoding the fluorescent IFN response reporter and those for expression of GPER1, as well as the PR8 strain of the IAV, are available from the corresponding author under a Material Transfer Agreement with Duke University. All other data are available in the manuscript or the supplementary materials.

SUPPLEMENTARY MATERIALS

science.sciencemag.org/content/371/6526/271/suppl/DC1
Materials and Methods
Figs. S1 to S17
Tables S1 and S2
References (*26*–*32*)
MDAR Reproducibility Checklist
Data S1

14 January 2020; resubmitted 23 July 2020
Accepted 4 December 2020
10.1126/science.aba9001

PLANT SCIENCE

Plant roots sense soil compaction through restricted ethylene diffusion

Bipin K. Pandey[1]*, Guoqiang Huang[2]*, Rahul Bhosale[1], Sjon Hartman[3,4], Craig J. Sturrock[1], Lottie Jose[1], Olivier C. Martin[5], Michal Karady[6], Laurentius A. C. J. Voesenek[3], Karin Ljung[7], Jonathan P. Lynch[8], Kathleen M. Brown[8], William R. Whalley[9], Sacha J. Mooney[1], Dabing Zhang[2,10]†, Malcolm J. Bennett[1]†

Soil compaction represents a major challenge for modern agriculture. Compaction is intuitively thought to reduce root growth by limiting the ability of roots to penetrate harder soils. We report that root growth in compacted soil is instead actively suppressed by the volatile hormone ethylene. We found that mutant *Arabidopsis* and rice roots that were insensitive to ethylene penetrated compacted soil more effectively than did wild-type roots. Our results indicate that soil compaction lowers gas diffusion through a reduction in air-filled pores, thereby causing ethylene to accumulate in root tissues and trigger hormone responses that restrict growth. We propose that ethylene acts as an early warning signal for roots to avoid compacted soils, which would be relevant to research into the breeding of crops resilient to soil compaction.

Soil compaction affects global crop cultivation by reducing root penetration in both the upper and deeper soil layers (*1*). Modern agricultural practices have exacerbated soil compaction, largely because of intensification of operations leading to the deployment of heavier machinery and tillage practices (*2*, *3*), severely degrading ~65 million hectares of land globally (*4*). Compaction increases soil bulk density and reduces soil porosity, limiting the availability and transport of water and nutrients (*4*, *5*). The decrease in soil pore space, especially in large air-filled pores (Fig. 1, A to D, figs. S1 and S2, and movies S1 and S2), also restricts diffusion of gases between roots and the rhizosphere (*6*). To deal with compacted soils and penetrate cracks, roots are reported to undergo adaptive growth responses, including increased radial expansion of root tips (*1*). However, the predominant response of roots is cessation of growth, for which the mechanistic basis remains unclear. Here, we report that entrapped ethylene functions as a key signal regulating root growth in compacted soils.

Ethylene is produced by root tissues, and its level increases when roots are exposed to compacted soil (*7*, *8*). Ethylene concentrations outside the root could increase as a result of the reduction in soil pore space in compacted soil, which affects gas diffusion from root tissues (Fig. 1, A to D, and figs. S1 and S2). To test this "restricted gas diffusion" model, we used the EIN3-GFP (green fluorescent protein) *Arabidopsis* ethylene response reporter (*9*) (fig. S3, A to C) and examined the effect of covering root tips with a gas-impermeable barrier. In agreement with model assumptions, restricting gas diffusion from root tip tissues triggered a rapid and sustained increase in EIN3-GFP in root elongation zone cell nuclei relative to controls (Fig. 1F versus Fig. 1E; fig. S3, D to G). This result is consistent with (i) limitation of ethylene release from root tip tissues and (ii) changes in gas diffusion rate between roots and the external environment,

[1]School of Biosciences, University of Nottingham, Sutton Bonington LE12 5RD, UK. [2]Joint International Research Laboratory of Metabolic and Developmental Sciences, School of Life Sciences and Biotechnology, Shanghai Jiao Tong University, Shanghai 200240, China. [3]Plant Ecophysiology, Institute of Environmental Biology, Utrecht University, 3584 CH Utrecht, Netherlands. [4]School of Biosciences, University of Birmingham, Birmingham B15 2TT, UK. [5]Universities of Paris-Saclay, Paris and Evry, CNRS, INRAE, Institute of Plant Sciences Paris-Saclay (IPS2), Bât. 630, 91192 Gif-sur-Yvette, France. [6]Laboratory of Growth Regulators, Institute of Experimental Botany of the Czech Academy of Sciences and Faculty of Science of Palacký University, CZ-78371 Olomouc, Czech Republic. [7]Department of Forest Genetics and Plant Physiology, Umeå Plant Science Centre, Swedish University of Agricultural Sciences, Umeå, Sweden. [8]Department of Plant Science, Pennsylvania State University, University Park, PA 16802, USA. [9]Rothamsted Research, West Common, Harpenden AL5 2JQ, UK. [10]School of Agriculture, Food and Wine, Waite Research Institute, University of Adelaide, Waite Campus, Glen Osmond, South Australia 5064, Australia.
*These authors contributed equally to this work.
†Corresponding author. Email: malcolm.bennett@nottingham.ac.uk (M.J.B.); zhangdb@sjtu.edu.cn (D.Z.)

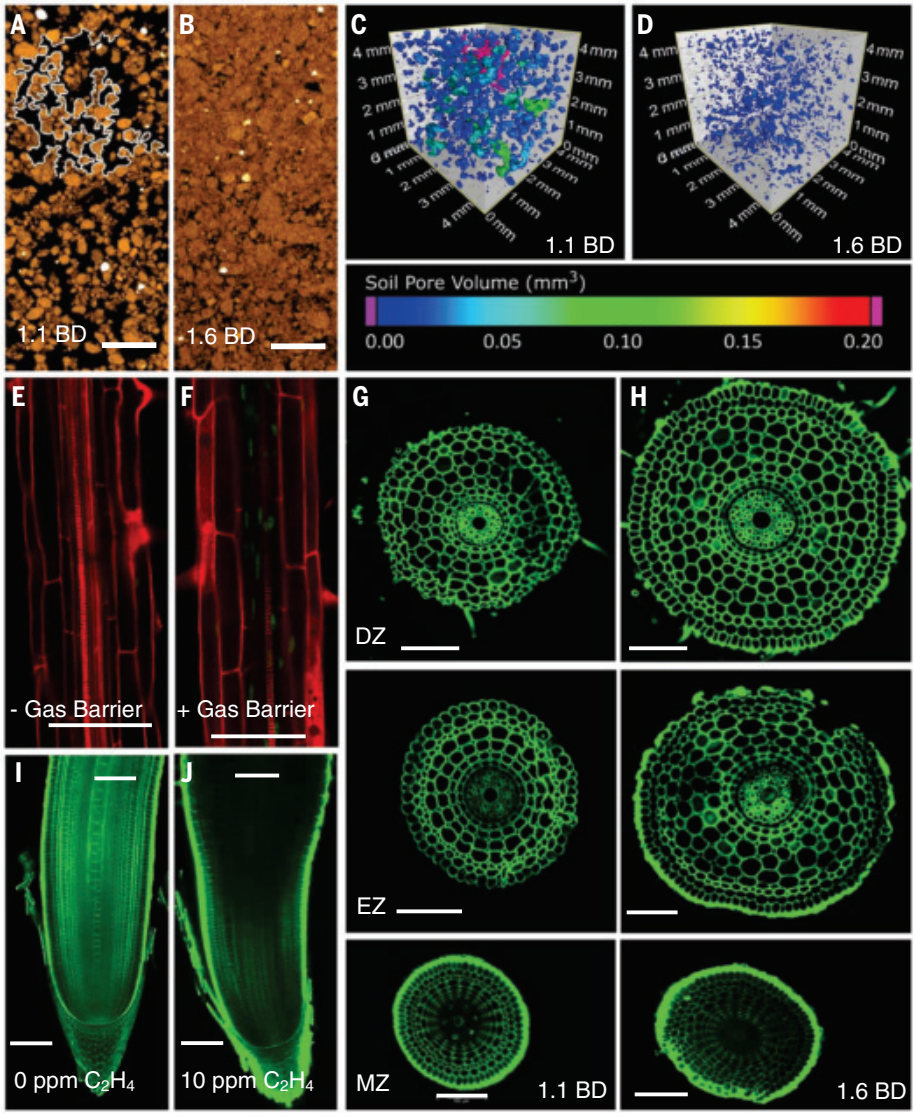


Fig. 1. Soil compaction reduces the larger pores and triggers root growth responses mimicking ethylene treatment. (**A** and **B**) CT images showing higher porosity (outlined in white) in uncompacted [1.1 g cm^{-3} bulk density (BD)] (A) versus compacted soil (1.6 BD) (B). (**C** and **D**) Representative three-dimensional images of air-filled soil pores for a 100 × 100 × 100 voxel region from 1.1 BD (C) and 1.6 BD (D) soil cores. (**E** and **F**) *Arabidopsis* EIN3-GFP reporter exhibits elevated signal after covering root tip with high-vacuum silicone grease (+Gas Barrier) for 10 hours (F) relative to control (−Gas Barrier) (E). (**G** and **H**) Confocal images of radial cross sections of rice primary roots through meristem (MZ), elongation (EZ), and differentiation (DZ) zones grown in 1.1 BD (G) and 1.6 BD (H) soils. (**I** and **J**) Relative to control rice roots (I), roots treated with 10 ppm ethylene exhibit cortical cell expansion (J), mimicking the effect of compacted soil conditions (H). Scale bars, 1.25 mm [(A) and (B)], 100 μm [(E) to (J)].

inducing ethylene accumulation and signaling. To rule out that changes in ethylene signaling were related to reduced oxygen levels in root tip tissues, we treated roots expressing the hypoxia markers *pPCO1:GFP-GUS*, *pPCO2:GFP-GUS* (*10*), and *RAP2.12-GFP* (*11*) with the gas-impermeable barrier. Hypoxia reporters were not induced by the gas barrier but were induced by submergence (figs. S4 to S6). We conclude that EIN3-GFP induction results from restricted ethylene diffusion rather than from hypoxic conditions (*11*).

Roots exposed to elevated levels of ethylene exhibited growth inhibition (Fig. 1, I and J), which phenocopied the impact of soil compaction (Fig. 1, G and H). We observed that rice roots grown in 1.1 g cm^{-3} (uncompacted) versus 1.6 g cm^{-3} (compacted) soil bulk densities exhibited reduced root length when exposed to compacted conditions (fig. S7, A and B). Root anatomical analysis revealed that compaction caused a factor of 3 decrease in epidermal cell length (fig. S7C), matched by a factor of 3 increase in cortical cell diameter (compare Fig. 1, G and H, and fig. S7D). Similarly, ethylene treatment reduced root length (fig. S8A) while increasing root width (Fig. 1, I and J) by decreasing epidermal cell length and increasing cortical cell diameter (fig. S8, B and C).

To directly test the functional importance of ethylene during soil compaction, we examined root growth responses of wild-type rice versus ethylene-insensitive mutants *osein2* and *oseil1* (*12*). *OsEIN2* (*ETHYLENE INSENSITIVE2*) encodes a key ethylene signaling component (*13*). *OsEIL1* (*EIN3-like 1*) encodes a critical transcription factor in the ethylene transduction pathway downstream of OsEIN2 (*9*). Mutations in rice *OsEIN2* and *OsEIL1* genes confer ethylene-insensitive root elongation phenotypes (*12*) (fig. S9, A and B). To analyze the impact of soil compaction on wild-type versus *osein2* root growth, we grew rice lines in columns entirely filled with either uncompacted soil (1.1 g cm^{-3}) or highly compacted soil (1.6 g cm^{-3}, with a 1-cm top layer packed at 1.1 g cm^{-3} to help establish seedling root growth). Penetrometer resistance analysis demonstrated that the root elongation rate was sensitive to increased soil strength (fig. S10).

To quantify the impact of soil compaction on root length of wild-type versus ethylene mutant lines, we used computed tomography (CT; Fig. 2, A to G). CT imaging revealed that unlike the wild type (Fig. 2B), both *osein2* and *oseil1* roots were able to penetrate highly compacted soil (Fig. 2, D and F; quantified in Fig. 2G). This result reveals that ethylene signaling is critical for triggering root growth responses upon soil compaction. Anatomical analysis of rice mutant roots further demonstrated that under compacted soil conditions,

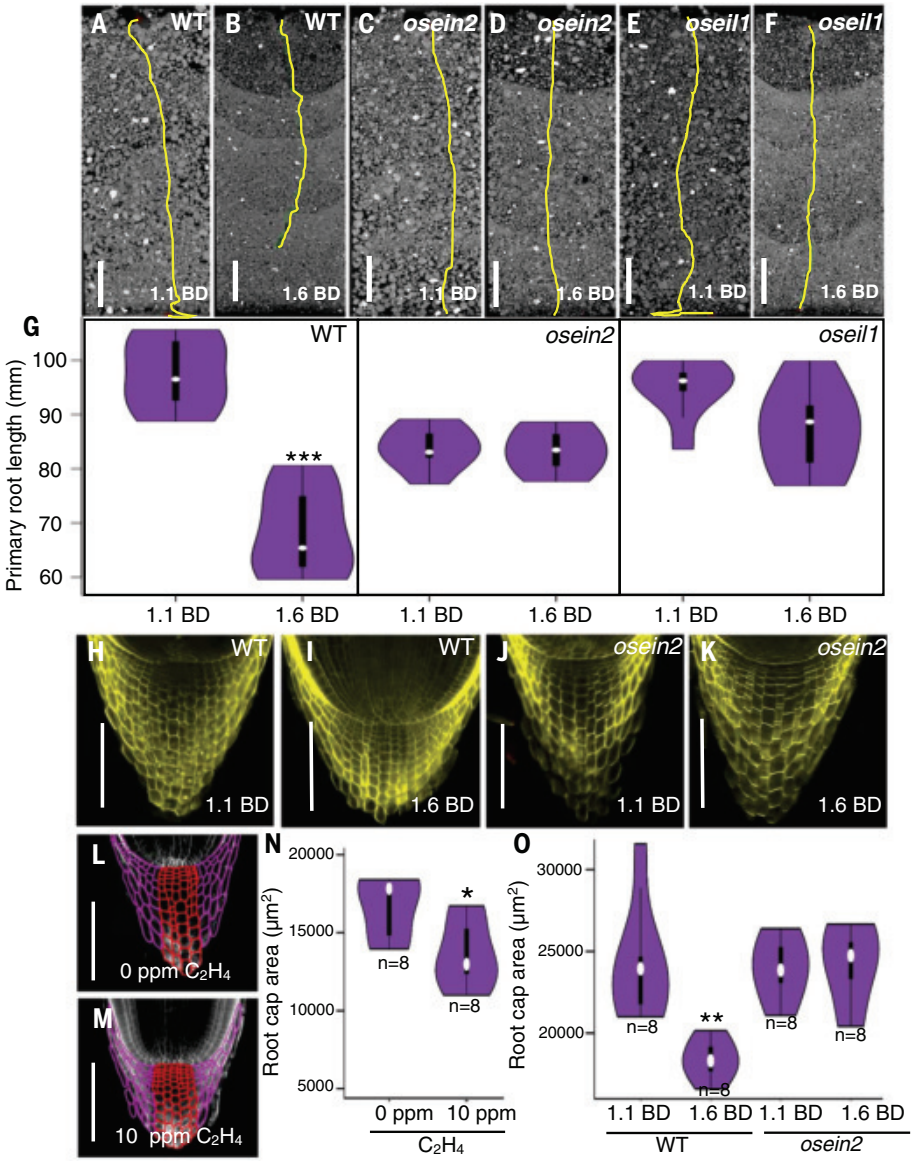


Fig. 2. Disrupting ethylene response in rice confers root growth resistance to compacted soil. (**A** to **F**) CT images of primary roots of wild-type (WT) [(A) and (B)], *osein2* [(C) and (D)], and *oseil1* [(E) and (F)] in 1.1 BD [(A), (C), and (E)] versus 1.6 BD [(B), (D), and (F)]. (**G**) Violin plots of primary root length in uncompacted (1.1 BD) versus compacted (1.6 BD) conditions for WT, *osein2*, and *oseil1* rice seedlings. (**H** to **K**) Representative images showing root cap area in WT [(H) and (I)] and *osein2* [(J) and (K)] in 1.1 BD [(H) and (J)] versus 1.6 BD [(I) and (K)] soils. (**L** and **M**) Ethylene treatment of WT roots showing reduction in root cap area [(M) versus (L)]. (**N**) Violin plots showing reduction of root cap area after ethylene treatment. (**O**) Violin plots showing reduction of root cap area of WT but not *osein2* roots when grown in 1.6 BD versus 1.1 BD soils. Columella cells are marked in red [(L) and (M)]. $^{*}P \le 0.05$, $^{**}P \le 0.001$, $^{***}P \le 0.0001$ (Student's *t* test). Scale bars, 10 mm [(A) to (F)], 100 μm [(H) to (M)].

osein2 and *oseil1* root epidermal cells continued to elongate normally, whereas cortical cells did not undergo radial expansion (figs. S11 and S12) relative to the wild type (fig. S13). Moreover, this growth response also occurred in other classes of roots: Primary and lateral root growth and cortical responses induced by soil compaction were blocked in the ethylene-insensitive *Arabidopsis* mutant *etr1* (figs. S14 to S17). Similarly, ethylene-insensitive mutants in rice (*osein2* and *oseil1*) and *Arabidopsis* (*ein3eil1*) accumulated significantly higher shoot and root biomass in compacted soil conditions relative to the wild type (figs. S18 and S19). Hence, our rice and *Arabidopsis* mutant analysis revealed that ethylene plays an inhibitory role in both monocot and eudicot root (and shoot) tissues when experiencing soil compaction.

Our results suggest that reduced root growth triggered by soil compaction does not arise from mechanical impedance, but instead represents a timely response controlled by ethylene, perhaps to avoid growth in compacted soils (*14*). To discriminate between the effects mediated by mechanical impedance and by ethylene, we compared their impact on root tip shape. Soil compaction caused wild-type rice roots to double in width and their root caps to develop a "flattened" shape (compare Fig. 2, H and I). Soil compaction–induced radial growth and root cap shape changes were blocked in *osein2* (Fig. 2, J, K, and O). Hence, root tip shape changes induced by soil compaction appear to be controlled primarily by ethylene and not by mechanical impedance. Indeed, ethylene treatment alone was sufficient to trigger equivalent changes in root width (Fig. 1, I and J, and fig. S8, B and C) and cap shape (Fig. 2, L to N, and fig. S20) similar to roots exposed to soil compaction. Therefore, in plants, ethylene represents a critical signal controlling shape changes that underpin root compaction responses.

Given ethylene's functional importance during root responses to compaction, we investigated whether soil mechanical impedance triggered increased ethylene signaling in root tissues. We used transgenic *Arabidopsis* and rice expressing either an ethylene biosensor featuring *EIN3* (*9*) or *OsEIL1* sequences fused with GFP (fig. S21). In uncompacted soil, *35S:EIN3-GFP* or *proOsEIL1:OsEIL1-GFP* reporters in root nuclei were not detectable (Fig. 3, A and D). However, when reporter lines were grown in compacted soil, both ethylene reporters were detected in root elongation zone cells (Fig. 3, B, C, and E). To probe the role of ethylene in other soil types, we grew rice reporter lines in two contrasting soils. Compaction triggered a root ethylene response in clay soil (figs. S21 and S22) and sandy loam

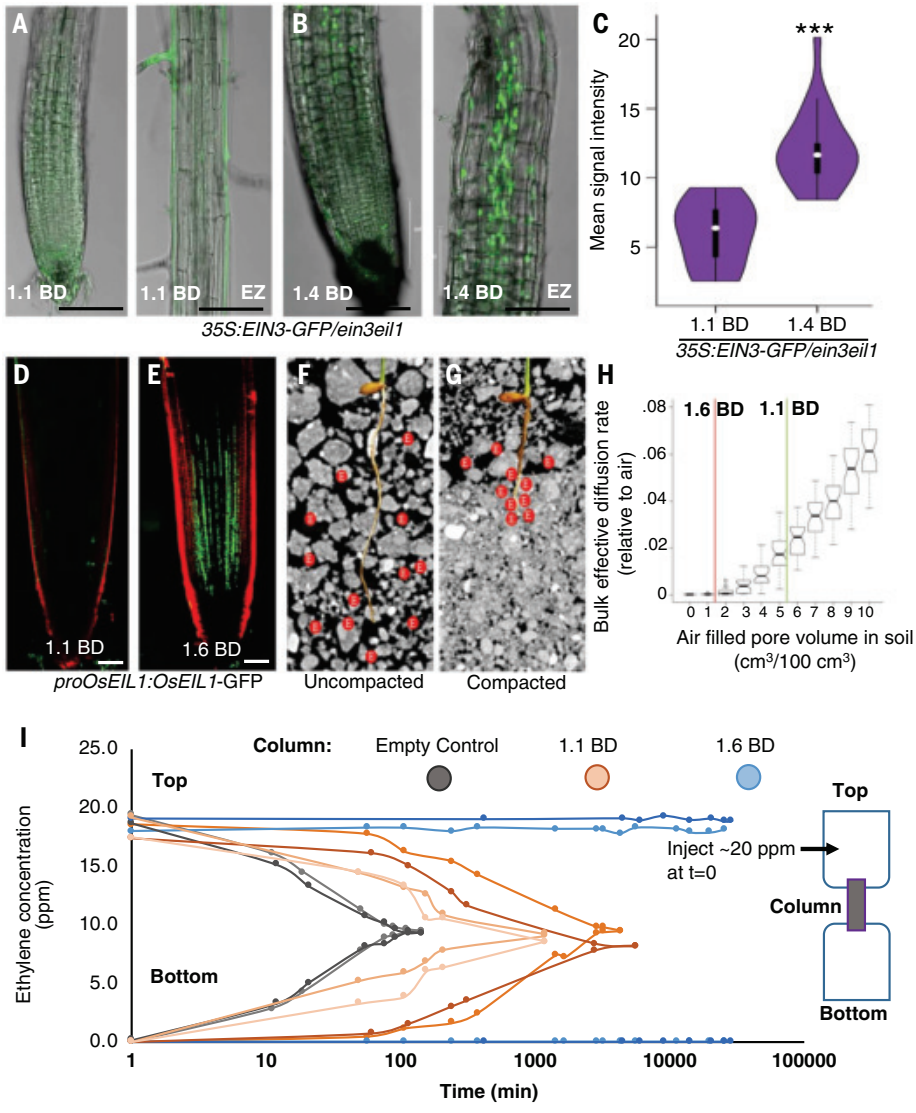


Fig. 3. Compacted soil reduces ethylene diffusion and enhances root ethylene signaling. (**A** and **B**) *Arabidopsis* ethylene reporter EIN3-GFP exhibits no nuclear GFP signal when grown in uncompacted soil (1.1 BD) (A) but is clearly detected in root EZ (elongation zone) cells when grown in compacted soil (1.4 BD) (B). (**C**) Violin plot of GFP signal in 1.1 BD versus 1.4 BD soil in EZ of *35S:EIN3-GFP/ein3eil1*. (**D** and **E**) Relative to 1.1 BD soil (D), a rice OsEIL1-GFP–based ethylene translational reporter exhibits elevated signal in compacted (1.6 BD) soil (E). (**F** and **G**) Schematic figures of ethylene diffusion (denoted by red circles) in uncompacted (F) versus compacted (G) soil, illustrating preferential accumulation of ethylene around and in root tissues. (**H**) Model simulation showing rate of bulk diffusion of ethylene in soil pores in uncompacted (green line) and compacted (red line) soil. (**I**) Graphical representation of quantification of ethylene across 1.1 BD and 1.6 BD soil layers (1 cm). After 20 ppm of ethylene was injected in the top chamber, we used gas chromatography–mass spectrometry to measure ethylene diffusion in the bottom chamber across empty, uncompacted (1.1 BD), and compacted (1.6 BD) soils. ***$P \leq 0.0001$ (Student's t test).

soil (Fig. 3E and fig. S23). Hence, the ethylene-based compaction mechanism appears to operate in different soil types.

How does soil compaction induce elevated ethylene signaling in root tissues? Mechanical impedance could cause roots to up-regulate ethylene synthesis. Profiling of the ethylene precursor 1-aminocyclopropane-1-carboxylic acid (ACC) in excised rice root tips detected no change in levels after growth in compacted soil versus uncompacted controls (fig. S24). Alternatively, plant roots may sense soil compaction by monitoring ethylene levels. Mathematical modeling predicted slower outward ethylene diffusion rates under compacted soil conditions (Fig. 3H and fig. S25) due to the decreased volume of air-filled pores (*1*) (Fig. 1, A to D, and movies S1 and S2). This will result in a higher ethylene concentration close to roots (Fig. 3, F and G) and therefore in root cells, consistent with soil compaction triggering an ethylene response (Fig. 3, B, C, and E).

We directly tested whether soil compaction restricted gas diffusion by experimentally measuring ethylene's ability to move through compacted versus uncompacted soil. A 1-cm-thick soil column (connecting two air-filled chambers) was either left empty (control) or filled with uncompacted soil (1.1 g cm^{-3}) or compacted soil (1.6 g cm^{-3}) (Fig. 3I and fig. S25B). Ethylene was injected into the upper chamber (an increase in pressure was avoided) and ethylene concentrations were subsequently measured over time in the lower chamber until an equilibrium was reached between the chambers. In agreement with gas diffusion simulations, ethylene levels rapidly reached an equilibrium with the lower chamber in control conditions without soil resistance (Fig. 3I). Ethylene was also able to diffuse through uncompacted soil, albeit more slowly than the empty control by a factor of 10 to 50; in contrast, ethylene was unable to diffuse through compacted soil and was still undetectable in the lower chamber at 20 days (Fig. 3I). This result demonstrates that soil compaction (and the associated increase in soil moisture due to decreased porosity) affects ethylene diffusion rates, consistent with our restricted gas diffusion model. This much slower ethylene diffusion in compacted soil results in an enhanced ethylene response in root cells. This entrapped ethylene gas provides a fast and reliable signal for plants to interact with their environment, because nearly all roots produce ethylene under normoxic conditions (*15*).

Our results reveal how roots regulate growth responses to soil compaction. First, the inhibition of root growth by compacted soils is triggered by ethylene signaling, rather than simply by mechanical forces. Second, rather than using a dedicated mechano-perception mechanism, roots appear to sense soil compaction through restricted diffusion of this gaseous signal from the plant cells to the soil, causing ethylene to accumulate in root expansion zone cells and inhibiting elongation

growth. Third, compaction and soil moisture status appear to have an impact on root elongation, not only because they control soil strength, but also through regulating ethylene diffusion. Fourth, we propose that ethylene acts as an early warning signal for roots to avoid compacted soils (*14*); if so, this could provide a pathway for how breeders might select crops resilient to soil compaction.

REFERENCES AND NOTES

1. J. Correa, J. A. Postma, M. Watt, T. Wojciechowski, *J. Exp. Bot.* **70**, 6019–6034 (2019).
2. B. D. Soane, J. W. Dickson, D. J. Campbell, *Soil Tillage Res.* **2**, 3–36 (1982).
3. S. Mangalassery *et al.*, *Sci. Rep.* **4**, 1–8 (2014).
4. M. A. Hamza, W. K. Anderson, *Soil Tillage Res.* **82**, 121–145 (2005).
5. R. Horn, H. Domżżał, A. Słowińska-Jurkiewicz, C. Van Ouwerkerk, *Soil Tillage Res.* **35**, 23–36 (1995).
6. T. Fujikawa, T. Miyazaki, *Soil Sci.* **170**, 892–901 (2005).
7. A. Hussain, C. R. Black, I. B. Taylor, J. A. Roberts, *Plant Physiol.* **121**, 1227–1238 (1999).
8. I. Potocka, J. Szymanowska-Pulka, *Ann. Bot.* **122**, 711–723 (2018).
9. F. An *et al.*, *Plant Cell* **22**, 2384–2401 (2010).
10. D. A. Weits *et al.*, *Nature* **569**, 714–717 (2019).
11. S. Hartman *et al.*, *Nat. Commun.* **10**, 4020 (2019).
12. B. Ma *et al.*, *Mol. Plant* **6**, 1830–1848 (2013).
13. J. M. Alonso, T. Hirayama, G. Roman, S. Nourizadeh, J. R. Ecker, *Science* **284**, 2148–2152 (1999).
14. K. D. Montagu, J. P. Conroy, B. J. Atwell, *J. Exp. Bot.* **52**, 2127–2133 (2001).
15. F. J. Romera, E. Alcantara, M. D. De la Guardia, *Ann. Bot.* **83**, 51–55 (1999).

ACKNOWLEDGMENTS

We thank R. Ashton for performing soil penetrometer assays; D. Weijers, X. Draye, and D. Grierson for advice while drafting the manuscript; J. Dewick and P. Mehra for assisting with its submission; O. van de Beek, H. Siekman, and M. Krijnen of Jobshop, Utrecht University, for designing and creating the ethylene diffusion device; J. Zhang for providing rice *oseil1/mhz6-1*, *osein2/mhz7-1*, and *proOsEIL1:GUS*; and F. Licausi for *PCO1/2:GFP-GUS* and X. Zhou for *Arabidopsis ein3eil1* lines. **Funding:** Supported by Biotechnology and Biological Sciences Research Council (BB/G023972/1, BB/R013748/1, BB/L026848/1, BB/M018431/1, BB/P016855/1, BB/M001806/1, BB/M012212, and BB/P016855/1); ERC FUTUREROOTS Advanced grant 294729; Future-Food Beacon and Challenge Grant–Royal Society (CHG\R1\170040) (B.K.P.); National Key Technologies Research and Development Program of China, Ministry of Science and Technology grants 2016YFD0100804 and 2016YFE0101000, and National Natural Science Foundation of China grants 31970803 and 31861163002 (D.Z.); China Postdoctoral Science Foundation Project (2019M661486) and Shanghai Post-doctoral Excellent Program (2018063) (G.H.); BBSRC Discovery and Future Food Beacon Nottingham Research Fellowships (R.B.); NWO grant 824.14.007 (S.H.); Saclay Plant Sciences-SPS (ANR-17-EUR-0007) (O.C.M.); Czech Science Foundation (20-25948Y) (M.K.); and the Swedish Foundation for Strategic Research, the Swedish Research Council, and the Knut and Alice Wallenberg Foundation (K.L.). **Author contributions:** B.K.P., G.H., R.B., S.H., L.A.C.J.V., J.P.L., K.M.B., W.R.W., S.J.M., K.L., D.Z., and M.J.B. designed experiments; B.K.P., G.H., R.B., S.H., L.J., C.J.S., and M.K. performed experiments; O.C.M. performed modeling; and B.K.P., G.H., D.Z., and M.J.B. wrote the manuscript. **Competing interests:** The authors declare no competing interests. **Data and materials availability:** No restrictions are placed on materials, such as materials transfer agreements. Details of all data, code, and materials used in the analysis are available in the main text or the supplementary materials.

SUPPLEMENTARY MATERIALS

science.sciencemag.org/content/371/6526/276/suppl/DC1
Materials and Methods
Figs. S1 to S25
Movies S1 and S2
References (*16*–*20*)
MDAR Reproducibility Checklist

16 October 2020; accepted 8 December 2020
10.1126/science.abf3013

PLASMONIC CHEMISTRY

Driving energetically unfavorable dehydrogenation dynamics with plasmonics

Katherine Sytwu[1], Michal Vadai[2], Fariah Hayee[3], Daniel K. Angell[2], Alan Dai[4], Jefferson Dixon[5], Jennifer A. Dionne[2]*

Nanoparticle surface structure and geometry generally dictate where chemical transformations occur, with higher chemical activity at sites with lower activation energies. Here, we show how optical excitation of plasmons enables spatially modified phase transformations, activating otherwise energetically unfavorable sites. We have designed a crossed-bar Au-PdH_x antenna-reactor system that localizes electromagnetic enhancement away from the innately reactive PdH_x nanorod tips. Using optically coupled in situ environmental transmission electron microscopy, we track the dehydrogenation of individual antenna-reactor pairs with varying optical illumination intensity, wavelength, and hydrogen pressure. Our in situ experiments show that plasmons enable new catalytic sites, including dehydrogenation at the nanorod faces. Molecular dynamics simulations confirm that these new nucleation sites are energetically unfavorable in equilibrium and only accessible through tailored plasmonic excitation.

Nanoparticle (NP) phase transformations and their transient states underlie many technologies in energy storage, memory, and catalysis (*1*–*3*). These intermediate states support distinct electronic and material configurations from equilibrium that have enabled novel reaction pathways for alloying and chemical reactions (*4*, *5*). However, modifying these phase transformation dynamics requires bridging the length-scale gap between the atomic-scale structural features (i.e., atomic coordination number, surface strain, etc.) that influence dynamics and the macroscale extrinsic parameters (i.e., temperature, chemical environment, etc.) that can be controlled.

Optical excitation of localized surface plasmon resonances (LSPRs) offers a solution for overcoming this size mismatch. LSPRs create regions of high electromagnetic field intensity, or electromagnetic (EM) "hotspots," which underpin increased chemical kinetics seen in plasmon photocatalysis and plasmon-driven NP growth (*6*–*8*). LSPRs can also modify electronic and molecular energy levels and enable access to excited-state dynamics, opening new reaction pathways that are difficult or impossible to achieve under typical conditions (*9*). As the spatial distribution of EM hotspots is determined by NP geometry, LSPRs could provide the required nanoscale spatial control over transient states, reshaping the energy landscape of reactants, intermediates, and products (*10*).

[1]Department of Applied Physics, Stanford University, 348 Via Pueblo, Stanford, CA 94305, USA. [2]Department of Materials Science and Engineering, Stanford University, 496 Lomita Mall, Stanford, CA 94305, USA. [3]Department of Electrical Engineering, Stanford University, 350 Jane Stanford Way, Stanford, CA 94305, USA. [4]Department of Chemical Engineering, Stanford University, 443 Via Ortega, Stanford, CA 94305, USA. [5]Department of Mechanical Engineering, Stanford University, 440 Escondido Mall, Stanford, CA 94305, USA.
***Corresponding author. Email: jdionne@stanford.edu**

Here, we provide a proof-of-concept demonstration that LSPRs can enable new transient states in NP transformations, specifically the dehydrogenation of palladium hydride (PdH_x) from its hydrogen-rich β-phase ($x \sim 0.6$) to a hydrogen-poor α-phase ($x \sim 0.01$). Our system concentrates EM enhancement at a site where chemical activity is inherently less favored, showing that LSPRs can transform a normally nonreactive NP surface facet into the preferred reaction site, in contrast to other studies in which the regions of plasmonic enhancement overlap with regions of high innate chemical activity. By exploring this intersection, we show how chemical hotspots can be tuned to coincide with the optical EM hotspot (*10*).

To demonstrate this result, it is crucial to simultaneously achieve sufficient spatial information to resolve NP features, temporal resolution to identify transient events, and chemical information to distinguish material transformations. Techniques such as super-resolution chemical imaging (*11*), ex situ NP markers (*6*), and environmental electron spectroscopy (*7*) have pushed toward simultaneous recording of spatial, temporal, and chemical information with high resolution at the nanoscale. We used optically coupled environmental transmission electron microscopy (TEM) (*12*) (Fig. 1A) to track the phase transition in situ in individual NPs with ~100-ms temporal resolution under various illumination conditions and gas pressures.

The dehydrogenation phase transition is controlled by the surrounding temperature and chemical potential (i.e., H_2 pressure) and at 246 K is endothermic (enthalpy change $\Delta H > 0$) and nonspontaneous (free energy change $\Delta G \gg k_B T$, where k_B is the Boltzmann constant and T is temperature). We used light to excite LSPRs to overcome the energetic activation barrier from the thermodynamically stable

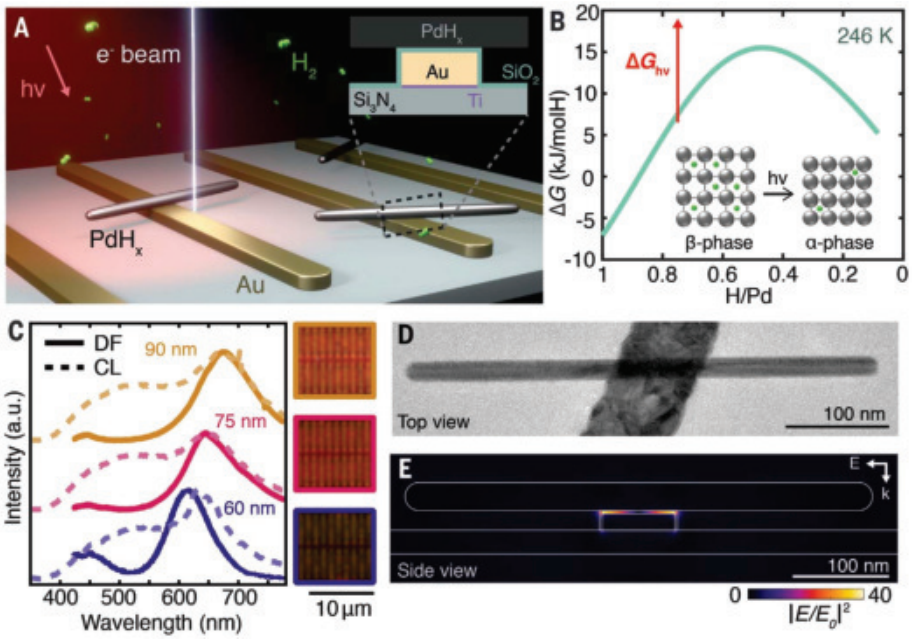


Fig. 1. The plasmonic Au-PdH$_x$ crossed-bar nanostructure. (**A**) Schematic of the experiment in real space, with the inset showing a cross-sectional view of the intersection between the Au nanobar and PdH$_x$ nanorod. (**B**) Schematic of the experiment in energy space, showing the Gibbs free energy of formation for PdH$_x$ at 246 K, calculated using a mean-field lattice gas model with finite size corrections (see methods) and the excited plasmon overcoming the energy barrier. (**C**) Dark-field optical (DF) and cathodoluminescence (CL) spectra of SiO_2-coated Au nanobars of varying width (60 to 90 nm) and their corresponding dark-field optical images (right). The CL spectra are of the structure with Pd NPs scattered on top. a.u., arbitrary units. (**D**) TEM image showing a top-down view of a single Au-Pd crossed-bar nanoparticle system. (**E**) Cross-sectional view of the simulated electromagnetic enhancement of the Au-Pd system on resonance under transverse excitation. E is the electric field polarization direction, and k is the wave vector.

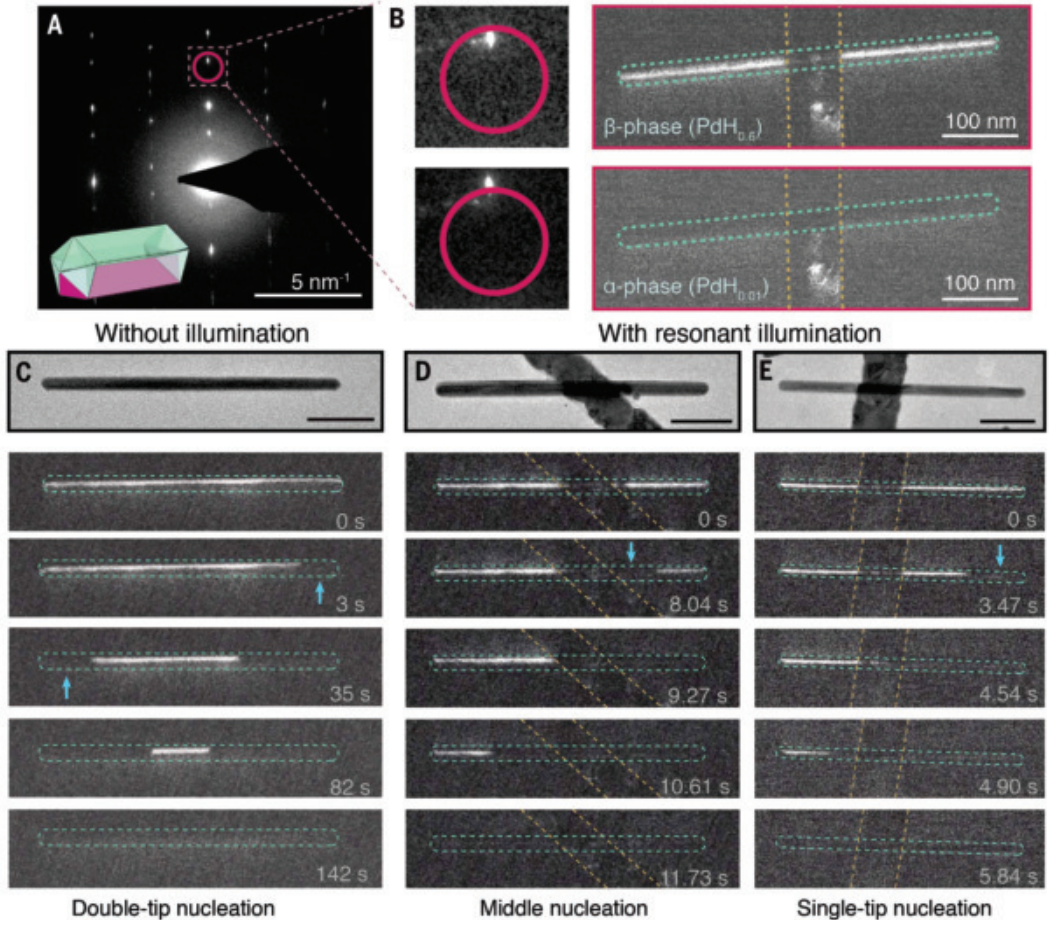


Fig. 2. Live displaced-aperture dark-field (DADF) imaging of the PdH$_x$ dissociation dynamics. (**A**) Electron diffraction pattern of a pentatwinned PdH$_x$ nanorod. The pink circle designates the approximate location of the objective aperture around the (220) diffraction point for DADF imaging, with inset schematic highlighting the corresponding bottom crystallite. (**B**) Zoom-in of the diffraction points relative to the actual position of the objective aperture (pink) and corresponding DADF image of the nanorod in β-phase (top) and α-phase (bottom). (**C**) TEM image and DADF snapshots of the dehydrogenation mechanism of a 498-nm PdH$_x$ nanorod without illumination, with blue arrows indicating nucleation sites. Time labels refer to the time from the first nucleation event. See fig. S6 for more examples. (**D** and **E**) TEM and DADF snapshots of the dehydrogenation mechanism of the Au-PdH$_x$ system under resonant illumination [(D) 627 nm with 50-nm bandwidth and (E) 640 nm with 20-nm bandwidth] for (D) a 446-nm nanorod at 75 Pa of H_2 gas and (E) a 447-nm nanorod at 70 Pa of H_2 gas. Time labels refer to the time from the start of illumination. Aqua and yellow dashed lines serve as guides-to-the-eye of nanoparticle boundaries. All scale bars are 100 nm.

β-phase to the metastable α-phase (Fig. 1B). Experimental studies have reported this activation barrier to span from 20 to 80 kJ/mol H (0.2 to 0.8 eV) (*13*, *14*), which can be readily overcome by visible-frequency photons.

The plasmonic antenna-reactor structure consisted of a 60- to 90-nm-wide plasmonic Au nanobar antenna surrounded by a thin 2-nm SiO_2 spacer layer and a PdH_x nanorod crossed on top. This geometry spatially separated the EM hotspots from the favorable nucleation sites at the NP tips (*15*, *16*). The Au nanobars are lithographically patterned onto a Si_3N_4 TEM grid and support a transverse-mode dipolar LSPR whose resonant wavelength ranges from 600 to 680 nm with varying nanobar width, as seen in the dark-field optical images and spectra in Fig. 1C and verified with simulations (fig. S5). Next, colloidally synthesized pentatwinned Pd nanorods 350 to 550 nm in length were drop-cast onto the prefabricated TEM grid, and the crossed geometry was randomly formed (Fig. 1D). Cathodoluminescence (CL) spectra of the structure with the drop-cast Pd NPs (Fig. 1C) revealed a broad shoulder from 400 to 600 nm originating from the Si_3N_4 substrate and a LSPR peak in agreement with the dark-field optical spectra. A slight shift in the LSPR peak for the 60-nm-wide Au nanobars was caused by electron beam–induced radiative defects in the SiO_2 (fig. S7). At the crossing junction, the transverse dipolar LSPR mode transformed into a gap LSPR mode, resulting in EM hotspots localized in the gap between the Pd nanorod and Au nanobar (Fig. 1E).

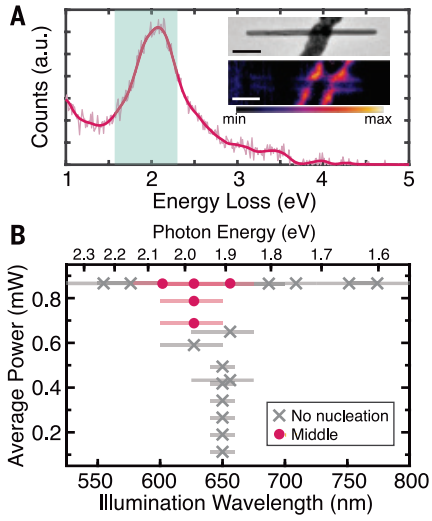


Fig. 3. Illumination dependence of nucleation site. (**A**) Electron energy loss spectra of the LSPR mode (pink is smoothed spectra), with the corresponding TEM image and EELS map of the NP (top and bottom inset, respectively). Aqua shaded region indicates the illumination range in the nucleation site experiments in (B). All scale bars are 100 nm. (**B**) Nucleation site of the α-phase for various illumination wavelengths and powers on the Au-PdH_x pair in (A) in 77 Pa of H_2 gas. Bars show the illumination bandwidth.

To track the dehydrogenation, we used displaced-aperture dark-field (DADF) imaging to exploit the 2 to 3% decrease in lattice parameter as the NP transformed from the β- to the α-phase (*17*). After setting the temperature and hydrogen pressure such that the NP was stable in the hydrogenated β-phase (see methods), we placed an objective aperture around a diffraction point of the PdH_x nanorod (Fig. 2A) to obtain a dark-field image of the bottom PdH_x nanorod crystallite (Fig. 2B, top). Upon transformation to the α-phase, the lattice shrinks and shifts the diffraction point outside the aperture such that the DADF image could not be formed (Fig. 2B, bottom). We used this presence or absence of the DADF image as a real-time proxy for the NP hydrogenation state.

By continually dropping the hydrogen pressure (see methods), we tracked the natural dehydrogenation pathway of an isolated PdH_x nanorod (Fig. 2C). The DADF images showed the right nanorod tip transforming into α-phase, and then a second nucleation from the opposite tip after 35 s, until the NP was fully transformed into the α-phase. In eight measurements of five isolated PdH_x nanorods, we exclusively observed nucleation of the α-phase growing from both ends of the NP, herein referred to as double-tip nucleation. Our prior measurements of the thermodynamic hydrogenation behavior of long nanorods showed that Pd nanorods at these lengths (>350 nm) were more likely to nucleate their new phase at both tips (*16*). Not only were the tips the active site for our dissolution process, but PdH_x nanorods of this length energetically preferred two nucleation sites.

The addition of plasmonic hotspots modified the dehydrogenation behavior. We set the H_2 partial pressure such that the nanorods were kinetically trapped in the β-phase. Using a tunable pulsed laser, we illuminated the sample near its resonant wavelength and tracked the response of a single crossed-bar system. For some nanorods, the middle section of the PdH_x nanorod, near the EM hotspot, dehydrogenated first (Fig. 2D), showing one phase front propagating toward the nearest nanorod tip, followed by the opposite phase front propagating toward the other end. We also observed nanorods that upon illumination dehydrogenated exclusively from one of the tips (Fig. 2E) but, unlike the dark condition, did not have a second nucleation event at the opposite tip.

This single-tip nucleation was not spatially correlated with the EM hotspot, suggesting that the optical hotspot was not the sole determinant of where a reaction happens. Given the differences in experimental setup, the kinetics with and without illumination cannot be quantitatively compared, but we note that the plasmon-driven dehydrogenation process was faster, in agreement with our prior observations of PdH_x nanocubes (*12*). Furthermore, upon turning illumination off, some observed particles immediately switched back to β-phase, indicating that this phase transition is indeed driven by the optical illumination rather than only electron-beam excitation (fig. S8).

Wavelength-dependent studies verified that this process was driven by optically excited plasmons. We tracked the nucleation site in two individual Au-PdH_x pairs as a function of illumination wavelength and power to confirm LSPR dependence. By comparing electron energy loss spectroscopy (EELS) measurements with wavelength-dependent nucleation dynamics of the same nanobar system, we found that middle nucleation only occurs for illumination wavelengths that overlap with the LSPR of the crossed-bar structure. For example, in Fig. 3A, the LSPR mode peaked at 2.07 eV (599 nm), and its corresponding EELS map verified its transverse LSPR origin. When the system was then illuminated, the nanorod only underwent middle nucleation for illumination from 575 to 675 nm, that is, near the LSPR peak (Fig. 3B). This result was also consistent with the faster reaction times observed under 600-nm center illumination (fig. S11).

Illumination at higher photon energies but the same power did not induce middle nucleation, confirming that resonance conditions are needed and that the phase transition was not mainly driven by an absorption process (i.e., the radiative defect in SiO_2, laser heating, etc.). Likewise, at lower illumination powers, we did not observe nucleation of the dehydrogenated phase at the resonant illumination wavelength, suggesting a threshold power to induce the phase transition. The possibility of a threshold power is further supported by the observation of off-resonant illumination initiating a phase transition at higher powers than on-resonant illumination (fig. S12).

This plasmon-induced behavior not only depended on the LSPR characteristics but also the thermodynamic state of the PdH_x nanorod, indicated by the surrounding hydrogen pressure. To isolate the role of inherent thermodynamics, we tracked the nucleation site in 22 Au-PdH_x pairs under constant resonant illumination but at various H_2 pressures, six of which are highlighted in Fig. 4A (additional statistics are shown in fig. S14). As individual NPs had different dehydrogenation pressures and illumination intensities (fig. S13 and table S2), we can only quantitatively compare across a single Au-PdH_x pair, not across NPs.

Under illumination, we observed five different phase transition mechanisms: no phase

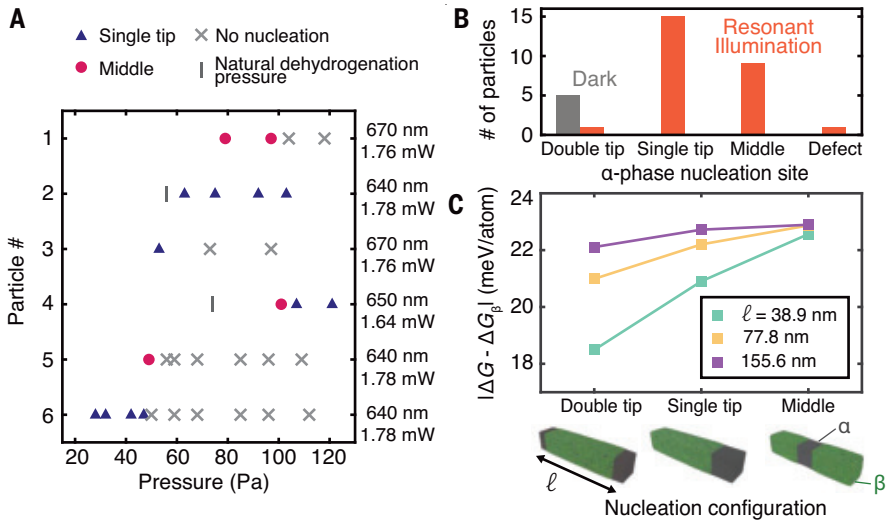


Fig. 4. Different dehydrogenation configurations of the PdH_x nanorod. (**A**) Pressure-dependent nucleation behavior for six different Au-PdH_x pairs under resonant illumination (with average illumination wavelength and power specified in the right column). (**B**) Particle statistics of α-phase nucleation site under dark and resonant illumination conditions for five NPs under dark conditions and 21 particles under illumination conditions. Some particles are counted twice because they show different responses, depending on the surrounding hydrogen pressure. (**C**) The difference in free energy between three different nucleation configurations and a fully hydrogenated nanobar (ΔG_β), calculated via MD simulations of 20-nm-width and 38.9- (aqua), 77.8- (yellow), and 155.6-nm-length (purple) nanobars.

transition, single-tip nucleation (15 NPs), double-tip nucleation (one NP), middle nucleation (nine NPs), and defect nucleation (one NP) (the statistics are summarized in Fig. 4B). Many NPs showed different dehydrogenation mechanisms depending on the surrounding hydrogen pressure. Consistently, when the PdH_x nanorod was very stable in its β-phase (higher H_2 pressure), the energetic barrier to nucleate a phase transition was too high, and we either observed no dehydrogenation within our data acquisition period (180 s) or a more energetically favorable mechanism such as single-tip nucleation. However, once the pressure was lowered to near the natural dehydrogenation pressure, we started to see both middle and single-tip nucleation.

We hypothesized that plasmons not only supplied the system with enough energy to undergo a less favorable transition, but careful tailoring of the conditions also allowed for new transition mechanisms such as middle nucleation. To verify this hypothesis, we qualitatively compared the energies of our three nucleation configurations using molecular dynamics simulations. We calculated the ΔG of three nanobars with identical β-phase volume fractions but different spatial configurations, simulating double-tip, single-tip, and middle nucleation, and compared it against that of a fully hydrogenated nanobar, or our starting configuration (Fig. 4C). For all nanobar lengths, we found that double-tip nucleation was the closest in energy to the fully hydrogenated nanobar, whereas middle nucleation had the largest energy difference. Single-tip and middle nucleation are close in energy, suggesting why both single-tip and middle nucleation are observed in near-equal probabilities under resonant illumination.

The LSPR decay products of light, hot carriers, and heat can all induce dehydrogenation and reduce the nucleation energy barrier. Increased radiation at the EM hotspot can locally reduce the energy barrier for hydrogen recombination and desorption, allowing hot carriers to populate the necessary Pd-H orbitals (*18*), as previously demonstrated with PdH_x cubes (*12*). The hot carriers' short lifetime (tens of femtoseconds) and mean free path [~40 nm for Au and between 10 and 20 nm for PdH_x (*19*)] imply that their spatial distribution should also follow the localized profile of the EM enhancement. The thermal distribution, however, initially follows the spatial profile of the EM enhancement but then spatially broadens over time owing to nanoscale heat transfer (fig. S15).

Therefore, activity far away from the EM hotspot could only be induced by plasmonic heating and is likely the dominant mechanism for single-tip nucleation. The overall increased temperature allowed the PdH_x nanorod to transform from the otherwise stable β-phase into α-phase but without preferential bias toward the EM hotspot. Our pressure-dependent measurements (specifically particle 4 in Fig. 4A) show single-tip nucleation at high pressures but middle nucleation at lower pressures despite identical illumination conditions. Assuming that the slight difference of 6 Pa has minimal effects on heat dissipation, then these two nucleation events had comparable heat profiles. Thus, we hypothesize that middle nucleation is primarily caused by a combination of EM enhancement and hot carriers.

REFERENCES AND NOTES

1. Y. Liu, G. Zhou, K. Liu, Y. Cui, *Acc. Chem. Res.* **50**, 2895–2905 (2017).
2. M. Wuttig, H. Bhaskaran, T. Taubner, *Nat. Photonics* **11**, 465–476 (2017).
3. F. F. Tao, P. A. Crozier, *Chem. Rev.* **116**, 3487–3539 (2016).
4. Y. Niu *et al.*, *Angew. Chem. Int. Ed.* **58**, 4232–4237 (2019).
5. X. Zhang *et al.*, *Nat. Catal.* **3**, 411–417 (2020).
6. E. Cortés *et al.*, *Nat. Commun.* **8**, 14880 (2017).
7. W. D. Yang *et al.*, *Nat. Mater.* **18**, 614–619 (2019).
8. H. Fujiwara, T. Suzuki, C. Pin, K. Sasaki, *Nano Lett.* **20**, 389–394 (2020).
9. L. Zhou *et al.*, *Science* **362**, 69–72 (2018).
10. J. Gargiulo, R. Berté, Y. Li, S. A. Maier, E. Cortés, *Acc. Chem. Res.* **52**, 2525–2535 (2019).
11. N. Zou *et al.*, *ACS Nano* **12**, 5570–5579 (2018).
12. M. Vadai, D. K. Angell, F. Hayee, K. Sytwu, J. A. Dionne, *Nat. Commun.* **9**, 4658 (2018).
13. A. Stolaś, I. Darmadi, F. A. A. Nugroho, K. Moth-Poulsen, C. Langhammer, *ACS Appl. Nano Mater.* **3**, 2647–2653 (2020).
14. T. B. Flanagan, W. Luo, J. D. Clewley, *J. Less Common Met.* **172–174**, 42–55 (1991).
15. K. Sytwu *et al.*, *Nano Lett.* **18**, 5357–5363 (2018).
16. F. Hayee *et al.*, *Nat. Commun.* **9**, 1775 (2018).
17. T. Yokosawa, T. Alan, G. Pandraud, B. Dam, H. Zandbergen, *Ultramicroscopy* **112**, 47–52 (2012).
18. V. A. Spata, E. A. Carter, *ACS Nano* **12**, 3512–3522 (2018).
19. W. E. Vargas, I. Rojas, D. E. Azofeifa, N. Clark, *Thin Solid Films* **496**, 189–196 (2006).

ACKNOWLEDGMENTS

The authors acknowledge D. Swearer for helpful discussions, R. Kim for TEM assistance, and all members of the Dionne group for helpful scientific feedback and support. **Funding:** We gratefully acknowledge funding support from C.-C. Kao at SLAC National Accelerator Laboratory; the National Science Foundation's Alan T. Waterman Award; and the U.S. Department of Energy, Office of Science, Division of Materials Science and Engineering under contract DE-AC02-76SF00515. Part of this work was performed at the Stanford Nanofabrication Facility (SNF) and Stanford Nano Shared Facilities (SNSF), supported by the National Science Foundation under award ECCS-1542152. K.S. was supported by the Gabilan Stanford Graduate Fellowship and the National Science Foundation Graduate Research Fellowship (DGE-1656518). M.V. was supported by a postdoctoral fellowship from the TomKat Center for Sustainable Energy at Stanford University. F.H. was supported by the Diversifying Academia, Recruiting Excellence (DARE) Doctoral Fellowship Program by Stanford University. J.D. was supported as part of the Department of Energy "Photonics at Thermodynamic Limits" Energy Frontier Research Center under grant DE-SC0019140. **Author contributions:** K.S., M.V., and J.A.D. conceived of the idea and designed the experiments. K.S. performed the experiments with assistance from M.V., A.D., and F.H. K.S. analyzed the data with assistance from M.V. and F.H. D.K.A. led the molecular dynamics simulations. K.S. led the heating simulations with assistance from J.D. J.A.D. supervised the project. K.S. wrote the initial draft and all authors contributed to the final manuscript. **Competing interests:** The authors declare no competing interests. **Data and materials availability:** All data and materials are available upon email request.

SUPPLEMENTARY MATERIALS

science.sciencemag.org/content/371/6526/280/suppl/DC1
Materials and Methods
Supplementary Text
Figs. S1 to S16
Tables S1 and S2
References (*20–27*)
Movie S1

16 June 2020; resubmitted 16 October 2020
Accepted 4 December 2020
10.1126/science.abd2847

VIROLOGY

Learning the language of viral evolution and escape

Brian Hie[1,2], Ellen D. Zhong[1,3], Bonnie Berger[1,4]*, Bryan Bryson[2,5]*

The ability for viruses to mutate and evade the human immune system and cause infection, called viral escape, remains an obstacle to antiviral and vaccine development. Understanding the complex rules that govern escape could inform therapeutic design. We modeled viral escape with machine learning algorithms originally developed for human natural language. We identified escape mutations as those that preserve viral infectivity but cause a virus to look different to the immune system, akin to word changes that preserve a sentence's grammaticality but change its meaning. With this approach, language models of influenza hemagglutinin, HIV-1 envelope glycoprotein (HIV Env), and severe acute respiratory syndrome coronavirus 2 (SARS-CoV-2) Spike viral proteins can accurately predict structural escape patterns using sequence data alone. Our study represents a promising conceptual bridge between natural language and viral evolution.

Viral mutations that allow an infection to escape from recognition by neutralizing antibodies have prevented the development of a universal antibody-based vaccine for influenza (*1*, *2*) or HIV (*3*) and are a concern in the development of therapies for severe acute respiratory syndrome coronavirus 2 (SARS-CoV-2) infection (*4*, *5*). Escape has motivated high-throughput experimental techniques that perform causal escape profiling of all single-residue mutations to a viral protein (*1*–*4*). Such techniques, however, require substantial effort to profile even a single viral strain, and testing the escape potential of many (combinatorial) mutations in many viral strains remains infeasible.

Instead, we sought to train an algorithm that learns to model escape from viral sequence data alone. This approach is not unlike learning properties of natural language from large text corpuses (*6*, *7*) because languages such as English and Japanese use sequences of words to encode complex meanings and have complex rules (for example, grammar). To escape, a mutant virus must preserve infectivity and evolutionary fitness—it must obey a "grammar" of biological rules—and the mutant must no longer be recognized by the immune system, which is analogous to a change in the "meaning" or the "semantics" of the virus.

Currently, computational models of protein evolution focus either on fitness (*8*) or on functional or semantic similarity (*9*–*11*), but we want to understand both (Fig. 1A). Rather than developing two separate models of fitness and function, we developed a single model that simultaneously achieves these tasks. We leveraged state-of-the-art machine learning algorithms called language models (*6*, *7*), which learn the probability of a token (such as an English word) given its sequence context (such as a sentence) (Fig. 1B). Internally, the language model constructs a semantic representation, or an "embedding," for a given sequence (*6*), and the output of a language model encodes how well a particular token fits within the rules of the language, which we call "grammaticality" and can also be thought of as "syntactic fitness" (supplementary text, note S2). The same principles used to train a language model on a sequence of English words can train a language model on a sequence of amino acids. Although immune selection occurs on phenotypes (such as protein structures),

[1]Computer Science and Artificial Intelligence Laboratory, Massachusetts Institute of Technology, Cambridge, MA 02139, USA. [2]Ragon Institute of MGH, MIT, and Harvard, Cambridge, MA 02139, USA. [3]Computational and Systems Biology, Massachusetts Institute of Technology, Cambridge, MA 02139, USA. [4]Department of Mathematics, Massachusetts Institute of Technology, Cambridge, MA 02139, USA. [5]Department of Biological Engineering, Massachusetts Institute of Technology, Cambridge, MA 02139, USA.
*Corresponding author. Email: bab@mit.edu (B.Be.); bryand@mit.edu (B.Br.)

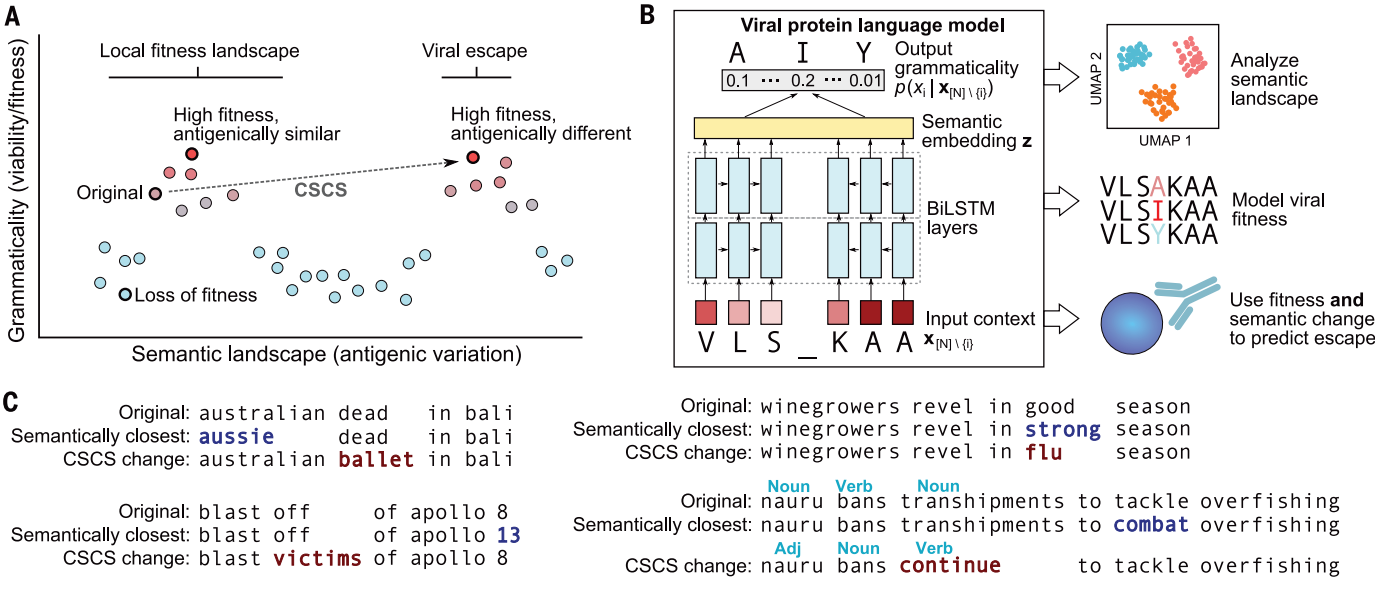


Fig. 1. Modeling viral escape requires characterizing semantic change and grammaticality. (**A**) Constrained semantic change search (CSCS) for viral escape prediction is designed to search for mutations to a viral sequence that preserve fitness while being antigenically different. This corresponds to a mutant sequence that is grammatical (conforms to the structure and rules of a language) but has high semantic change with respect to the original (for example, wild type) sequence. (**B**) A neural language model with a bidirectional long short-term memory (BiLSTM) architecture was used to learn both semantics (as a hidden layer output) and grammaticality (as the language model output). CSCS combines semantic change and grammaticality to predict escape (*12*). (**C**) CSCS-proposed changes to a news headline (implemented by using a neural language model trained on English news headlines) makes large changes to the overall semantic meaning of a sentence or to the part-of-speech structure. The semantically closest mutated sentence according to the same model is largely synonymous with the original headline.

evolution dictates that selection is reflected within genotypes (such as protein sequences), which language models can leverage to learn functional properties from sequence variation.

We hypothesize that (i) language model–encoded semantic change corresponds to antigenic change, (ii) language model grammaticality captures viral fitness, and (iii) both high semantic change and grammaticality help predict viral escape. Searching for mutations with both high grammaticality and high semantic change is a task that we call constrained semantic change search (CSCS) (Fig. 1C) (*12*). Our language model implementation of CSCS uses sequence data alone (which is easier to obtain than structure) and requires no explicit escape information (is completely unsupervised), does not rely on multiple sequence alignment (MSA) preprocessing (is "alignment-free"), and captures global relationships across an entire sequence (for example, because word choice at the beginning of a sentence can influence word choice at the end) (supplementary text, notes S2 and S3).

We assessed the generality of our approach across viruses by analyzing three proteins: influenza A hemagglutinin (HA), HIV-1 envelope glycoprotein (Env), and SARS-CoV-2 spike glycoprotein (Spike). All three are found on the viral surface, are responsible for binding host cells, are targeted by antibodies, and are drug targets (*1*–*5*). We trained a separate language model for each protein using a corpus of virus-specific amino acid sequences (*12*).

We initially sought to understand the semantic patterns learned by our viral language models. We therefore visualized the semantic embeddings of each sequence in the influenza, HIV, and coronavirus corpuses using Uniform Manifold Approximation and Projection (UMAP) (*13*). The resulting two-dimensional semantic landscapes show clustering patterns that correspond to subtype, host species, or both (Fig. 2), suggesting that the model was able to learn functionally meaningful patterns from raw sequence.

We quantified these clustering patterns, which are visually enriched for particular subtypes or hosts, with Louvain clustering (*14*) to group sequences on the basis of their semantic embeddings (fig. S1, A to C). We then measured the clustering purity on the basis of the percent composition of the most represented metadata category (sequence subtype or host species) within each cluster (*12*). Average cluster purities for HA subtype, HA host species, and Env subtype are 99, 96, and 95%, respectively, which are comparable with or higher than the clustering purities obtained with MSA-based phylogenetic reconstruction (Fig. 2, D and F, and fig. S1D) (*12*).

Within the HA landscape, clustering patterns suggest interspecies transmissibility. The sequence for 1918 H1N1 pandemic influenza belongs to the main avian H1 cluster, which contains sequences from the avian reservoir for 2009 H1N1 pandemic influenza (Fig. 2C and fig. S1, A to C). Antigenic similarity between H1 HA from 1918 and 2009, although nearly a century apart, is well supported (*15*). Within the landscape of SARS-CoV-2 Spike and homologous proteins, clustering proximity

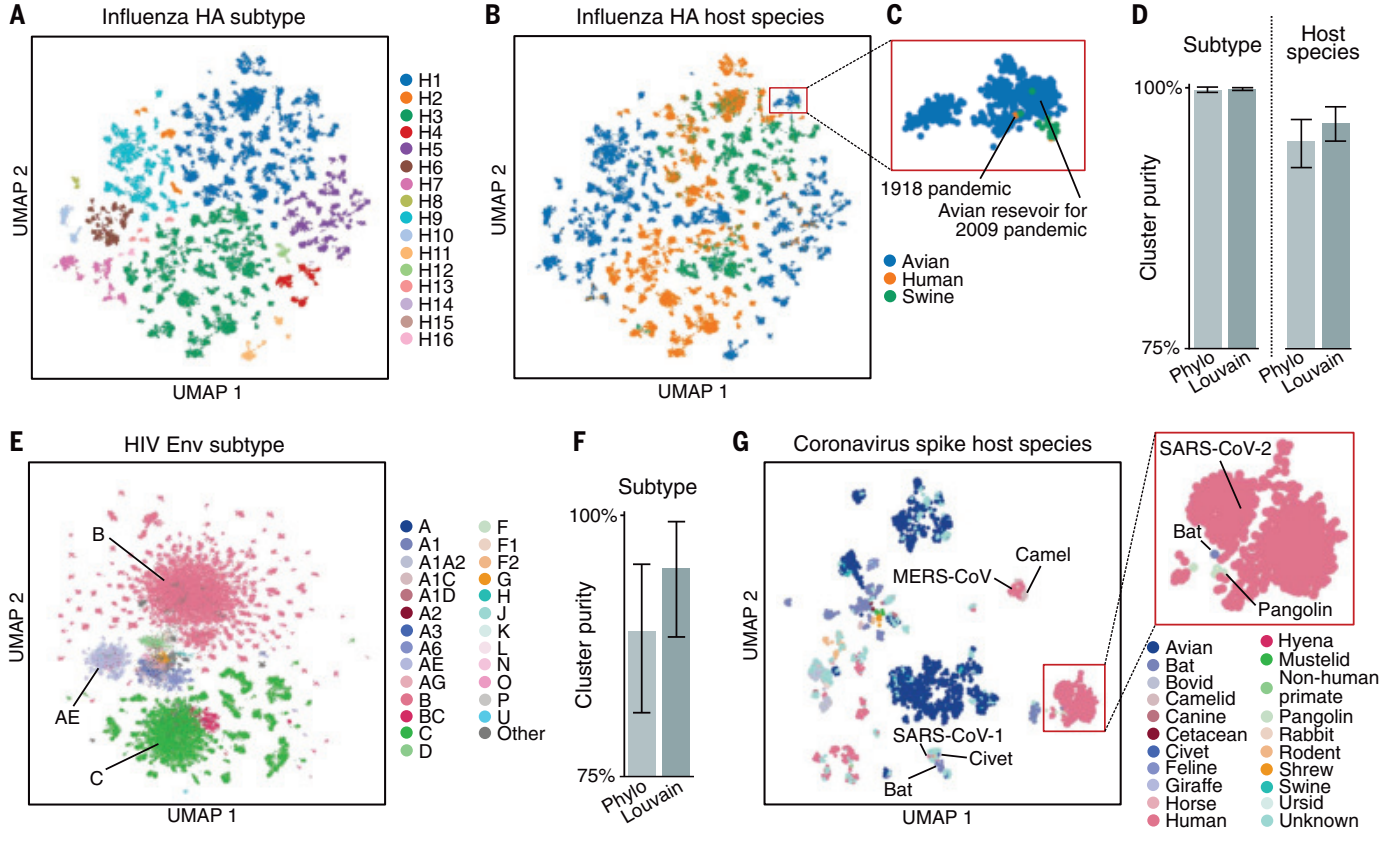


Fig. 2. Semantic embedding landscape is antigenically meaningful. (**A** and **B**) UMAP visualization of the high-dimensional semantic embedding landscape of influenza HA. (**C**) A cluster consisting of avian sequences from the 2009 flu season onward also contains the 1918 pandemic flu sequence, which is consistent with their antigenic similarity (*15*). (**D**) Louvain clusters of the HA semantic embeddings have similar purity with respect to subtype or host species compared with phylogenetic sequence clustering (Phylo). Bar height, mean; error bars, 95% confidence. (**E** and **F**) The HIV Env semantic landscape shows subtype-related distributional structure and high Louvain clustering purity. Bar height, mean; error bars, 95% confidence. (**G**) Sequence proximity in the semantic landscape of coronavirus spike proteins is consistent with the possible zoonotic origin of SARS-CoV-1, MERS-CoV, and SARS-CoV-2.

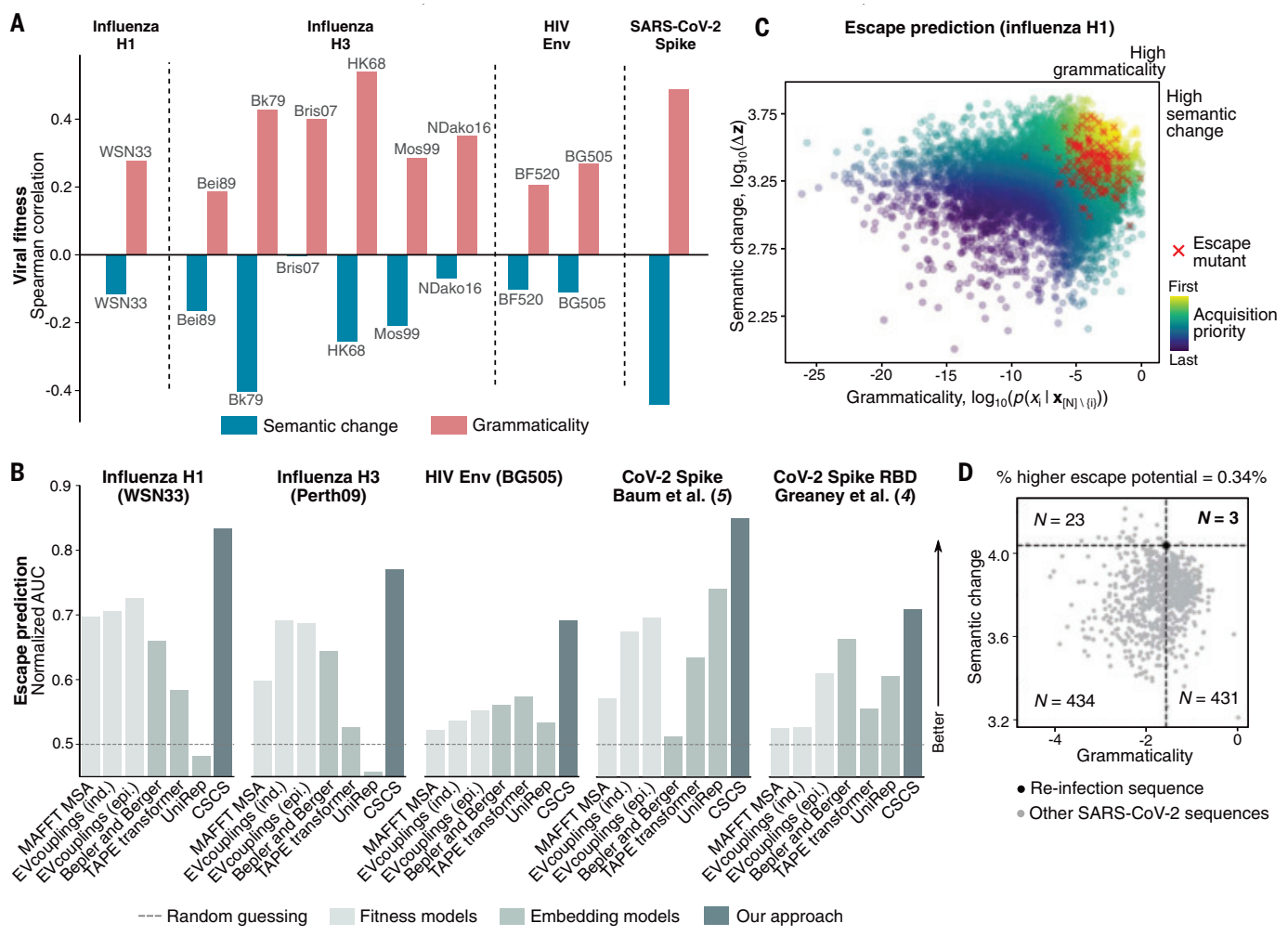


Fig. 3. Biological interpretation of language model semantics and grammaticality enables escape prediction. (**A**) Whereas grammaticality is positively correlated with fitness, semantic change has negative correlation, suggesting that most semantically altered proteins lose fitness. (**B** and **C**) However, a mutation with both high semantic change and high grammaticality is more likely to induce escape. Considering both semantic change and grammaticality enables identification of escape mutants that is consistently higher than that of previous fitness models or generic functional embedding models. (**D**) Across 891 surveilled SARS-CoV-2 Spike sequences, only three have both higher semantic change and grammaticality than a Spike sequence with four mutations that is associated with a potential reinfection case.

is consistent with the suggested zoonotic origin of several human coronaviruses (Fig. 2G), including bat and civet for SARS-CoV-1, camel for Middle East respiratory syndrome-related coronavirus (MERS-CoV), and bat and pangolin for SARS-CoV-2 (*16*). Analysis of these semantic landscapes strengthens our hypothesis that our viral sequence embeddings encode functional and antigenic variation.

We then assessed the relationship between viral fitness and language model grammaticality using high-throughput deep mutational scan (DMS) characterization of hundreds or thousands of mutations to a given viral protein. We obtained datasets measuring replication fitness of all single-residue mutations to A/WSN/1933 (WSN33) HA H1 (*17*), combinatorial mutations to antigenic site B in six HA H3 strains (*18*), or all single-residue mutations to BG505 and BF520 HIV Env (*19*), as well as a dataset measuring the dissociation constant (K_d) between combinatorial mutations to yeast-displayed SARS-CoV-2 Spike receptor-binding domain (RBD) and human ACE2 (*20*), which we used to approximate the fitness of Spike.

Language model grammaticality was significantly correlated (table S1, *t*-distribution *P* values) with viral fitness across all viral strains and across studies that examined single or combinatorial mutations (Fig. 3A), even though our language models were not given any explicit fitness-related information nor trained on the DMS mutants. When we compared viral fitness with the magnitude of mutant semantic change (rather than grammaticality), we observed significant negative correlation (table S1, *t*-distribution *P* values) in 8 out of 10 strains tested (Fig. 3A). This makes sense biologically because a mutation with a large effect on function is on average more likely to be deleterious and result in a loss of fitness. These results suggest that "grammaticality" of a given mutation captures fitness information and add an additional dimension to our understanding of how semantic change encodes perturbed protein function.

We then tested whether combining semantic change and grammaticality enables us to predict mutations that lead to viral escape. Our experimental setup involved making, in silico, all possible single-residue mutations to a given viral protein sequence; next, each mutant was ranked according to the CSCS objective that combines semantic change and grammaticality. We validated this ranking on the basis of enrichment of experimentally verified mutants that causally induce escape from neutralizing antibodies. Three of these causal escape datasets used a DMS with antibody selection to identify escape mutations to WSN33

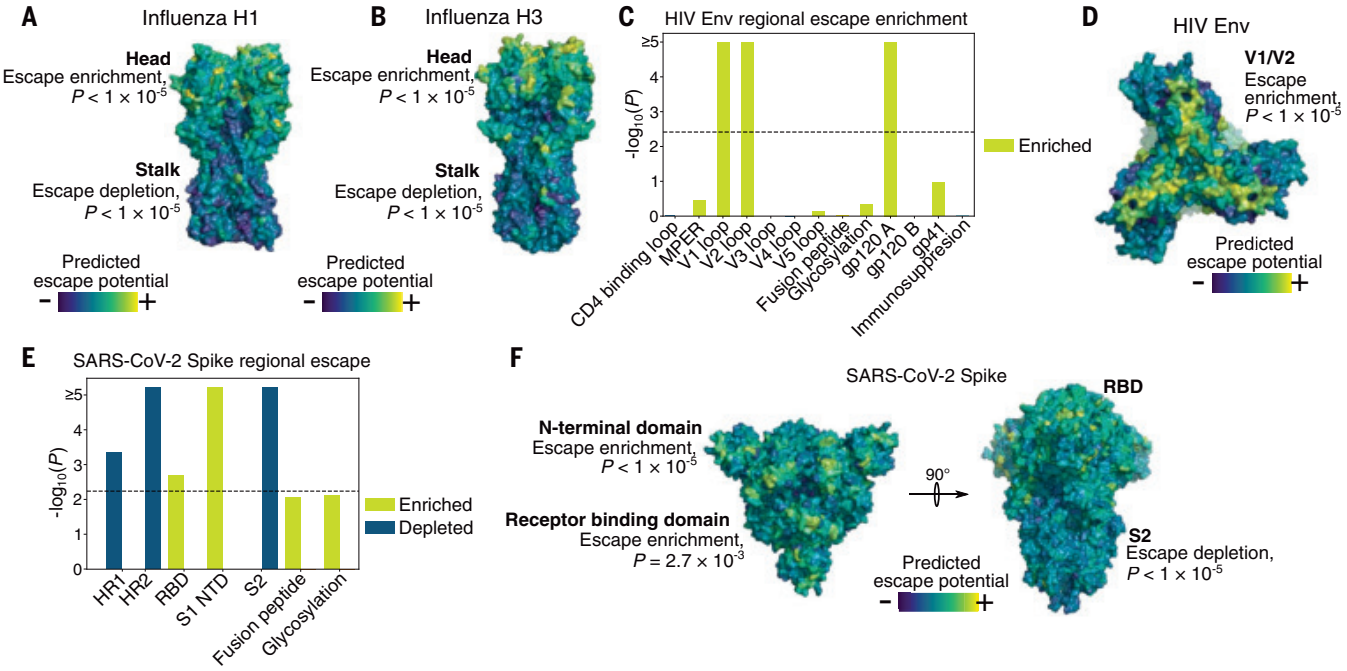


Fig. 4. Structural localization of predicted escape potential. (**A** and **B**) HA trimer colored by escape potential. (**C**) Escape potential *P* values for HIV Env. The gray dashed line indicates the statistical significance threshold. (**D**) The Env trimer colored by escape potential, oriented to show the V1/V2 regions. (**E** and **F**) Potential for escape in SARS-CoV-2 Spike is significantly enriched at the N-terminal domain and receptor binding domain (RBD) and significantly depleted at multiple regions in the S2 subunit. The gray dashed line indicates the statistical significance threshold.

HA H1 (*1*), A/Perth/16/2009 (Perth09) HA H3 (*2*), and BG505 Env (*3*). The fourth identified escape mutations to SARS-CoV-2 Spike by using natural replication error after in vitro passages under antibody selection (*5*), whereas the fifth performed a DMS to identify mutants that affect antibody binding to yeast-displayed Spike RBD (*4*).

We computed the area under the curve (AUC) of acquired escape mutations versus the total acquired mutations (*12*). In all five cases, escape prediction with CSCS resulted in both statistically significant and strong AUCs of 0.83, 0.77, 0.69, 0.85, and 0.71 for H1 WSN33, H3 Perth09, Env BG505, Spike, and Spike RBD, respectively (one-sided permutation-based $P < 1 \times 10^{-5}$ in all cases) (Fig. 3B and table S2). We did not provide the model with any information on escape, a setup in machine learning referred to as "zero-shot prediction" (*7*). The AUC decreased when ignoring either grammaticality or semantic change, evidence that both are useful in predicting escape (Fig. 3C, fig. S2A, and table S2). Although semantic change is negatively correlated with fitness, it is positively predictive (along with grammaticality) of escape (table S2), indicating that functional mutations are often deleterious, but when fitness is preserved, they are associated with antigenic change and subsequent escape from immunity.

We also tested how well alternative models of fitness (each requiring MSA preprocessing) (*8*, *21*) or of semantic change (pretrained on generic protein sequence) (*9*–*11*) predict escape, although these models are not explicitly designed for escape prediction. Fitness models associate more frequently observed patterns with higher fitness and greater escape potential, whereas semantic models associate larger functional changes with escape (*12*). CSCS with our viral language models was more predictive of escape across all five datasets (Fig. 3B and fig. S2A). Moreover, the individual grammaticality or semantic change components of our language models often outperformed benchmark models (table S2).

Language modeling can also characterize sequence changes beyond single-residue mutations, such as from accumulated replication error or recombination (*22*), although our approach is agnostic to how a sequence acquires its mutations. We therefore estimated the antigenic change and fitness of a set of four mutations to the SARS-CoV-2 Spike associated with a reported reinfection event (*23*). Among 891 other distinct, surveilled Spike sequences, we found that only three (0.34%) represent both higher semantic change and grammaticality (Fig. 3D). We estimate significant escape potential of these four mutations (random mutant null distribution $P < 1 \times 10^{-8}$) (*12*), and we observed similar patterns for known antigenically dissimilar sequences (fig. S2B) (*12*). Our analysis suggests a way to quantify the escape potential of interesting combinatorial sequence changes, such as those from possible reinfection (*23*), and calls for more information that relates combinatorial mutations to reinfection and escape.

To further assess whether our model could learn structurally relevant patterns from sequence alone, we scored each residue on the basis of the CSCS objective, visualized escape potential across the protein structure, and quantified enrichment or depletion of escape (*12*). Escape potential is significantly enriched in the HA head (permutation-based $P < 1 \times 10^{-5}$) and significantly depleted in the HA stalk (permutation-based $P < 1 \times 10^{-5}$) (Fig. 4, A and B; fig. S3; and table S3), which is consistent with literature on HA mutation rates and supported by the successful development of antistalk broadly neutralizing antibodies (*24*). We also detected, consistent with existing knowledge, a significant enrichment (permutation-based $P < 1 \times 10^{-5}$) of escape mutations in the V1/V2 hypervariable regions of the HIV Env (Fig. 4, C and D; fig. S3; and table S3) (*3*). Our model only learns escape patterns linked to mutations, rather than post-translational changes such as glycosylation that contribute to HIV escape (*3*), which may explain the lack of escape potential specifically assigned to Env glycosylation sites (Fig. 4C and table S3).

The escape potential within the SARS-CoV-2 Spike is significantly enriched in both the RBD (permutation-based $P = 2.7 \times 10^{-3}$)

and N-terminal domain (permutation-based $P < 1 \times 10^{-5}$), whereas escape potential is significantly depleted in the S2 subunit (permutation-based $P < 1 \times 10^{-5}$) (Fig. 4, E and F; fig. S3; and table S3). These results are supported by the greater evolutionary conservation at S2 antigenic sites (*25*). Our model of Spike escape therefore suggests that immunodominant antigenic sites in S2 (*5*, *25*) may be more stable target antibody epitopes and underscores the need for more exhaustive causal escape profiling of Spike in regions beyond the RBD.

Our study leverages the principle that evolutionary selection is reflected in sequence variation. This principle may allow CSCS to generalize beyond viral escape to different kinds of natural selection (such as T cell selection) or drug selection. CSCS and its components could be used to select elements of a multivalent or mosaic vaccine. Our techniques also lay the foundation for more complex modeling of sequence dynamics. We anticipate that the "distributional hypothesis" from linguistics (*26*), in which co-occurrence patterns can model complex concepts and on which language models are based, can further inform viral evolution.

REFERENCES AND NOTES

1. M. B. Doud, J. M. Lee, J. D. Bloom, *Nat. Commun.* **9**, 1386 (2018).
2. J. M. Lee *et al.*, *eLife* **8**, e49324 (2019).
3. A. S. Dingens, D. Arenz, H. Weight, J. Overbaugh, J. D. Bloom, *Immunity* **50**, 520–532.e3 (2019).
4. A. J. Greaney *et al.*, *Cell Host Microbe* 10.1016/j.chom.2020.11.007 (2020).
5. A. Baum *et al.*, *Science* **369**, 1014–1018 (2020).
6. M. Peters *et al.*, Deep contextualized word representations. *Proc. NAACL-HLT*, 2227–2237 (2018).
7. A. Radford *et al.*, *OpenAI Blog* **1**, 9 (2019).
8. T. A. Hopf *et al.*, *Bioinformatics* **35**, 1582–1584 (2019).
9. T. Bepler, B. Berger, Learning protein sequence embeddings using information from structure. arXiv:1902.08661 [cs.LG] (2019).
10. R. Rao *et al.*, Evaluating protein transfer learning with TAPE. *Proc. Adv. Neural Inf. Process. Syst.*, 9686–9698 (2019).
11. E. C. Alley, G. Khimulya, S. Biswas, M. AlQuraishi, G. M. Church, *Nat. Methods* **16**, 1315–1322 (2019).
12. Materials and methods are available as supplementary materials.
13. L. McInnes, J. Healy, UMAP: Uniform Manifold Approximation and Projection for dimension reduction. arXiv:1802.03426 [stat.ML] (2018).
14. V. D. Blondel, J. L. Guillaume, R. Lambiotte, E. Lefebvre, *J. Stat. Mech. Theory Exp.* **2008**, P10008 (2008).
15. R. Xu *et al.*, *Science* **328**, 357–360 (2010).
16. K. G. Andersen, A. Rambaut, W. I. Lipkin, E. C. Holmes, R. F. Garry, *Nat. Med.* **26**, 450–452 (2020).
17. M. B. Doud, J. D. Bloom, *Viruses* **8**, 155 (2016).
18. N. C. Wu *et al.*, *Nat. Commun.* **11**, 1233 (2020).
19. H. K. Haddox, A. S. Dingens, S. K. Hilton, J. Overbaugh, J. D. Bloom, *eLife* **7**, e34420 (2018).
20. T. N. Starr *et al.*, *Cell* **182**, 1295–1310.e20 (2020).
21. K. Katoh, D. M. Standley, *Mol. Biol. Evol.* **30**, 772–780 (2013).
22. Y. Xiao *et al.*, *Cell Host Microbe* **19**, 493–503 (2016).
23. K. K.-W. To *et al.*, *Clin. Infect. Dis.* ciaa1275 (2020).
24. E. Kirkpatrick, X. Qiu, P. C. Wilson, J. Bahl, F. Krammer, *Sci. Rep.* **8**, 10432 (2018).
25. S. Ravichandran *et al.*, *Sci. Transl. Med.* **12**, eabc3539 (2020).
26. Z. S. Harris, *Word* **10**, 146–162 (1954).
27. B. Hie, brianhie/viral-mutation: viral-mutation release 0.3. Zenodo (2020).
28. B. Hie, Data for "Learning the language of viral evolution and escape". Zenodo (2020).

ACKNOWLEDGMENTS

We thank A. Balazs, H. Fraser, O. Leddy, A. Lerer, A. Lin, A. Nitido, U. Roy, and A. Schmidt for helpful discussions. We thank S. Chun, B. DeMeo, A. Narayan, A. Nguyen, S. Nyquist, and A. Wu for assistance with the manuscript. **Funding:** B.H. is partially supported by the U.S. Department of Defense (DOD) through the National Defense Science and Engineering Graduate Fellowship (NDSEG). E.Z. is partially supported by the National Science Foundation (NSF) Graduate Research Fellowship. **Author contributions:** All authors conceived the project and methodology. B.H. performed the computational experiments and wrote the software. All authors interpreted the results and wrote the manuscript. **Competing interests:** B.H., B.Be., and B.Br. have filed a provisional patent application (serial no. 53/049,676) related to this work. **Data and materials availability:** Code, scripts for plotting and visualizing, and pretrained models are deposited to Zenodo at doi:10.5281/zenodo.4034681 (*27*) and are also available at https://github.com/brianhie/viral-mutation. We used the following publicly available datasets for model training: Influenza A HA protein sequences from the NIAID Influenza Research Database (IRD) (www.fludb.org); HIV-1 Env protein sequences from the Los Alamos National Laboratory (LANL) HIV database (www.hiv.lanl.gov); *Coronavidae* spike protein sequences from the Virus Pathogen Resource (ViPR) database (www.viprbrc.org/brc/home.spg?decorator=corona); SARS-CoV-2 Spike protein sequences from NCBI Virus (www.ncbi.nlm.nih.gov/labs/virus/vssi); and SARS-CoV-2 Spike and other Betacoronavirus spike protein sequences from GISAID (www.gisaid.org). We used the following publicly available datasets for fitness and escape validation: Fitness single-residue DMS of HA H1 WSN33 from Doud and Bloom (2016) (*17*); Fitness combinatorial DMS of antigenic site B in six HA H3 strains from Wu *et al.* (*18*); Fitness single-residue DMS of Env BF520 and BG505 from Haddox *et al.* (*19*); ACE2 binding affinity combinatorial DMS of Spike RBD from Starr *et al.* (*20*); Escape single-residue DMS of HA H1 WSN33 from Doud *et al.* (2018) (*1*); Escape single-residue DMS of HA H3 Perth09 from Lee *et al.* (*2*); Escape single-residue DMS of Env BG505 from Dingens *et al.* (*3*); Escape mutations of Spike from Baum *et al.* (*5*); Escape single-residue DMS of Spike RBD from Greaney *et al.* (*4*); Training and validation datasets are deposited to Zenodo at doi:10.5281/zenodo.4029296 (*28*), and links to this data are also available at https://github.com/brianhie/viral-mutation.

SUPPLEMENTARY MATERIALS

science.sciencemag.org/content/371/6526/284/suppl/DC1
Materials and Methods
Supplementary Text
Figs. S1 to S3
Tables S1 to S3
References (*29*–*49*)
MDAR Reproducibility Checklist

8 July 2020; accepted 9 November 2020
10.1126/science.abd7331

CORONAVIRUS

Three-quarters attack rate of SARS-CoV-2 in the Brazilian Amazon during a largely unmitigated epidemic

Lewis F. Buss[1]*, Carlos A. Prete Jr.[2]*, Claudia M. M. Abrahim[3]*, Alfredo Mendrone Jr.[4,5]*, Tassila Salomon[6,7]*, Cesar de Almeida-Neto[4,5], Rafael F. O. França[8], Maria C. Belotti[2], Maria P. S. S. Carvalho[3], Allyson G. Costa[3], Myuki A. E. Crispim[3], Suzete C. Ferreira[4,5], Nelson A. Fraiji[3], Susie Gurzenda[9], Charles Whittaker[10], Leonardo T. Kamaura[11], Pedro L. Takecian[11], Pedro da Silva Peixoto[11], Marcio K. Oikawa[12], Anna S. Nishiya[4,5], Vanderson Rocha[4,5], Nanci A. Salles[4], Andreza Aruska de Souza Santos[13], Martirene A. da Silva[3], Brian Custer[14,15], Kris V. Parag[16], Manoel Barral-Netto[17], Moritz U. G. Kraemer[18], Rafael H. M. Pereira[19], Oliver G. Pybus[18], Michael P. Busch[14,15], Márcia C. Castro[9], Christopher Dye[18], Vítor H. Nascimento[2], Nuno R. Faria[1,16,18]†, Ester C. Sabino[1]†

Severe acute respiratory syndrome coronavirus 2 (SARS-CoV-2) spread rapidly in Manaus, the capital of Amazonas state in northern Brazil. The attack rate there is an estimate of the final size of the largely unmitigated epidemic that occurred in Manaus. We use a convenience sample of blood donors to show that by June 2020, 1 month after the epidemic peak in Manaus, 44% of the population had detectable immunoglobulin G (IgG) antibodies. Correcting for cases without a detectable antibody response and for antibody waning, we estimate a 66% attack rate in June, rising to 76% in October. This is higher than in São Paulo, in southeastern Brazil, where the estimated attack rate in October was 29%. These results confirm that when poorly controlled, COVID-19 can infect a large proportion of the population, causing high mortality.

Brazil has experienced one of the world's most rapidly growing COVID-19 epidemics, with the Amazon being the worst-hit region (*1*). Manaus is the largest metropolis in the Amazon, with a population of more than 2 million and a population density of 158 inhabitants/km^2. The first severe acute respiratory syndrome coronavirus 2 (SARS-CoV-2) case in Manaus was confirmed on 13 March 2020 (*2*) and was followed by an explosive epidemic, peaking in early May with 4.5-fold excess mortality (*3*). This was followed by a sustained drop in new cases despite relaxation of nonpharmaceutical interventions (NPIs). The prevalence of antibodies to SARS-CoV-2 is an estimate of the attack rate in Manaus and provides a data-based estimate of the extent of COVID-19 spread in the absence of effective mitigation.

Given a basic reproduction number (R_0) of 2.5 to 3.0 for Amazonas state (*4*), the expected attack rate during an unmitigated epidemic in

a homogeneously mixed population is 89 to 94% (*5*). When the percentage of infected people exceeds the herd immunity threshold of 60 to 67%, or $100 \times [1 - (1/R_0)]$, each infection generates fewer than one secondary case (case reproduction number $R_t < 1$) and incidence declines. We sought to measure the SARS-CoV-2 attack rate in Manaus and to explore whether the epidemic was contained ($R_t < 1$) because infection reached the herd immunity threshold, or because of other factors such as behavioral changes and NPIs. We compared data from Manaus with findings from São Paulo, where the first Brazilian COVID-19 cases were detected (*2*, *6*) and both the rise and fall in mortality were slower and more protracted.

We used a chemiluminescent microparticle immunoassay (CMIA; AdviseDx, Abbott) that detects immunoglobulin G (IgG) antibodies to the SARS-CoV-2 nucleocapsid (N) protein. To infer the attack rate from antibody test positivity, we need to account for the sensitivity and specificity of the test (*7*). The specificity of the CMIA is high (>99.0%) (*8*–*10*), but previous high (>90.0%) sensitivity estimates (*8*, *10*) may not apply to blood donor screening (*11*, *12*) for two reasons. First, most SARS-CoV-2 infections in blood donors are asymptomatic, and weaker antibody responses in asymptomatic disease (*13*) may lead to a lower initial seroconversion rate (i.e., more "serosilent" infections). Second, as a result of antibody waning, sensitivity falls over time (*14*), such that test positivity increasingly underestimates the true attack rate.

We used a variety of clinical samples at different time points to gain insight into the dynamics of the anti-N IgG detected by the Abbott CMIA (Fig. 1). In samples from hospitalized COVID-19 patients collected at 20 to 33 days after symptom onset, reflecting high disease severity and optimal timing of blood collection, sensitivity was 91.8% [95% confidence interval (CI), 80.8% to 96.8%], which suggests that ~8% of severe convalescent cases do not develop detectable antibodies. Among a cohort of symptomatic cases with mild disease also tested in the early convalescent period, sensitivity fell to 84.5% (95% CI, 78.7% to 88.9%), indicating that initial seroconversion is lower in milder cases. In samples drawn later (50 to 131 days) from the same mild disease cohort, sensitivity was lower still (80.4%; 95% CI, 71.8% to 86.8%), reflecting antibody waning. Indeed, in a subset of 104 patients with two consecutive blood draws, the signal-to-cutoff (S/C) declined over the period observed (Fig. 1B) and among 88 individuals with a positive reading at the first time point, the mean rate of decay was −0.9 $\log_2$ S/C units every 100 days (95% CI, −1.1 to −0.75), equating to a half-life of 106 days (95% CI, 89 to 132 days) (Fig. 1C).

Finally, we tested 1000 blood donations given in São Paulo in July 2020 in parallel, using a second high-specificity [>99.0% (*15*)] immunoassay less prone to antibody waning (*14*) (Roche Elecsys). Of these, 103 samples were positive using the Abbott CMIA and an additional 30 were positive using the Roche assay. Assuming that all 133 samples were true positives, the sensitivity of the Abbott N IgG assay was 77.4% (95% CI, 69.6% to 83.7%) on asymptomatic blood donor samples. Samples in July were donated 4 months into the ongoing epidemic in São Paulo; accordingly, the false negatives using the Abbott assay include cases that did not initially seroconvert, as well as past infections that had subsequently seroreverted.

Because specificity was high, with only one false positive result in 821 pre-epidemic donations from Manaus (Fig. 1A), we also attempted to improve assay performance by reducing the threshold for a positive result from 1.4 S/C (as per the manufacturer) to 0.4 S/C. This resulted in 27 false positives and a specificity of 96.7% but substantially improved sensitivity at this threshold (Fig. 1A and table S1).

To estimate the proportion of the population with IgG antibodies to SARS-CoV-2, we used a convenience sample of routine blood donations made at the Fundação Pró-Sangue blood bank in São Paulo and the Fundação Hospitalar de Hematologia e Hemoterapia do Amazonas (HEMOAM) in Manaus. The monthly sample size and sampling dates, spanning February to October, are shown in table S2.

The prevalence of SARS-CoV-2 antibodies in February and March was low (<1%) in both São Paulo and Manaus. This is consistent with the timing of the first confirmed cases that were diagnosed on 13 March in Manaus and on 25 February in São Paulo (*2*). In Manaus, after adjustment for the sensitivity and specificity of the test (but not antibody waning) and reweighting for age and sex, the prevalence of SARS-CoV-2 IgG antibodies was 4.8% (95% CI, 3.3% to 6.8%) in April and 44.5% (95% CI, 39.2% to 50.0%) in May, reaching a peak of 52.5% (47.6% to 57.5%) in June (Fig. 2 and table S2). The increasing seroprevalence closely followed the curve of cumulative deaths. In São Paulo, the prevalence of SARS-CoV-2 IgG in blood donors also increased steadily, reaching 13.6% (95% CI, 12.0% to 8.1%) in June.

Between June and October, the effect of seroreversion became apparent in both cities. In Manaus, after the peak antibody prevalence in June, the proportion of blood donors who tested positive fell steadily to 25.8% in October. Excluding extreme negative samples (<0.4 S/C), the median assay signal fell steadily from May: 3.9 (May), 3.5 (June), 2.3 (July), 1.7 (August), 1.4 (September), and 1.3 (October) (Fig. 2B). Similarly, in São Paulo, antibody prevalence remained stable between June and October while the number of daily COVID-19 deaths also remained relatively stable, reflecting a balance between antibody waning from infections earlier in the outbreak and seroconversions following recent infections (Fig. 2C).

In Manaus, the effect of antibody waning on apparent prevalence was partially ameliorated by reducing the threshold for a positive result from 1.4 S/C to 0.4 S/C and correcting for the resulting increased false positive rate. However, the results in São Paulo were largely unchanged by this correction (Fig. 2 and table S2).

We further corrected for seroreversion with a model-based approach (see supplementary materials). Briefly, we assumed that the probability of an individual seroreverting exactly m months after recovery decays exponentially with m. We estimated the decay rate and the proportion of patients who seroreverted using the seroprevalence data from Manaus to find the decay rate that minimized the number of new cases in July and August while avoiding decreases in prevalence—that is, assuming there were few cases in Manaus in July and August and that changes in seroprevalence were due mainly to waning antibodies. The results of these corrections are shown in Fig. 2 and table S2. After adjusting for seroreversion, we find that cumulative incidence in Manaus

[1]Departamento de Molestias Infecciosas e Parasitarias and Instituto de Medicina Tropical da Faculdade de Medicina da Universidade de São Paulo, São Paulo, Brazil. [2]Departamento de Engenharia de Sistemas Eletrônicos, Escola Politécnica da Universidade de São Paulo, São Paulo, Brazil. [3]Fundação Hospitalar de Hematologia e Hemoterapia do Amazonas, Manaus, Brazil. [4]Fundação Pró-Sangue–Hemocentro de São Paulo, São Paulo, Brazil. [5]Laboratório de Investigação Médica em Patogênese e Terapia dirigida em Onco-Imuno-Hematologia (LIM-31), Departamento de Hematologia, Hospital das Clínicas HCFMUSP, Faculdade de Medicina da Universidade de São Paulo, São Paulo, Brazil. [6]Fundação Hemominas–Fundação Centro de Hematologia e Hemoterapia de Minas Gerais, Belo Horizonte, Brazil. [7]Faculdade Ciências Médicas de Minas Gerais, Belo Horizonte, Brazil. [8]Department of Virology and Experimental Therapy, Institute Aggeu Magalhaes, Oswaldo Cruz Foundation, Recife, Brazil. [9]Department of Global Health and Population, Harvard T. H. Chan School of Public Health, Boston, MA, USA. [10]Department of Infectious Disease Epidemiology, School of Public Health, Imperial College London, London, UK. [11]Institute of Mathematics and Statistics, University of São Paulo, São Paulo, Brazil. [12]Center of Mathematics, Computing and Cognition–Universidade Federal do ABC, São Paulo, Brazil. [13]Oxford School of Global and Area Studies, Latin American Centre, University of Oxford, Oxford, UK. [14]Vitalant Research Institute, San Francisco, CA, USA. [15]University of California, San Francisco, CA, USA. [16]MRC Centre for Global Infectious Disease Analysis, J-IDEA, Imperial College London, London, UK. [17]Instituto Gonçalo Moniz–Fundação Oswaldo Cruz (Fiocruz), Salvador, Brazil. [18]Department of Zoology, University of Oxford, Oxford, UK. [19]Institute for Applied Economic Research–Ipea, Brasília, Brazil.

*These authors contributed equally to this work.

†Corresponding author. Email: sabinoec@usp.br (E.C.S.); nfaria@ic.ac.uk (N.R.F.)

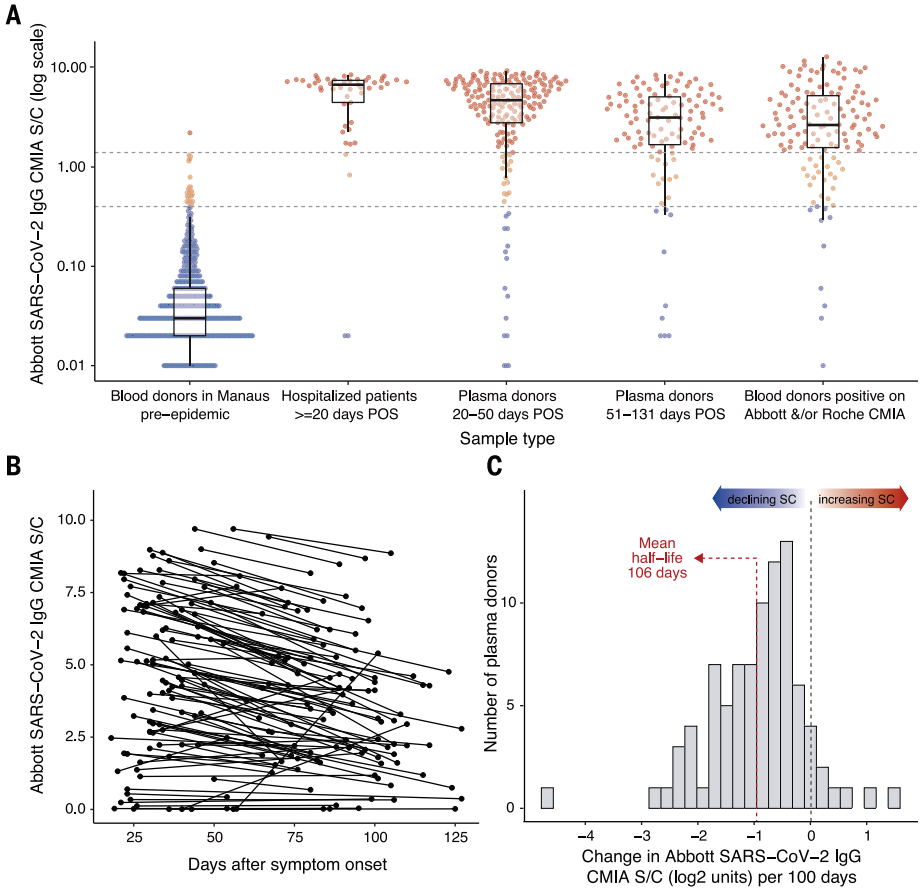


Fig. 1. Abbott SARS-CoV-2 N IgG chemiluminescence assay performance and antibody dynamics in different clinical samples. (**A**) Signal-to-cutoff (S/C) values using the Abbott chemiluminescence assay (CMIA) in the following clinical samples (from left to right): 821 routine blood donation samples from Manaus in February 2020, >1 month before the first notified case in the city; 49 samples collected at 20 to 33 days after symptom onset from SARS-CoV-2 PCR-positive patients in São Paulo requiring hospital care; 193 patients in São Paulo with PCR-confirmed symptomatic COVID-19 not requiring hospital care, with plasma donation samples taken in the early convalescent period; 107 samples from the same nonhospitalized plasma donor cohort from the late convalescent period; 133 samples that tested positive on either the Abbott CMIA or the Roche Elecsys assay out of 1000 routine blood donations collected in July 2020 and tested in parallel from the Fundação Pró-Sangue blood center (São Paulo). Upper dashed line denotes the manufacturer's threshold for positive result of 1.4 S/C; lower dashed line denotes an alternative threshold of 0.4 S/C. In the box plots of Abbott IgG CMIA S/C, the central line is the median; upper and lower hinges are the 25th and 75th centiles, respectively; whiskers show the range, extending to a maximum of 1.5 times the interquartile range from the hinge. (**B**) S/C values of the Abbott CMIA for 104 convalescent plasma donors who were sampled at two different times. (**C**) Histogram of the slopes among 88 individuals shown in (B) who tested positive (>1.4 S/C) at the first time point. POS, post–onset of symptoms.

may have reached as high as 66.2% (95% CI, 61.5% to 80.1%) in July and 76.0% (95% CI, 66.6% to 97.9%) in October. The reliability of this estimate depends on the validity of the exponential decay assumption, and in the absence of an accepted approach to account for seroreversion, these results should be interpreted with caution.

To calculate infection fatality ratios (IFRs), we used the prevalence (adjusted for sensitivity and specificity, and reweighted for age and sex) in June, as this followed the epidemic peak in Manaus but preceded appreciable seroreversion. In Manaus, the IFRs were 0.17% and 0.28%, taking into consideration the numbers of polymerase chain reaction (PCR)–confirmed COVID-19 deaths and probable COVID-19 deaths based on syndromic identification, respectively. In São Paulo, the global IFRs were 0.46% and 0.72%, respectively. The difference may be explained by an older population structure in São Paulo (fig. S1A). Supporting this inference, the age-specific IFRs were similar in the two cities, and were similar to estimates based on data from China (*16*) (fig. S1B) and a recent systematic review (*17*). We also obtained similar age-specific IFRs using the seroreversion-corrected prevalence estimates from October (fig. S1).

Blood donors may not be representative of the wider population. In both cities, the eligible age range for blood donation in Brazil (16 to 69 years) and the sex distribution of donors are different from those of the underlying population (fig. S2). Reweighting our estimates for age and sex (Fig. 2 and table S2) resulted in a slight reduction in prevalence, particularly in Manaus, where men were overrepresented among donors and also had a higher seroprevalence (fig. S3). Self-reported ethnicity in donors was similar to that of the census populations (fig. S2). The median income in blood donors' census tracts of residence was marginally higher than a population-weighted average for both cities (fig. S4). Regarding the spatial distribution of donors, there was a similar antibody prevalence across different regions sampled in both cities (fig. S5), and we achieved good geographic coverage in both cities (see supplementary materials and fig. S5).

Because potential donors are deferred if they have a positive SARS-CoV-2 PCR test or clinical diagnosis of COVID-19, increasing access to testing might have reduced the pool of eligible donors through time. However, only 2.7% of residents in Manaus and 8.5% in São Paulo reported having a PCR test performed by September (fig. S6). As such, changing access to testing is unlikely to have been important. Considering these factors together, we suggest that our results can be cautiously extrapolated to the population aged 16 to 69 years in Manaus and São Paulo. Within this group, studies of blood donors may underestimate the true exposure to SARS-CoV-2 because donors may have higher socioeconomic profiles and greater health awareness and engagement, and because symptomatic donors are deferred. However, it is likely that seroprevalence in children and older adults is lower.

Our results show that between 44% and 66% of the population of Manaus was infected with SARS-CoV-2 by July, following the epidemic peak there. The lower estimate does not account for false negative cases or antibody waning; the upper estimate accounts for both. R_t fell to <1 (fig. S7) in late April when cumulative infections were between 5% and 46% of the population. NPIs (table S3) were implemented in mid- to late March when physical distancing also increased (fig. S8). It is likely that these factors worked in tandem with growing population immunity to contain the

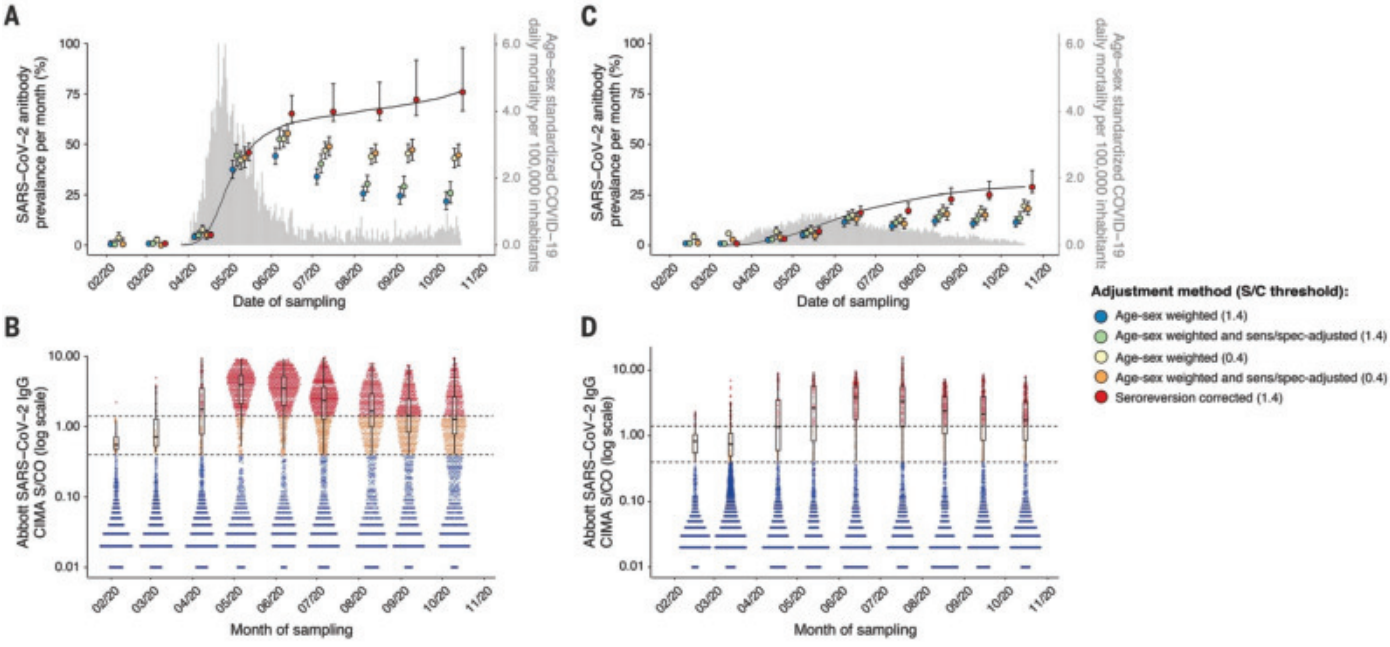


Fig. 2. Monthly antibody prevalence and signal-to-cutoff (S/C) reading in Manaus and São Paulo. (**A** and **C**) SARS-CoV-2 antibody prevalence estimates in Manaus (A) and São Paulo (C) with a range of corrections, from left to right: reweighting positive tests, at positivity threshold of 1.4 S/C, to the age and sex distribution of each city; further correcting for sensitivity and specificity at this assay threshold; reweighting positive tests for age and sex at a reduced threshold of 0.4 S/C; correcting for sensitivity and specificity at this threshold; and finally correcting for seroreversion. Error bars are 95% confidence intervals. Gray bars are standardized daily mortality using confirmed COVID-19 deaths from the SIVEP-Gripe (Sistema de Informação de Vigilância Epidemiológica da Gripe; https://covid.saude.gov.br/) notification system and standardized by the direct method using the total projected Brazilian population for 2020 as reference. Black lines are rescaled cumulative deaths, such that the maximum is set to the maximum seroprevalence estimate for each city. Mortality data are plotted according to the date of death. (**B** and **D**) Distribution of S/C values over the nine monthly samples are shown for Manaus (B) and São Paulo (D). Each point represents the S/C reading for a single donation sample. Upper dashed line denotes the manufacturer's threshold (1.4 S/C units); lower dashed line denotes an alternative threshold (0.4 S/C units); black box plots show the median (central lines), interquartile range (hinges), and range extending to 1.5 times the interquartile range from each hinge (whiskers) of S/C values above 0.4 (i.e., excluding very low and likely true-negative values).

epidemic. Transmission has since continued in Manaus, albeit to a lesser extent than in April and May (Fig. 2 and fig. S7). From the second week of August there has been a small increase in the number of cases (*18*), which, at the time of writing, has begun to decline. Consequently, the attack rate rose to 76% in October. This remains lower than predicted in a homogeneously mixed population with no mitigation strategies (~90%). Homogeneous mixing is unlikely to be a valid assumption (*19*), and behavioral change and NPIs may explain why the estimated final epidemic size has not yet reached 89 to 94%, as expected for R_0 values between 2.5 and 3.0 (*4*).

By 1 October, Manaus recorded 2642 [1193/million inhabitants (mil)] COVID-19 confirmed deaths and 3789 (1710/mil) severe acute respiratory syndrome deaths; São Paulo recorded 12,988 (1070/mil) and 20,063 (1652/mil), respectively. The cumulative mortality proportions were similar in both cities and high relative to other locations such as the United Kingdom (620/mil), France (490/mil), or the United States (625/mil) as of 1 October (*20*). The different attack rates in Manaus and São Paulo (76% versus 29% of people infected), despite similar overall mortality rates, are due to the higher IFR in São Paulo. The age-standardized mortality ratio was 2.0 comparing observed deaths in Manaus to those expected from projecting the age-specific mortality in São Paulo onto the age structure of Manaus. The R_0 was similar in the two cities (fig. S7), but cases and deaths increased and then decreased more slowly in São Paulo than in Manaus where both the rise and fall were more abrupt (fig. S7). The lower attack rate in São Paulo is partly explained by the larger population size (2.2 million versus 12.2 million inhabitants). As population size increases, the time to reach a given attack rate also increases (*21*).

The attack rate in Manaus is higher than estimates based on seroprevalence studies conducted in Europe and North America (*8*, *22*, *23*) and on recent results from Kenyan blood donors (*24*). A similarly high seroprevalence (~50%) was observed in slums in Mumbai, India (*25*). In Brazil, one population-based serosurvey in São Paulo (*26*) found a prevalence similar to that in our study (26.2% versus 28.8% in blood donors, in October). In Manaus, a lower seroprevalence (14%, in June) was found in a random household sample of 250 people (*1*). But this study was not powered at the city level and used the lower-sensitivity Wondfo (*27*) rapid test. As such, the results are not directly comparable.

Future investigations should be conducted to determine what accounted for such extensive transmission of SARS-CoV-2 in Manaus. Possible explanations include socioeconomic conditions, household crowding (*28*), limited access to clean water, and reliance on boat travel (*1*) in which overcrowding results in accelerated contagion, similar to that seen on cruise ships (*29*). The young mobile population with potentially low preexisting immunity to SARS-CoV-2 (*30*), as well as the early circulation of multiple virus lineages introduced from multiple locations, may have contributed to the large scale of the outbreak.

Our data show that >70% of the population had been infected in Manaus about 7 months after the virus first arrived in the city. This is above the theoretical herd immunity threshold. However, prior infection may not confer

long-lasting immunity (*30*, *31*). Indeed, we observed rapid antibody waning in Manaus, consistent with other reports that have shown signal waning on the Abbott IgG assay (*14*, *32*). However, other commercial assays, with different designs or targeting different antigens, have more stable signal (*14*), and there is evidence for a robust neutralizing antibody response several months out from infection (*33*). Rare reports of reinfection have been confirmed (*34*), but the frequency of its occurrence remains an open question (*35*). Manaus represents a "sentinel" population, giving us a data-based indication of what may happen if SARS-CoV-2 is allowed to spread largely unmitigated. Further seroepidemiological, molecular, and genomic surveillance studies in the region are required urgently to determine the longevity of population immunity, the correlation with the observed antibody waning, and the diversity of circulating lineages. Monitoring of new cases and the ratio of local versus imported cases will also be vital to understand the extent to which population immunity might prevent future transmission, and the potential need for booster vaccinations to bolster protective immunity.

REFERENCES AND NOTES

1. P. C. Hallal *et al*., *Lancet Glob. Health* **8**, e1390–e1398 (2020).
2. D. da S. Candido *et al*., *Science* **369**, 1255–1260 (2020).
3. J. D. Y. Orellana, G. M. da Cunha, L. Marrero, B. L. Horta, I. da Costa Leite, *Cad. Saude Publica* **36**, e00120020 (2020).
4. W. M. de Souza *et al*., *Nat. Hum. Behav.* **4**, 856–865 (2020).
5. J. Ma, D. J. D. Earn, *Bull. Math. Biol.* **68**, 679–702 (2006).
6. J. G. de Jesus *et al*., *Rev. Inst. Med. Trop. São Paulo* **62**, e30 (2020).
7. F. I. Lewis, P. R. Torgerson, *Emerg. Themes Epidemiol.* **9**, 9 (2012).
8. A. Bryan *et al*., *J. Clin. Microbiol.* **58**, e00941-20 (2020).
9. Public Health England, "Evaluation of Abbott SARS-CoV-2 IgG assay for the detection of anti-SARS-CoV-2 antibodies" (2020); www.gov.uk/government/publications/covid-19-laboratory-evaluations-of-serological-assays.
10. D. L. Ng *et al*., *Nat. Commun.* **11**, 4698 (2020).
11. D. W. Eyre *et al*., medRxiv 20159038 [preprint]. 25 July 2020.
12. F. Hamilton *et al*., *J. Infect.* 10.1016/j.jinf.2020.07.031 (2020).
13. Q.-X. Long *et al*., *Nat. Med.* **26**, 1200–1204 (2020).
14. F. Muecksch *et al*., *J. Infect. Dis.* jiaa659 (2020).
15. Public Health England, "Evaluation of Roche Elecsys Anti-SARS-CoV-2 serology assay for the detection of anti-SARS-CoV-2 antibodies" (2020); www.gov.uk/government/publications/covid-19-laboratory-evaluations-of-serological-assays.
16. R. Verity *et al*., *Lancet Infect. Dis.* **20**, 669–677 (2020).
17. N. Brazeau *et al*., "Report 34: COVID-19 infection fatality ratio: estimates from seroprevalence" (Imperial College London, 2020).
18. MAVE, Grupo de Métodos Analíticos em Vigilância Epidemiológica (PROCC/Fiocruz e EMAp/FGV), Resumo do Boletim InfoGripe–Semana Epidemiológica (SE) 42; https://gitlab.procc.fiocruz.br/mave/repo/tree/master/Boletins%20do%20InfoGripe.
19. T. Britton, F. Ball, P. Trapman, *Science* **369**, 846–849 (2020).
20. Our World in Data, "Coronavirus Pandemic (COVID-19)" (2020); https://ourworldindata.org/coronavirus.
21. B. Ridenhour, J. M. Kowalik, D. K. Shay, *Am. J. Public Health* **104**, e32–e41 (2014).
22. M. Pollán *et al*., *Lancet* **396**, 535–544 (2020).
23. S. Stringhini *et al*., *Lancet* **396**, 313–319 (2020).
24. S. Uyoga *et al*., *Science* 10.1126/science.eabe1916 (2020).
25. A. Malani *et al*., *Lancet Glob. Health* 10.1016/S2214-109X(20)30467-8 (2020).
26. SoroEpi MSP: Serial soroepidemiological survey to monitor the prevalence of SARS-CoV-2 infection in the Municipality of São Paulo, SP, Brazil (2020); www.monitoramentocovid19.org/.
27. V. A. dos Santos, M. M. Rafael, E. C. Sabino, A. J. da S. Duarte, *Clinics* **75**, e2013 (2020).
28. B. Rader *et al*., *Nat. Med.* 10.1038/s41591-020-1104-0 (2020).
29. K. Mizumoto, K. Kagaya, A. Zarebski, G. Chowell, *Euro Surveill.* **25**, 2000180 (2020).
30. A. W. D. Edridge *et al*., *Nat. Med.* **26**, 1691–1693 (2020).
31. K. A. Callow, H. F. Parry, M. Sergeant, D. A. J. Tyrrell, *Epidemiol. Infect.* **105**, 435–446 (1990).
32. S. F. Lumley *et al*., medRxiv 20224824 [preprint]. 4 November 2020.
33. A. Wajnberg *et al*., *Science* **370**, 1227–1230 (2020).
34. K. K.-W. To *et al*., *Clin. Infect. Dis.* ciaa1275 (2020).
35. J. Shaman, M. Galanti, *Science* **370**, 527–529 (2020).
36. Data and code for "Three-quarters attack rate of SARS-CoV-2 in the Brazilian Amazon during a largely unmitigated epidemic"; doi:doi.org/10.5061/dryad.c59zw3r5n.

ACKNOWLEDGMENTS

Funding: Supported by the Itau Unibanco "Todos pela Saude" program and by CADDE/FAPESP (MR/S0195/1 and FAPESP 18/14389-0) (http://caddecentre.org/); Wellcome Trust and Royal Society Sir Henry Dale Fellowship 204311/Z/16/Z (N.R.F.); the National Heart, Lung, and Blood Institute Recipient Epidemiology and Donor Evaluation Study (REDS, now in its fourth phase, REDS-IV-P) for providing the blood donor demographic and zip code data for analysis (grant HHSN268201100007I); and the UK Medical Research Council under a concordat with the UK Department for International Development and Community Jameel and the NIHR Health Protection Research Unit in Modelling Methodology. **Author contributions:** Conception, M.B.-N., L.F.B., M.C., B.C., C.d.A.N., N.R.F., S.C.F., A.M.J., A.S.N., R.H.M.P., V.R., E.C.S., N.A.S., T.S., M.A.d.S., and C.W.; acquisition, A.C.M.M., M.P.S.S.C., A.G.C., M.A.E.C., C.d.A.N., A.A.d.S.S., N.R.F., S.C.F., N.A.F., P.L.T., A.M.J., M.K.O., N.V., R.H.M.P., V.R., E.C.S., N.A.S., T.S., P.d.S.P., and M.A.d.S.; analysis, L.F.B., C.d.A.N., R.H.M.P., C.W., E.C.S., C.A.P., K.V.P., V.H.N., and M.C.B.; interpretation, A.C.M.M., L.F.B., M.P.S.S.C., A.G.C., M.A.E.C., C.d.A.N., N.R.F., N.A.F., E.C.S., M.A.d.S., C.W., C.D., M.U.G.K., O.P., and V.H.N.; drafting, L.F.B. and E.C.S.; revising, all authors; funding, M.B.-N., A.G.C., B.C., N.R.F., N.A.F., E.C.S., and N.A.S. **Competing interests:** The authors declare no competing interests. **Data and materials availability:** The data and code required to reproduce the results in this article can be found on Dryad (*36*). This project was approved by the Brazilian national research ethics committee, CONEP CAAE - 30178220.3.1001.0068. This work is licensed under a Creative Commons Attribution 4.0 International (CC BY 4.0) license, which permits unrestricted use, distribution, and reproduction in any medium, provided the original work is properly cited. To view a copy of this license, visit https://creativecommons.org/licenses/by/4.0/. This license does not apply to figures/photos/artwork or other content included in the article that is credited to a third party; obtain authorization from the rights holder before using such material.

SUPPLEMENTARY MATERIALS

science.sciencemag.org/content/371/6526/288/suppl/DC1
Materials and Methods
Figs. S1 to S9
Tables S1 to S3
References (*37*–*41*)
MDAR Reproducibility Checklist

28 September 2020; accepted 2 December 2020
Published online 8 December 2020
10.1126/science.abe9728

BEHAVIOR

Local convergence of behavior across species

Toman Barsbai[1,2]*†, Dieter Lukas[3]*†, Andreas Pondorfer[4,5]*†

Behavior is a way for organisms to respond flexibly to the environmental conditions they encounter. Our own species exhibits large behavioral flexibility and occurs in all terrestrial habitats, sharing these environments with many other species. It remains unclear to what extent a shared environment constrains behavior and whether these constraints apply similarly across species. Here, we show that foraging human populations and nonhuman mammal and bird species that live in a given environment exhibit high levels of similarity in their foraging, reproductive, and social behaviors. Our findings suggest that local conditions may select for similar behaviors in both humans and nonhuman animals.

Wherever they live, animals display diverse behaviors to cope with the many challenges they face—from foraging for food to finding shelter and protection to meeting with mates for reproduction (*1*). In any particular environment, a diversity of behavioral solutions might be expected given the differences in how animals experience and exploit their environment, especially if species fill specific niches to reduce resource competition (*2*). At the same time, local ecological constraints might only permit a certain range of behaviors. In this case, species with similar behaviors would be expected to assemble in a given environment. Convergence of behavior to ecological conditions has been found among closely related species (*3*–*5*), and consistent influences of ecological conditions on evolutionary patterns across distantly related taxonomic groups have been described for morphology [e.g., Bergman's rule (*6*) or Allen's rule (*7*)] and life history (*8*). On the basis of this interplay of competition and adaptation, we predict that

[1]School of Economics, University of Bristol, Bristol, UK. [2]Research Center International Development, Kiel Institute for the World Economy, Kiel, Germany. [3]Department of Human Behavior, Ecology and Culture, Max Planck Institute for Evolutionary Anthropology, Leipzig, Germany. [4]Department of Economics, University of Bonn, Bonn, Germany. [5]TUMCS for Biotechnology and Sustainability, Technical University of Munich, Munich, Germany.
***Corresponding author. Email: toman.barsbai@bristol.ac.uk (T.B.); dieter_lukas@eva.mpg.de (D.L.); andreas.pondorfer@tum.de (A.P.)**
†These authors contributed equally to this work.

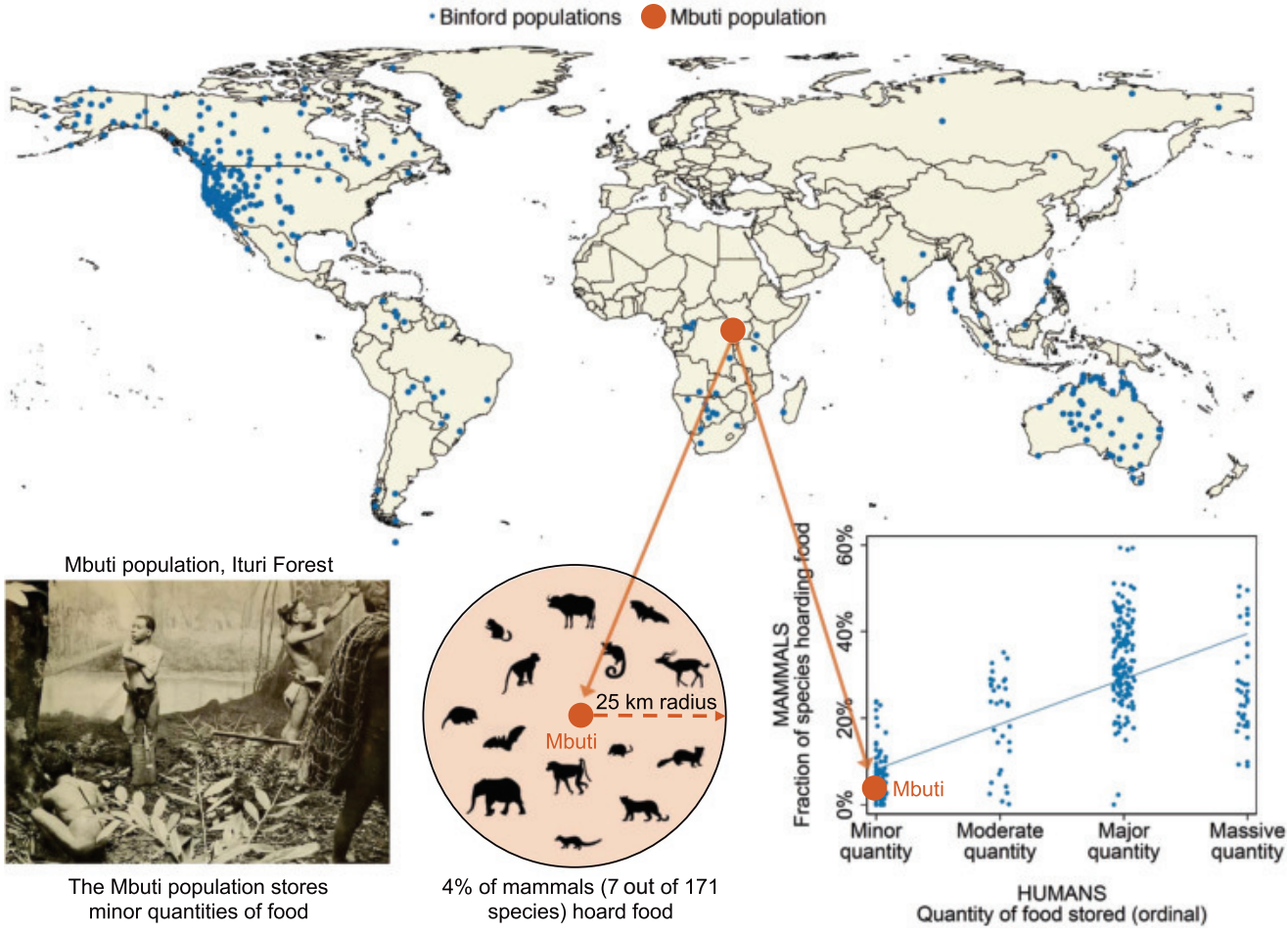


Fig. 1. Matching the behavioral variation of foraging humans, mammals, and birds around the world. For each of the 339 small-scale, subsistence-foraging populations from around the world (dots on map), we determined which mammal and bird species lived in the same location and computed their average behavior. For example, in the Mbuti population, which lives in the African rainforests, food storage is only minor and only 4% of the 171 mammal species living within a 25-km radius around the center of their population hoard food. Combining this information across populations shows that generally in locations where food storage among humans is more common, a higher proportion of local mammal species hoard food, as indicated by the upward slope in the scatter plot. Photo credit: Flickr Commons/PhyloPic public domain.

a limited subset of behaviors will exist at each locality, with similar behaviors found in similar environments around the world.

The role of ecological conditions in constraining behavioral variation is particularly debated with regards to our own species, which has colonized essentially all terrestrial environments in the world. On the one hand, there is evidence that cultural processes are responsible for the large variation in behavior observed across societies (*9*) and that we humans build our own ecological niche (*10*). By influencing the local ecology, humans might also make it more difficult for species with similar behaviors to coexist (*11*). Alternatively, human behavioral ecology contends that even if behavioral variation among societies primarily originates through cultural processes, the ecological constraints that influence behavior in other species also generally apply to our own species (*12*–*14*). We predict an interplay of competition and adaptation for humans, too: Different human societies might acquire different behaviors through different paths, but specific behaviors will be present where they fit into the local environment (*15*–*18*).

In this work, we take a unifying perspective and scrutinize the central tenet of behavioral ecology—that there are consistent and predictable adaptations to ecological conditions, which potentially operate across very different taxonomic groups. Specifically, we study whether the foraging, reproductive, and social behaviors of humans, mammals (we use the term mammal to refer to all species in the class Mammalia excluding humans), and birds are more similar to the behaviors of other species found in the same environment than they are to the behaviors found in different environments.

We built our analysis around an ethnographic database that provides data on the behavior of 339 human hunter-gatherer populations from around the world (*19*). Our focus is on small-scale, subsistence-foraging human populations because these populations are generally tied to a specific location. Additionally, their reliance on acquiring food from the available local resources means that we are more likely to detect ecological influences on their behavior, should they exist (*20*). For each of the human populations, we first identified all mammal and bird species that live in the same location. We then identified 15 behavioral variables encoded in the human database (six foraging, five reproductive, and four social behaviors) for which closely comparative data existed for the nonhuman species (tables S1 to S3). We assigned the typically observed behavior to each species (because both the extent and availability of data on behavioral variation within other species is limited) and computed average mammal and bird behaviors at the different locations. We were thus able to analyze the association between human, mammal, and bird behaviors across locations (Fig. 1).

Our results show that foraging human populations, mammals, and bird species that share a local environment converge in their foraging, reproductive, and social behaviors (Fig. 2). Specifically for foraging behavior (see also fig. S5), we detected the following: (i) Human populations that rely more on hunting terrestrial vertebrates for food occur where a higher proportion of local mammals and birds rely on vertebrates. (ii) Human populations that rely more on aquatic organisms for food occur where a higher proportion of local mammals and birds eat fish. (iii) We observed associations between the reliance of humans on food storage and the proportion of local mammals and birds that hoard food. (iv) There were associations in short-term movements to acquire resources, with human populations being central-place foragers (which is usually associated with longer day ranges because of local resource depletion) in locations where mammals have longer daily foraging trips (no bird data available). (v) There were also associations in long-term movements between resource locations, with humans moving longer distances between foraging locations in environments where birds migrate longer distances (no mammal data available). (vi) We observed associations between the total distribution area occupied by a human population and that occupied by the local mammal and bird species.

For reproductive behavior (see also fig. S6), we found the following connections in behavior: (i) Global variation in the age of first reproduction is linked across humans, mammals, and birds. (ii) Males are more likely to monopolize matings in certain places, with a higher proportion of human men being married to multiple women, more mammals living in unstable groups [providing monopolization potential (*21*)], and male birds investing more into their plumage to attract multiple females. (iii) In those locations where humans marry outside their group, mammals show longer breeding dispersal movements but birds show shorter ones. (iv) Splits between mating partners are more likely in some areas, with divorce permitted in human populations and bird pairs more likely to split up each year. (v) We did not find consistent associations between humans, mammals, and birds for patrilocality, where males stay at and females move away from their place of birth.

For social behavior (see also fig. S7), our analyses revealed the following associations: (i) The relative role of fathers contributing

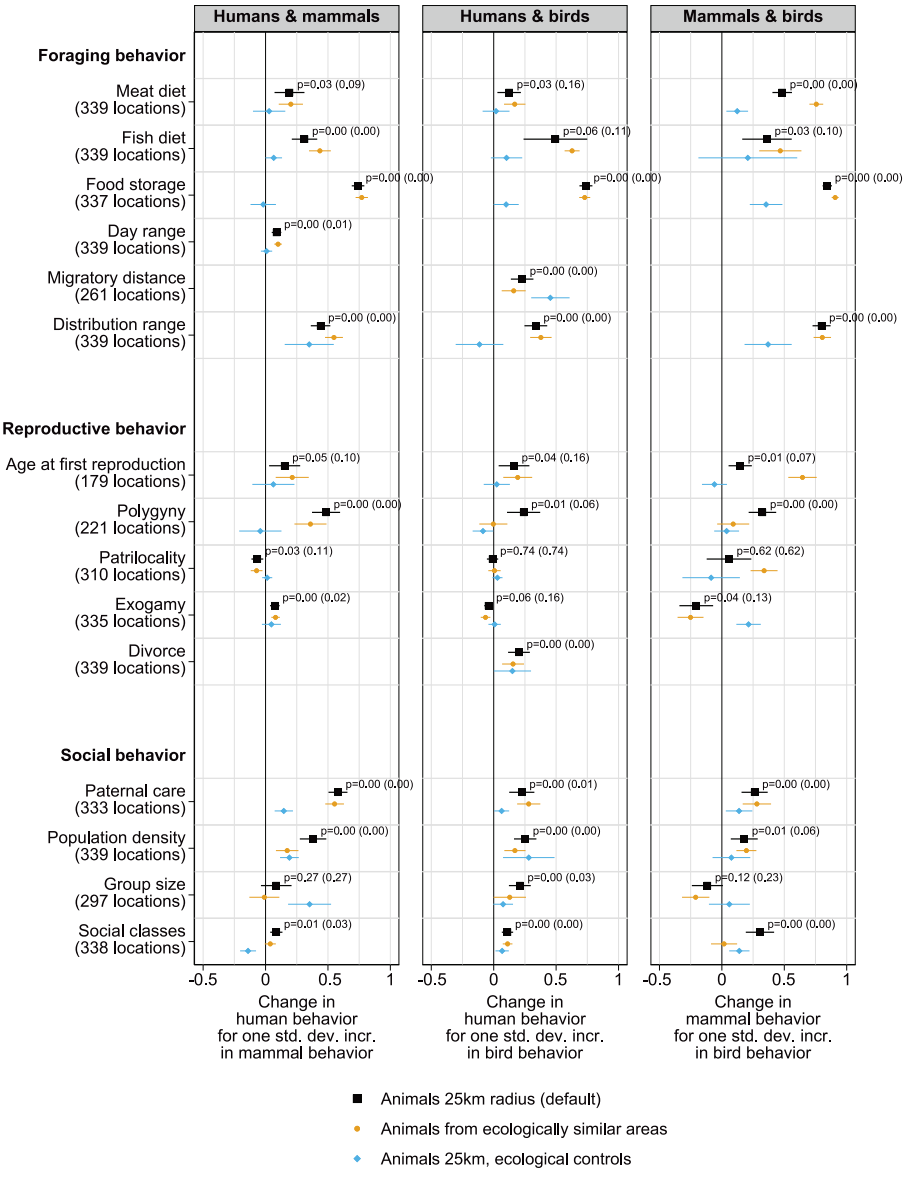


Fig. 2. Association in behavior between humans, mammals, and birds living at the same location. Dots show the estimated marginal effect of an ordinary least squares (OLS) regression and lines show the 90% confidence intervals. For the main specification, the figure also provides the unadjusted *P* values and *P* values that are adjusted for multiple testing in parentheses. All variables are standardized with a mean of 0 and a standard deviation (SD) of 1. The marginal effect thus shows by how many SDs human behavior changes for a 1-SD increase (std. dev. incr.) in mammal behavior (column 1), by how many SDs human behavior changes for a 1-SD increase in bird behavior (column 2), and by how many SDs mammal behavior changes for a 1-SD increase in bird behavior (column 3). For binary outcomes, the marginal effect reflects the change in the likelihood of a positive outcome for a 1-SD increase in mammal or bird behavior. We present estimates from three different specifications: (i) average behavior of all nonhuman species found within a 25-km radius of the center of the range of human populations (main specification), (ii) average behavior of nonhuman species in ecologically similar areas, and (iii) same as (i) but additionally controlling for ecological conditions.

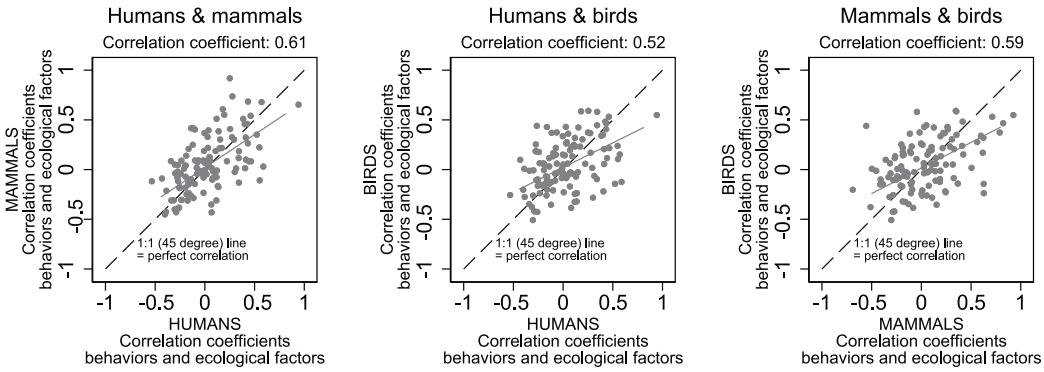


Fig. 3. Similarity in the correlation between behaviors and ecological factors across humans, mammals, and birds living at the same location. These plots visualize the similarity in correlation coefficients between different behaviors and ecological factors for humans, mammals, and birds. They reflect correlations between all 12 behaviors that we observe for the three groups and 10 ecological variables (including main biomes, in which Binford populations are located, latitude, altitude, and proximity to coast). See fig. S11 for more details on the underlying correlations.

resources to offspring differed—in locations in which human males provide a higher proportion of the diet for their family, males contribute to the feeding and carrying of offspring in a higher proportion of mammal species and are the sole providers of parental care in a higher proportion of bird species. (ii) Where humans live in higher densities, so do other mammals and birds. (iii) In locations in which residential group sizes in humans are larger, social group sizes of mammals are larger and birds are more likely to forage in groups than to rely on solitary foraging. (iv) Where human populations have social classes, more mammals and birds have a social system with dominant breeders and subordinate nonbreeding helpers.

Similarities in the behaviors of humans, mammals, and birds appear to result from selection pressures of the local environment. First, associations across species decline when we include ecological variables as covariates to explain the variation in behaviors (including biomes, latitude, altitude, and proximity to coast) (Fig. 2 shows results with ecological controls), which is consistent with the argument that ecological conditions constrain behavior. Second, associations between the same ecological variables and behaviors are very similar across humans, mammals, and birds (Fig. 3). Third, human behavior from one location matches that of animals found at another location with similar ecological characteristics (Fig. 2 shows results for animals from ecologically similar areas), which corroborates the hypothesis that associations arise from a consistent influence of ecological factors rather than spatial autocorrelation. Local convergence of behavior across species occurs in all environments, and the associations are not the result of extreme behaviors in extreme environments [fig. S2 shows results with controls for coastal and (sub)arctic areas]. In line with this evidence, although the associations in behavior across species are strongest when tested in the large worldwide sample, most associations are also present on a smaller scale when tested in an independent dataset of human populations in North America (fig. S4). Our results recapture several of the previously described associations between specific ecological factors and individual human (*22*, *23*) or nonhuman behaviors (*3*–*5*), which suggests that combining findings from different taxonomic groups might lead to a deeper understanding of how ecology shapes behavior.

Overall, our results highlight that environmental conditions appear to constrain the behaviors of humans and other animals in similar ways. Although our findings cannot reveal the processes of adaptation and how ecology interacts with cultural transmission processes that shape behavior, they suggest that there generally tends to be a specific set of behavioral solutions to the environmental challenges at a given location that is shared by humans, mammals, and birds. This pervasive influence of ecology on behavior raises the question of whether the behavioral diversity of modern human populations still reflects local ecological conditions, even though agriculture, market integration, and technology might modulate the response of behavior to local conditions.

REFERENCES AND NOTES

1. N. B. Davies, J. R. Krebs, S. A. West, *An Introduction to Behavioural Ecology* (Wiley, 2012).
2. M. S. Di Bitetti, C. D. De Angelo, Y. E. Di Blanco, A. Paviolo, *Acta Oecol.* **36**, 403–412 (2010).
3. P. H. Harvey, M. D. Pagel, *The Comparative Method in Evolutionary Biology* (Oxford Univ. Press, 1991), vol. 239.
4. J. H. Crook, *The Evolution of Social Organisation and Visual Communication in the Weaver Birds (Ploceinae)* (Behaviour, Brill, 1964).
5. D. R. Rubenstein, P. Abbot, *Comparative Social Evolution* (Cambridge Univ. Press, 2017).
6. S. Meiri, T. Dayan, *J. Biogeogr.* **30**, 331–351 (2003).
7. M. R. E. Symonds, G. J. Tattersall, *Am. Nat.* **176**, 188–197 (2010).
8. K. Healy *et al.*, *Proc. R. Soc. B* **281**, 20140298 (2014).
9. S. Mathew, C. Perreault, *Proc. R. Soc. B* **282**, 20150061 (2015).
10. J. Kendal, J. J. Tehrani, J. Odling-Smee, *Phil. Trans. R. Soc. B* **366**, 785–792 (2011).
11. N. L. Boivin *et al.*, *Proc. Natl. Acad. Sci. U.S.A.* **113**, 6388–6396 (2016).
12. M. Tallavaara, J. T. Eronen, M. Luoto, *Proc. Natl. Acad. Sci. U.S.A.* **115**, 1232–1237 (2018).
13. C. D. Forde, *Habitat, Economy and Society* (Methuen and Company Ltd., 1934).
14. B. Winterhalder, E. A. Smith, *Evol. Anthropol.* **9**, 51–72 (2000).
15. V. V. Venkataraman, T. S. Kraft, N. J. Dominy, K. M. Endicott, *Proc. Natl. Acad. Sci. U.S.A.* **114**, 3097–3102 (2017).
16. K. Hawkes, K. Hill, J. F. O'Connell, *Am. Ethnol.* **9**, 379–398 (1982).
17. M. B. Mulder, *Trends Ecol. Evol.* **3**, 260–264 (1988).
18. G. R. Brown, T. E. Dickins, R. Sear, K. N. Laland, *Phil. Trans. R. Soc. B* **366**, 313–324 (2011).
19. L. Binford, *Constructing Frames of Reference: An Analytical Method for Archaeological Theory Building Using Ethnographic and Environmental Data Sets* (Univ. California Press, 2001).
20. J. Helm, *Am. J. Sociol.* **67**, 630–639 (1962).
21. T. H. Clutton-Brock, *Proc. R. Soc. Lond. B* **236**, 339–372 (1989).
22. R. L. Kelly, *The Lifeways of Hunter-Gatherers: The Foraging Spectrum* (Cambridge Univ. Press, 2013).
23. R. B. Lee, I. DeVore, *Man the Hunter* (Routledge, 2017).
24. T. Barsbai, D. Lukas, A. Pondorfer, Title: Local convergence of behavior across species [Data set], version 1, Zenodo (2020); http://doi.org/10.5281/zenodo.4159697.

ACKNOWLEDGMENTS

We thank S. Bazzi, M. Borgerhoff Mulder, G. Brown, J. Call, I. Crawford, S. Gaechter, O. Galor, J. Henrich, K. Hill, K. Laland, C. Logan, S. Michalopoulos, M. Sutter, A. Whiten, participants of various conferences and seminars, and three anonymous reviewers for helpful feedback and discussions. **Funding:** We did not receive specific funding to conduct this study. During the study, T.B. was supported by the University of Bristol, the University of St Andrews, and the Kiel Institute for the World Economy; D.L. was supported by the Department of Human Behavior, Ecology and Culture at the Max Planck Institute for Evolutionary Anthropology; and A.P. was supported by the University of Bonn. **Ethics statement:** The data used are publicly available and cannot be used to identify individuals. **Author contributions:** All authors contributed equally to the conceptualization, data curation, methodology, formal analysis, visualization, validation, and article writing for this study. Authors are arranged alphabetically. **Competing interests:** The authors declare no conflicts of interest in relation to the content of this article. **Data and materials availability:** Final data on which analyses were run and the code necessary to replicate the analyses are available at Zenodo (*24*).

SUPPLEMENTARY MATERIALS

science.sciencemag.org/content/371/6526/292/suppl/DC1
Materials and Methods
Supplementary Text
Figs. S1 to S11
Tables S1 to S7
References (*25*–*71*)

16 March 2020; accepted 12 November 2020
10.1126/science.abb7481

QUANTUM GASES

Topological pumping of a 1D dipolar gas into strongly correlated prethermal states

Wil Kao[1,2]*, Kuan-Yu Li[1,2]*, Kuan-Yu Lin[2,3], Sarang Gopalakrishnan[4,5], Benjamin L. Lev[1,2,3]†

Long-lived excited states of interacting quantum systems that retain quantum correlations and evade thermalization are of great fundamental interest. We create nonthermal states in a bosonic one-dimensional (1D) quantum gas of dysprosium by stabilizing a super-Tonks-Girardeau gas against collapse and thermalization with repulsive long-range dipolar interactions. Stiffness and energy-per-particle measurements show that the system is dynamically stable regardless of contact interaction strength. This enables us to cycle contact interactions from weakly to strongly repulsive, then strongly attractive, and finally weakly attractive. We show that this cycle is an energy-space topological pump (caused by a quantum holonomy). Iterating this cycle offers an unexplored topological pumping method to create a hierarchy of increasingly excited prethermal states.

Highly excited eigenstates of interacting quantum systems are generically "thermal," in the sense that they obey the eigenstate thermalization hypothesis (*1*): Physical observables behave in these excited states as they would in thermal equilibrium. For generic thermal systems, all initial conditions give rise to locally thermal behavior at times past the intrinsic dynamical time scale. Systems in which thermalization is absent are of great fundamental interest because they violate equilibrium statistical mechanics, and of technological interest because some quantum information in these states evades decoherence. Nonthermal excited states exist in integrable (*2*, *3*) and many-body localized (*3*, *4*) systems. More recently, it has been realized that even nonintegrable systems might have special excited initial states for which thermalization is absent; these states are called quantum many-body scars (*5*–*10*). Both integrability and scars are fine-tuned, and can thus only be approximately realized in actual experiments, in the form of long-lived prethermal states. As anticipated in (*10*, *11*), approximate integrability can give rise to states that closely resemble scars: i.e., atypical initial states with unexpectedly long relaxation times. In such prethermal states, one would expect observables to remain far from their thermal value for long times. Much about the classification, physical origins, and lifetimes of such atypical initial states remains unclear.

In this work, we demonstrate a "topological" pumping protocol for creating a hierarchy of atypical prethermal states by cyclically varying the short-range (contact) interaction strength of a dipolar Bose gas confined in one dimension. The cycles are made possible through dipolar stabilization of the gas. In a conventional topological pump (*12*), the Hamiltonian returns to itself after one cycle, but the state is translated by one lattice site. In the present setup, by contrast, the state is translated up the many-body energy spectrum; thus, this protocol maps each eigenstate to an eigenstate with an extensively higher energy. This effect is called a "quantum holonomy" (*13*). A toy example that illustrates this effect is a particle subject to a δ-function potential. The nth even-parity eigenstate for an infinitely repulsive potential is identical to the $(n + 1)$th even-parity eigenstate for an infinitely attractive potential. Hence, by cycling the potential from zero to infinitely repulsive, to infinitely attractive and back to zero, one can wind up the phase of the wave function and create a sequence of increasingly excited states (*14*). Here, we show that dipolar interaction-stabilized approximate integrability allows one to implement a many-body version of this cycle without simply heating up the system. This many-body cycle enables one to generate nonthermal highly excited states with high fidelity.

The one-dimensional (1D) gas system forms an attractively interacting, excited "super-Tonks-Girardeau" gas (sTG) at an intermediate stage of the many-body holonomy cycle implemented here. The bosons in this state are even more strongly anticorrelated than free fermions (*15*–*20*). As one quenches deeper into the sTG regime by making the contact interactions less strongly attractive, one expects the sTG to become unstable; this is indeed seen in gases with purely short-range interactions (*18*). Unexpectedly, however, even though the dipole-dipole interaction (DDI) breaks integrability (*21*), it enhances the stability of the sTG regime (relative to the purely short-range case). This allows one to implement the entire cycle, thus realizing this previously unobserved topological pumping phenomenon. [Dipolar sTGs have been predicted to exist in contexts different from that realized here; see (*22*) for discussion.]

We implement the following protocol. First, we create a low-temperature dipolar 1D Bose gas in a regime with weak repulsive contact interactions. We then tune the scattering length across confinement-induced resonances (CIRs) of colliding atoms (*23*–*26*) in the following stages. First, we ramp up the contact interactions toward the resonance, so the gas adiabatically enters the strongly antibunched Tonks-Girardeau (TG) state (*27*–*29*). At this point, we quench these interactions across the resonance, from strongly repulsive to strongly

[1]Department of Applied Physics, Stanford University, Stanford, CA 94305, USA. [2]E. L. Ginzton Laboratory, Stanford University, Stanford, CA 94305, USA. [3]Department of Physics, Stanford University, Stanford, CA 94305, USA. [4]Physics and Astronomy, CUNY College of Staten Island, Staten Island, NY 10314, USA. [5]Physics Program and Initiative for Theoretical Sciences, The Graduate Center, CUNY, New York, NY 10016, USA.
*These authors contributed equally to this work.
†Corresponding author. Email: benlev@stanford.edu

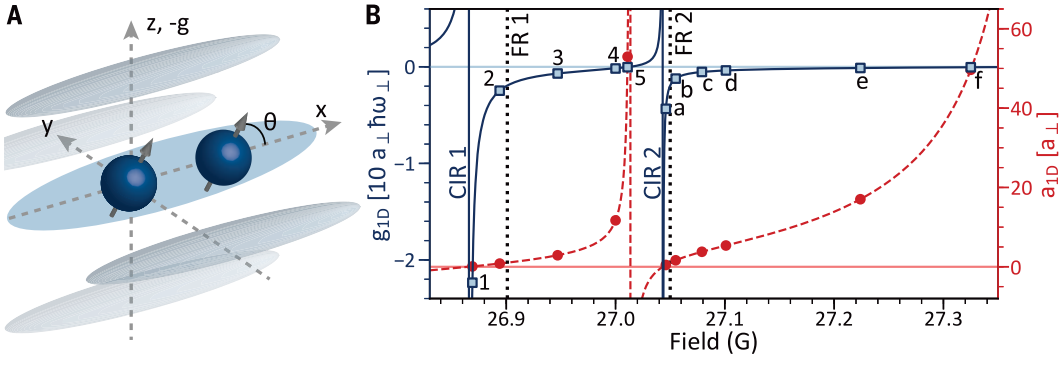


Fig. 1. Experimental concept. (**A**) Atoms are loaded into 1D traps formed by a 2D optical lattice. Atomic dipoles are aligned by a magnetic field at angle θ from $\hat{x}$ in the x–z plane. (**B**) The applied field magnitude tunes the contact interaction strength g_{1D} (solid blue line) and 1D scattering length a_{1D} (dashed red line) via two confinement-induced resonances (CIRs) located on the low-field side of Feshbach resonances (FRs) indicated by black dotted lines. $g_{1D} < 0$ measurements are labeled by numbers and letters for the first and second holonomy cycles, respectively.

attractive, to create the sTG. As the attractive interactions are tuned away from this unitary contact regime, the sTG gas usually becomes thermodynamically unstable because the bosons can form soliton-like bound cluster states (*15*, *16*, *30*), as has been observed in a nondipolar Cs gas (*18*). By contrast, our dipolar system appears dynamically stable for very long times. This allows us to then ramp the attractive contact interaction strength toward zero again to generate a weakly attractive Bose gas in a highly excited nonthermal state. That the system remains dynamically stable throughout this procedure is a consequence of the repulsive dipolar interactions, as we will discuss below. Repeating the cycle by crossing another CIR produces even higher excited states. These claims are supported through gas stiffness and energy-per-particle measurements at various stages in the protocol.

We begin our experiments by preparing a nearly pure Bose-Einstein condensate (BEC) of highly magnetic Dy atoms at 26.69 G, just shy of the CIRs employed. (^{162}Dy's magnetic moment of $\mu = 10$ Bohr magnetons is 10 times that of, e.g., Cs's, yielding a DDI ~100 times stronger.) After adiabatically rotating the field to a target angle θ with respect to the 1D axis $\hat{x}$, we load the BEC into a 2D optical lattice (*21*) whose first transverse excited-state energy is $\hbar\omega_\perp/k_B = 1180(20)$ nK. The transverse frequency is $\omega_\perp = 2\pi \times 24.6(4)$ kHz; $\hbar = 2\pi\hbar$ is Planck's constant, and k_B is the Boltzmann constant. The lattice comprises an array of ~1000 1D optical traps with about 40 atoms in the central tube and 30 atoms per tube on average; see Fig. 1A and (*22*). Each tube approximates a 1D channel of finite length, where the ratio of longitudinal versus transverse oscillator lengths is $a_\parallel/a_\perp = 25$. The field is then further ramped (in a few milliseconds) to the target magnitude at which collective oscillation measurements are to be performed; see (*22*) for details. These measurements are consistent with zero-temperature ground state predictions (*22*), which implies that the temperature is sufficiently low to observe the sTG gas (*31*).

The system may be described with a Lieb-Liniger (LL) Hamiltonian (*32*, *33*) augmented by the magnetic DDI:

$$H = -\frac{\hbar^2}{2m}\sum_{j=1}^{N}\frac{\partial^2}{\partial x_j^2} + \sum_{1\le i<j\le N}\left[g_{1D}\delta(x_i - x_j) + V_{DDI}^{1D}(\theta, x_i - x_j)\right] \quad (1)$$

where the first two terms comprise the LL model and the third is the 1D-regularized DDI (*22*). Because the DDI scales as $1 - 3\cos^2\theta$, we can control its sign and strength by applying an external magnetic field **B** to polarize the dipoles at any θ. The contact interaction strength g_{1D} is independently controlled by setting the field magnitude B to be near a CIR while holding θ constant; see Fig. 1B.

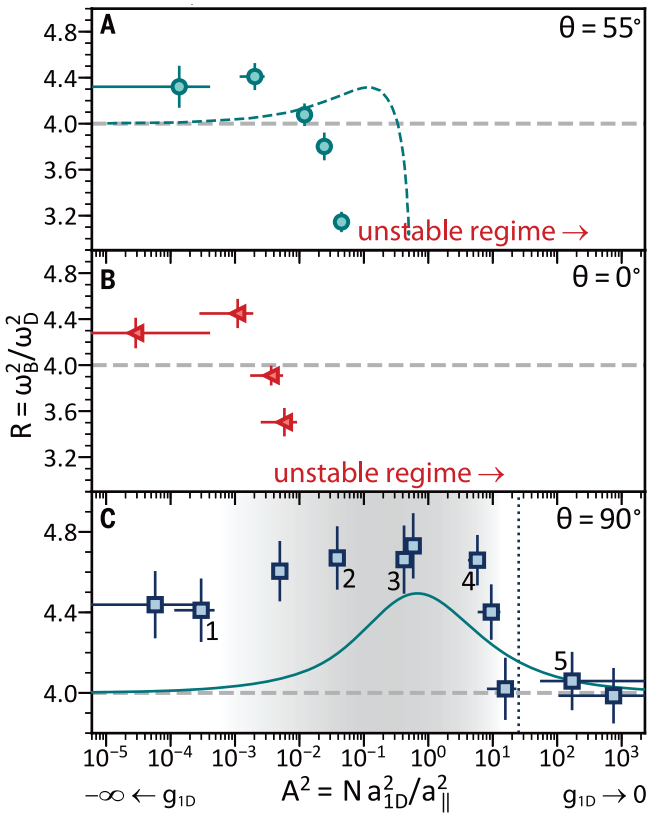


Fig. 2. Post-quench gas stiffness *R* versus interaction parameter A^2. Shown is the attractive $g_{1D} < 0$ regime of the first holonomy cycle for the (**A**) nondipolar ($\theta = 55°$) and (**B**) attractive DDI (0°) system, and for (**C**) the repulsive, 90° DDI-stabilized excited gas. In (A) and (B), an sTG gas exists in the unitary regime of $A^2 \lesssim 10^{-3}$. Beyond, however, the gas softens before collapsing near $A^2 \approx 10^{-1}$ and 10^{-2}, respectively. For comparison, the dashed green curve in (A) plots data from the nondipolar variational Monte Carlo simulation of (*15*). Unexpectedly, the repulsive DDI system in (C) remains stable beyond the unitary regime. This allows correlated prethermal states to emerge around intermediate coupling strengths, indicated by gray shading, before crossing over into the $R = 4$ weakly attractive, excited Bose gas regime beyond $A^2 \approx 10$. The solid curve is the Bethe ansatz prediction of (*18*). The vertical dotted line indicates where the contact and the short-range 1D-regularized DDI contributions become approximately equal (*21*). Numbers refer to points in Figs. 1B and 3. The error bars here and in subsequent figures represent the standard error.

A CIR appears when the bound state of the first transverse motional excited state of the 1D trap is degenerate with the open-channel transverse ground state. It modifies the contact interaction strength as follows:

$$g_{1D}(B) = -\frac{2\hbar^2}{m a_{1D}(B)} = \frac{2\hbar^2 a_{3D}(B)}{m a_\perp^2}\frac{1}{1 - C a_{3D}(B)/a_\perp} \quad (2)$$

Here, $C \approx 1$ and a_{3D} and a_{1D} are the 3D and 1D scattering lengths, respectively (*24*). We tune g_{1D} by controlling a_{3D} with a Feshbach resonance at fixed $a_\perp$. Feshbach resonances provide a means for tuning a_{3D} through control of B (*34*). The gas enters the unitary contact-interaction regime $\gamma \to \pm\infty$ when B sets $a_{3D} = a_\perp/C$ (*35*). The dimensionless LL parameter is $\gamma = g_{1D}m/\hbar^2 n_{1D}$, with n_{1D} the 1D atomic density.

Although the DDI has been predicted to affect CIRs (*22*, *36*), we resolve no shift of these resonances' positions or widths versus θ in our molecular bound-state measurements (*22*). Indeed, their positions are adequately predicted by the nondipolar theory result of Eq. 2. This simplifies the mapping of B to a_{3D} (and hence to g_{1D}) by rendering it θ-independent. We implement the holonomy cycle(s) by sweeping B up to a desired higher-field value, thereby preparing a state with a particular g_{1D}. The second holonomy cycle begins after point *5* in Fig. 1B, where g_{1D} turns positive again, and continues to point *f* where g_{1D} crosses zero again.

We measure gas stiffness through observations of collective oscillations of the atoms along the 1D trap axis (*18*, *37*, *38*). The frequency ω_B of the breathing mode of the gas is sensitive to its inverse compressibility (stiffness), and thus contains information about correlations. Normalizing ω_B by the frequency ω_D of the center-of-mass dipole (sloshing) mode accounts for nonuniversal aspects of the 1D potentials, such as trap frequencies (*38*). This allows one to compare the stiffness of disparate systems at different interaction strengths by plotting $R = (\omega_B/\omega_D)^2$ versus $A^2 = N a_{1D}^2/a_\parallel^2$. Here, A is the universal form of the coupling constant under the local density approximation

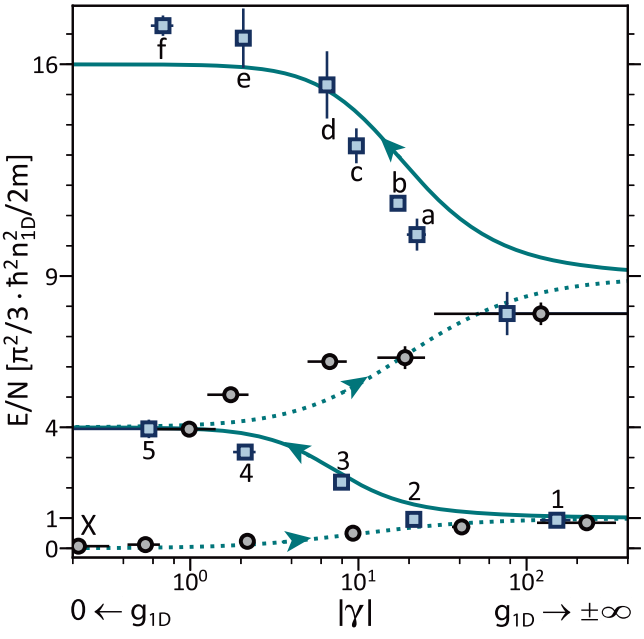


Fig. 3. Energy eigenstate spectrum across two complete quantum holonomy cycles. Shown is the energy per particle E/N for $\theta = 90°$. Black circles (blue squares) are data taken for positive (negative) g_{1D}'s of the repulsive (attractive) LL model. Likewise, dotted (solid) curves are solutions to the Bethe ansatz equations for the repulsive (attractive) nondipolar LL model. In the $g_{1D} \to 0$ and $\pm\infty$ limits, these solutions equal integer multiples of 1/3 times the Fermi energy $\hbar^2(\pi n_{1D})^2/2m$. Arrowheads indicate direction of cycles. The first cycle begins at the point labeled "*X*" and continues to point 5, where the second cycle begins and continues to *f*. The system passes through $|\gamma| \to \infty$ twice as the field increases first through CIR 1, then CIR 2.

(*38*). At strong coupling ($g_{1D} \to \pm\infty$), $A^2 \to 0$, whereas it diverges at weak coupling ($g_{1D} \to 0^{\pm}$). To measure oscillations, we selectively excite one of these two modes and hold the gas for a variable amount of time before releasing to image its width or center-of-mass in time-of-flight absorption imaging. We repeat for the other mode and fit the oscillations to extract collective-mode frequencies and R values (*22*).

Figure 2 shows stiffness data for excited states of the attractive ($g_{1D} < 0$) dipolar LL model at three different θ. [Data for ground states of the repulsive $g_{1D} > 0$ model are in (*22*).] We begin with the nondipolar case of $\theta = 55°$ (at which the DDI vanishes along the 1D tube) in Fig. 1A, so as to compare to prior nondipolar Cs measurements (*18*) and to nondipolar theory (*16*). After preparing a TG gas (for which $R = 4$) by tuning $\gamma \to +\infty$ (*22*), we quench into the attractive contact regime where $\gamma \to -\infty, A^2 \to 0$, and the TG gas crosses over into the sTG gas. Tuning A^2 larger causes the stiffness to rise above $R = 4$, indicating that a stiffer—more strongly (anti)correlated—sTG gas forms. At still larger A^2, R rapidly decreases as the gas softens, indicating an imminent collapse into bound cluster states. This trend resembles that reported for the Cs system (*18*), though the exact point of collapse differs from that exhibited in the Cs system. It also differs from the collapse point in the simplified nondipolar variational Monte Carlo calculation of (*15*) (shown as a dashed curve); see (*22*) for discussion. We additionally report metastable states just below $R = 4$: These might be gas-like states of clusters of two or three bound atoms (*17*).

Why should this nondipolar gas collapse, given that the attractive LL model remains integrable for all A^2? In the strictly integrable limit, collapse does not occur, and instead the stiffness rises above $R = 4$ until $A^2 \approx 1$, then decreases to 4 in the weakly attractive regime (*19*). Many-body states with and without clusters belong to separate sectors of Hilbert space, and do not mix. However, in realistic experiments [including nondipolar ones (*18*)], imperfections such as the transverse and longitudinal trap potentials break integrability (*39*–*41*) and yield matrix elements (proportional to the wave function overlap) between the sTG state and the bound cluster states, leading to collapse. In the strongly interacting unitary limit $A^2 \lesssim 10^{-3}$, antibunching strongly suppresses wave function overlap, so the model remains nearly integrable and stable despite experimental imperfections. However, in the intermediate interaction regime, cluster states form and the nondipolar gas is dynamically unstable, as seen in Fig. 2A.

The collapse ensues even earlier if an attractive DDI is introduced by rotating to $\theta = 0°$: Figure 2B shows a collapse beginning at roughly an order-of-magnitude lower in A^2. Evidently, the attractive DDI acts to break integrability at a point deeper within the unitary regime. Indeed, previous work using this experimental platform showed that DDIs generically break integrability (*21*), with equilibration lifetimes that are shortest at 90°. From this perspective, one might also expect an early collapse under a repulsive DDI. Unexpectedly, however, this is not the case: The $\theta = 90°$ data in Fig. 2C show that the sTG remains stable orders of magnitude beyond both that of the nondipolar gas and the 0° attractive DDI gas. Indeed, the repulsive gas never collapses: $R \gtrsim 4$ throughout the pumping sequence, regardless of contact strength in the first holonomy cycle. This includes the regime of vanishing contact interactions wherein nondipolar sTG gases collapse. By contrast, dipolar BECs in higher dimensions collapse whenever the attractive contact exceeds the DDI (*42*), and thus cannot be stably tuned through the regime of intermediate contact interactions.

How the repulsive DDI inhibits the sTG eigenstate from mixing with cluster eigenstates is unclear. Variational Monte Carlo simulations of a nondipolar gas in a harmonic trap may provide some intuition. Such calculations exhibit an energy barrier to collapse that shrinks as A^2 grows (*15*), and the repulsive (attractive) DDI may serve to raise (lower) this barrier. However, given the relatively low DDI energy scale, a more appropriate physical picture may be the following: The attractive and repulsive DDIs induce opposite first-order corrections to the wave function (leading to bunching in one case and antibunching in the other), which respectively enhance or suppress the effects of other integrability-breaking terms. Indeed, the low DDI energy scale does not seem to change the Thomas–Fermi–to–TG crossover of the ground states of the repulsive LL model (*22*). Nevertheless, the DDI does have a pronounced affect on the stability of the excited states, rendering their R dependence quite similar to that predicted by the Bethe ansatz equations (*19*). Quantitative discrepancies are not surprising, as the Bethe ansatz solutions exclude effects caused by, e.g., the DDI, trap, and imperfect state preparation.

Next, we explore those states obtained by sweeping B past the second CIR, thereby entering the second holonomy cycle in g_{1D} as reflected in the eigenenergy spectrum (*13*). Energy per particle E/N is measured in time-of-fight absorption imaging. The average momentum is determined from the expansion time and gas width, ensemble averaged over the 1D trap array (*22*). This is shown in Fig. 3, where E/N is plotted versus γ along with the eigenenergy bands derived from the Bethe ansatz equations (*13*, *19*, *22*). We see that crossing the second CIR maps the system to higher-energy eigenstates than those at the same g_{1D} in the previous topological pumping cycle. The orientation of the quench cycle is crucial: Reversing the sense of the cycle does not implement the topological pump, but leads to collapse (*13*, *22*). The measured energies are in good agreement with the Bethe ansatz predictions.

In the regime between the unitary and weakly interacting regimes—i.e., for $10^{-3} < A^2 < 10$ ($1 < \gamma < 10^2$)—the states that we generate form a hierarchy of long-lived, highly excited

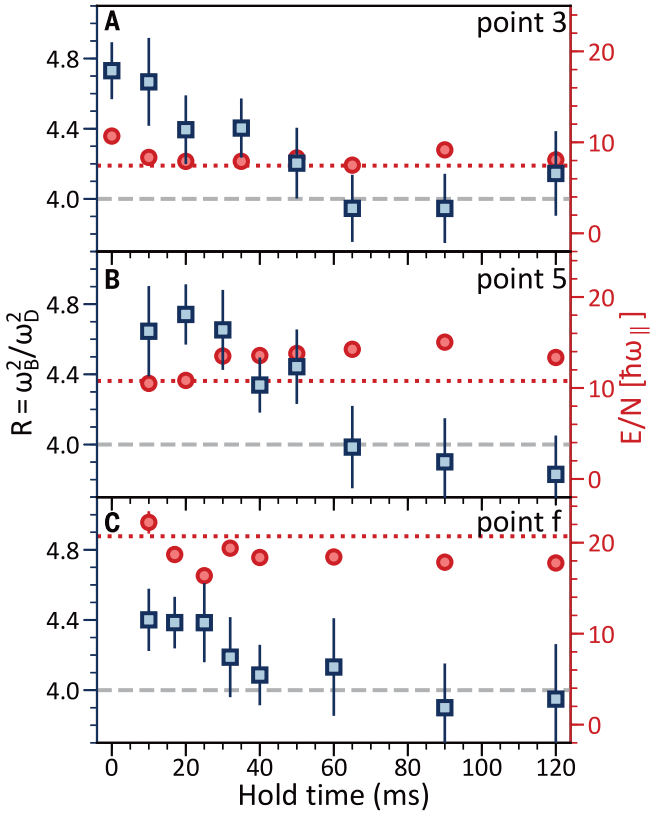


Fig. 4. Evidence for slow thermalization without heating. Plotted are stiffness R (squares) and energy per particle $\frac{E}{N}$ (circles) versus hold time for excited-state gases prepared in the attractive first and second holonomy levels. For reference, $\omega_\parallel = \omega_D$ is $2\pi \cdot 38$–43 Hz for these data and $\theta = 90°$. The time scale associated with the value of ω_B at $t = 0$ in these data is 11 to 12 ms, indicating that the states persist over many oscillation periods. The error bars for the energy per particle data are of the same size or smaller than the data markers. (**A**) Data for the state at point 3. (**B**) and (**C**) show similar data for weakly attractive excited states at points 5 and *f*, respectively. These data are taken by sweeping the field up to the point 5 or *f*, holding, and then sweeping back down to point 3 before making measurements of E/N and R; see text for details. The energy stays approximately constant near the Bethe ansatz prediction (red dotted line) in all cases. This implies that the decay in stiffness toward the thermal-state value $R = 4$ is caused purely by thermalization and is not due to heating (i.e., to an increase in entropy rather than energy). Thus, atypical excited states can be prepared and persist for long times in both the strongly and weakly interacting regimes. Data for points 5 and *f* at $t = 0$ are absent, as these points simply possess the R of the state at point 3.

states that exhibit persistent athermal behavior. (In this respect, they resemble quantum many-body scars.) To establish this, we demonstrate that they are atypical and distinct from thermal states at the same E/N. We do so by observing both R and the energy of these states as a function of time held in that state. We begin with point 3. Figure 4A shows that although R slowly decreases to the $R = 4$ value of a thermal state (*43*), its E/N stays the same. Thus, in becoming a thermal state, the gas must be increasing its entropy because it does not heat. This implies that the initial strongly correlated state with $R = 4.7$ is atypical, yet sufficiently long-lived to be well-characterized by collective oscillation measurements.

To show that the gas is nonthermal throughout the holonomy cycles, we repeat this measurement for two weakly interacting excited states: points 5 and *f* in the first and second attractive holonomy levels; see Fig. 4, B and C, respectively. Bethe ansatz predicts that these states will have R's close to 4 [as confirmed in (*22*)], inconveniently just like thermal states. To distinguish them from thermal states using stiffness, we sweep B back to point 3 after a variable hold time. Point 3's stiffness is naturally above 4; thus, this method for measuring R should yield values greater than 4 as long as the excited state held at point 5 or *f* is nonthermal. Recall that R is a proxy for anticorrelations in the sTG state. As shown in Fig. 4, B and C, we indeed find that neither gas immediately relaxes to an $R = 4$ thermal state nor significantly heats.

In conclusion, we experimentally realized a spectral topological pump that takes a Bose gas from its ground state to a "ladder" of nonthermal excited states; we demonstrated the first two steps on this ladder. The central topological feature of this pump—quantum holonomy—is only strictly well-defined in the integrable limit. The imperfections in any realistic experiment imply that one is never at the integrable limit, and render the system unstable. However, dipolar interactions (which themselves break integrability) stabilize the sTG against the effects of other integrability-breaking perturbations and increase the lifetime of the prethermal states long enough that one can complete a full cycle and thus experimentally utilize the holonomy. The observation that two integrability-breaking perturbations can counteract each other might have wide-ranging implications for understanding the onset of chaos in nearly integrable quantum systems (*21*, *44*, *45*, *46*). Future work can characterize these excited states through measurements of dynamic susceptibility and lifetime versus θ.

REFERENCES AND NOTES

1. L. D'Alessio, Y. Kafri, A. Polkovnikov, M. Rigol, *Adv. Phys.* **65**, 239–362 (2016).
2. M. Rigol, V. Dunjko, M. Olshanii, *Nature* **452**, 854–858 (2008).
3. R. Vasseur, J. E. Moore, *J. Stat. Mech.* **2016**, 064010 (2016).
4. D. A. Abanin, E. Altman, I. Bloch, M. Serbyn, *Rev. Mod. Phys.* **91**, 021001 (2019).
5. H. Bernien *et al.*, *Nature* **551**, 579–584 (2017).
6. N. Shiraishi, T. Mori, *Phys. Rev. Lett.* **119**, 030601 (2017).
7. C. J. Turner, A. A. Michailidis, D. A. Abanin, M. Serbyn, Z. Papić, *Nat. Phys.* **14**, 745–749 (2018).
8. E. J. Heller, *Phys. Rev. Lett.* **53**, 1515–1518 (1984).
9. S. Moudgalya, S. Rachel, B. A. Bernevig, N. Regnault, *Phys. Rev. B* **98**, 235155 (2018).
10. F. Marcus Kollar, A. Wolf, M. Eckstein, *Phys. Rev. B* **84**, 054304 (2011).
11. V. Khemani, C. R. Laumann, A. Chandran, *Phys. Rev. B* **99**, 161101 (2019).
12. D. J. Thouless, *Phys. Rev. B* **27**, 6083–6087 (1983).
13. N. Yonezawa, A. Tanaka, T. Cheon, *Phys. Rev. A* **87**, 062113 (2013).
14. S. Kasumie, M. Miyamoto, A. Tanaka, *Phys. Rev. A* **93**, 042105 (2016).
15. G. E. Astrakharchik, D. Blume, S. Giorgini, B. E. Granger, *Phys. Rev. Lett.* **92**, 030402 (2004).
16. G. E. Astrakharchik, J. Boronat, J. Casulleras, S. Giorgini, *Phys. Rev. Lett.* **95**, 190407 (2005).
17. M. T. Batchelor, M. Bortz, X. W. Guan, N. Oelkers, *J. Stat. Mech. Theory Exp* **2005**, L10001 (2005).
18. E. Haller *et al.*, *Science* **325**, 1224–1227 (2009).
19. S. Chen, L. Guan, X. Yin, Y. Hao, X.-W. Guan, *Phys. Rev. A* **81**, 031609 (2010).
20. P. Solano *et al.*, *Phys. Rev. Lett.* **123**, 173401 (2019).
21. Y. Tang *et al.*, *Phys. Rev. X* **8**, 021030 (2018).
22. See supplementary materials.
23. M. Olshanii, *Phys. Rev. Lett.* **81**, 938–941 (1998).
24. T. Bergeman, M. G. Moore, M. Olshanii, *Phys. Rev. Lett.* **91**, 163201 (2003).
25. H. Moritz, T. Stöferle, K. Günter, M. Köhl, T. Esslinger, *Phys. Rev. Lett.* **94**, 210401 (2005).
26. E. Haller *et al.*, *Phys. Rev. Lett.* **104**, 153203 (2010).
27. M. Girardeau, *J. Math. Phys.* **1**, 516–523 (1960).
28. B. Paredes *et al.*, *Nature* **429**, 277–281 (2004).
29. T. Kinoshita, T. Wenger, D. S. Weiss, *Science* **305**, 1125–1128 (2004).
30. J. B. McGuire, *J. Math. Phys.* **5**, 622–636 (1964).
31. M. Kormos, G. Mussardo, A. Trombettoni, *Phys. Rev. A* **83**, 013617 (2011).
32. T. Giamarchi, *Quantum Physics in One Dimension*, International Series of Monographs on Physics (Clarendon, 2003).
33. M. A. Cazalilla, R. Citro, T. Giamarchi, E. Orignac, M. Rigol, *Rev. Mod. Phys.* **83**, 1405–1466 (2011).
34. C. Chin, R. Grimm, P. Julienne, E. Tiesinga, *Rev. Mod. Phys.* **82**, 1225–1286 (2010).
35. G. De Rosi, G. E. Astrakharchik, S. Stringari, *Phys. Rev. A* **96**, 013613 (2017).
36. S. Sinha, L. Santos, *Phys. Rev. Lett.* **99**, 140406 (2007).
37. C. Menotti, S. Stringari, *Phys. Rev. A* **66**, 043610 (2002).
38. G. E. Astrakharchik, *Phys. Rev. A* **72**, 063620 (2005).
39. I. E. Mazets, J. Schmiedmayer, *New J. Phys.* **12**, 055023 (2010).

40. S. Tan, M. Pustilnik, L. I. Glazman, *Phys. Rev. Lett.* **105**, 090404 (2010).
41. I. E. Mazets, *Eur. Phys. J. D* **65**, 43–47 (2011).
42. T. Lahaye, C. Menotti, L. Santos, M. Lewenstein, T. Pfau, *Rep. Prog. Phys.* **72**, 126401 (2009).
43. H. Moritz, T. Stöferle, M. Köhl, T. Esslinger, *Phys. Rev. Lett.* **91**, 250402 (2003).
44. B. Bertini, F. H. L. Essler, S. Groha, N. J. Robinson, *Phys. Rev. Lett.* **115**, 180601 (2015).
45. K. Mallayya, M. Rigol, W. De Roeck, *Phys. Rev. X* **9**, 021027 (2019).
46. A. J. Friedman, S. Gopalakrishnan, R. Vasseur, *Phys. Rev. B* **101**, 180302 (2020).
47. W. Kao, K.-Y. Li, K.-Y. Lin, S. Gopalakrishnan, B. L. Lev, *Harvard Dataverse* (2020). https://doi.org/10.7910/DVN/H8LX1V.

ACKNOWLEDGMENTS

We thank V. Khemani, G. Astrakharchik, E. Demler, D. Weiss, C. Chin, J. Bohn, D. Petrov, M.-L. Chiofalo, R. Citro, and S. De Palo for stimulating discussions. **Funding:** We acknowledge funding support from AFOSR FA9550-17-1-0266, NSF PHY-2006149, and NSF DMR-1653271. W.K. and K.-Y.Lin acknowledge partial support from NSERC and the Olympiad Scholarship from the Taiwan Ministry of Education, respectively. **Author contributions:** W.K., K.-Y.Li., K.-Y.Lin, and B.L.L. carried out the experiments, and B.L.L. oversaw the work. All authors were involved in the analysis of the results and contributed to writing the paper. **Competing interests:** The authors declare no competing interests. **Data and materials availability:** All experimental data in figures are archived (*47*).

SUPPLEMENTARY MATERIALS

science.sciencemag.org/content/371/6526/296/suppl/DC1
Materials and Methods
Supplementary Text
Figs. S1 to S8
Table S1
References (*48*–*86*)

27 February 2020; accepted 4 December 2020
10.1126/science.abb4928

STRUCTURAL BIOLOGY

Cryo-EM structure of the B cell co-receptor CD19 bound to the tetraspanin CD81

Katherine J. Susa[1], Shaun Rawson[1], Andrew C. Kruse[1]*, Stephen C. Blacklow[1,2]*

Signaling through the CD19-CD81 co-receptor complex, in combination with the B cell receptor, is a critical determinant of B cell development and activation. It is unknown how CD81 engages CD19 to enable co-receptor function. Here, we report a 3.8-angstrom structure of the CD19-CD81 complex bound to a therapeutic antigen-binding fragment, determined by cryo–electron microscopy (cryo-EM). The structure includes both the extracellular domains and the transmembrane helices of the complex, revealing a contact interface between the ectodomains that drives complex formation. Upon binding to CD19, CD81 opens its ectodomain to expose a hydrophobic CD19-binding surface and reorganizes its transmembrane helices to occlude a cholesterol binding pocket present in the apoprotein. Our data reveal the structural basis for CD19-CD81 complex assembly, providing a foundation for rational design of therapies for B cell dysfunction.

B cells, a critical component of the adaptive immune system, enable development of long-lasting immunity after infection (*1*). Upon activation, B cells mature into plasma cells, which circulate in the bloodstream and secrete antibodies that can specifically bind and eliminate the foreign antigen that stimulated their production. Activated B cells also mature into long-lived memory B cells, providing durable immunity after infection. In cell-mediated immunity, B cells also serve as antigen-presenting cells that capture and present antigen to T cells.

B cell activation and maturation are initiated when an antigen is recognized by a cell surface B cell receptor (BCR). Signaling through the BCR leads to B cell maturation and contributes to stimulation of somatic hypermutation and heavy-chain class switching events associated with affinity maturation and antibody secretion. BCR signaling is also frequently subverted by B cell malignancies to drive their proliferation, growth, and survival (*2*, *3*).

[1]Department of Biological Chemistry and Molecular Pharmacology, Blavatnik Institute, Harvard Medical School, Boston, MA 02115, USA. [2]Department of Cancer Biology, Dana-Farber Cancer Institute, Boston, MA 02215, USA.
***Corresponding author. Email: stephen_blacklow@hms.harvard.edu (S.C.B.); andrew_kruse@hms.harvard.edu (A.C.K.)**

The BCR functions in association with a co-receptor complex that contains the complement receptor CD21, the signaling protein CD19, and the tetraspanin CD81 (*4*). Analogous to the CD4 and CD8 co-receptors of T cells, the B cell co-receptor complex boosts the response to antigen by lowering the signaling threshold for activation by about 1000-fold (*5*). CD19, a single-pass transmembrane protein belonging to the immunoglobulin superfamily, is the key signaling subunit of this complex, acting as a docking and recruitment site for various kinases and signaling components within the B cell signaling pathway (*6*, *7*). Patients with homozygous mutations in the CD19 gene develop common variable immune deficiency, an immune disorder characterized by recurrent and severe infections, primarily of the respiratory tract, ears, and sinuses (*8*), highlighting the importance of CD19 in immune cell function. The restriction of CD19 expression to the B cell lineage has also made it an attractive target of cell-based therapies for cancer and autoimmune diseases (*9*–*15*).

Complex formation between CD19 and the tetraspanin CD81 is critical for proper B cell function (*16*). Tetraspanins are a highly conserved family of four-transmembrane proteins that interact with each other and with a variety of partner proteins to regulate many signal transduction pathways (*17*). Through their interactions with partner proteins, tetraspanins play critical roles in numerous cellular functions, including protein trafficking, adhesion, cell signaling, and cell migration (*18*–*22*). CD81 chaperones CD19 through the secretory pathway, allowing for cell surface expression of mature, properly folded CD19 (*23*, *24*). On the B cell membrane, the CD19-CD81 interaction is dynamically regulated upon B cell activation (*25*). CD81 may regulate the diffusion of CD19 by immobilizing CD19 and associated signaling scaffolds in distinct locations in the membrane, thereby regulating the engagement of CD19 with the BCR, for example, to prevent high-level constitutive tonic signaling (*21*).

Our structure of apo-CD81 revealed a cholesterol binding pocket in its intramembrane cavity (*26*). However, there is no structural information showing the molecular details of how tetraspanins mediate complex formation with partner proteins to regulate their trafficking and signaling. Molecular dynamics simulations suggested that CD81 exists in both closed and open conformations and that cholesterol binding may favor a closed state with lower affinity for CD19 (*26*). Thus, cholesterol binding by CD81 may regulate its association with CD19 and, subsequently, B cell signaling. To better understand how these two proteins function together, we characterized their interaction in detail through a combination of cryo–electron microscopy (cryo-EM) and biochemical methods.

To produce CD19 in complex with CD81 for cryo-EM studies, we developed and validated a fusion protein approach (*25*). The fusion protein contains the full extracellular and transmembrane domains of CD19 and the first 15 amino acids of its cytoplasmic tail (fig. S1A). Because the cytoplasmic region of CD19 is predicted to be disordered and is not required for CD19 to bind to CD81 (*27*), we removed most of this segment to facilitate structural studies and linked CD19 to full-length CD81 with a Gly-Gly-Ser (GGS)×4 sequence.

To facilitate structure determination by cryo-EM, the CD19-CD81 complex (62 kDa) was bound to coltuximab, a therapeutic anti-CD19 antigen-binding fragment (Fab), increasing the molecular weight to ~110 kDa (*28*, *29*). The

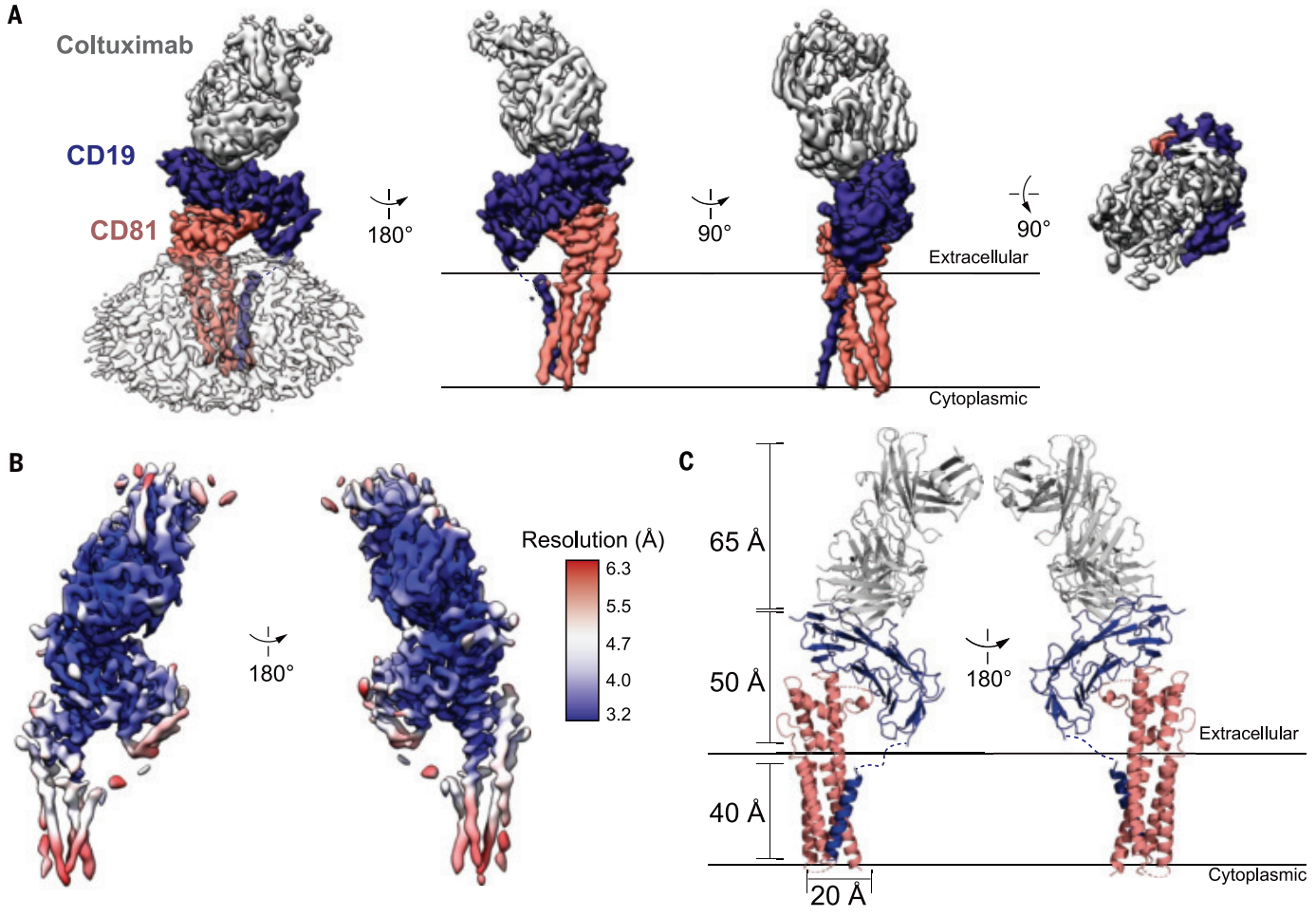


Fig. 1. 3D reconstruction and atomic model of the human CD19-CD81 complex bound to coltuximab. (**A**) Different views of the cryo-EM map of the CD19-CD81-coltuximab complex, colored by subunit. Density associated with the detergent micelle is rendered transparently in white in the left panel. (**B**) Locally filtered cryo-EM map of the CD19-CD81-coltuximab complex colored according to local resolution, calculated in cryoSPARC. (**C**) Ribbon representation of the structure of the complex. CD19, CD81, and coltuximab are colored as in (A).

purified complex contained CD19-CD81 and the Fab in stoichiometric quantities (fig. S1B). Cryo-EM imaging of this complex revealed well-dispersed single particles. Two-dimensional (2D) class averages showed clear secondary structure features in both the transmembrane region and the ectodomain (fig. S2). After 2D and 3D classifications, a homogeneous dataset of ~245,000 particles was used to produce a final density map at an overall nominal resolution of 3.8 Å (fig. S2 and table S1).

The structure of the CD19-CD81 complex is elongated, with the Fab-bound CD19 ectodomain resting directly on top of the CD81 ectodomain and the transmembrane helices arranged in a five-helix bundle (Fig. 1A). The crystal structures of the CD19 ectodomain (*30*), coltuximab (*31*), and full-length CD81 (*26*) were docked into the cryo-EM density map. Whereas the CD19 ectodomain and Fab fit easily into the density, CD81 did not, and the large extracellular loop (EC2), transmembrane domains 1 and 2 (TM1-TM2), and TM3-TM4 regions of CD81 were instead separately docked into the density. The quality of the density was sufficient for sequence-specific assignment for most of the ectodomains of both CD19 and CD81, including the contact interface, and for the variable domain of the Fab (Fig. 1B and fig. S3). Secondary structure is visible in the transmembrane domains, but this region is less well resolved than the ectodomains, precluding the modeling of side chains within this region (Fig. 1B and fig. S3). The final model of the CD19-CD81 complex contains the heavy and light chains of coltuximab, the complete ectodomain and transmembrane helix (modeled as polyalanine) of CD19, and full-length CD81, including the small extracellular loop (EC1), which was not resolved in the CD81 crystal structure (Figs. 1C and 2A).

The most distinctive feature of the CD19-CD81 structure is the large-scale conformational change within the tetraspanin CD81 (Fig. 2). The transmembrane helices of apo-CD81 resemble a cone, with two pairs of closely associated helices, TM1-TM2 and TM3-TM4, converging near the cytoplasmic side of the membrane (Fig. 2A) (*26*). These helices surround a large central cavity, enclosing a total volume of 3300 $Å^3$ (*26*). The five helices that make up EC2 contain a three-helix "stalk" comprising helices A, B, and E and a "top" face consisting of helices C and D. Upon complex formation, the EC2 of CD81 extends into an open conformation, with the A, B, and E helices swinging as a rigid body ~60° relative to the membrane plane (Fig. 2B), positioning helices A and E to be near-continuous with helices TM3 and TM4, respectively. The C and D helices also rearrange markedly with helices D and E merging to become one continuous helix, comparable in length to helix A (Fig. 2C), while helix C partially unravels. The conformation of helix C is buttressed by a conserved Cys-Cys-Gly (CCG) motif, which uses two disulfide bonds to stabilize its N-terminal end. The opening and reorganization of the ectodomain is also associated with inward movement of the

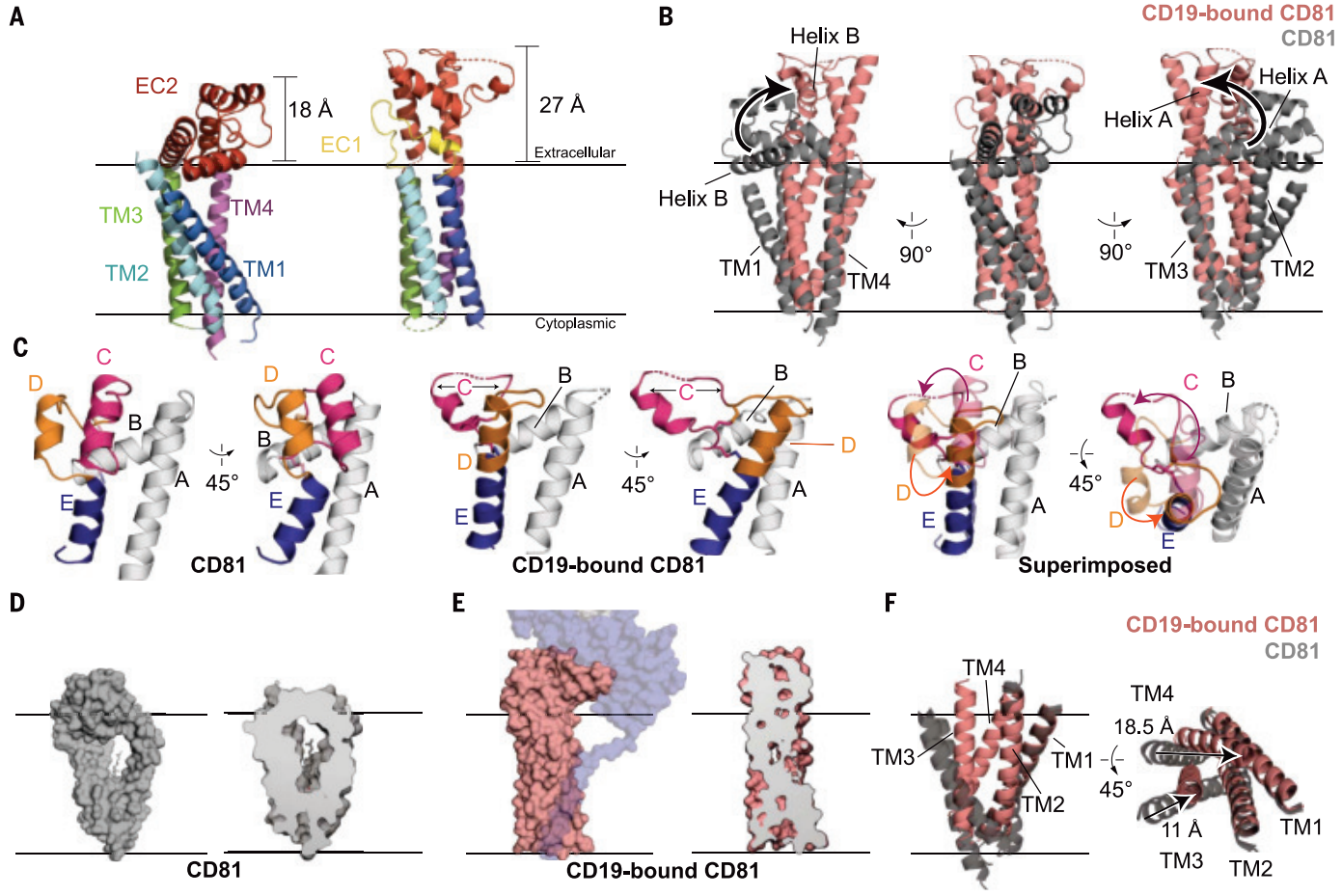


Fig. 2. Comparison of apo-CD81 and CD19-CD81 complex structures. (**A**) Comparison of apo-CD81 (left) with complexed CD81 (right). The structures are aligned on the TM3-TM4 helices and colored by domain. (**B**) Overlay of apo-CD81 on complexed CD81. Structures were aligned on the TM3-TM4 helices. Helices A and B of the large extracellular loop (EC2) are highlighted to show the hinge-opening movement of the ectodomain. (**C**) Comparison of the large extracellular loops of apo-CD81 (left) and complexed CD81 (middle), and superposition of the two conformations (right). Helices C to E are colored. In the superposition, the large extracellular loop of complexed CD81 is solid, and apo-CD81 is transparent. (**D**) Surface representation of apo-CD81 (left) and cross section highlighting the cholesterol binding pocket (right). (**E**) Surface representation of complexed CD81 (left) and cross section highlighting the occlusion of the cholesterol binding pocket (right). CD81 was modeled with side chains in the transmembrane domain for (E). (**F**) Overlay of the transmembrane region of apo-CD81 on complexed CD81, aligned on the TM1-TM2 helices. Movements within the transmembrane domain are indicated with black arrows. See also movie S1.

TM1-TM2 and TM3-TM4 pairs of helices, decreasing the distance between TM1 and TM4 by ~15 Å, virtually eliminating the central cavity and thus preventing cholesterol binding (Fig. 2, D to F).

In the crystal structure of CD81, no electron density was visible for EC1, suggesting that this region is disordered in the apoprotein. Upon complex formation with CD19, however, the movement of helix B away from the membrane allows interactions between EC1 and EC2, consistent with a role for EC1 in stabilizing the open conformation of the ectodomain (Fig. 2A). In contrast to CD81, the conformation of the CD19 ectodomain within the complex is nearly identical to that of the isolated ectodomain in the absence of CD81 (fig. S4).

The CD19-CD81 complex buries a total of ~700 Å^2 at an interface between the ectodomain of CD19 and the EC2 of CD81 (Fig. 3A). The observation that the ectodomains constitute the primary interaction site is consistent with our previous results from domain swap experiments (*25*) and is inconsistent with a prior report that the primary interaction site lies within the transmembrane region (*24*). The interface between the CD19 and CD81 ectodomains is highly hydrophobic, with aliphatic hydrophobic residues on helices C and D of CD81 surrounding a patch of exposed tryptophan, phenylalanine, and histidine residues on CD19 (Fig. 3B). Several polar residues nearby approach within hydrogen-bonding distance, providing specificity to this otherwise hydrophobic contact site. The CCG motif anchoring the base of the variable C helix is a defining feature of the tetraspanin family (*17*), and the overall three-helix bundle architecture of the EC2, capped by the variable and conformationally dynamic C and D helix region, is conserved (*32*), suggesting that the use of the C and D helices for recognition of partner proteins will be a general feature of the tetraspanin family.

Our structure also reveals that the therapeutic Fab coltuximab binds to the upper face of CD19 (Fig. 1A). Coltuximab binds to the same region as the therapeutic anti-CD19 antibody B43, and it also competes for binding with two other therapeutic antibodies, inebilizumab and denintuzumab, suggesting that current antibody selection strategies converge on a dominant CD19 epitope (fig. S5).

Previous work uncovered a human CD81 truncation mutation that results in type VI immunodeficiency (*16*). Whereas wild-type CD81 rescues export of CD19 to the cell surface in CD81-knockout HEK293T cells, the CD81 disease-associated mutation does not allow CD19 surface delivery in these cells (fig. S6),

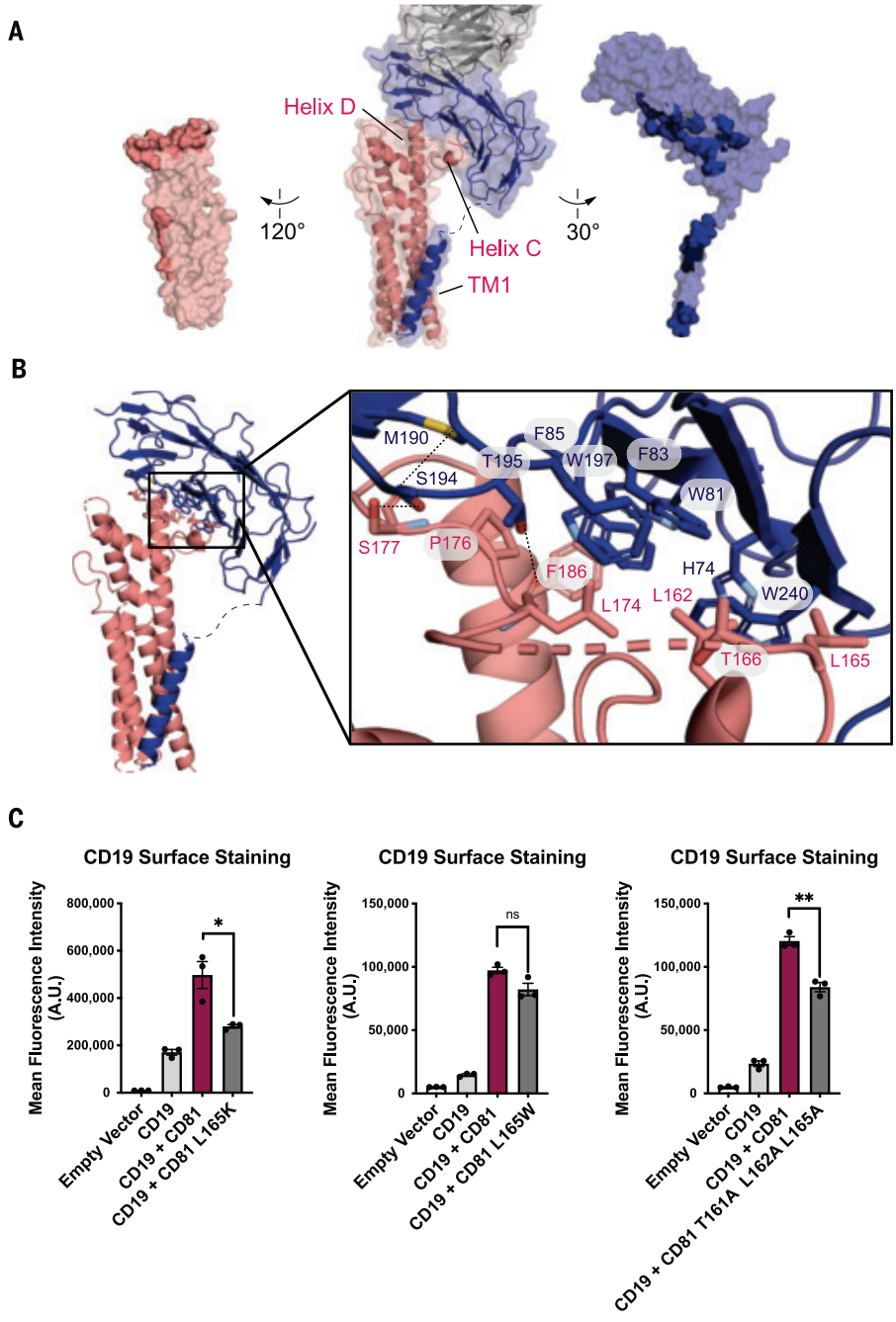


Fig. 3. CD19-CD81 interface. (**A**) Open-book representation of the CD19-CD81 interface. CD81 is salmon, CD19 is blue, and the Fab is gray. Residues at the binding interface are colored in a darker shade. (**B**) CD19-CD81 binding interface. Zoomed-in view shows hydrogen bonds and van der Waals interactions with dotted lines. (**C**) Effect of CD81 interface mutations on CD19 export. Surface CD19 was detected by flow cytometry using an Alexa 488–coupled anti-CD19 antibody. Expression of CD81 mutants was confirmed by flow cytometry (fig. S7). Error bars represent mean ± SEM of three independent experiments. Statistical analysis was performed in GraphPad Prism using an unpaired *t* test. *$P \leq 0.05$; **$P \leq 0.01$; ns, not significant. Single-letter abbreviations for the amino acid residues are as follows: A, Ala; C, Cys; D, Asp; E, Glu; F, Phe; G, Gly; H, His; I, Ile; K, Lys; L, Leu; M, Met; N, Asn; P, Pro; Q, Gln; R, Arg; S, Ser; T, Thr; V, Val; W, Trp; and Y, Tyr. A.U., arbitrary units.

consistent with prior observations that it fails to traffic CD19 to the cell surface in B cells (*16*) and in other non–B cell lines (*33*). To assess whether the observed CD81-CD19 interface is required for the function of CD81 in CD19 surface export, we mutated residues on CD81 at the observed interface and tested the ability of these mutants to traffic CD19 to the cell surface (Fig. 3C). The mutants we tested did not affect cell surface abundance of CD81 (fig. S7). Leu^{165}→Lys (L165K), which would place a charged residue in the hydrophobic interface, nearly abolishes the ability of CD81 to traffic CD19 to the surface, whereas an L165W mutation does not interfere with trafficking. A triple mutant, T161A/L162A/L165A, also disrupts trafficking. These results are consistent with the hydrophobic character of the CD19-CD81 interface. Although our structure also reveals contact between the transmembrane domain of CD19 and TM1 of CD81, the density in this region is more poorly resolved (Fig. 1B), and our prior experiments showed that this interaction is not necessary for complex formation or for export of CD19 to the cell surface by CD81 (*25*).

CD9 is the closest human homolog of tetraspanin CD81, sharing 45% amino acid sequence identity, yet it does not export CD19 to the cell surface (Fig. 4A) (*24*). Its overall structure is highly similar to CD81 (backbone root mean square deviation: 1.35 Å), with minor structural differences only in the C and D helix region of EC2 (*32*). An accompanying low-resolution structure of CD9 in complex with EWI-2 (immunoglobulin superfamily member 8) only made it possible to roughly fit an EWI-2 homology model and the CD9 crystal structure into the cryo-EM map, which has a very different overall architecture from the CD19-CD81 complex (*32*). A separate cryo-EM structure of CD9 in complex with EWI-F adopts a nearly identical architecture as the CD9-EWI-2 complex and suggests that CD9 can adopt a more open conformation when bound (*34*). To understand the basis of the specificity of CD81 for CD19, we simulated the open, cholesterol-free conformation of CD9 with a homology model of the structure of CD19-bound CD81 (*35*). The comparison shows that the hydrophobic loop of CD81 that engages CD19 is highly polar in the model of CD9, providing an explanation for the CD19 selectivity of CD81 (Fig. 4B).

The structural and biochemical results reported here reveal molecular details about the B cell co-receptor complex that have previously eluded definition (*4*). The CD19-CD81 complex is assembled in the endoplasmic reticulum (ER), where cholesterol accounts for only 5% of lipids (compared with up to 50% of plasma membrane lipids) (*36*). The low cholesterol concentration could favor CD19-CD81 complex formation in the ER, where it then travels through the secretory pathway and is inserted into the B cell membrane in the open, cholesterol-free conformation. Upon B cell activation, the BCR and co-receptor complex have been shown to partition into cholesterol-rich lipid rafts, and CD81 is necessary for this movement (*37*, *38*). Thus, cholesterol binding may allow CD81 to release CD19 in response to B cell activation, allowing CD19 to interact with the BCR and carry out signal amplification during antigen recognition.

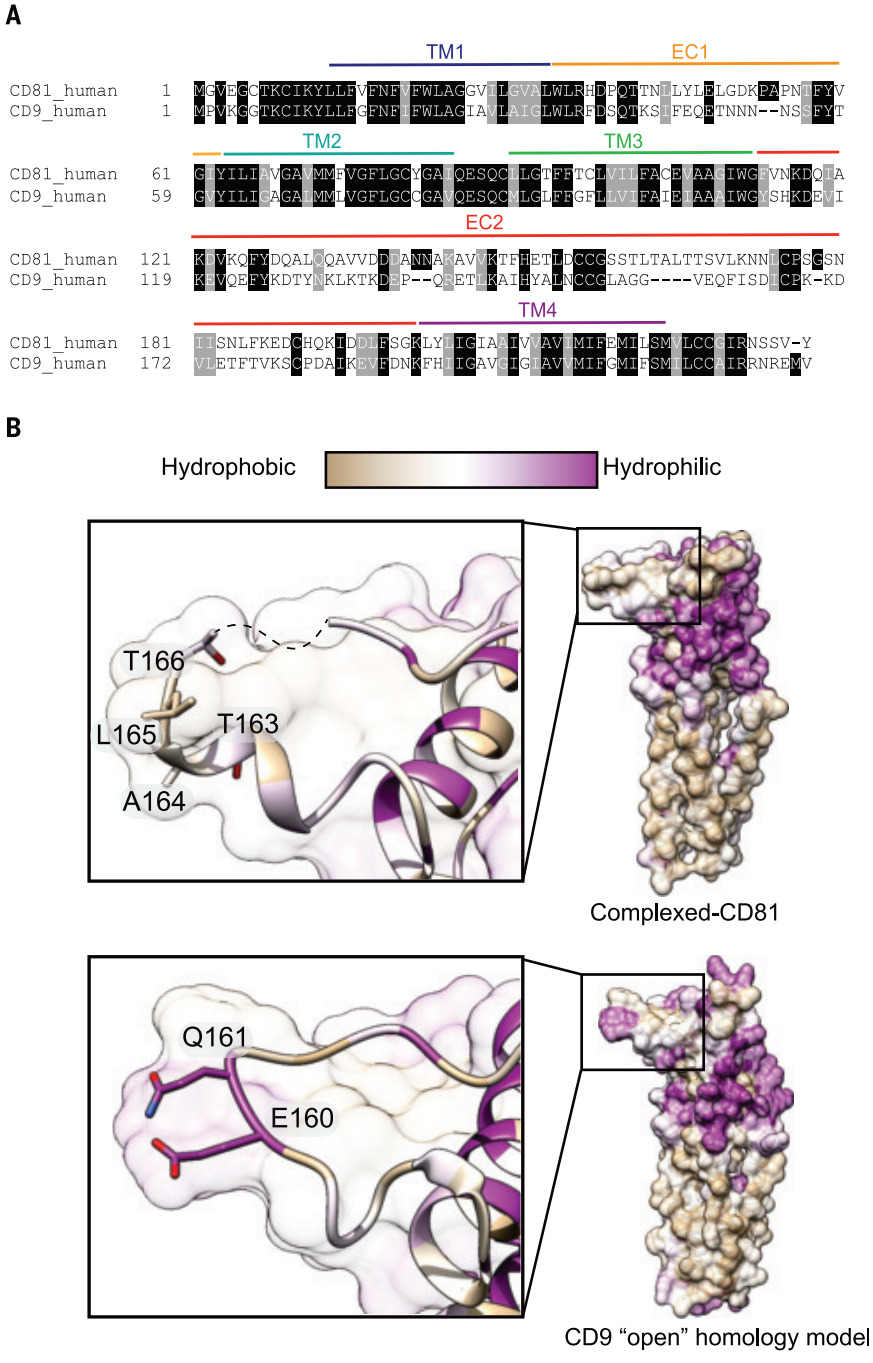


Fig. 4. Structural comparison of CD81 to its tetraspanin CD9 homolog explains CD19-binding specificity. (**A**) Sequence alignment of human CD81 and human CD9. (**B**) Homology model of open CD9 and CD19-complexed CD81 with surfaces colored by amino acid hydrophobicity on the Kyte-Doolittle scale. Zoomed-in panels show the key hydrophobic TALT sequence that is necessary for CD81 to recognize CD19, which is replaced with a hydrophilic region in the analogous position on CD9.

The switch that triggers the transition from cholesterol-free to cholesterol-bound CD81 remains an area of further investigation, but some studies suggest that the palmitoylation of CD81 modulates cholesterol binding (*39*, *40*).

The mechanism of conformational regulation in response to lipid binding is likely a general feature of the tetraspanin family. The functional relationship between cholesterol and numerous tetraspanins has been discussed (*41*–*44*), although never directly shown, and analysis of sequence conservation for the 33 tetraspanin paralogs in humans highlights tight evolutionary constraints within the transmembrane region (*26*). Residue N18, which forms a hydrogen bond to cholesterol in the apo-CD81 structure, is conserved in 27 of 33 human tetraspanins (*26*). The structure of CD9 also revealed electron density consistent with a bound lipid within its intramembrane cavity (*32*). Our structure of the CD19-CD81 complex confirms that there are at least two distinct conformations of a tetraspanin and suggests that tetraspanins regulate the subcellular localization of their partner proteins on the basis of differences in cholesterol concentration.

We previously showed that the anti-CD81 antibody 5A6 recognizes a conformational epitope that is masked when CD81 is in complex with CD19 but becomes accessible upon B cell activation (*25*). This antibody is competitive with CD19 for binding to CD81, and the angle of approach of the 5A6 Fab is nearly identical to that of CD19 (fig. S8) (*25*). 5A6 inhibits B cell lymphoma growth in a xenograft model as effectively as rituximab, a standard treatment for this disease (*45*). However, unlike rituximab, 5A6 selectively kills human lymphoma cells while sparing normal cells (*45*), suggesting that conformationally selective antibodies that distinguish unbound CD81 on chronically active malignant cells from the CD19-CD81 complex on resting B cells show therapeutic promise.

In addition to its function as a signaling subunit of the B cell co-receptor, CD19 is also a target of chimeric antigen receptor T cells, which have revolutionized the treatment of B cell malignancies and show promise for treatment of autoimmune disorders (*14*, *15*, *46*). It is currently not possible to selectively target resting or chronically activated malignant B cells on the basis of differences in CD19 conformation, leading to depletion of all B cells and recurrent infections owing to loss of humoral immunity. It should be possible to select antibodies that discriminate between CD81-complexed CD19 and free CD19 by raising antibodies that recognize a composite epitope on our CD19-CD81 fusion protein. Such an antibody could be used to trap CD19 in complex with CD81, raising the threshold for B cell activation in autoimmune diseases. Alternatively, an antibody that binds to the region of the CD19 ectodomain that interacts with CD81 on resting B cells could selectively deplete chronically activated malignant B cells, preventing the undesired complication of destroying all B cells with current-generation CAR-T approaches.

REFERENCES AND NOTES

1. T. W. LeBien, T. F. Tedder, *Blood* **112**, 1570–1580 (2008).
2. R. E. Davis *et al.*, *Nature* **463**, 88–92 (2010).
3. K. Bojarczuk *et al.*, *Blood Cells Mol. Dis.* **55**, 255–265 (2015).
4. L. E. Bradbury, G. S. Kansas, S. Levy, R. L. Evans, T. F. Tedder, *J. Immunol.* **149**, 2841–2850 (1992).
5. R. H. Carter, D. T. Fearon, *Science* **256**, 105–107 (1992).
6. M. Fujimoto, J. C. Poe, P. J. Jansen, S. Sato, T. F. Tedder, *J. Immunol.* **162**, 7088–7094 (1999).
7. D. A. Tuveson, R. H. Carter, S. P. Soltoff, D. T. Fearon, *Science* **260**, 986–989 (1993).
8. M. C. van Zelm *et al.*, *N. Engl. J. Med.* **354**, 1901–1912 (2006).
9. R. J. Brentjens *et al.*, *Sci. Transl. Med.* **5**, 177ra38 (2013).
10. S. A. Grupp *et al.*, *N. Engl. J. Med.* **368**, 1509–1518 (2013).
11. M. Kalos *et al.*, *Sci. Transl. Med.* **3**, 95ra73 (2011).
12. J. N. Kochenderfer, S. A. Rosenberg, *Nat. Rev. Clin. Oncol.* **10**, 267–276 (2013).

13. D. L. Porter, B. L. Levine, M. Kalos, A. Bagg, C. H. June, *N. Engl. J. Med.* **365**, 725–733 (2011).
14. R. Kansal *et al.*, *Sci. Transl. Med.* **11**, eaav1648 (2019).
15. N. Yazawa, Y. Hamaguchi, J. C. Poe, T. F. Tedder, *Proc. Natl. Acad. Sci. U.S.A.* **102**, 15178–15183 (2005).
16. M. C. van Zelm *et al.*, *J. Clin. Invest.* **120**, 1265–1274 (2010).
17. M. E. Hemler, *Nat. Rev. Drug Discov.* **7**, 747–758 (2008).
18. F. Berditchevski, E. Odintsova, *Traffic* **8**, 89–96 (2007).
19. S. Levy, S. C. Todd, H. T. Maecker, *Annu. Rev. Immunol.* **16**, 89–109 (1998).
20. J. Lammerding, A. R. Kazarov, H. Huang, R. T. Lee, M. E. Hemler, *Proc. Natl. Acad. Sci. U.S.A.* **100**, 7616–7621 (2003).
21. P. K. Mattila *et al.*, *Immunity* **38**, 461–474 (2013).
22. L. Liu *et al.*, *J. Biol. Chem.* **282**, 31631–31642 (2007).
23. F. Braig *et al.*, *Blood* **129**, 100–104 (2017).
24. T. Shoham *et al.*, *J. Immunol.* **171**, 4062–4072 (2003).
25. K. J. Susa, T. C. Seegar, S. C. Blacklow, A. C. Kruse, *eLife* **9**, e52337 (2020).
26. B. Zimmerman *et al.*, *Cell* **167**, 1041–1051.e11 (2016).
27. L. E. Bradbury, V. S. Goldmacher, T. F. Tedder, *J. Immunol.* **151**, 2915–2927 (1993).
28. E. E. Hong *et al.*, *Mol. Pharm.* **12**, 1703–1716 (2015).
29. H. M. Kantarjian *et al.*, *Clin. Lymphoma Myeloma Leuk.* **16**, 139–145 (2016).
30. A. Teplyakov, G. Obmolova, J. Luo, G. L. Gilliland, *Proteins* **86**, 495–500 (2018).
31. J. Ereño-Orbea *et al.*, *J. Mol. Biol.* **430**, 322–336 (2018).
32. R. Umeda *et al.*, *Nat. Commun.* **11**, 1606 (2020).
33. F. Vences-Catalán *et al.*, *J. Clin. Immunol.* **35**, 254–263 (2015).
34. W. Oosterheert *et al.*, *Life Sci. Alliance* **3**, e202000883 (2020).
35. A. Waterhouse *et al.*, *Nucleic Acids Res.* **46**, W296–W303 (2018).
36. A. Radhakrishnan, J. L. Goldstein, J. G. McDonald, M. S. Brown, *Cell Metab.* **8**, 512–521 (2008).
37. A. Cherukuri, P. C. Cheng, H. W. Sohn, S. K. Pierce, *Immunity* **14**, 169–179 (2001).
38. A. Cherukuri *et al.*, *J. Immunol.* **172**, 370–380 (2004).
39. A. Cherukuri *et al.*, *J. Biol. Chem.* **279**, 31973–31982 (2004).
40. C. Delandre, T. R. Penabaz, A. L. Passarelli, S. K. Chapes, R. J. Clem, *Exp. Cell Res.* **315**, 1953–1963 (2009).
41. S. Charrin *et al.*, *Eur. J. Immunol.* **33**, 2479–2489 (2003).
42. J. Buschiazzo *et al.*, *PLOS ONE* **8**, e62919 (2013).
43. O. Silvie *et al.*, *J. Cell Sci.* **119**, 1992–2002 (2006).
44. S. J. Israels, E. M. McMillan-Ward, *Thromb. Haemost.* **98**, 1081–1087 (2007).
45. F. Vences-Catalán *et al.*, *J. Exp. Med.* **216**, 1497–1508 (2019).
46. D. Chen, S. Gallagher, N. L. Monson, R. Herbst, Y. Wang, *J. Clin. Med.* **5**, 107 (2016).

ACKNOWLEDGMENTS

We thank members of the Blacklow and Kruse laboratories for helpful discussions and M. Bao for critical reading of the manuscript. Cryo-EM data were collected at the Harvard Cryo-EM Center for Structural Biology at Harvard Medical School. We thank S. Sterling and R. Walsh for helpful comments and advice during grid screening and data collection. **Funding:** Financial support for this work was provided by NIH grants R35 CA220340 (S.C.B.), F31 HL147459 (K.J.S.), and DP5 OD021345 (A.C.K.). **Author contributions:** K.J.S., A.C.K., and S.C.B. designed the project. K.J.S. expressed and purified the proteins, prepared samples for cryo-EM, and performed all cell-based assays. K.J.S., together with S.R., processed the electron microscopy data. K.J.S. performed model building and refinement with input from A.C.K. and S.C.B. K.J.S., A.C.K., and S.C.B. drafted the manuscript, and all authors edited and reviewed the final manuscript. **Competing interests**: S.C.B. receives funding for an unrelated project from Novartis; is on the scientific advisory board for Erasca, Inc.; is an adviser to MPM Capital; and is a consultant for IFM, Scorpion Therapeutics, and Ayala Pharmaceuticals for unrelated projects. A.C.K. is a cofounder and adviser on unrelated projects for the Institute for Protein Innovation, a nonprofit research institute, and a founder of Tectonic Therapeutic, a for-profit biotechnology company. **Data and materials availability:** Materials will be made available upon request. Protein Data Bank (PDB) IDs of the CD19-CD81-coltuximab Fab model and map are 7JIC and EMD-22344, respectively.

SUPPLEMENTARY MATERIALS

science.sciencemag.org/content/371/6526/300/suppl/DC1
Materials and Methods
Figs. S1 to S8
Table S1
References (*47*–*54*)
MDAR Reproducibility Checklist
Movie S1

23 July 2020; accepted 9 December 2020
10.1126/science.abd9836

RNA SPLICING

Structure of a transcribing RNA polymerase II–U1 snRNP complex

Suyang Zhang[1], Shintaro Aibara[1], Seychelle M. Vos[1]*, Dmitry E. Agafonov[2]†, Reinhard Lührmann[2], Patrick Cramer[1]‡

To initiate cotranscriptional splicing, RNA polymerase II (Pol II) recruits the U1 small nuclear ribonucleoprotein particle (U1 snRNP) to nascent precursor messenger RNA (pre-mRNA). Here, we report the cryo–electron microscopy structure of a mammalian transcribing Pol II–U1 snRNP complex. The structure reveals that Pol II and U1 snRNP interact directly. This interaction positions the pre-mRNA 5′ splice site near the RNA exit site of Pol II. Extension of pre-mRNA retains the 5′ splice site, leading to the formation of a "growing intron loop." Loop formation may facilitate scanning of nascent pre-mRNA for the 3′ splice site, functional pairing of distant intron ends, and prespliceosome assembly. Our results provide a starting point for a mechanistic analysis of cotranscriptional spliceosome assembly and the biogenesis of mRNA isoforms by alternative splicing.

The production of mRNA in eukaryotic cells involves precursor mRNA (pre-mRNA) synthesis and processing—in particular, 5′ end capping, splicing, and 3′ end cleavage and polyadenylation. During splicing, noncoding introns are predominantly removed from the pre-mRNA in a cotranscriptional manner as the nascent RNA emerges from RNA polymerase II (Pol II) (*1*–*6*). Cotranscriptional splicing enhances the efficiency and accuracy of pre-mRNA processing and explains why splicing is at least 10 times faster in vivo than in vitro (*7*). In metazoan cells, introns are often several thousand nucleotides long, which raises the question of how the ends of an intron are functionally paired for splicing. Cotranscriptional splicing has been suggested to facilitate juxtaposition of the 5′ splice site (5′SS) and the 3′SS (*8*). Consistent with this idea, the rate of Pol II elongation can affect selection of splice sites in pre-mRNA (*9*), leading to alternative splicing and different mRNA isoforms (*10*). Pol II can recruit splicing factors via its flexible C-terminal domain (CTD) [reviewed in (*6*)]; however, this is insufficient to stimulate splicing (*11*). Despite these advances, the mechanisms underlying cotranscriptional splicing remain unknown.

As a first step to investigate the mechanisms of cotranscriptional splicing, we studied the interaction between transcribing Pol II and the U1 small nuclear ribonucleoprotein particle (U1 snRNP) biochemically and structurally. U1 snRNP is the first building block of the spliceosome to engage with nascent pre-mRNA (*12*). Human U1 snRNP consists of U1 snRNA, seven Sm proteins, and three U1-specific proteins (U1-70k, U1-A, and U1-C) (*12*). U1 snRNA recognizes the 5′SS through base pairing (*13*). When the branch point sequence emerges on nascent pre-mRNA, U2 snRNP joins, forming the prespliceosome or A complex. The A complex later associates with the U4/U6.U5 tri-snRNP to form the pre-B complex (*14*), which is subsequently converted to the B complex and activated for splicing.

To assemble a transcribing Pol II–U1 snRNP complex, we used Pol II from the domestic pig, *Sus scrofa domesticus*, which has 99.9% sequence identity to human Pol II. We further used human U1 snRNP and a DNA-RNA scaffold that contains a DNA mismatch bubble and a modified MINX pre-mRNA with a 5′ cap. The scaffold enables formation of a 9–base pair DNA-RNA hybrid duplex inside the bubble and contains a 145-nucleotide (nt) RNA that comprises a 5′ exon and a truncated intron of 29 nts (Fig. 1A and fig. S1, A and B). We incubated purified Pol II with the DNA-RNA scaffold and phosphorylated the resulting complex with the kinase-positive transcription elongation factor b, which stabilizes an active Pol II elongation complex (*15*). The phosphorylated Pol II–DNA-RNA complex was purified by size exclusion chromatography and incubated with purified U1 snRNP (fig. S1C).

The obtained sample was subjected to single-particle cryo–electron microscopy (cryo-EM) analysis (see materials and methods). A tilt angle of 40° was applied during data collection to resolve orientation bias (fig. S1, D to F, and table S1). Processing of the cryo-EM data showed that 17.5% of Pol II particles contained densities corresponding to U1 snRNP (fig. S2, A to F). Three-dimensional (3D) classification followed by 3D refinement of the class with the best

[1]Department of Molecular Biology, Max Planck Institute for Biophysical Chemistry, Am Fassberg 11, 37077 Göttingen, Germany. [2]Cellular Biochemistry, Max Planck Institute for Biophysical Chemistry, Am Fassberg 11, 37077 Göttingen, Germany.
*Present address: Department of Biology, Massachusetts Institute of Technology, Cambridge, MA 02139, USA. †Present address: Department of Cellular Logistics, Max Planck Institute for Biophysical Chemistry, Am Fassberg 11, 37077 Göttingen, Germany.
‡Corresponding author. Email: patrick.cramer@mpibpc.mpg.de

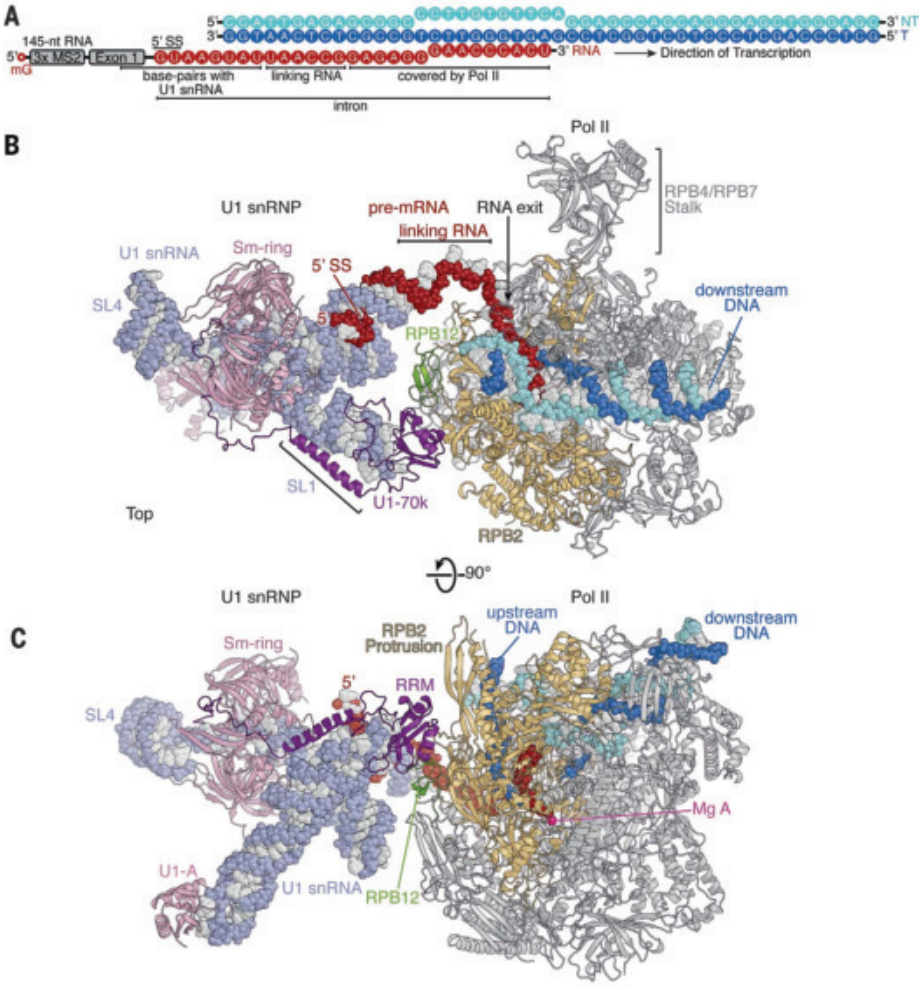


Fig. 1. Structure of the transcribing Pol II–U1 snRNP complex. (**A**) Nucleic acid scaffold with template DNA (T) in dark blue, nontemplate DNA (NT) in cyan, and RNA in red. mG, 5′ cap. (**B** and **C**) Two views of the structure. Nucleic acids are shown in spheres. The backbone of U1 snRNA is in pale slate and U1 snRNP proteins are in pink, except for U1-70k, which is in purple. Pol II subunits (ribbons) are in gray, except for RPB2 in gold and RPB12 in green. During transcription, Pol II moves to the right and RNA exits to the left. A magenta sphere depicts the Pol II active site. SL, stem loop.

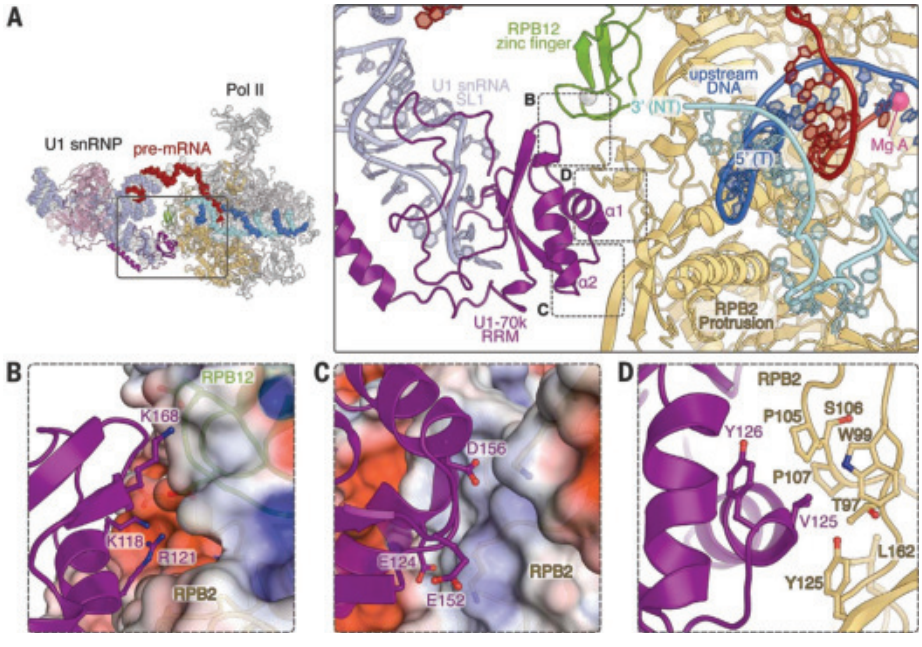


Fig. 2. Direct Pol II–U1 snRNP interaction. (**A**) Close-up view of the Pol II–U1 snRNP interface showing interactions between the RRM domain of U1-70k (purple) and Pol II subunits RPB2 (gold) and RPB12 (green). The Pol II active site is depicted with a magenta sphere. (**B** to **D**) Detailed views of interactions between residues of U1-70k RRM and Pol II. The electrostatic surface potential displays a range of ±5 k_BT/e (where k_B is the Boltzmann constant, T is temperature, and e is electron charge), where blue and red represent positively and negatively charged areas, respectively. Amino acid abbreviations: D, aspartic acid; E, glutamic acid; K, lysine; L, leucine; P, proline; R, arginine; S, serine; T, threonine; W, tryptophan; Y, tyrosine.

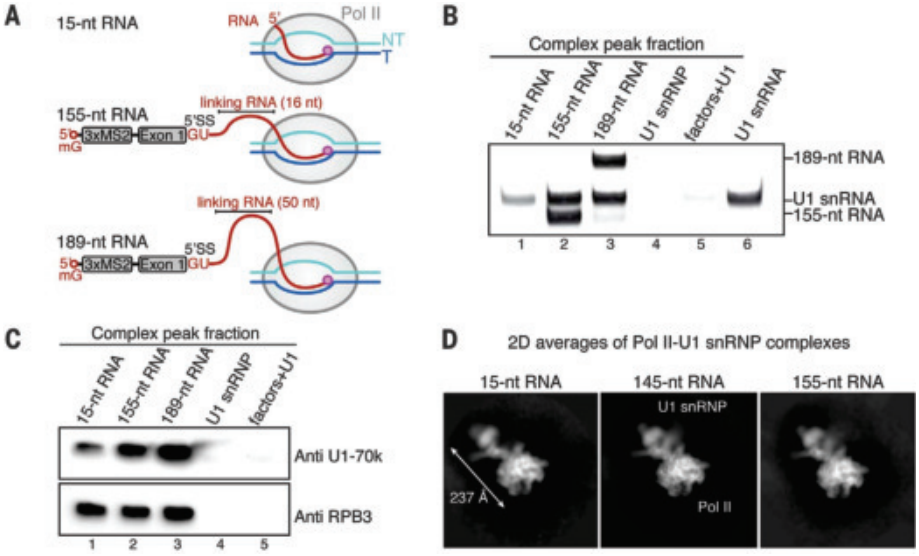


Fig. 3. RNA-independent Pol II–U1 snRNP interaction. (**A**) Schematic of Pol II complexes with various RNAs. The active site of Pol II is depicted with a magenta sphere. (**B** and **C**) EC* associates with U1 snRNP in the presence of RNA lacking the 5′SS (15-nt RNA) or RNAs with an extended linking region (155-nt and 189-nt RNAs). Shown is the analysis of the complex peak fraction (fraction 2 of fig. S7A) obtained by size exclusion chromatography using denaturing gel electrophoresis (B) or Western blotting (C). Lanes 4 and 5 are control runs with U1 snRNP alone or U1 snRNP with phosphorylated elongation factors. (**D**) Cryo-EM analysis of Pol II–U1 snRNP complexes containing 15-nt RNA or 155-nt RNA showed 2D averages resembling those of the refined structure with 145-nt RNA.

density for U1 snRNP yielded a final reconstruction of the Pol II–U1 snRNP complex at an overall resolution of 3.6 Å, and focused 3D refinement improved densities for Pol II, U1 snRNP, and the Pol II–U1 snRNP interface region (figs. S2, G to I, S3, and S4 and movie S1). Fitting and adjustment of the structures of Pol II (*15*) and U1 snRNP (*16*–*18*) resulted in a model of the Pol II–U1 snRNP complex with good stereochemistry (Fig. 1, B and C, table S1, and movie S2).

The structure shows that U1 snRNP binds directly to the surface of Pol II near upstream DNA and the site of RNA exit (Fig. 1 and movie S2). U1 snRNP engages Pol II via its conserved and functionally essential (*17*) subunit U1-70k, which contacts the protrusion domain in Pol II subunit RPB2 and the zinc finger domain in subunit RPB12 (Figs. 1, B and C, and 2A). U1-70k interacts with Pol II through its RNA recognition motif (RRM) domain that is resolved at ~3.5-Å resolution, revealing bulky side chains and enabling an unambiguous fit (figs. S3D and S4, B and C). We did not observe any densities indicative of the Pol II CTD.

Our structure provides details of the Pol II–U1 snRNP interface. The U1-70k RRM interacts with Pol II mainly through its two conserved α helices (human residues 116 to 126 and 154 to 164) (Fig. 2A). The Pol II–U1 snRNP interacting surfaces have reverse charges (fig. S5, A and B). The side chain of the positively charged U1-70k RRM residue Arg^{121} inserts into a negatively charged pocket formed by RPB2 and RPB12 (Fig. 2B). Three negatively charged residues (Glu^{124}, Glu^{152}, and Asp^{156}) of U1-70k RRM contact a positively charged surface of the RPB2 protrusion domain (Fig. 2C). In addition, Val^{125} of U1-70k RRM binds to a hydrophobic patch of RPB2 (Fig. 2D).

Residues in U1-70k that contact Pol II are highly conserved among metazoa (fig. S5C). RPB2 residues that interact with U1-70k are also well conserved among multicellular eukaryotes but differ from those in the counterpart subunits of Pol I and Pol III (fig. S5D). This indicates that the observed U1 snRNP interaction with Pol II is conserved among metazoa and specific to the Pol II transcription system. By contrast, the interacting residues in both U1-70k and RPB2 are only partially conserved in yeasts (fig. S5, C and D), implying that the mechanism of cotranscriptional splicing may differ in some unicellular eukaryotes, which contain fewer and shorter introns.

Superposition of our Pol II–U1 snRNP structure with the activated Pol II elongation complex EC* (*15*) revealed that binding of U1 snRNP, as observed in our structure, is compatible with the presence of the transcription elongation factors DSIF, SPT6, and PAF1 complex (PAF) on the Pol II surface (fig. S6). Consistent with this compatibility, we found that a stable complex containing EC* and U1 snRNP can be formed (Fig. 3, A to C, and fig. S7, A to F). In summary, these results reveal an unexpected direct Pol II–U1 snRNP interaction that is compatible with the presence of general elongation factors in the transcribing Pol II complex EC*.

Our structure additionally shows one turn of an RNA duplex formed by base pairing of the 5′SS with U1 snRNA (Fig. 1 and fig. S4, A and D), as observed in previous U1 snRNP structures (*16*–*18*). By RNA duplex formation, the pre-mRNA tethers Pol II to U1 snRNP with a 6-nt linking RNA region (Fig. 1A and fig. S4A). To investigate the role of RNA tethering, we performed analytical size exclusion assays using the activated elongation complex EC* (see materials and methods). We prepared EC* containing a minimal scaffold with a 15-nt RNA that lacks the 5′SS and is completely sequestered within the Pol II core (Fig. 3A and fig. S1, A and B), excluding any RNA-based tethering of Pol II and U1 snRNP. The resulting minimal EC* still bound U1 snRNP, although at apparently substoichiometric levels (Fig. 3, B and C, and fig. S7, A and B).

To confirm that the same direct Pol II–U1 snRNP interaction occurs in the absence of a tethering RNA, we subjected a Pol II–U1 snRNP complex containing the nucleic acid scaffold with the 15-nt RNA to cryo-EM analysis. We obtained the same two-dimensional (2D) particle averages as for our original structure (Fig. 3D). The percentage of Pol II–U1 snRNP particles was lower, hindering 3D reconstruction. Nevertheless, these results show that RNA tethering is not required for direct Pol II–U1 snRNP interaction in vitro and may explain how U1 snRNP can be recruited to transcription units independent of splicing in vivo (*19*).

Our observations suggested that transcription elongation may generate an RNA loop between Pol II and U1 snRNP while the direct Pol II–U1 snRNP interaction is maintained. To investigate this, we tested whether insertion of additional nucleotides into the linking RNA region allows for U1 snRNP binding to Pol II or EC*. We designed scaffolds that contained either a 155-nt RNA, which has a 10-nt extension in the linking RNA compared with the 145-nt RNA in the cryo-EM structure, or a 189-nt RNA, which contains a linking RNA of 50 nts and would be sufficient for formation of an active spliceosomal B complex (*20*) (Fig. 3A and fig. S1, A and B). We found that both scaffolds with extended RNAs allowed formation of an EC*-U1 snRNP complex (Fig. 3, B and C, and fig. S7, A to D). These results support the model in which, during elongation of the pre-mRNA, the 5′SS is retained near the Pol II surface whereas the intron loops out.

To confirm that the same direct Pol II–U1 snRNP interaction is maintained when the

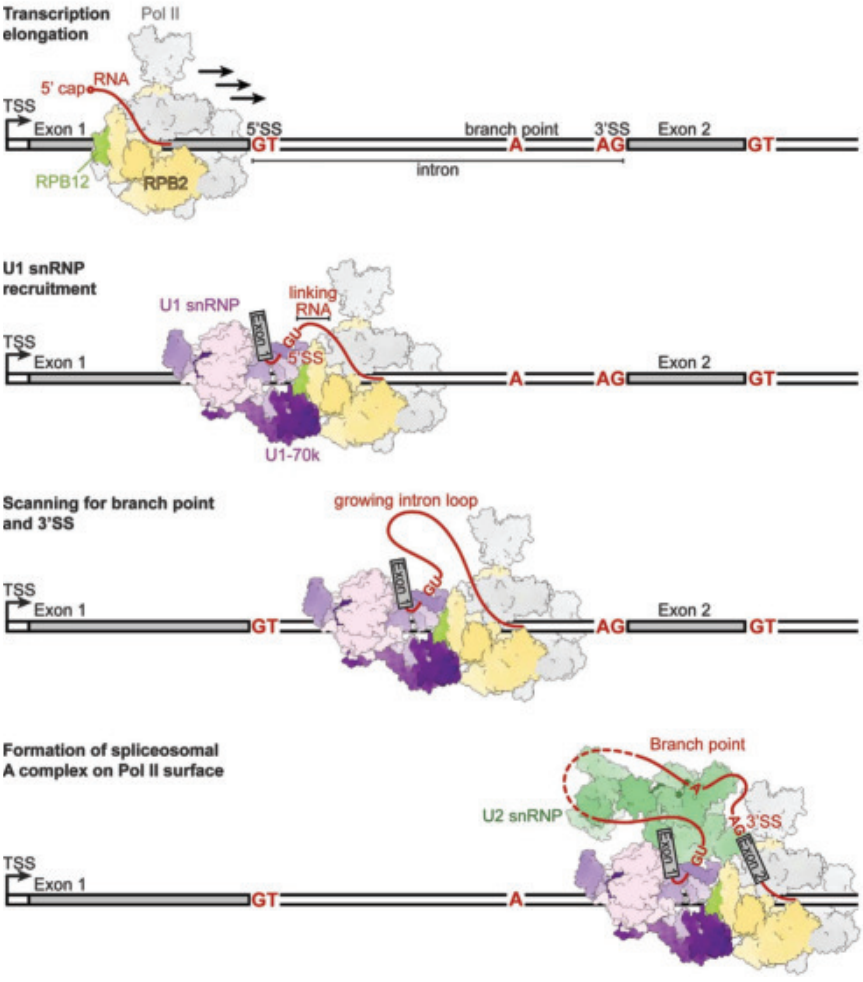


Fig. 4. Growing intron loop model of cotranscriptional spliceosome assembly. The intron is defined by the 5′SS, branch point, and 3′SS (conserved nucleotides in red). When the 5′SS emerges in nascent pre-mRNA, U1 snRNP (purple) is recruited and directly binds Pol II subunits RPB2 (gold) and RPB12 (green). U1 snRNP and the 5′SS are retained near the RNA exit site during transcription elongation, resulting in the formation of an RNA loop. Loop formation facilitates scanning for the downstream branch point and 3′SS and assembly of the A complex.

linking RNA is extended, we determined the cryo-EM structure of the Pol II–U1 snRNP complex with the scaffold containing the 155-nt RNA at a nominal resolution of 3.9 Å (fig. S8). The structure was essentially unaltered compared with our first structure, revealing the same direct Pol II–U1 snRNP interaction (Fig. 3D and fig. S8). In addition, in vitro RNA elongation activities of Pol II or EC* were not affected by the presence of U1 snRNP (fig. S7, G and H). These results indicate that U1 snRNP can remain bound to Pol II as pre-mRNA is elongated during transcription.

To investigate whether assembly of spliceosomal complexes may be possible on Pol II, we compared our structure with the yeast A complex (*21*) (fig. S9, A and B). This suggested that U2 snRNP can be accommodated and the A complex can form on the Pol II surface without moving U1 snRNP. Human A complex formation requires binding of stem loop 4 (SL4) of U1 snRNA to the U2 snRNP subunit SF3A1 (*22*). Consistent with this, SL4 faces away from Pol II in our structure and is available for SF3A1 interaction (Fig. 1, B and C). Superposition of our structure onto the human pre-B complex (*23*, *24*) resulted in clashes between Pol II and the U4/U6.U5 tri-snRNP (fig. S9C). However, the tri-snRNP is flexibly attached to the remainder of the pre-B complex (*14*), and structural adjustments may therefore allow formation of the pre-B complex on Pol II.

Our findings suggest a topological model for cotranscriptional spliceosome assembly that we refer to as the growing intron loop model (Fig. 4). In this model, a direct Pol II–U1 snRNP interaction retains the 5′SS near the RNA exit site of Pol II during transcription. This results in formation of a growing loop in the nascent pre-mRNA that facilitates scanning for the downstream branch point and 3′SS. Recruitment of U2 snRNP then leads to formation of the A complex on the Pol II surface. Formation of the A complex may be further stimulated by the downstream 5′SS (*25*) and binding of the downstream exon to regulatory factors that facilitate U2 snRNP recruitment (*26*). After A complex formation, the U4/U6.U5 tri-snRNP may join, leading to the pre-B complex. The subsequent transition to the B complex displaces U1 snRNP (*12*), liberating the precatalytic spliceosome from Pol II. Therefore, the growing intron loop model implies that the assembly of the spliceosome occurs cotranscriptionally, whereas the ensuing catalytic steps of splicing may be functionally independent of Pol II, although they occur predominantly on the nascent pre-mRNA.

Finally, U1 snRNP inhibits 3′ end RNA processing (*27*), suppresses premature transcription termination (*28*), and impairs premature termination in the sense direction of bidirectional promoters (*29*, *30*). To explain these findings, we speculate that U1 snRNP binding to the Pol II surface interferes with productive binding of the 3′ end processing machinery. Thereby, U1 snRNP may suppress premature termination and keep Pol II in an actively transcribing state until a genuine 3′ end processing signal is detected in the nascent RNA.

REFERENCES AND NOTES

1. K. M. Kotovic, D. Lockshon, L. Boric, K. M. Neugebauer, *Mol. Cell. Biol.* **23**, 5768–5779 (2003).
2. S. A. Lacadie, M. Rosbash, *Mol. Cell* **19**, 65–75 (2005).
3. I. Listerman, A. K. Sapra, K. M. Neugebauer, *Nat. Struct. Mol. Biol.* **13**, 815–822 (2006).
4. E. W. J. Wallace, J. D. Beggs, *RNA* **23**, 601–610 (2017).
5. G. Bird, D. A. Zorio, D. L. Bentley, *Mol. Cell. Biol.* **24**, 8963–8969 (2004).
6. M. Tellier, I. Maudlin, S. Murphy, *WIREs RNA* **11**, e1593 (2020).
7. P. J. Curtis, N. Mantei, C. Weissmann, *Cold Spring Harb. Symp. Quant. Biol.* **42**, 971–984 (1978).
8. M. J. Dye, N. Gromak, N. J. Proudfoot, *Mol. Cell* **21**, 849–859 (2006).
9. L. E. Giono, A. R. Kornblihtt, *Biochem. J.* **477**, 3091–3104 (2020).
10. M. de la Mata *et al.*, *Mol. Cell* **12**, 525–532 (2003).
11. B. J. Natalizio, N. D. Robson-Dixon, M. A. Garcia-Blanco, *J. Biol. Chem.* **284**, 8692–8702 (2009).
12. C. L. Will, R. Lührmann, *Cold Spring Harb. Perspect. Biol.* **3**, a003707 (2011).
13. S. M. Mount, I. Pettersson, M. Hinterberger, A. Karmas, J. A. Steitz, *Cell* **33**, 509–518 (1983).
14. C. Boesler *et al.*, *Nat. Commun.* **7**, 11997 (2016).
15. S. M. Vos *et al.*, *Nature* **560**, 607–612 (2018).
16. G. Weber, S. Trowitzsch, B. Kastner, R. Lührmann, M. C. Wahl, *EMBO J.* **29**, 4172–4184 (2010).
17. Y. Kondo, C. Oubridge, A. M. van Roon, K. Nagai, *eLife* **4**, e04986 (2015).
18. D. A. Pomeranz Krummel, C. Oubridge, A. K. Leung, J. Li, K. Nagai, *Nature* **458**, 475–480 (2009).
19. B. Spiluttini *et al.*, *J. Cell Sci.* **123**, 2085–2093 (2010).
20. K. Bertram *et al.*, *Cell* **170**, 701–713.e11 (2017).
21. C. Plaschka, P. C. Lin, C. Charenton, K. Nagai, *Nature* **559**, 419–422 (2018).
22. S. Sharma, S. P. Wongpalee, A. Vashisht, J. A. Wohlschlegel, D. L. Black, *Genes Dev.* **28**, 2518–2531 (2014).
23. C. Charenton, M. E. Wilkinson, K. Nagai, *Science* **364**, 362–367 (2019).
24. X. Zhan, C. Yan, X. Zhang, J. Lei, Y. Shi, *Cell Res.* **28**, 1129–1140 (2018).
25. B. L. Robberson, G. J. Cote, S. M. Berget, *Mol. Cell. Biol.* **10**, 84–94 (1990).
26. J. Ule, B. J. Blencowe, *Mol. Cell* **76**, 329–345 (2019).

27. S. Vagner, U. Rüegsegger, S. I. Gunderson, W. Keller, I. W. Mattaj, *RNA* **6**, 178–188 (2000).
28. D. Kaida *et al*., *Nature* **468**, 664–668 (2010).
29. A. E. Almada, X. Wu, A. J. Kriz, C. B. Burge, P. A. Sharp, *Nature* **499**, 360–363 (2013).
30. P. K. Andersen, S. Lykke-Andersen, T. H. Jensen, *Genes Dev.* **26**, 2169–2179 (2012).

ACKNOWLEDGMENTS

We thank C. Dienemann and U. Steuerwald for support at the microscope and maintaining the EM facility, T. Schulz for maintaining cells and thymus tissue, and P. Rus and U. Neef for running the insect cell facility. **Funding:** S.Z. was supported by an EMBO long-term fellowship (ALTF 830-2018). S.A. was supported by H2020 Marie Curie Individual Fellowship (894862). P.C. was supported by the Deutsche Forschungsgemeinschaft (EXC 2067/1-390729940) and the European Research Council Advanced Investigator Grant CHROMATRANS (grant agreement 882357).

Author contributions: S.Z. designed and performed all experiments, collected and analyzed cryo-EM data, determined the structure, and carried out biochemical analysis. S.A. assisted with cryo-EM data processing. R.L., S.A., and S.M.V. provided advice. S.M.V. and D.E.A. performed related preliminary experiments. D.E.A. and R.L. provided U1 snRNP. P.C. supervised research. S.Z. and P.C. wrote the manuscript, with input from R.L. **Competing interests:** The authors declare no competing interests. **Data and materials availability:** The cryo-EM maps and atomic coordinates were deposited in the Electron Microscopy Data Bank under accession codes EMD-11972 (overall map), 11973 (focused refined map at interface), 11974 (focused refined map of U1 snRNP), and 11975 (map with 155-nt RNA) and in the Protein Data Bank under ID 7B0Y. Materials are available from P.C. upon request under a material transfer agreement with the Max Planck Society.

SUPPLEMENTARY MATERIALS

science.sciencemag.org/content/371/6526/305/suppl/DC1
Materials and Methods
Figs. S1 to S9
Table S1
References (*31*–*47*)
MDAR Reproducibility Checklist
Movies S1 and S2

9 October 2020; accepted 7 December 2020
10.1126/science.abf1870



Ultraviolet Monochromator

The McPherson 234/302 compact vacuum-ultraviolet spectrometer has a digital grating drive for precise wavelength selection and positioning from 30 nm to 1,100 nm. Micrometer adjustable slits vary from 0.01 mm~3 mm in width and 2 mm~20 mm in height. Software is available along with LabVIEW drivers. This instrument's normal incidence design has optional multiple input or output ports. It can also be easily used as a spectrograph with a microchannel plate intensifier or charge-coupled device detector, or as a scanning monochromator—one instrument can do both functions while remaining under vacuum. There are many options for customization: We can provide ultrahigh vacuum nonmagnetic versions or customized adapters for the customer's vacuum pumps, detectors, or light sources. Double monochromators for exceptionally low stray light and high spectral purity are also available. Special or standard, every instrument ships with certified spectral calibration.

McPherson
For info: 800-255-1055
www.mcphersoninc.com

Rack Scanner

Compatible with all 2D-barcoded tube racks in SBS format and with a footprint of only slightly more than one plate/rack position, the Ziath DataPaq Express offers a space-saving way to integrate a fast full-rack scanner onto a liquid-handling robot. Designed with a separate power and processing box that can be positioned under your liquid-handling robot and under your deck, this compact scanner frees up vital deck space. Its uniquely low form factor allows liquid-handling robots easy gripper access to simply pick up and dispense from racks on top of the scanner. Offering rapid image scanning and decoding in just 2 s, the camera-based DataPaq Express will also help improve your robotic workflow. Baseplates and drivers are available to enable easy integration with most commercial liquid-handling robots.

Ziath
For info: 858-880-6920
www.ziath.com

Personal Benchtop Evaporator for DMSO and DMF Samples

The Smart Evaporator C1 from BioChromato is an easy-to-use, affordable system optimized to concentrate or dry single samples directly from any tube or vial (up to 32-mm neck diameter) in even high-boiling solvents such as DMSO, DMF, or water. Drawing on BioChromato's patented spiral plug evaporation technology, the compact, benchtop system offers fast, effective evaporation in tubes or vials without solvent bumping, eliminating the risk of sample loss and cross-contamination and saving valuable time. The Smart Evaporator C1 can handle solvent volumes up to 40 mL, which can be extremely useful for concentrating compounds after organic synthesis or for drying analytical samples at relatively high speeds. The versatile C1 can also manage small tubes and vials (e.g., 1.5 mL) where solvent volumes can be as little as 0.1 mL or less.

BioChromato
For info: +81-(0)-466-23-8382
biochromato.com/smart-evaporator

Specialist Microplates

Porvair Sciences provides a complete design and manufacture service to help customers develop new and innovative custom microplates for specialist applications. We are widely recognized as a leader in the field of molding ultrapure plastic materials such as polystyrene, polypropylene, and polycarbonate. Decades of experience in ultrasonic welding, surface treatment techniques, co-sintering of polymers/silicas, and specialist assembly, combined with a strong understanding of analytical applications, make us an ideal OEM partner for development and production of optimized custom microplate solutions. From single-well to 1,536-well microplates, Porvair Sciences has the knowledge, expertise, and flexibility to design and manufacture to customer specifications. Our team of engineers and creative thinkers allows us to develop high-quality products for filtration, storage, and separation and to push the boundaries of microplate design for the life science and analytical markets.

Porvair Sciences
For info: 800-552-3696
www.microplates.com/custom-manufacturing

High-Pressure Reactor

With its unique safety-locking mechanism and robust, adjustable support frame/lifting platform option, the Multicell PLUS high-pressure reactor from Asynt sets a new benchmark for operator safety, all-round accessibility, and ease-of-use. Manufactured from 316 stainless steel, the unit operates at pressures up to 50 barg and temperatures up to 200°C. Asynt offers options for the system to be manufactured from alternative materials that can withstand highly corrosive/caustic chemicals, and for increased operational conditions up to 200 barg and temperatures of over 300°C. While the Multicell PLUS accommodates 8 × 30 mL cells as standard, options are offered for 4-, 6-, and 10-cell arrangements with individual cell volumes up to 100 mL. Motor-driven, magnetically coupled overhead stirring is also offered as an option for more viscous reaction mixtures. Optional independent isolation of each cell allows the user to charge each vessel with differing chemistry and pressures without cross-contamination between cells.

Asynt
For info: +44-(0)-1638-781709
www.asynt.com/product/multicell-plus

Single-Cell Westerns

Milo is the world's first automated single-cell Western (scWestern) platform. The instrument measures protein expression in thousands of cells in a single run, allowing you to profile heterogeneity in your samples through single-cell analysis. Just load your cell suspension, and the scWest chip captures ~1,000 single cells. Milo then performs a fast, 1-min SDS-PAGE (sodium dodecyl sulphate–polyacrylamide gel electrophoresis) separation on each single-cell lysate on-chip. Then just probe with your favorite conventional Western blot antibodies to measure ~12 proteins per cell using a variety of multiplexing strategies. Milo's Single-Cell Western technology unlocks the single-cell proteome to measure more of the proteome than is possible with any other single-cell protein analysis technique.

ProteinSimple
For info: 888-607-9692
www.proteinsimple.com

Electronically submit your new product description or product literature information! Go to www.sciencemag.org/about/new-products-section for more information.

Newly offered instrumentation, apparatus, and laboratory materials of interest to researchers in all disciplines in academic, industrial, and governmental organizations are featured in this space. Emphasis is given to purpose, chief characteristics, and availability of products and materials. Endorsement by *Science* or AAAS of any products or materials mentioned is not implied. Additional information may be obtained from the manufacturer or supplier.

Massachusetts Institute of Technology

Faculty Position
Department of Biological Engineering

The MIT Department of Biological Engineering invites applications for tenure-track faculty positions at the assistant professor level, to begin July 2021 or on a mutually agreeable date thereafter. Applicants should hold a Ph.D. in a science or engineering discipline related to biological engineering by the beginning of employment. A more senior faculty appointment may be considered in special cases. Candidates should aspire to direct a leading research program that fuses molecular/cellular bioscience with quantitative engineering analysis/synthesis approaches. Areas of high priority include non-medical biotechnology, including applications in materials, chemicals, agriculture, sustainability, energy and the environment. Faculty duties include teaching at the graduate and undergraduate levels as well as oversight of research, and candidates should be capable of instructing in our core biological engineering educational curricula.

Candidates must register with the BE search website at http://be-fac-search.mit.edu, and must submit application materials electronically to this website. Candidate applications should include a description of professional interests and goals in both teaching and research. Each application should include a curriculum vita and the names and addresses of three or more references who will provide recommendation letters. References should submit their letters directly at the http://be-fac-search.mit.edu website.

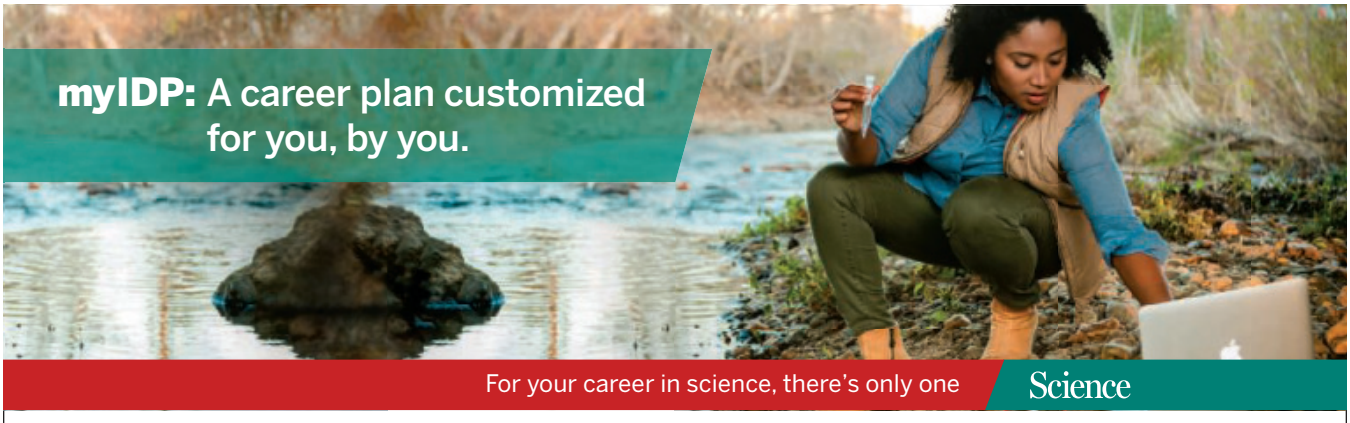
Applications received by February 28, 2021 will be given priority.

Questions may be directed to: Prof. Angela Belcher, Head, Department of Biological Engineering MIT16-343, Cambridge MA 02139, bedh@mit.edu.

With MIT's strong commitment to diversity in engineering and science education and research, we especially encourage those who will contribute to our diversity and outreach efforts to apply.

MIT is an equal employment opportunity employer. All qualified applicants will receive consideration for employment and will not be discriminated against on the basis of race, color, sex, sexual orientation, gender identity, religion, disability, age, genetic information, veteran status, ancestry, or national or ethnic origin. MIT's full policy on nondiscrimination can be found at https://policies.mit.edu/policies-procedures/90-relations-and-responsibilities-within-mit-community/92-nondiscrimination

http://web.mit.edu



Features in myIDP include:

- Exercises to help you examine your skills, interests, and values.
- A list of 20 scientific career paths with a prediction of which ones best fit your skills and interests.

myIDP

Visit the website and start planning today!
myIDP.sciencecareers.org

Science Careers | AAAS In partnership with:

FASEB Federation of American Societies for Experimental Biology
University of Massachusetts Medical School
UCSF University of California San Francisco
UIC
BURROUGHS WELLCOME FUND

ScienceCareers online @sciencecareers.org

ScienceCareers
FROM THE JOURNAL SCIENCE AAAS

Confused about your next career move?

Download Free Career Advice Booklets!

ScienceCareers.org/booklets





FIND YOUR HAPPIER PLACE.



Find your next job at ScienceCareers.org

There's scientific proof that when you're happy with what you do, you're better at what you do. Access career opportunities, see who's hiring and take advantage of our proprietary career-search tools. Get tailored job alerts, post your resume and manage your applications all in one place: sciencecareers.org

ScienceCareers

FROM THE JOURNAL SCIENCE AAAS

By **Gabriela Goldberg**

No use in shouting

A ping interrupts the podcast coming through my headphones. It's 6 a.m. and I am working in the tissue culture room after an early start because of pandemic-related social distancing requirements. The message is probably from my family who live across the country, 3 hours ahead of me. I finish adding media to my cells, return the dishes to the incubator, take off my gloves, and grab my phone. I read the screen and let out a deep sigh. It's a WhatsApp message from my mom, with a link to a petition she started and wants me to sign.

She heard the promising preliminary results for the COVID-19 vaccines, and she argues that government officials should get vaccinated first because they are essential workers making critical decisions. It sounds rational. But knowing my mom, it stems from her belief in conspiracies. She probably thinks government workers should be the ones forced to prove the vaccines are safe.

You see, what I've learned in my pursuit of a biomedical Ph.D. doesn't exactly match up with the beliefs I grew up with—that all pharmaceutical drugs are bad, the government has the cure for cancer, and natural remedies can cure all ailments. When I had a stomachache, we would call my grandmother to practice reiki healing from a continent away. My mom would place her hands on my belly and channel my grandmother's energy. I believed that whether the pain subsided depended on outside sources, such as a lunar eclipse or tropical storm, either amplifying or blocking her energy.



"I don't try to convince my parents that their beliefs are wrong."

My thinking began to evolve when I took biology in high school and learned that bananas release ethylene gas, causing surrounding fruits to ripen. This sounded like a cousin of the energy that relieved my aching stomach! I enthusiastically explained every detail to my parents. At first, they welcomed my excitement; they have always been completely supportive of me and my scientific pursuits. But as the topics we discussed progressed from ethylene gas to medicine, the dinner table transformed from a classroom to a debate floor. When I told them how chemotherapy targets rapidly dividing cells, for example, they argued that the treatment is prescribed solely for the financial benefit of doctors and pharmaceutical companies, and they noted a friend who beat cancer with a superfood-rich diet.

Over time, I learned that our dinner table debates would never bridge the gap between my parents' views and mine. We needed to make it more of a conversation, in which I tried to understand their beliefs before offering my knowledge. For example, after learning about penicillins in college, I was eager to tell my parents. First, though, I asked what they knew about these antibiotics. I learned that they assume doctors prescribe them for everything, and they believe natural remedies are safer and more effective. I told them I agree that doctors overprescribe antibiotics, and I went on to share that penicillins were discovered in naturally occurring fungi. Now they were listening, and we went on to have a fruitful discussion.

We had some tense, contentious moments over the years, but we finally got to a good place. I don't try to convince my parents that their beliefs are wrong; instead, I try to help them find the balance between honoring their beliefs and recognizing scientific truths.

Then, COVID-19 happened. They reached out to me with their questions and concerns, and it quickly became clear that they had fallen victim to dangerous conspiracy theories, believing masks and social distancing were a form of government control. Over several phone calls, I listened first and considered their views when I shared what I knew about the virus. And thanks to the hard work we had all done to understand each other's perspectives and practice our communication, they ultimately accepted that the virus is real and they need to take precautions.

Now that there are approved vaccines, I'm gearing up for the next round of give-and-take conversation. At times it's frustrating to feel we keep starting over—but I remind myself that we aren't back at square one. We've built a foundation of mutual understanding and respect, and that makes all the difference. ■

Gabriela Goldberg is a Ph.D. student at the University of California, San Diego. Send your career story to SciCareerEditor@aaas.org.

ILLUSTRATION: ROBERT NEUBECKER

CALL FOR PAPERS

SPJ
SCIENCE PARTNER JOURNALS



Journal of Remote Sensing

The *Journal of Remote Sensing* is an online-only Open Access Science Partner Journal published in affiliation with **Aerospace Information Research Institute, Chinese Academy of Sciences (AIR-CAS)** and distributed by the **American Association for the Advancement of Science (AAAS)**. Like all partners participating in the Science Partner Journal program, the *Journal of Remote Sensing* is editorially independent from the *Science* family of journals and AIR-CAS is responsible for all content published in the journal. This journal covers multiple research areas that include theory, science, technology of remote sensing, and interdisciplinary research with earth science and information science. Particular topics of interest within the journal include radiative transfer modeling, biogeosciences remote sensing, remote sensing of energy, and more.

Submit your research to the *Journal of Remote Sensing* today!

Learn more at **spj.sciencemag.org/remotesensing**

The Science Partner Journal (SPJ) program was established by the American Association for the Advancement of Science (AAAS), the nonprofit publisher of the *Science* family of journals. The SPJ program features high-quality, online-only, Open Access publications produced in collaboration with international research institutions, foundations, funders and societies. Through these collaborations, AAAS furthers its mission to communicate science broadly and for the benefit of all people by providing top-tier international research organizations with the technology, visibility, and publishing expertise that AAAS is uniquely positioned to offer as the world's largest general science membership society.

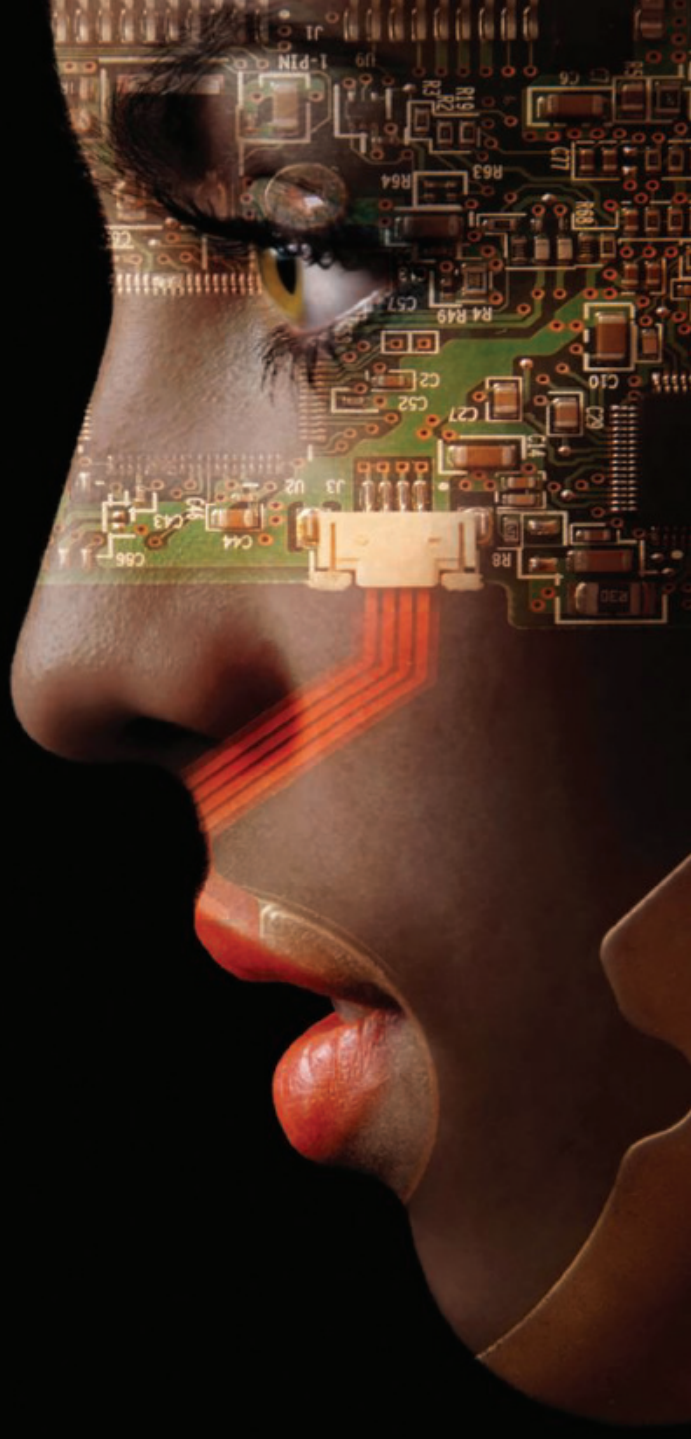
Visit us at **spj.sciencemag.org**

@SPJournals **@SPJournals**

OPEN ACCESS

ARTICLE PROCESSING CHARGES WAIVED UNTIL JULY 2023

ScienceRobotics.org



DOESN'T YOUR RESEARCH DESERVE THE BEST READERS?

Submit your research: **cts.ScienceMag.org**

Science Robotics
AAAS

Twitter: @SciRobotics
Facebook: @ScienceRobotics